A multi-scale, MPMxDEM, numerical modelling approach for geotechnical structures under severe loading

Sacha Duverger

Aix*Marseille université
Socialement engagée

NNT/NL : 2023AIXM0035/003ED353

THÈSE DE DOCTORAT

Soutenue à Aix-Marseille Université
le 10 février 2023 par

Sacha DUVERGER

A multi-scale, MPMxDEM, numerical modelling approach for geotechnical structures under severe loading

Discipline
Sciences pour l'Ingénieur

Spécialité
Mécanique des solides

École doctorale
ED 353 Sciences pour l'ingenieur : Mécanique, Physique, Micro et Nanoélectronique

Laboratoire/Partenaires de recherche
INRAE, Aix Marseille Univ, RECOVER

Composition du jury

Frédéric DUFOUR Professeur des Universités Grenoble INP	Rapporteur
Guillaume CHAMBON Directeur de Recherche, INRAE	Rapporteur
Alba YERRO-COLOM Assistant Professor, Virginia Tech	Examinatrice
Pierre PHILIPPE Directeur de Recherche, INRAE	Directeur de thèse
Jérôme DURIEZ Chargé de recherche, INRAE	Co-directeur de thèse
Stéphane BONELLI Directeur de Recherche, INRAE	Examinateur

INRAE

Affidavit

Je soussigné, Sacha Duverger, déclare par la présente que le travail présenté dans ce manuscrit est mon propre travail, réalisé sous la co-direction scientifique de Pierre Philippe et Jérôme Duriez, dans le respect des principes d'honnêteté, d'intégrité et de responsabilité inhérents à la mission de recherche. Les travaux de recherche et la rédaction de ce manuscrit ont été réalisés dans le respect à la fois de la charte nationale de déontologie des métiers de la recherche et de la charte d'Aix-Marseille Université relative à la lutte contre le plagiat.

Ce travail n'a pas été précédemment soumis en France ou à l'étranger dans une version identique ou similaire à un organisme examinateur.

Fait à Aix-en-Provence le 25/11/2022

Liste de publications et participation aux conférences

Liste des publications réalisées dans le cadre du projet de thèse :

1. Sacha Duverger and Jérôme Duriez (Aug. 2021). *PyCBG, a python module for generating CB-Geo MPM input files*. Version 1.1.4. DOI: 10.5281/zenodo.5179973
2. Hidetaka Saomoto, Naotaka Kikkawa, Shuji Moriguchi, et al. (2023). "Round robin test on angle of repose: DEM simulation results collected from 16 groups around the world". In: *Soils and Foundations* 63
3. Sacha Duverger, Vasileios Angelidakis, Jérôme Duriez, et al. (2023). "Methodological and physical aspects of angle of repose studies". In: *To be decided*. En phase de finalisation

Participation aux conférences au cours de la période de thèse :

1. Sacha Duverger, Jérôme Duriez, Pierre Philippe, et al. (2021). "Rattlers' involvement for possibly looser critical states under higher mean stress". In: *EPJ Web of Conferences*. Vol. 249. EDP Sciences, p. 11002 (Powders and Grains 2021)
2. Sacha Duverger, Jérôme Duriez, Pierre Philippe, et al. (2022). "Multi-scale granular mechanics using MPM x DEM". In: *Congrès Français de Mécanique (CFM-2022)*

Participation aux écoles d'été au cours de la période de thèse :

1. 32th ALERT Doctoral School (september 2021) organized by ALERT Geomaterials in Aussois (Savoie)
2. Mécanique et risques en génie civil (february 2020) organized by RECOVER in Marseille
3. Physics of granular suspensions : micro-mechanics of geophysical flows (june 2021) organized by CISM in Udine (Italy)

Résumé

Des barrages et des digues sont construits à travers le monde afin d'assurer la production d'énergie et la sécurité des populations. De telles constructions peuvent avoir des tailles conséquentes, s'étendant sur des kilomètres, et sont souvent construites avec des matériaux granulaires. Leur comportement découle de mécanismes complexes ayant lieu à l'échelle du grain et s'en trouve difficile à décrire. Les lois constitutives utilisées habituellement pour d'autres matériaux plus homogènes, tels que l'acier, peinent à reproduire le comportement des matériaux granulaires pour des chemins de chargement quelconques. Des modèles plus précis ont été mis au point en se basant sur une description non continue du matériau à l'échelle du grain, permettant ainsi la prise en compte de phénomènes microscopiques importants. Parmi ces modèles, la Méthode des Éléments Discrets (DEM) décrit le comportement des matériaux granulaires avec une bonne précision en modélisant directement l'ensemble des grains qu'il contient. Le coût numérique de cette méthode est cependant assez élevé, un mètre cube de matériau granulaire pouvant contenir des dizaines de milliards de grains, ce qui nécessiterait des années de calculs sur la plupart des super-ordinateurs actuels. La DEM ne permet donc pas d'accéder à l'échelle des ouvrages.

Cette thèse propose une façon d'utiliser la DEM pour décrire le comportement de matériaux granulaires au sein d'une méthode basée sur la continuité du matériau, la Méthode du Point Matériel (MPM), remplaçant ainsi de fait la loi constitutive phénoménologique. Un tel couplage MPMxDEM peut-être envisagé pour modéliser de grands ouvrages avec la précision de la DEM, même dans les cas où des déformations importantes empêcheraient la Méthode des Éléments Finis (FEM) de poursuivre son calcul.

Dans une première partie, deux études DEM sont menées à l'aide du logiciel open-source YADE sur un matériau réel et concernent d'abord l'angle de repos formé par un empilement de grains soumis à la gravité puis l'implication des "rattlers" (particules avec 0 ou 1 contact) dans la description de l'état critique en l'absence de gravité. Ensuite, une analyse des paramètres fondamentaux de la formulation de la MPM est menée, dans le cadre de l'utilisation du code open source CB-Geo MPM. La dissipation excessive d'énergie que présentent certains schémas MPM est mise en évidence dans le cas simple d'un cube élastique qui rebondit.

Dans une seconde partie, le couplage MPMxDEM est formulé explicitement, en détaillant l'hypothèse de quasi-staticité faite à l'échelle microscopique. Différents aspects de notre implémentation MPMxDEM sont discutés, notamment l'intégration de l'interface Python de YADE dans le code C++ de CB-Geo MPM. Cela inclut la

présentation d'un module Python, développé dans le cadre de cette thèse, qui sert d'interface à CB-Geo MPM en intégrant les spécificités du couplage MPMxDEM. Une analyse des performances de notre implémentation montre par la suite que, si judicieusement paramétrée, une parallélisation du code peut considérablement accélérer les simulations MPMxDEM. Notre implémentation MPMxDEM est ensuite validée sur la base de résultats d'un essai triaxial pur DEM, réalisé sur un modèle numérique du sable de Camargue.

Le cas de l'effondrement d'une colonne de sable est finalement étudié, en pure MPM avec le modèle de Mohr-Coulomb et en MPMxDEM. Une analyse de la déformation imposée par la MPM pour le calcul local DEM démontre que notre hypothèse de quasi-staticité est indispensable afin de réaliser une telle simulation en un temps raisonnable. Il est observé que la MPM ralentit excessivement la chute de la colonne, par rapport à des résultats expérimentaux mais aussi numériques, obtenus avec d'autres méthodes. Cependant, l'étalement final obtenu pour nos colonnes MPMxDEM est en accord raisonnable avec les résultats produits à l'aide d'une autre approche multi-échelles similaire.

Mots clés : Multi-échelles, DEM, MPM, matériaux granulaires

Abstract

Throughout the world, dam and dikes are constructed to ensure energy production and security of the populations. Such hydraulic structures can be quite large, spanning over kilometers, and are often made of granular materials. The study of the latter has long been challenging because their behaviour emerges from complex phenomena occurring between grains, at the microscopic scale. Usual constitutive laws used for other materials, e.g. for steel, thus struggle to handle the variety of loading paths a granular material may be subjected to. More accurate models were developed by considering a non-continuous description of the material at the grain scale, making possible the inclusion of important microscopic phenomena. For instance, Discrete Element Method (DEM) directly models all constitutive grains, resulting in an expensive but also very accurate description of any granular material. Indeed, a cubic meter of granular material can contain tens of billions particles, requiring years of calculation on most super-computers. The structure scale is thus unreachable with DEM simulations.

This thesis demonstrates how DEM can be used to describe the behaviour of granular materials within a continuum-based method, the Material Point Method (MPM), thus replacing the usual constitutive laws. Such a MPMxDEM coupling can be implemented to model earth dams and dikes at large scales with a DEM accuracy, even when deformations reach a point where the traditional Finite Element Method (FEM) is unable to continue the simulation.

First, two DEM studies are performed on an artificial real-life material using the open-source software YADE. The angle of repose formed by a heap of particles and the role of rattlers at critical state are therein examined through the execution of many simulations. As for the MPM, a parametric study is performed after detailing its formulation, which is linked to the MPM open-source code used in this thesis (CB-Geo MPM). More precisely, the excessive dissipative properties of PIC-based MPM velocity update strategies are highlighted in the simple case of a bouncing elastic cube.

A MPMxDEM formulation is next provided, including specifics of the quasi-static assumption made at the microscopic scale. Technical aspects on how our MPMxDEM implementation embeds the Python user interface available in YADE into the C++ source code of CB-Geo MPM are discussed. In particular, details are given on how a Python module developed during this thesis implements an interface for CB-Geo MPM and the MPMxDEM framework. A speed-up analysis of our MPMxDEM implementation performed on a server machine then assesses its performances, demonstrating that simulations can be considerably accelerated through paral-

lelization. Our MPMxDEM implementation is shown to be capable of reproducing accurately pure DEM results in the case of a one cell triaxial test, performed on a numerical replica of Camargue's sand.

The well-known case of the collapse of a granular column is finally investigated, using both pure MPM with the Mohr-Coulomb constitutive law and the MPMxDEM coupling, the latter using the best set of parameters determined in the former. An analysis of the deformation involved at each MPM iteration establishes that our quasi-static assumption is necessary to perform a MPMxDEM simulation at this scale, within a reasonable amount of time. It is highlighted that using MPM unrealistically decreases the collapse rate of the column, compared to experimental results as well as results obtained with other numerical methods. However, the final run-out of the collapsed column is found to be in accordance with the values obtained in the literature using a similar multi-scale model.

Keywords: Multi-scale, DEM, MPM, granular materials

Remerciements

Je tiens à exprimer ma gratitude à toutes les personnes qui m'ont permis de réaliser cette thèse, notamment mes encadrants pour leur mentorat ainsi que leur bienveillance. Plus précisément, merci à mon directeur de thèse Pierre Philippe pour ses conseils éclairés durant ces trois années, merci à mon encadrant principal Jérôme Duriez pour sa disponibilité et l'expertise qu'il a pu me transmettre, et merci à Stéphane Bonelli pour la rigueur qu'il a apporté à mon travail.

Un grand merci à Frédéric Dufour, professeur des universités de Grenoble INP, de m'avoir fait l'honneur de présider le jury durant ma soutenance, ainsi que d'avoir rapporté mon manuscrit. Je remercie également Guillaume Chambon, directeur de recherche à l'INRAE de Grenoble, d'avoir lui aussi rapporté mon manuscrit. Merci également à Alba Yerro-Colom, assistant professor at Virginia Tech, d'avoir examiné mes travaux en tant que membre du jury lors de ma soutenance. Je tiens également à exprimer ma reconnaissance à Thierry Faug, directeur de recherche à l'INRAE de Grenoble, et à Patrick Richard, directeur de recherche à l'université Gustave Eiffel, de m'avoir fait part de leur expertise vis-à-vis de mon travail.

J'aimerais aussi remercier l'INRAE de m'avoir accueilli au sein du laboratoire RECOVER, dont l'équipe mérite tout autant de reconnaissance. Merci en particulier à mes collègues doctorants, de m'avoir aiguillé au début de ma thèse mais aussi d'avoir partagé de nombreuses conversations intéressantes avec moi.

Je souhaite remercier finalement ma famille pour le soutien qu'ils m'ont apporté durant ma thèse mais aussi au cours de toutes mes études.

Table des matières

Table des figures

Liste des tableaux

Introduction

Necessity of modeling heavily loaded granular materials at large scale

Human activities such as industries, agriculture, or simply dwelling lead to the necessity for energy production, irrigation, and security. Dams fulfill these needs by serving as energy production facilities and flow regulator on rivers, while dikes protect habitations and roads to insure the people's security. Such constructions may be subject to harsh environmental loading conditions that would threaten the safety of populations, making the accuracy of their study a crucial challenge. These large structures are often made of granular materials and the prediction of their behaviour requires an understanding of the microscopic mechanisms inside the material that can be very challenging to grasp. Moreover, the weight and environment of such constructions solicit them at a point where common mechanical models suited for small deformations are not efficient enough to provide an accurate prediction.

(a) A dam
https://images.app.goo.gl/6LiVsFbFfHb4KqAm8

(b) A dike
https://images.app.goo.gl/GVJnDuYNaVLpzQBC7

FIGURE 0.1. – Example of large hydraulic constructions

Example of the Teton dam

The Teton dam in Idaho (United States of America) is an example of a large hydraulic construction (spanning over almost 1 km and 93 m hight) that collapsed, causing many human and material damages (see figure 0.2). This dam's construction

began in February 1972 and was completed in November 1975, after which it was impounded. The 5^{th} June 1976 as the filling was almost complete, a leak was found to contain sediment, which means that the dam began to be internally eroded. Two hours later, the water flowed through the leak at an alarming rate of more than half a cubic meter every second. Less than five hours after the leak was first noticed, the dam had collapsed.

(a) Leak has started
https://en.wikipedia.org/wiki/File:Teton_Dam_Sequence_00.jpg

(b) Leak has grown wider
https://en.wikipedia.org/wiki/File:Teton_Dam_Sequence_13.jpg

(c) Dam has collapsed
https://en.wikipedia.org/wiki/File:Teton_Dam_failure.jpg

FIGURE 0.2. – Teton dam collapse

The failure was attributed to a lack of impermeability which led to the internal erosion of the dam: water flowing through the leak teared some grains out of the dam, making the leak wider and wider, until failure. The collapse of the Teton dam killed 16 people, and cost approximately billions dollars, which is 20 times its construction cost. A better understanding of the phenomena occurring within the dam at the microscopic scale would have certainly help preventing such a catastrophe, making essential the study of granular materials used for geotechnical structures.

Modelling methods

In mechanics, the behaviour of materials is modelled using constitutive laws, i.e. equations connecting the stress path the material follows to its deformation state. However, the behaviour of most of the materials used in civil engineering depends on the history they went through, meaning that their constitutive laws have to include a description of the material's current state, leading to the addition of several parameters. In the case of granular materials, the numerous possible arrangements the grains can have between each other make considerably harder the determination of a set of parameters adequate to characterize the material's state. Indeed, the huge variability in microstructural configurations leads to very different macroscopic behaviours and can change the conclusions of a study. Naturally, using a larger set of parameters improves the state characterization, but these extra parameters often prove difficult to interpret in terms of material properties, and they can hardly manage various loading conditions. An accurate description of a granular material's state thus requires an efficient modelling of its microstructure, involving a limited number of parameters compared to the variety of cases it can handle.

A great efficiency can be reached by considering a set of interacting discrete elements, representing the granular assembly directly at the microscopic scale and thus automatically accounting for the material's history. However, because the grain scale is significantly smaller than the structure scale, an tremendous amount of discrete elements have to be accounted for civil engineering problems. In practice, nowadays' computers are far from capable of modelling an entire geotechnical structure with a microscopic resolution, thus imposing the use of a constitutive law.

Traditionally, the evolution of a structure under a specific loading condition is determined by assuming the continuity of the material it is made of, and then computing its behaviour only at a finite set of points. Recent approaches aimed to replace the usual constitutive law by an accurate microscopic model for the material's behaviour, such as the one mentioned in the previous paragraph. The resulting method can be qualified as multi-scale, since it describes both the material at the microscopic scale and the structure, at a much larger scale. This technique makes possible the modelling of an entire geotechnical structure on nowadays' computers, while retaining valuable microscopic insights, necessary to the accurate description of granular materials. However, such models are still quite new and only a very limited amount of studies have implemented them, specially in the case of large deformations.

This thesis aims to study the accuracy of a multi-scale method when large deformations are involved, a situation of great interest for geotechnical structures.

Outline

The chapter 1 of this manuscript gives an overview of the current numerical methods suitable to granular materials. The influence of microscopic parameters on

the global behaviour of granular materials is then investigated using the Discrete Element Method (DEM) in chapter 2, first by considering the angle of repose formed by an unconstrained sample of granular material, second by determining its shear resistance. A formulation of the Material Point Method (MPM), capable of handling large deformations at large scales, is then given and linked to the C++ open source code (CB-Geo MPM [Kumar, Salmond, Kularathna, et al. 2019]) in chapter 3. In this chapter, the dissipative nature of the MPM is also determined with respect to different choices in the formulation, for the simple case of an elastic cube bouncing on the floor. The multi-scale coupling of the MPM and DEM methods is formulated in chapter 4, where technical details on how CB-Geo MPM was combined with the DEM open-source code YADE [Smilauer et al. 2021] are given as well. Finally, a study on the collapse of a granular column is performed using pure MPM simulations and a MPMxDEM simulation in chapter 5, taking advantage of the multi-scale possibilities offered by the coupling.

1. Literature review

Sommaire

1.1. Granular materials' modelling with the Discrete Element Method

The microscopic insights necessary to predict the behaviour of a granular material are usually captured either by establishing a complex mathematical model or by directly modelling the material at the microscopic scale. Both approaches require a time discretization, although the former is traditionally based on the assumption that the material is continuous, which introduces the need for a spatial discretization. This operation is often assured by a mesh that provides a decomposition of the domain into many elements where the governing equations can be solved. A numerical implementation of these methods is essential to perform the enormous quantity of operations necessary to obtain a useful and reliable result.

The Discrete Element Method (DEM) is a microscopic model able to account for all interactions between the grains constituting a granular sample, making it very suitable to describe the behaviour of such materials. It was first developed in [Cundall and Strack 1979], where a DEM analysis was found to be in accordance with experiments performed on photo-elastic discs [De Josselin de Jong 1969]. It has since been extensively used and improved to predict the behaviour of more probable granular assemblies, such as soils or industrial powders [Ketterhagen and Wassgren 2022]; [Mori and Sakai 2022]. Indeed, DEM is able to describe accurately the material's microscopic features such as grain shape, grain's contact properties or even complex interactions beyond the simple physical contact.

1.1.1. Grain's shape

The use of spheres as grain shape is an evident choice to simplify the computation: contacts are detected based on the vector connecting the centers of the two grains considered, i.e. the branch vector, whose norm is compared to the sum of the grain's radii. The contact's normal direction simply is the branch vector's direction. This very basic model was first employed and is still widely used today [Bono and McDowell 2022]; [Hilse, Kriegeskorte, Illana, et al. 2022]. However, it finds its limitations when modelling realistic materials such as sand, in which grains are non-spherical and can have very sharp edges that prevent them to roll against each other. A simple but efficient improvement is to form grains using several spheres clumped together, i.e. clumps [Kafashan, Wiącek, Abd Rahman, et al. 2019]; [Sibille, Villard, Darve, et al. 2019]. This effectively suppress the excessive rolling between the grains, at the cost of a minor increased computation time for the contacts' detection.

Another shape model is the polyhedron model, able to model sharp grains more accurately. A contact detection formulation is given in [Gilbert, Johnson, and Keerthi 1988], although it is limited to convex shapes it still gives accurate results [Mohamed, Duriez, Veylon, et al. 2022]. A more recent formulation for rounded 2D polygons and 3D polyhedrons is given and experimentally validated on a packing containing a

variety of polyhedral objects in [Langston, Ai, and Yu 2013]; [Mack, Langston, Webb, et al. 2011]. More advanced polyhedron models were developed to extend capabilities to non-convex polyhedron. For instance, [Smeets, Odenthal, Vanmaercke, et al. 2015] proposed a surface mesh based contact detection procedure that is able to handle independently multiple contact points between arbitrarily shaped polyhedra. Efforts were made in [Rakotonirina, Delenne, and Wachs 2017] and in [Govender, Wilke, Wu, et al. 2018] to extend the exclusively convex polyhedron model to non-convex particles using a convex decomposition of the particles' geometry, at the cost of higher memory requirements.

A more complex shape model is the "potential particles" model [Boon, Houlsby, and Utili 2013]; [Houlsby 2009], giving angular particles with rounded edges. It actually constructs the grains as a combination between a sphere and a polyhedron, restricting its shape to convex particles. More recently, a generic shape description was formulated for DEM, namely the Level Set DEM (LS-DEM), which is able to describe any shape at a reasonable computational cost [Duriez and Galusinski 2021]; [Kawamoto, Andò, Viggiani, et al. 2016]. This shape model uses a finite number of nodes on a particle's surface along with a distance function to determine the contact existence and geometry. It was found to benefit from an OpenMP parallelization (presented in section 1.1.5) with a speedup to number of threads ratio of almost 0.5 [Duriez and Bonelli 2021], making this shape model a good compromise between a realistic description of the grain's geometry and computational cost.

Figure 1.1 shows an example of particles created using each of these shape models.

1.1.2. Contact model

The contact between two grains is usually based on a simple elastic contact, with the resulting force being proportional to the inter-particle displacement, but can also include different phenomena like friction or viscosity. Basically, two springs in the normal and tangential directions describe the elastic part of the contact, while a sliding condition in the tangential direction represents its frictional part. A description of the contact's geometry is thus necessary and can be quite difficult to obtain depending on the grain's shape. For a contact between two spheres, [Cundall and Strack 1979] computes the normal and tangential displacements incrementally, which is indispensable for the tangential direction but not necessary for the normal direction. Indeed, in many DEM formulations, discrete elements are allowed to overlap each other so the normal displacement is simply the difference between the radii's sum

1. Mohamed, Duriez, Veylon, et al. 2022.

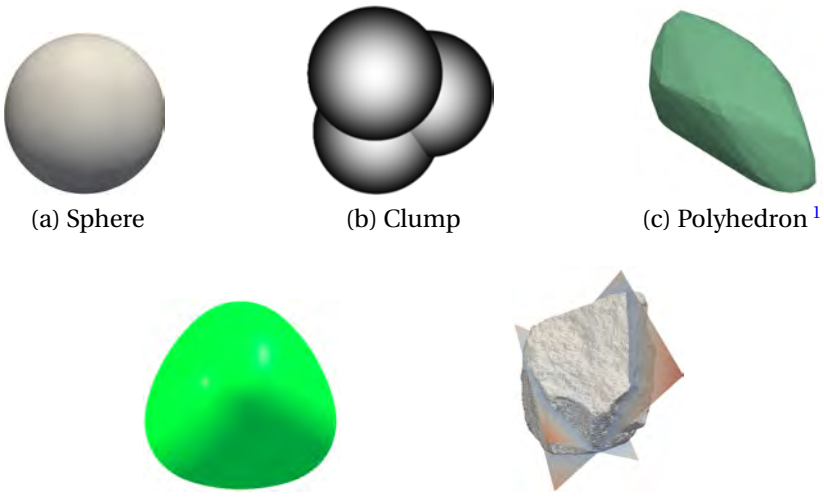

(a) Sphere (b) Clump (c) Polyhedron [1]

(d) Potential particles (e) Level set grain (courtesy of J. Duriez)

FIGURE 1.1. – Several particle's shape models used in DEM

and the branch vector's norm. This overlap mitigates the effects of using a rigid body description for the discrete elements. The frictional force is limited through the consideration of the Coulomb criterion using a friction coefficient that depends on the involved particles' material, defining a threshold above which particles can slide against each other. This basic contact model can be summarized by the following expressions for the contact force:

$$F_n = K_n u_n \tag{1.1}$$

$$F_t = \min\left(K_t u_t, F_n \tan\varphi\right) \tag{1.2}$$

With F_n, F_t the magnitudes of the normal and tangential contact forces, u_n, u_t the normal and tangential displacements, $\tan\varphi$ the friction coefficient defined using the inter-body friction angle φ, K_n the normal stiffness, and K_t the tangential stifness.

However, using such a model doesn't dampen significantly the granular assembly, leading to almost never ending scenarios where particles oscillate around an expected final position. The addition of damping is thus necessary in most cases and can be done in different ways: by considering a constant, arbitrarily defined, damping coefficient for all contacts, or by introducing viscous dissipation in the contact model. The former is usually denoted as "Cundall's damping" and is easy to implement but relies on a non-physical parameter, making the results harder to interpret. Indeed, it increases or decreases the overall contact force applied to each particle component-wise, by a fraction of its value, depending on the orientation of the forces with respect to the particle's velocity. As a contrast to Cundall's damping, viscous damping is considered directly in the contact model by adding to the normal

force a velocity-dependent term, whose importance is determined by a physical viscous coefficient c_n. The sketch in figure 1.2 illustrates such a visco-elastic contact model.

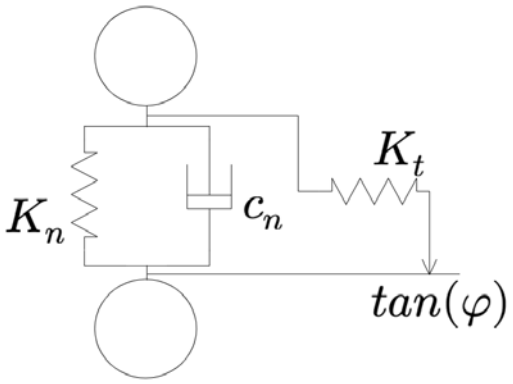

FIGURE 1.2. – Visco-elastic contact model

The contact model can also include rolling and twisting resistances, which effectively solves the excessive rolling between spheres [Sibille, Villard, Darve, et al. 2019]. The resistance is modelled through the addition of a rolling (or twisting) moment opposed to the particles' relative rotation, computed incrementally with a rolling (or twisting) stiffness parameter. A threshold above which plastic rolling (or twisting) occurs should also be defined using a Coulomb-like criterion.

Since DEM simulates all grains in the material, more complex configurations can be easily modelled. For instance, some specific pair of grains can have different contact properties, accounting for the diversity of the grains' properties. One could then consider a material composed of a mixture of grains having different stiffnesses or friction angle. In addition, it is possible to incorporate some randomness, eventually from a series of experimental measurements on the grains' contact properties given as a distribution. Indeed, pairs of grains can be carefully associated with a contact property value so the overall distribution in the DEM assembly matches the one experimentally measured.

1.1.3. Multiphysics capability

Describing the material at the microscopic scale allows the inclusion of different physics in the model, without the need for a complex macroscopic description of the phenomena in question.

A simple way to incorporate a relevant mechanism to a DEM simulation is to consider an additional interaction along with the contact interaction. The cohesion of some granular materials can for instance be accounted for by adding an adhesive force to each contact, depending on relevant parameters for the physical origin of the cohesion. An example of additional cohesive force is the one that arises from the capillary pressure in partially saturated soils. Such an interaction force depends on

the shapes of the capillary bridges of water, linking together neighboring particles and described by the Laplace-Young equation, studied for spheres, e.g. in [Duriez and Wan 2017]. Figure 1.3 shows the general shape of a capillary bridge inducing an attractive force. This model requires a criterion to determine between which grain such water bridges are formed, typically a maximum distance above which a bridge cannot be created.

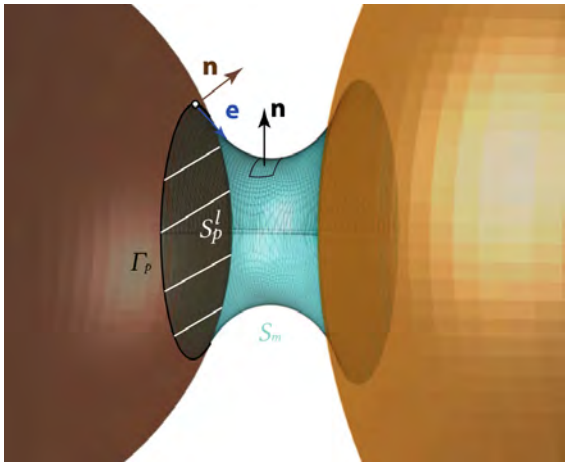

FIGURE 1.3. – Capillary bridge as described in [Duriez and Wan 2017]

Another example is the consideration of a fluid flowing through the porous space between the grains, making possible the description of internal erosion and permeability. Ideally, the fluid should be modelled with a high space resolution, far below the grain scale, to make possible the direct resolution of the fluid's governing equations (i.e. Navier-Stokes equations) through a Direct Numerical Simulation (DNS), using for instance the Lattice-Boltzmann Method (LBM) [He and Luo 1997] or the Finite Volume Method (FVM) [Eymard, Gallouët, and Herbin 2000]. This approach requires a huge amount of computational ressources and thus limits the maximum sample size to a couple hundred particles on standard desktop machines [Chareyre, Cortis, Catalano, et al. 2012]. Using an upscaled model reduces effectively the computational cost while still keeping an accurate description of the fluid, e.g. the continuum-discrete model based on Darcy's law whose formulation is given in [Goodarzi, Kwok, and Tham 2015]. The idea is to model the fluid continuously using an Eulerian mesh where the fluid's density, velocity and pressure are evaluated in each cell. The movements of the grains create a pressure gradient, inducing the fluid flow as well as a drag force on the solid phase. Since the equation of the solid and fluid phases are solved separately, this is considered to be a partially coupled approach. A more accurate description of the fluid/solid interactions was developed in [Chareyre, Cortis, Catalano, et al. 2012], based on the geometry of the pore network separated in many sub-domains using a regular Delaunay triangulation from spheres' centers and radii. Such a model is able to accurately determine the forces on each grain, and to quantify the permeability of the material. An even better accuracy

can be reached using LBM to describe the fluid's motion through the sample and its interactions with the solid phase. In [Han and Cundall 2013], it has been showed able to reproduce qualitatively phenomena observed during experiments, such as buoyancy. Note however that, in some simple situations as during undrained test simulations, the presence of water can be modelled simply by considering a constant sample's volume [Aboul Hosn, Sibille, Benahmed, et al. 2017].

The multi-physics possibilities of DEM are not limited to the addition of interactions between grains. For instance, more complex phenomena like grain breakage can be accounted for [Zhu and Zhao 2019]. Indeed, depending on the granular assembly's loading conditions, some grains might be subject to enough stress for them to break, leading to a noticeable change in important parameters such as the porosity or the particle size distribution.

1.1.4. Periodic boundary conditions

Some DEM simulations might suffer from the existence of boundary effects, such as an excess of voids near a sample's bounding wall, or a uniform contact orientation on the boundary. These issues can be addressed by considering the simulated sample to be the smallest pattern of a material presenting a periodic microscopic structure [Radjai 2018], making the simulation a sort of window on an infinite sample. All particles in the simulation are contained in a main parallelepipedic cell, defined by three base vectors, and their motion originates either from their interactions or from the deformation of the cell. The cell and all the particles it contains can then be reproduced indefinitely, creating an infinite number of particles which are images of the particles in the main cell. The cell's deformations induce an affine velocity field on all particles, which cannot be periodic, thus an extra attention has to be given when considering the relative velocity of a contact involving an image particle.

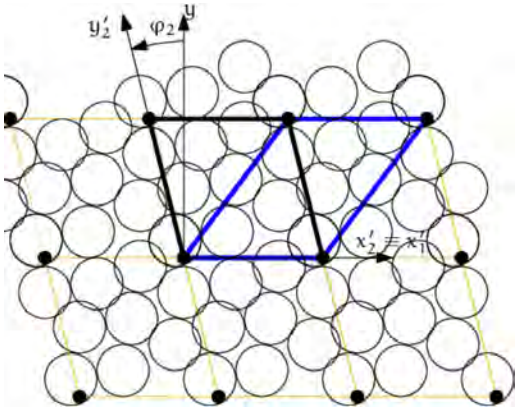

FIGURE 1.4. – Cell flipping in a periodic DEM simulation [Smilauer et al. 2021]

When excessive shearing occurs, the main cell might be distorted at a point where some particles span over more than half the cell, preventing the simulation to conti-

nue. In such scenarios, it is possible to take advantage of the periodicity to rotate the cell's base vectors when the angle between two of them is too low, allowing to indefinitely shear the sample [Kraynik and Reinelt 1992]; [Smilauer et al. 2021]. Indeed, the vertices of the main cell form an infinite regularly spaced grid on which the cell's base vectors can be conveniently redefined. Figure 1.4 shows in 2D how the blue cell can be flipped into the black cell by linear combinations of the base vectors. Limiting the flip to grid points ensures that no particle are duplicated or erased during the flipping process.

1.1.5. Computational aspects

The obvious strength of DEM is its ability to simulate all grains constituting a system and thus derive all microscopic data. However, this comes at a very expensive cost due to the necessity of looping repeatedly over a huge number of particles.

Computational complexity

Contacts' detection is the most expensive step in the DEM procedure. Indeed, the geometries of all particles have to be tested against each other to assess the existence of contacts, which requires a double loop with a complexity of $\mathcal{O}(N_p^2)$, where N_p is the number of particles in the sample. Efforts have been made to improve the efficiency of this nested loop, for instance the so-called sweep and prune algorithm [Cohen, Lin, Manocha, et al. 1995] performs a first approximative detection to reduce the complexity to roughly $\mathcal{O}(N_p \log N_p)$[Smilauer et al. 2021]. Basically, all particles are enclosed in conveniently oriented boxes (i.e. axis aligned bounding boxes) which are sorted in each direction at each time step using an aperiodic insertion sorting algorithm. It is possible to decrease even more the complexity of the contact detection by enlarging each bounding box: if a particle stays inside its enlarged bounding box between two iterations, there is no need to test it again against all other boxes at the second iteration. The resulting complexity depends on how many particles move in the simulation. If for instance all particles stay in their initial enlarged bounding boxes, the set of possible contacts are determined only at the first step and the complexity is thus linear with respect to N_p. Using the sweep and prune technique with enlarged bounding boxes, the contact detection's complexity is thus bounded between $\mathcal{O}(N_p)$ and $\mathcal{O}({N_p}^2)$.

Advanced shape models can increase contacts' detection cost because of the necessity for additional operations for each couple of particles, like in LS-DEM which uses a Discrete Function Representation (DFR) [Williams and O'Connor 1995] to compare complex particle shapes, see figure 1.5. This requires to loop over all surface nodes of a particle, increasing the maximum complexity of the sample-wide contact detection to $\mathcal{O}(N_p \log N_p) + \mathcal{O}(N_{ps} N_c)$, with N_{ps} the number of points on the particles' surface and N_c the number of contacts in the simulation.

Another expensive task is the integration of the equation of motion for all particles. Indeed, all particles have to be moved independently according to their contacts,

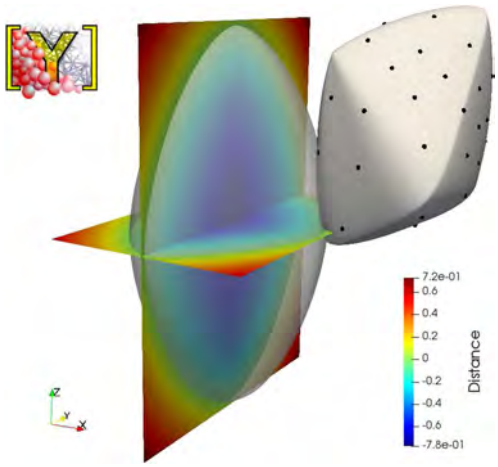

FIGURE 1.5. – LS-DEM contact detection using boundary nodes and a distance function [Duriez and Galusinski 2021]

adding a complexity of $\mathcal{O}(N_p)$. Along with the contacts' detection, these two DEM steps accounts for most of the computation time. Indeed, benchmark simulations [2] performed with the open source code YADE [Smilauer et al. 2021] were found to spend more than 90% of their computation time only on the contact detection and the motion integration. The overall complexity of a DEM simulation using the sweep and prune method with enlarged bounding boxes is thus bounded between $\mathcal{O}(N_p)$ and $\mathcal{O}(N_p(N_p+1))$.

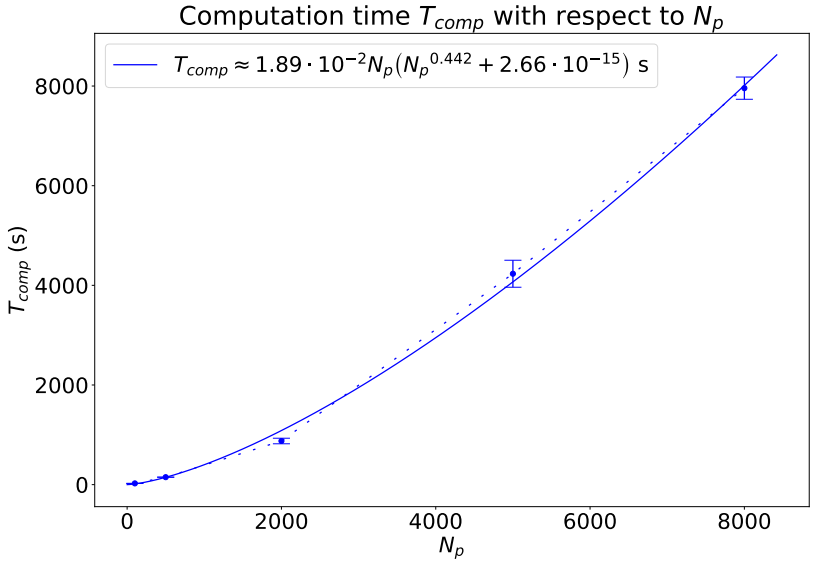

FIGURE 1.6. – DEM computational time cost with respect to N_p

2. See performance scripts in YADE's source code git revision f890b0, examples/test/performance/checkPerf.py

Figure 1.6 shows the total DEM computational time cost T_{comp} for a gravity settlement simulation performed sequentially with different number of particles over $7.5 \cdot 10^5$ iterations using a time step of 10^{-7} s, repeated 5 times for each N_p. The initial state is a cloud of non-overlapping spheres subject to a uniform gravity field, described by the particle size distribution and contact model calibrated on Camargue's sand in [Aboul Hosn, Sibille, Benahmed, et al. 2017]. The DEM results obtained with the calibrated parameters were found to be in great agreement with experiments, see figure 1.7. A model based on the DEM complexity can be determined for the evolution of the computational time cost with respect to N_p:

$$T_{comp} = a N_p \left(N_p^b + c \right) \tag{1.3}$$

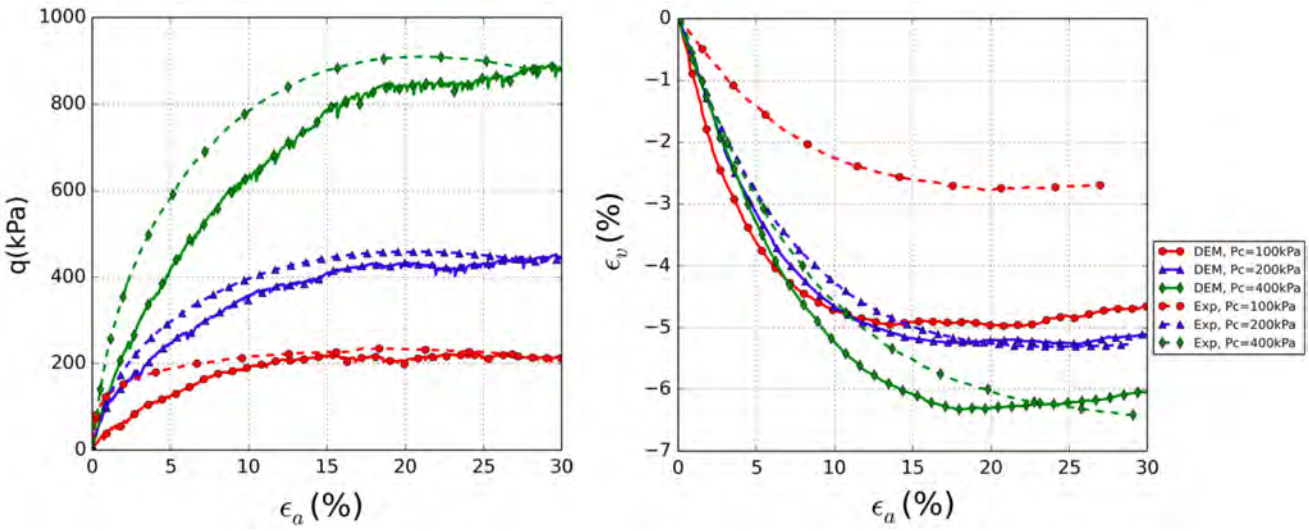

(a) Deviatoric stress

(b) Volumetric strain

FIGURE 1.7. – Triaxial tests results performed in drained conditions on Camargue's sand [Aboul Hosn, Sibille, Benahmed, et al. 2017]

Where a and c are greater than zero, and b is in the interval $[0,1]$, specifically $b \approx 0.44$ in the present example. Note that $b = 1$ without the sweep and prune technique, and $b = 0$ with the sweep and prune technique when particles never leave their enlarged bounding boxes.

Parallelization

These expensive steps can be speeded up using different multiprocessing approaches. For instance the strategy implemented in the OpenMP API (Open Multi-Processing Application Programming Interface) [Dagum and Menon 1998] splits the loops over the particles into several chunks, each fed to a CPU thread. The efficiency of this strategy rests on how the chunks of iterations are determined: when many

threads are available, the loop splitting operation has more importance with respect to the DEM operations, the optimum number of threads to be used thus strongly depends on the simulation. Also, the inter-dependency of the operations performed at each iteration in a split loop can limit the OpenMP efficiency. Indeed, if two iterations managed by two different threads require access to the same global variable at the same time, one of the thread has to wait. This procedure is called "process synchronization" and can be quite solicited in OpenMP-parallelized DEM simulations, for instance during the interaction loop, where each iteration requires access to the particle's data. In [Duriez and Bonelli 2021], it was shown that a LS-DEM triaxial test containing 8000 discrete elements doesn't benefit from using more than ≈ 50 CPU threads on a 104 threads machine, where the speedup reaches ≈ 22. However, the same model was used to simulate the settling of a cloud of particles on the same machine in [Duriez and Galusinski 2021] and no maximum speedup was observed. The former study also shows that using more than 60 threads on a classical DEM simulation, with spheres, results in a slowdown (i.e. a speedup less than 1).

Another strategy is the Message Passing Interface (MPI), which splits the simulation into several subdomains attributed to different threads or even different machines, all managed by a "master" process. For DEM simulations, the contact detection and motion integration steps are thus performed individually in each subdomain, limiting the complexity to $\mathcal{O}(N_p^{sub}(\log N_p^{sub}+1))$, with N_p^{sub} the number of particle in the subdomains. The decomposition into subdomains procedure has then a critical role in the MPI efficiency: N_p^{sub} must be of the same magnitude in each subdomains in order for every processes to work for the same duration. The MPI strategy also alleviates the process synchronization difficulties since less data is common to several threads, i.e. the data at the subdomains interfaces, and it is managed only by the master process. In [Rakotonirina and Wachs 2018], the MPI implementation in the Grains3D DEM code was found to give a linearly increasing speedup with respect to the number of CPU cores, at a rate of 0.91. By its linear evolution, MPI's performances are boundless when OpenMP's performances quickly finds a peak [Duriez and Bonelli 2021], MPI offers thus a better scalability for DEM simulations. Another advantage of MPI is that it allows to relatively easily distribute a simulation to several machines within a cluster, in order to optimize the utilization of the available hardware. Many implementations of this strategy exists, among them the open source code OpenMPI [Graham, Woodall, and Squyres 2005] is one of the most popular.

The use of graphical processing units (GPU) for DEM is tempting because of the large number of threads they make available. However, since GPUs cores are slower and less adaptable than traditional central processing units (CPU), the efficiency difference is difficult to determine. Yet, there are some remarkable implementation of GPU parallelization in the literature. As an example, in [Govender, Wilke, and Kok 2015] more than $32 \cdot 10^6$ polyhedrons are simulated on a NVIDIA Quadro K6000 GPU using BlazeDEM3D-GPU with a contact detection cost of less than 14 seconds per iteration.

Computer \ Sample size	1 m^3 ($5.471 \cdot 10^{10}$ particles)	Teton dam - $2.27 \cdot 10^7$ m^3 ($4.05 \cdot 10^{18}$ particles)
Desktop $\approx 1.25 \cdot 10^{11}$ FLOPS/core [3]	$1.82 \cdot 10^6$ years	$7.37 \cdot 10^{16}$ years
Jean Zay supercomputer $\approx 2.8 \cdot 10^{16}$ FLOPS [4]	8 years and 46 days	$3.29 \cdot 10^{11}$ years
Frontier supercomputer $\approx 1.685 \cdot 10^{18}$ FLOPS [5]	49 days	$5.47 \cdot 10^9$ years

TABLE 1.1. – DEM's roughly estimated computational time cost on large sample of settling Camargue's sand, assuming a perfect parallelization speedup

Reaching large scales

In order to be able to perform a DEM simulation in a reasonable time, samples are limited to a few thousands particles [Aboul Hosn, Sibille, Benahmed, et al. 2017]; [Duverger, Duriez, Philippe, et al. 2021]; [Mohamed, Duriez, Veylon, et al. 2022]; [Sibille, Villard, Darve, et al. 2019], which is usually enough to constitute a Representative Volume Element (RVE). However, some valuable insights provided by DEM on the microscopic mechanisms might not be captured because force chains within the granular medium thus are limited in size, preventing the emergence of large scale phenomena. Combined with powerful computers, the MPI parallelization strategy mentioned above allows for larger scale simulations: [Gardner, Kolb, and Sitar 2017] performs simulations on $8.192 \cdot 10^6$ polyhedrons of various shapes, [Yan and Regueiro 2018] models 10^7 polydisperse ellipsoidal particles, [Rakotonirina and Wachs 2018] is able to consider more than $2.3 \cdot 10^8$ mono-dispersed spheres. These performances are encouraging, however modelling a large construction scale such as a dam or a dike in its entirety is still out of reach. For the emblematic case of the Teton dam, table 1.1 shows extrapolated DEM computational costs using the results presented in figure 1.6. Denoting V_{sample} the sample's volume, the estimated number of particles necessary to model a given volume of material is computed from the ratio $N_p/V_{sample} = 5.471 \cdot 10^{10}$ particles $\cdot m^{-3}$, the latter being measured in the case of $N_p = 8,000$ particles. The Teton dam shape was approximated by an extruded isosceles triangle, with a height, width and length of 93 m, 520 m and 940 m respectively. Note that these estimations assume an optimum speedup: the full performance of supercomputers can only be attained by using all the processing units they make available, the observed performances then strongly depend on the parallelization's efficiency.

3. As measured with a "single presicion general matrix multiply" algorithm, see https://browser.geekbench.com/v4/cpu/compare/16316142?baseline=16316142

4. Currently best French Supercomputer, see https://www.cnrs.fr/en/jean-zay-frances-most-powerful-supercomputer-research

5. Currently best supercomputer worldwide, see https://en.wikipedia.org/wiki/Frontier_(supercomputer)

1.2. Modelling of granular materials as a continuous medium

While DEM is quite handy because of its accuracy, adaptability and robustness, its use at large scales seems yet out of reach. Indeed, as shown in the previous section, performing a DEM simulation on a 1 m^3 sample is conceivable on the best supercomputers but the dam's scale is still inaccessible. Besides, it does not appear necessary to have a complete microscopic description of the grain scale data for most practical applications. Other methods such as the Finite Element Method (FEM) relies on a model of a material's behaviour, i.e. constitutive law, to determine the reaction of a supposedly continuous sample to some loading conditions. The continuous assumption makes possible the modelisation of large size of samples: the behaviour of the material is computed on a finite number of points often defined by a mesh, whose fineness depends on the desired resolution.

1.2.1. Constitutive laws

The constitutive law is the part of the numerical model that describes how the material reacts to a specific loading condition, in the form of a stress-strain relation that depends on the nature of the material in question. The behaviour of purely elastic materials can be characterized using simply Hooke's law, which requires only two parameters for an isotropic homogeneous media. However, materials cannot usually be considered as purely elastic since many applications bring the materials beyond their elasticity limits. A description of the material's plasticity thus has to be included in the constitutive laws. For instance, the behaviour of most metallic materials can be modelled using a stress-strain relation based on the von Mises yield surface [Kobayashi 1982]; [Krieg and Krieg 1977], and Newtonian fluids' behaviour can be modelled using a state equation [Pironneau 1989]. As for granular materials, plasticity is accounted for in constitutive laws by considering either Tresca or Mohr-Coulomb yield surface [Brinkgreve 2005]; [Sloan and Booker 1992]; [Ti, Huat, Noorzaei, et al. 2009]. The latter leads to the Mohr-Coulomb model which is widely used in engineering applications, due to its relative simplicity. A basic implementation of the Mohr-Coulomb model requires only 5 parameters:

- two elastic moduli, to describe the stiffness of the material and the directional repartition of its deformations (e.g. Young's modulus and Poisson's ratio);
- the dilatancy angle, to describe the sample's volume evolution under plastic shearing;
- the friction angle, to define the Mohr-Coulomb yield surface;
- the cohesive strength, to account for cohesion in the Mohr-Coulomb yield surface.

The Mohr-Coulomb yield surface has a hexagonal shape in the principal stress space. If the problem involves a single stress path, the yield surface can alternatively

be approximated by a simple cone (see figure 1.8), this model is referred to as the Drucker-Prager model [Drucker and Prager 1952]; [Brinkgreve 2005].

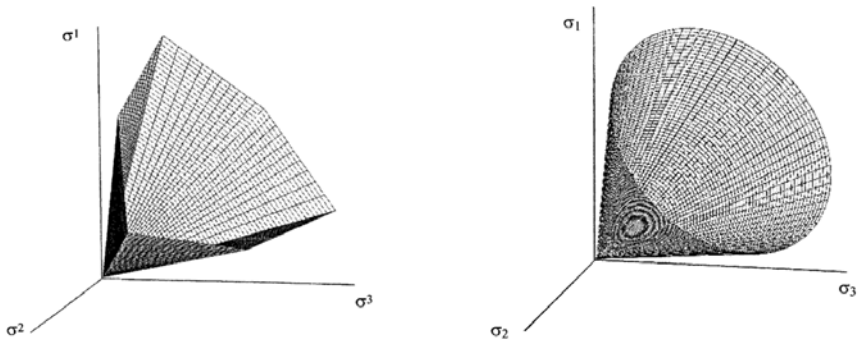

(a) Mohr-Coulomb (b) Drucker-Prager

FIGURE 1.8. – Yields surfaces [Brinkgreve 2005]

Non-linear models have also been developed in order to describe soils with a better accuracy. For instance the Duncan-Chang model [Duncan and Chang 1970] assumes the stiffness to vary with the stress according to a power law. This consideration improves the model's efficiency before failure, but is unable to describe dilatancy and irreversibility [Brinkgreve 2005]. The critical state theory, which states that at some point a soil sample can be subject to further shear deformations without stress or volume variation, is at the basis of the Cam-Clay model [Schofield and Wroth 1968]. Note that a modification of this model aimed at incorporating a logarithmic relationship between the effective mean stress and the void ratio, which leads to a stress dependant stiffness. This model is denoted as Modified Cam-Clay model [Brinkgreve 2005]; [Burland 1965]. The Nor-sand model [Jefferies 1993] is also based on the critical state theory through the use of the so-called state parameter ψ [Been and Jefferies 1985], supposed to account for the stress and void configuration of a granular material. It requires however 8 soil-dependent parameters and several triaxial tests to be fully calibrated [Jefferies 1993].

1.2.2. Large scale modelling with the Finite Element Method

FEM's development began even before the invention of electronic digital computers [Courant 1943]; [Hrennikoff 1941] and is today at the basis of many studies. Its applications are :

— civil engineering, for instance to determine the hydrodynamics around bridges [Selvam, Tarini, and Larsen 1998], or to study the propagation of cracks in concrete constructions [Gerstle and Xie 1992];
— geotechnical engineering, for instance to investigate the soil-structure interactions of large constructions [Ellis and Springman 2001], to study the soil's failure process under seismic solicitations [Ma, Liao, Dang, et al. 2021];

— metallurgical engineering, for instance to model metal forming [Chung, Cho, and Belytschko 1998] or metal casting [Venkatesan, Gopinath, and Rajadurai 2005];
— others, including nuclear engineering to model nuclear reactors [Oku, Akiba, Suzuki, et al. 2010] and electrical engineering to study high-voltage devices erosion [Soldera, Lasagni, Mücklich, et al. 2005].

Procedure

FEM splits the object to be modelled into several elements on which the governing equations are solved. The resulting set of all elements and their connections is called the mesh and follows the material as it deforms, making FEM a Lagrangian method. Mesh's elements can be of any shape: hexahedrons [Cifuentes and Kalbag 1992]; [Schneiders and Bünten 1995], tetrahedrons [Cifuentes and Kalbag 1992]; [Nguyen-Thoi, Liu, Vu-Do, et al. 2009], or even a combination of prisms and tetrahedrons [Yamakawa and Shimada 2009]. Elements can be all identical, forming then a structured mesh, or they can have different dimensions to fit better systems with peculiar geometries, forming then an unstructured mesh [Zavattieri, Dari, and Buscaglia 1996]. Unstructured meshes make possible the refinement of the grid around a zone of interest to optimize the resolution versus computational cost ratio. Furthermore, mesh's refinement can be performed dynamically, as the simulation runs and the zones of interest move [Lo 2002]. Such a meshing technique is qualified as adaptative.

The resolution of the governing equations involves integrating some quantities over all elements for each element. However, these quantities can only be known at a finite set of points in an element. FEM thus requires a quadrature rule to correctly compute the integral after choosing for these points appropriate locations and weights, compensating the infinity of points missing for the integration. For instance, the approximate integration of f on an interval $[-1,1]$ can be written as follows:

$$\int_{-1}^{1} f(x)dx \approx \sum_{p=1}^{n} w_p f(x_p) \tag{1.4}$$

where $\{w_p; i \in [\![1,n]\!]\}$ are the weights attributed to the values of f at the points $\{x_p; i \in [\![1,n]\!]\}$. Typically, $\{x_p; i \in [\![1,n]\!]\}$ are chosen as the roots of Legendre's polynomial, the quadrature is then denoted "Gauss-Legendre quadrature" [Bathe and Saunders 1984]; [Rathod, Venkatesudu, and Nagaraja 2006]. Depending on the integrand's characteristics, it might be necessary to use a different set of points and weights. The Gauss-Jacobi quadrature [Ralston and Rabinowitz 2001]; [Yang, Wang, Yuan, et al. 2022] and the Chebyshev-Gauss quadrature [Yan, Mi, and Liu 2019] are examples of other popular quadrature rules used on the interval $[-1,1]$. For multi-dimensional problems, the weight can be obtained simply by multiplying the one-dimensional weights computed in each direction. The mesh elements being deformed, their vertices coordinates can be transformed onto the interval $[-1,1]$

for the quadrature rule to be directly applied. The points $\{x_p; p \in [\![1, n]\!]\}$ are called integration points, or Gauss' points, and correspond to the locations where the behaviour of the material is determined using the constitutive law.

Traditionally, data such as the velocity or the mass density is stored on the grid points. As a consequence, it is necessary to frequently transport quantities from grid points to Gauss' points and vice versa. Shape functions S_i defined at every grid point i ensure this interpolation procedure, the simplest ones being linear:

$$S_i(x) = \begin{cases} \dfrac{x - x_{i-1}}{x_i - x_{i-1}} & \text{if } x \in [x_{i-1}, x_i] \\ \dfrac{x_{i+1} - x}{x_{i+1} - x_i} & \text{if } x \in [x_i, x_{i+1}] \\ 0 \quad \text{otherwise} \end{cases} \tag{1.5}$$

with $\{x_i\}$ the set of all the grid points' positions.

Elements deformations are a consequence of the grid points displacements, driven by their velocities. Shape functions thus have to be recomputed at each iteration.

Limitations of the FEM

Although FEM is efficient for simple problems, it suffers from inaccuracies when dealing with complex systems. For instance, the presence of discontinuities in the material due to cracks or simply their nature (e.g. granular materials) requires the mesh to match the interfaces and track them as they move. In the case of cracks propagation, an expensive remeshing step is often necessary. The extended finite element method (XFEM) [Chessa, Smolinski, and Belytschko 2002]; [Moës, Dolbow, and Belytschko 1999] aims to solve this problem by representing discontinuities independently of the mesh, based on the Partition of Unity Finite Element Method (PUFEM) [Melenk and Babuška 1996]. The latter brings the possibility to include an approximation of the solution locally, which is used in XFEM along shape functions to account for cracks in the simulated object. Even though XFEM is suitable to study discontinuities, it still suffers from the fact that non-continuous materials, as granular materials, require complex constitutive laws being often hard to calibrate and generalize poorly to different loading paths.

Another issue is the mesh resolution necessary to solve some problems. Indeed, even though FEM is able to reach large scales, it might be necessary to capture some lower scale features of the material with precision, limiting the maximum size of the mesh's elements. FEM's convergence toward the solution of the continuous governing equations is often studied [Garau, Morin, and Zuppa 2011]; [Gwinner 2013]; [Shi 1987], and several variations of the FEM are found to achieve better convergence rates than classical FEM. The hp-FEM [Babuška and Guo 1992] for instance, uses various element sizes and shape function order to reach an exponential convergence rate [Ainsworth and Parker 2021]; [Melenk and Xenophontos 2016].

An important problem with the FEM is a consequence of its fully Lagrangian nature: when the material is subject to high deformations, elements may be highly

distorted, which leads to inaccurate solutions or even the impossibility to continue the computation. Many variations of the FEM aim to solve this problem by releasing it from its mesh dependance. Among them, the Smoothed Finite Element Method (SFEM) [Zeng and Liu 2018], based on the mesh-free Smoothed Point Interpolation Method (SPIM) [Khoshghalb, Shafee, Tootoonchi, et al. 2020]; [Liu and Zhang 2013], takes advantage of FEM's mesh without its drawbacks. Basically, it smooths the derivatives of the field functions over the whole mesh, and beyond, to modify the strain field. The Particle Finite Element Method (PFEM) [Oñate, Idelsohn, Del Pin, et al. 2004] was developed in order to handle the large deformations involved in the case of fluid-structure interactions. It solves the high distortion problem by remeshing at the end of each step if some elements are too severely deformed. While managing to preserve the Lagrangian nature of the FEM, PFEM is quite expensive due to the frequent remeshing and the detection of the free surfaces that has to be performed at each iteration. A numerical method worth mentioning is the mesh-free Smoothed Particle Hydrodynamics method (SPH). This method was first developed to study stellar motions [Gingold and Monaghan 1977]; [Lucy 1977] and was later adapted to different research domains, including geomechanics [Bui and Nguyen 2021]; [Chambon, Bouvarel, Laigle, et al. 2011]. It considers the material as a finite set of points which interact over a specific domain defined by a kernel function, and move according to the governing equation solution. This purely Lagrangian mesh-free method handles well large deformations and is specially efficient for problems involving free surfaces, however the imposition of boundary condition is challenging [Shadloo, Oger, and Le Touzé 2016].

Pursuing the idea of making FEM more robust in the case of large deformations, several hybrid Eulerian-Lagrangian methods were proposed. The Finite Element Method with Lagrangian Integration Points (FEMLIP) [Dufour 2002]; [Moresi, Dufour, and Mühlhaus 2003] is one of them. It consists in keeping the mesh fixed during the whole simulation, but allowing the integration points to move, even to switch from an element to another. This consideration allows to track the material's deformations while keeping the resolution of the motion equation on an immobile background mesh, bringing the Eulerian aspect to the method. The unpredictable positions of the integration points in their mesh element complexifies considerably the determination of the integration weights: the usual quadrature rules in FEM being defined at specific positions in the elements, FEMLIP thus requires a general expression of the quadrature to compute the integration weights for any integration points layout. Such a task is carried out by an algorithm which iteratively determines the values of the weights, based on a set of constraints which arise from equation 1.4 when considering a specific form for the integrated function. A simple choice could be to consider the function linear according to each dimension, which leads to great simplifications. In parallel to the FEMLIP, a rather similar hybrid Eulerian-Lagrangian method was developed: the Material Point Method (MPM).

1.2.3. The Material Point Method

The MPM was first formulated in [Sulsky, Chen, and Schreyer 1994] as a hybrid Eulerian-Lagrangian method, based on the Particle In Cell method (PIC) [Harlow 1962]. In this method, the material is represented by a set of material points where mechanical parameters are stored along with history-dependent parameters necessary to compute for instance a granular material's behaviour. These material points move according to the velocity obtained by resolving the equation of motion on a fixed "background" mesh, where the quantities are transported at each time step. The Lagrangian part of the formulation thus comes from the material points that follows the material as it deforms, while the Eulerian part comes from the fixed mesh, unaffected by the material deformations.

The material points correspond to FEM's Gauss' points, with the difference that their location and number inside each mesh element is unknown as they freely move within the mesh. The usual quadratures used in FEM are thus not usable in the MPM, raising the need for an arguable assumption: the integration weights are considered to be equal to a "volume" attributed to each material point. In its most basic formulation [Sulsky, Chen, and Schreyer 1994], a common volume is initially assigned to all material points in the same cell, no matter their location. Efforts have been made since to improve this weight computation [Bardenhagen and Kober 2004]; [Vaucorbeil, Nguyen, Sinaie, et al. 2020] through the attribution of a specific domain to each material point, described by a so-called particle characteristic function. Such a variation of the MPM is in fact a generalization of the method, hence called Generalized Interpolation Material Point method (GIMP), and can be declined into several sub-methods depending on the material points' domain description (e.g. contiguous particle GIMP, fuzzy particle GIMP, ...[Bardenhagen and Kober 2004]). This generalization is a substantial improvement for the MPM, however, the difficulty to describe the evolution of the material point's domain often requires the use of simplifications such as the consideration of a constant volume.

Because of the numerous transportation of the information between grid points and material points, the MPM relies strongly on the shape functions. In the classical MPM, these shape functions are linear by parts, their derivative are thus not continuous (as illustrated in figure 1.9 (a)) which induces a drastic change in the internal force when material points cross cells, possibly leading to ringing instabilities. The use of higher order shape functions, such as B-splines of order at least 2 [Steffen, Kirby, and Berzins 2008]; [Vaucorbeil, Nguyen, Sinaie, et al. 2020], addresses this problem. Indeed, B-spline functions are very suitable to MPM since their $k-2$ first derivatives are continuous (k being the order of the B-spline) and are equal to 0 outside the domain of interest. Also, because of their definition by parts, the determination of overlapping B-spline functions such that they form a partition of unity of space is straightforward, see figure 1.9 (b).

Another important choice in the MPM formulation is the velocity transportation strategy, from grid points to material points after solving the equation of motion. Clas-

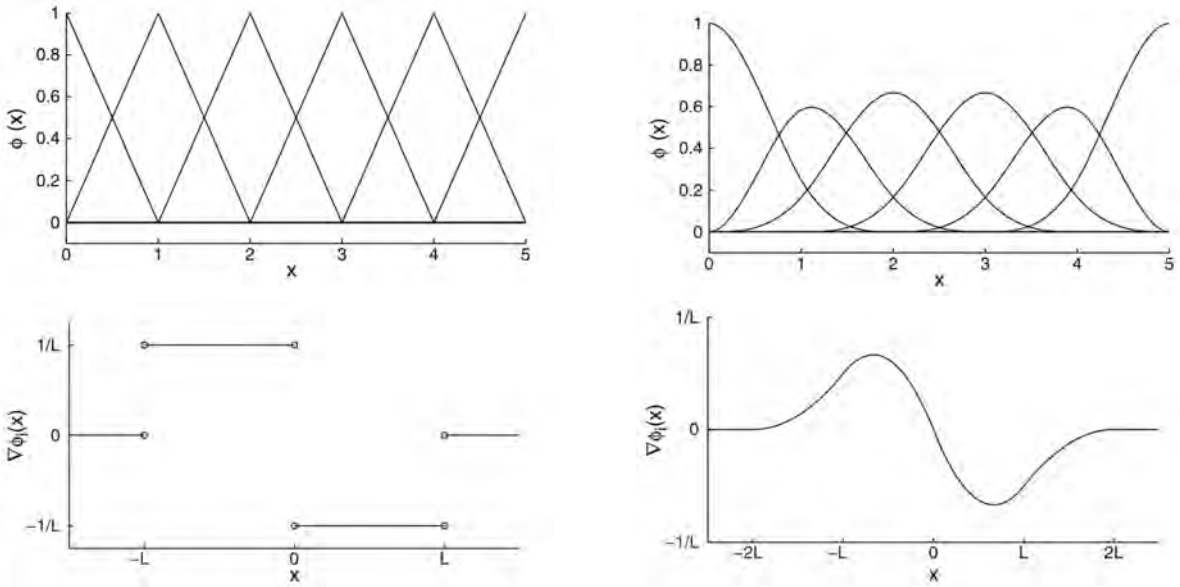

(a) Linear shape functions

(b) Cubic B-spline shape functions

FIGURE 1.9. – Shape functions used in MPM and their first derivative [Steffen, Kirby, and Berzins 2008]

sical MPM transports directly the new velocity to the material point the same way PIC does, which is known to be highly dissipative. Many alternatives have been proposed, such as the so-called FLIP strategy which was implemented in the FLuid Implicit Particle method [Brackbill and Ruppel 1986] where the acceleration is transported rather than the velocity. This small change effectively corrects the excessive energy dissipation, but it makes the method more subject to instabilities and usually requires a smaller time step. Combining the FLIP and PIC strategies is a common practice to dissipate artificially the energy and thus mitigate instabilities. Also, FLIP can lead to spurious results as the velocities used to move the material points are different from the one assigned to them, to be used at the next iteration. This was addressed in [Stomakhin, Schroeder, Chai, et al. 2013], resulting in a variation of the FLIP strategy called Naturally-modified FLIP (NFLIP) in [Fei, Guo, Wu, et al. 2021]. Another alternative is the Affine Particle In Cell (APIC) strategy [Jiang, Schroeder, Selle, et al. 2015], based on the PIC approach, which aims to conserve angular momentum during the transport operation. The latter was generalized into the Polynomial PIC strategy (PolyPIC) [Fu, Guo, Gast, et al. 2017] to improve its energy conservation with a low computational cost. Basically, it considers during the interpolation process a general expression for the velocity at material points, where APIC only considers affine forms. The PolyPIC velocity update strategy was even further generalized with the Moving Least Square method (MLS) [Hu, Fang, Ge, et al. 2018], which essentially adds to the

shape functions a dependency on the momentum, based on a certain polynomial basis. More recently, other strategies were proposed in [Fei, Guo, Wu, et al. 2021] with the goal of reducing artificial diffusion and viscosity for simulating brittle materials. These NFLIP-based strategies, namely SFLIP (Separable FLIP) and ASFLIP (Affine-augmented Separable FLIP), aim to make the displacements of the material points less dependent on the velocities of other material points in the same mesh cell. This task is carried out through the consideration of an additional parameter defined for each material point, the so-called trap-breaking ratio.

1.3. Multiscale modelling

Although it is possible to overcome FEM's sensibility to large deformations, the lack of adaptability and precision of constitutive laws hinders the accurate modelling of materials displaying complex microscopic structures, such as granular materials. Indeed, the non-continuous nature of granular materials makes it difficult to determine a direct relation between the material's stress and deformation increments. Recent progress in the matter are based on the incorporation of microscopic features in these macroscale relations, providing a concise description of relevant parameters such as contact orientation or void repartition.

1.3.1. Microscopically-inspired constitutive models

A first step toward incorporating microscopic details into a constitutive law is to express the dependance of granular material's macroscopic parameters in terms of grain's properties, such as inter-particle friction or particle stiffness. For instance, the constitutive model presented in [Wan and Guo 1998] allows to include a simple depiction of the particle shape in the void ratio description, which is taken into account in the stress-dilatancy relation. It is able to reflect sand's behaviour both for compression and extension triaxial tests, but requires 11 parameters. The constitutive model proposed in [Sun and Sundaresan 2011] describes the behaviour of granular materials in quasi-static conditions, based on a DEM-inspired stress expression accounting for the microscopic fabric and average coordination number. It was found to accurately handle flow problems, using DEM simulations as reference, when the trace of the normalized rate of deformation tensor is negligible with respect to 1. Another microscopically enriched constitutive model presented in [Chang and Hicher 2005] takes into account inter-particle forces and displacements. It was shown able to reproduce the main features of granular materials during drained triaxial tests performed from various initial states.

A more advanced model, proposed in [Nicot and Darve 2011] and based on the "microdirectional model" [Nicot 2003], simulates the interactions between several grains arranged in plausible ways to reach a scale slightly higher than the microscopic scale: the so-called mesoscale. Although simple, the hexagonal arrangement

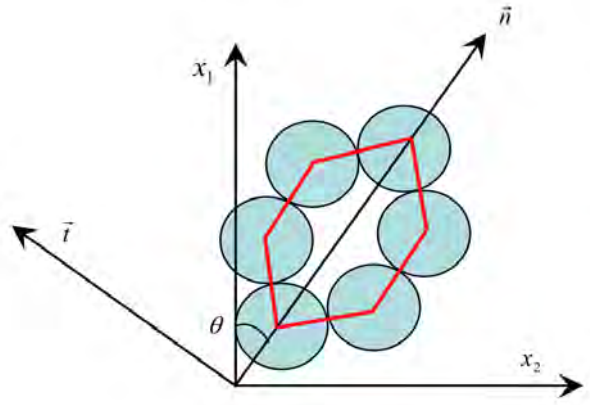

FIGURE 1.10. – Hexagonal arrangement of particles for the H model [Nicot and Darve 2011]

between 6 grains (in 2D, see figure 1.10) was found to allow the emergence of complex kinematic mechanisms, this model was consistently coined as the "H model". It relies on a homogenization scheme which involves the determination of a global stress given a set of contacts through the Love formula [Love 1892]. It was shown to be able to give an accurate quantitative prediction of granular materials where the microdirectional model gave only a qualitative prediction.

1.3.2. DEM as a microscopic model

The H model takes advantage of a direct description of the granular material at a mesoscale to accurately predict a granular material's behaviour without the need to determine complex global parameters, but it considers only one particles arrangement. Going further with this idea, a whole DEM simulation can be used as constitutive model for granular materials. Indeed, DEM is the most straightforward way to account for all complex phenomena occurring inside a granular material without the need to thoroughly understand them. When used as a material's behaviour descriptor, a DEM sample must be large enough for all global variables to be independent of the number of particles in the assembly. However, it is also preferred to use samples as small as possible in order to keep a reasonable computation time cost. Such a sample is referred to as a Representative Volume Element (RVE).

Similarly to the H model, a homogenization process is necessary to determine a global stress value $\underline{\underline{\sigma}}^{glob}$ given a set of interacting particles. A demonstration of such a formula is available in [Nicot, Hadda, Guessasma, et al. 2013] for both static and dynamic granular assemblies. For the latter, the expression of the global stress tensor corresponds to Love-Weber formula with additional terms, based on the rotational velocity of all grains:

$$\sigma_{ij}^{glob} = \frac{1}{V}\sum_{c=1}^{N_c} f_i^c l_j^c - \frac{1}{V}\sum_{p\in\{p\}}\left(\mathcal{E}_{ikj}\dot{\Omega}_k^p \chi_{jl}^p + \Omega_i^p \Omega_k^p \chi_{jk}^p - \left\|\underline{\Omega}^p\right\|^2 \chi_{ij}^p\right) \tag{1.6}$$

with Einstein's notation and:

$$\mathcal{E}_{a_1 a_2 a_3} = \prod_{1\le i<j\le 3} sgn(a_j - a_i);\ \text{the Levi-Civita symbol,}$$

$$\chi_{ij}^p = \int_{V_p} \rho\, r_i r_j\, dV;\ \text{the inertia matrix,}$$

$\underline{\Omega}^p$: the spin velocity of the particle p,

$\{p\}$: the set of all particles in the RVE,

N_c : the number of contacts in the granular assembly,

$\underline{f}^c$: the interaction force of the contact c,

$\underline{l}^c$: the branch vector of the contact c.

Regarding the deformations, the strain rate can be seen as a velocity gradient applied to the all particles, which is directly prescribed when using periodic boundary conditions in DEM. Figure 1.11 summarizes the coupling algorithm: loading conditions computed at a Gauss' point (denoted material point on the figure) are applied to a DEM granular assembly on which a global stress tensor is determined and sent back to the FEM.

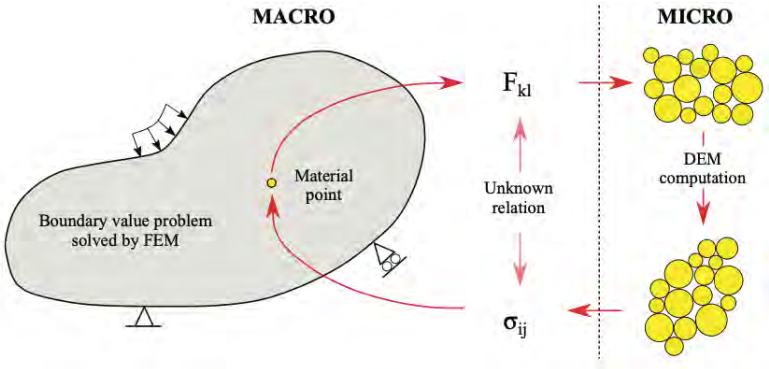

FIGURE 1.11. – Multiscale FEMxDEM procedure [Nguyen, Desrues, Vo, et al. 2022]

Such a FEMxDEM coupling is proposed in [Nitka, Combe, Dascalu, et al. 2011] for fully 2D simulations, where the coupling results were consistent with pure DEM simulations. It has been generalized to include 3D DEM [Nguyen, Claramunt, Caillerie, et al. 2017]; [Nguyen, Desrues, Vo, et al. 2022] and shown capable of modelling strain localization. Another fully 2D implementation of the multiscale FEMxDEM coupling was proposed in [Kien, Trung, and Hoang 2021], and found to be in agreement with

pure DEM simulations in the case of a biaxial elementary test. However, this study highlights the FEM mesh dependency on a hollow cylinder simulation where strain localization occurs.

1.3.3. The MPMxDEM coupling

Replacing the FEM by the MPM is an immediate improvement to the mesh dependance problem. Such a coupling was developed in [Liang and Zhao 2019] using the open source softwares NairnMPM [Nairn 2011] for the MPM part and YADE [Smilauer et al. 2021] for the DEM part of the model. It reveals that the MPMxDEM coupling is also able to capture strain localization on biaxial tests, but it suffers from a lack of accuracy when the mesh is not fine enough, or when the number of material points per mesh element is too low. This mentioned study also takes advantage of the coupling capacity to describe different soil states: various initial void ratios were used to perform footing problem simulations, and different failure mechanisms were observed. It also includes a dynamic simulation of the collapse of a granular column.

2. Two studies using the Discrete Element Method

The DEM offers the possibility for complex phenomena to emerge from an assembly of discrete objects using only a characterization of the microstructure, making it probably the most accurate model for granular materials. As a consequence, DEM is a promising candidate to represent the behaviour of granular materials within continuum-based (FEM-like) methods, instead of the traditional constitutive laws, and this motivates the present thesis work. In fact, DEM can even be used as an alternative to experiments when investigating the intricacies of the microstructures of a granular assembly, which would require experimentally some advanced and expensive techniques (e.g. X-ray tomography). This chapter starts this thesis with two studies applying only DEM, both investigating the properties of an artificial material made of non spherical grains. The latter was created by the Japanese Geotechnical Society in the context of a DEM benchmark in which we participated.

The first study, "Methodological and physical aspects of angle of repose studies" was motivated by the observation that the angle of repose formed by an unconstrained granular heap depends on its geometry. Eventually, it led to a collaboration with another team participating to the same benchmark, namely Vasileios Angelidakis, Sadegh Nadimi and Stefano Utili, from the School of Engineering, Newcastle University (Newcastle upon Tyne, United Kingdom), who used a completely convex model (the potential particles model) for the grain shape. As first author of this study, I ran all the simulations which are presented, and redacted the first draft. I also improved the implementation of the visco-elastic contact model for potential particles, in the open source code YADE.

The second study, "Rattlers' involvement for possibly looser critical states under higher mean stress", presented at the international conference "Powders & Grains 2021", aimed to characterize the previous artificial material using many triaxial tests. This study highlights the limitations of the DEM when serving as a substitute to experiments, in the case where the material has reached the critical state.

Methodological and physical aspects of angle of repose studies

Sacha Duverger[1], Vasileios Angelidakis[2,3], Jérôme Duriez[1], Sadegh Nadimi[2], Stefano Utili[2], Stéphane Bonelli[1] and Pierre Philippe[1]

[1]INRAE, Aix Marseille Univ, RECOVER, Aix-en-Provence, France
[2]School of Engineering, Newcastle University, Newcastle upon Tyne, United Kingdom
[3]Institute for Multiscale Simulation, Friedrich-Alexander-Universität Erlangen-Nürnberg, Germany

Abstract

The repose of granular materials is investigated using two Discrete Element Method (DEM) formulations in comparison with an experimental reference recently proposed as a benchmark by the Japanese Geotechnical Society. On a methodological standpoint, a rigorous measurement method of the angle of repose (AOR) is first proposed for plane-strain and axial-symmetric conditions. Additionally, two systematic procedures are designed in order to also access the void ratio of the heap, as a fundamental property of granular matter possibly influencing the AOR. From a physical point of view, a discussion is developed on the description of particle shape, that differs in the two DEM modelling approaches, adopting non-convex multi-spheres aggregates i.e. clumps and potential particles as a convex simplification of the physical particles. In the comparison with experiments, the clump approach sucessfully predicted the AOR within a 8% tolerance, whereas the potential particles approach logically underestimated to a greater extent the AOR due to the artificial convexity. While the physical particle has a convexity value of $C = 0.954$, neglecting its local concavities brings down the AOR from $35.95 \pm 0.88°$ to $31.26 \pm 0.95°$. The AOR is eventually shown here to bear no constitutive nature. It is for instance independent of initial void ratio but still different than the critical friction angle. The latter may actually serve as a lower bound for the process-dependent AOR. The conclusions are drawn from a statistical analysis of a large set of results, accounting for the random nature of the microscopic arrangement in the studied process.

Keywords: Angle of repose ; Granular materials ; Discrete Element Method ; Non-spherical particles

2.1. Introduction

Under loading, particulate matter strains in the form of a fluid-like flow as long as the applied load is high enough. Then, once loading no longer prevails against internal dissipation in terms of energy input, particulate matter comes at rest in a solid-like heap configuration. The corresponding slope, expressed in terms of an angle of repose (AOR), rules the spatial extents of the deposit for a given matter quantity. The AOR is therefore of interest for countless applications involving particulate materials, for instance the design of industrial facilities for granular-conveying processes, or the prediction of the coverage of natural deposits after e.g. snow or rock avalanches. Several standardised measurement procedures have been proposed in the literature to measure the AOR of granular materials employing empirical and geometrical concepts [Geldart, Abdullah, Hassanpour, et al. 2006]; [Al-Hashemi and Al-Amoudi 2018] but they unfortunately often lead to differing results, as demonstrated in [Rousé 2014]. As such, a one-to-one correlation of AOR to theoretically-established mechanical material properties is not always demonstrated even though it may be often assumed, e.g. in [Bolton 1986] in Geotechnics. A part of the complexity certainly stems from an influence of non-constitutive parameters such as the heap construction history [Matuttis, Luding, and Herrmann 2000] and possible geometrical effects [Matsuo, Nishiura, and Sakaguchi 2014]; [Zhou, Xu, Yu, et al. 2001]. The latter adds to the more natural influence of physical parameters pertaining to the micro-, respectively meso-, scale properties such as particle shape [Chen, Zhao, and Zhou 2020]; [Pöschel and Buchholtz 1993], contact friction [Chen, Zhao, and Zhou 2020]; [Pöschel and Buchholtz 1993]; [Zhou, Xu, Yu, et al. 2001], respectively fabric [Chen, Zhao, and Zhou 2020]. Last, it should be noted that granular heaps may not systematically conform a linear slope [Akbar, Yuliza, Amalia, et al. 2022]; [Topić, Gallas, and Pöschel 2012] which may prevent one to define a single-valued AOR.

Following up on these previous works, the aim of the present manuscript is twofold. First, rigorous simulation and measurement methods are proposed in order to ease evergoing AOR studies. Second, with the help of these methods, an analysis is conducted in order to gain further insights on the AOR variations with respect to physical and non-physical parameters. The present analysis combines the use of two Discrete Element Method (DEM) approaches and experimental results recently proposed by the Japanese Geotechnical Society (JGS) as part of a round robin series of tests [Japanase Geotechnical Society 2021].

Section 2.2 first presents the JGS experiments and the two DEM formulations both executed within the YADE code [Smilauer et al. 2021] while they differ in terms of their particle shape description. Section 2.3 then introduces new methods enhancing AOR studies, namely a systematic definition of the AOR value after detection of the external slope and versatile measurement methods of the compacity (void ratio) of the heap since the latter is a fundamental property of granular matter. It also provides a discussion on computational aspects of the two DEM approaches used to simulate the same JGS experiments. Section 2.4 finally provides new insights on the role of some physical and non-physical parameters on the AOR value, after conducting a large number of DEM simulations interpreted in a statistics fashion for robustness of the conclusions.

2.2. Reference benchmark experiments and DEM formulations

2.2.1. Reference benchmark experiments

Measurements of AOR data have been recently proposed by the JGS as part of a round robin test organised within the activities of Technical Committee 105 (TC105: Geo-Mechanics from Micro to Macro) of the International Society for Soil Mechanics and Geotechnical Engineering (ISSMGE) [Japanase Geotechnical Society 2021]. In a first step, data only included an experimental characterization of the granular material at hand, together with properties of the two experimental setups used for AOR measurement, before that blind DEM predictions of the AOR values could be proposed by international participants to the round robin and compared with experimental values.

An artificial granular material was considered with non-spherical particles made of 3D-printing resin. Particles constituting the mono-dispersed material resemble a tetrahedral arrangement of four spheres clumped together (see figure 2.1). Individual spheres have a radius of $r_s = 0.3101\,cm$, while each global particle is inscribed in a radius $r_{clump} = 0.5\,cm$.

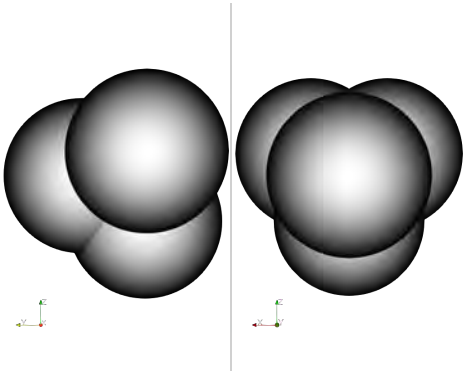

FIGURE 2.1. – Physical particle made of 4 clumped spheres.

The newly proposed AOR setups employ two devices in the form of either a cylindrical (see figure 2.2) or cuboidal (see figure 2.3) container with acrylic walls, aiming to compare how the AOR varies for heaps of different shapes. For the cylindrical case forming an axial-symmetric configuration, the container encloses the particles before the surrounding wall is lowered until a small, final, height of 1 cm. For the second device corresponding to a plane-strain configuration of the repose state, the cuboidal box encloses the particles initially, until one of the side walls is removed upwards, leaving eventually only a fixed 0.5 cm ridge to retain the lowest particles on that side. The reference number of particles, walls' velocity and boxes' dimensions are given in table 2.1 for both configurations, as per the specifications of the round robin test. These parameters were set to different values for some series of simulations in this study, see sections B and 2.4.5.

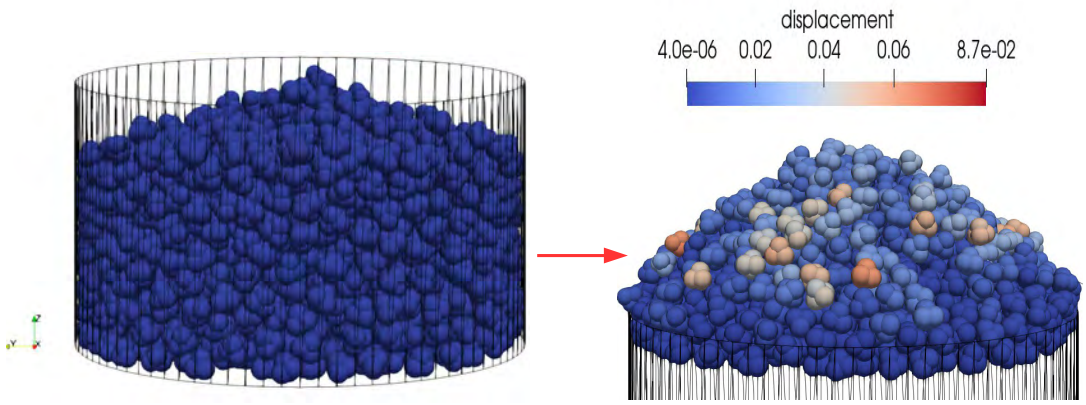

FIGURE 2.2. – Initial (left) and final (right) states of the heap in the axisymmetric configuration.

TABLE 2.1. – Default configuration of AOR simulations

Configuration	Initial number of particles	Side wall's velocity	Container's height	Container's width
Axial-symmetric	$N_{part} = 2468$	$V_{cyl} = 6{,}67 \cdot 10^{-4}\ m/s$	$H_{cyl} = 9 \cdot 10^{-2}\ m$	$R_{cyl} = 8 \cdot 10^{-2}\ m$
Plane strain	$N_{part} = 2150$	$V_{par} = 4{,}3 \cdot 10^{-2}\ m/s$	$H_{par} = 1{,}9 \cdot 10^{-1}\ m$	$L_{par} = 1 \cdot 10^{-1}\ m$

2.2.2. DEM shape description with clump and potential particles approaches

2.2.2.1. Clumps of spheres

In line with the physical particles at hand (see figure 2.1), a first DEM approach adopts the traditional multi-sphere technique to simulate non-spherical particles. A rigid agglomeration of four spheres is created to reflect the particle morphology as a so-called clump, e.g. as shown in [Angelidakis, Nadimi, Otsubo, et al. 2021]. This technique leads to an increased total number of discrete elements in a simulation, compared to the number of physical particles, however it benefits from the low computational cost of collision detection among spheres. To define the inertial properties of a clump, many DEM codes still simply add the masses of the clump members and directly combine their inertia matrices, which leads to an overestimation in the case of clumps with overlapping members, like the one adopted to simulate the present 3D-printed particle. To mitigate this issue, methods to adjust the density of each sphere-member have been proposed in the literature, such as the one of Ferellec and McDowell [Ferellec and McDowell 2010] to correct mass and inertia at the cost of some pre-processing efforts. YADE, along with PFC, provide an alternative solution, where a three-dimensional grid of voxels is generated in the bounding box of the particle, and it is evaluated for each voxel whether it belongs to at least one sphere-member of the clump. For the particles at hand in this study, a grid size of $1000 \times 1000 \times 1000$ voxels is used to

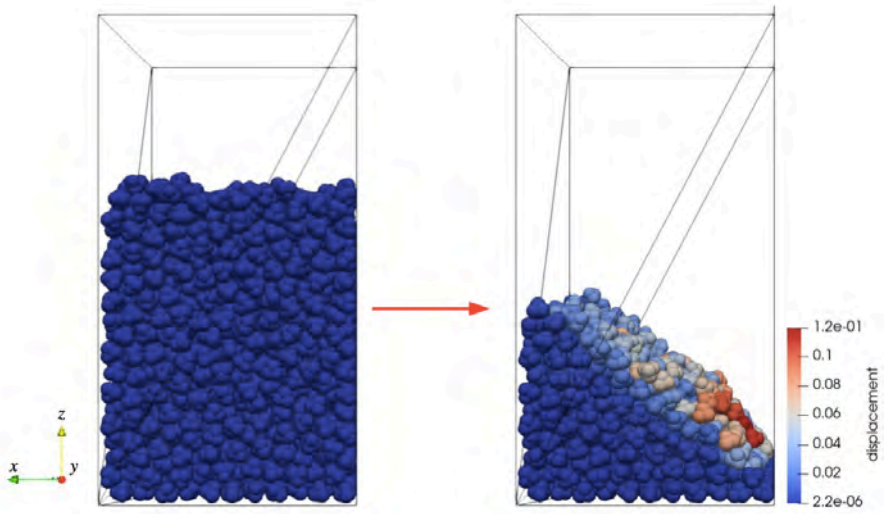

FIGURE 2.3. – Initial (left) and final (right) state of the heap in the plane strain configuration.

estimate the volume (and thus the mass) and inertia tensor, with negligible discretisation error induced by the grid resolution, since finer grids led to the same inertial properties.

2.2.2.2. Potential particles

While the above clump approach is a straightforward DEM strategy for describing the physical particles at hand (figure 2.1), a comparison is carried out with a second approach using the so-called “potential particles" introduced by Houlsby [Houlsby 2009], and extended to three-dimensions by Boon et al. [Boon, Houlsby, and Utili 2013]. The potential particles are generalised convex non-spherical particles, assembled as a combination of 2^{nd} degree polynomial functions and a fraction of a sphere, while their edges are rounded with a user-defined radius. In line with their inherent restriction to convexity, rather common in DEM with complex shapes, e.g. as in [Matuttis, Luding, and Herrmann 2000], the additional consideration of using potential particles will illustrate the mechanical implications of neglecting the concavity of the physical particles to the AOR.

For the exact definition of a potential particle, as detailed in Boon et al. [Boon, Houlsby, and Utili 2013], a set of N planes are assembled such that their normal vectors point outwards, with their interior forming a convex polytope. These planes are summed quadratically and expanded by a distance r, which is also related to the radius of the curvature at the corners. Furthermore, a 'shadow' spherical term is added, where R is its radius and $0 < k \leq 1$ denotes the fraction of sphericity of the particle. A value of $k \approx 0$ corresponds to a nearly sharp polyhedron, while $k = 1$ corresponds to a perfectly spherical particle.

A potential particle is eventually defined by a potential function f as in equation 2.1:

$$f(x,y,z) = (1-k)\left(\sum_{i=1}^{N} \frac{\langle a_i x + b_i y + c_i z - d_i \rangle^2}{r^2} - 1\right) + k\left(\frac{x^2+y^2+z^2}{R^2} - 1\right) \tag{2.1}$$

where:

(a_i, b_i, c_i) = is the normal vector of the i^{th} plane in local particle coordinates;
d_i = is the distance of the plane to the local origin;
$\langle\,\rangle$ = are Macaulay brackets, i.e., $\langle x \rangle = x$ for $x > 0$; $\langle x \rangle = 0$ for $x \leq 0$.

This potential function takes zero values ($f = 0$) on the particle surface, negative values ($f < 0$) inside the particle and positive values ($f > 0$) outside the particle. The contact point between two potential particles is found as the optimal point of a Second Order Conic optimisation Problem (SOCP) describing the contact detection problem, representing a point nearest to both the particles, based on their potential functions. The concept of using a potential measured from the particle surface for contact detection purposes can also been found in the Level-Set Discrete Element Method (LS-DEM) [Duriez and Bonelli 2021]; [Duriez and Galusinski 2021]; [Kawamoto, Andò, Viggiani, et al. 2016] where the potential is the actual distance function, with no need for a closed-form potential function and being possibly adapted to concave particle morphologies.

Here, the mathematical formulation of the potential particles enables one to approximate the given particle shape by a rounded tetrahedron. To decide which planes to use in order to assemble the potential particle of the 3D-printed material, two criteria were considered, a physical and a practical one, with the latter aiming to achieve post-processing convenience: (1) First, the potential particle should capture the morphology of the physical particle as faithfully as possible in terms of size, surface curvature, mass and inertia of the given physical particle, or other shape descriptors such as the sphericity; (2) To achieve comparable results with the clump models, for the evaluation of the AOR, it is convenient for each potential particle to be monitored via four points being located at the same positions than the centroids of the four spheres making the tetrahedron. Thus, it is sought that the potential particle has a straightforward analogy to this format. To satisfy these criteria, the planes used to assemble the potential particle were chosen as the faces of the tetrahedron connecting the centroids of the spheres making the physical particle (see table 2.2). This approach can be generalised to approximate any convex shape, given a tessellation of its surface, or a multi-sphere representation of a particle made of spheres with equal radii.

To match the local surface curvature of the physical particle, a radius $r = r_s$ was chosen in equation 2.1 to control the roundness of the edges and corners of the potential particle consistently with the r_s radius of each individual sphere in the physical particle. The radius of the shadow particle was assigned to $R = \sqrt{2} \cdot r_s$, to capture the curvature of faces of the given particle shape.The remaining parameter needed to be calibrated in order to match the given particle shape was the parameter k, which controls the curvature of the faces. A value of $k = 0.65$ led to a good match with the target geometry, i.e. it achieves an adequate representation of both the overall form of the real particle and features such as its main dimensions, while also approximating its curvature. The parameters r, R and k were chosen via a trial-and-error procedure. Figure 2.4 demonstrates visually the geometrical faithfulness of the generated potential particle to the shape of the real, physical particle.

TABLE 2.2. – Coefficients defining the planes making the faces of the tetrahedral potential particle as described in equation 2.1.

Plane coefficient	Plane 1	Plane 2	Plane 3	Plane 4
a	0	$\sqrt{2/3}$	0	$-\sqrt{2/3}$
b	0	$\sqrt{2}/3$	$2\sqrt{2}/3$	$\sqrt{2}/3$
c	-1	1/3	1/3	1/3
d (m)	0.00063299	0.00063299	0.00063299	0.00063299

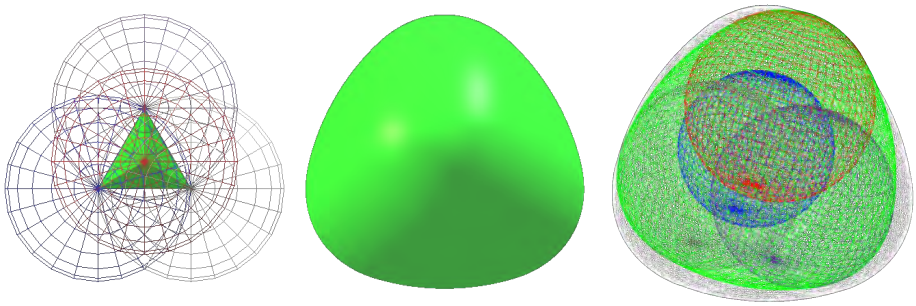

FIGURE 2.4. – Clumped tetrahedral particle (left); fitted potential particle (middle); overlap of the two (right).

In addition to modelling the rounded, tetrahedral-like particles, the potential particles also serve to simulate cuboidal elements of various sizes, making the moving and still parts of the plane-strain and axial-symmetric devices, enabling one to build YADE models using a single, unified approach and contact detection algorithm.

2.2.2.3. Particle shape characterization

As demonstrated in figure 2.4, the selected potential particle can approximate the morphology of the physical particle faithfully, as it qualitatively represents the main dimensions of the particle, determining particle form, along with the curvatures of its edges/corners, relating to particle roundness. However, the potential particles modelling approach cannot represent the concavity of the physical particle. A quantitative characterization of particle form was also performed using `SHAPE` [Angelidakis, Nadimi, and Utili 2021], an open-source shape analysation software for three-dimensional particles, in order to quantify in the table 2.3 the similarity between the the physical particle and its numerical description(s). For doing so, the surface mesh of the physical particle was first tessellated from its corresponding DEM clump, using the surface extraction module of `CLUMP` [Angelidakis, Nadimi, Otsubo, et al. 2021], an open-source code for the generation and processing of multi-sphere particles. Particle shape was characterized in terms of volume, surface area, principal inertia values, convexity and sphericity. Convexity is calculated in [0;1] as the ratio of the volume of each particle divided by the volume of its convex hull, while sphericity, also in [0;1], corresponds

TABLE 2.3. – Shape parameters of the physical particle in comparison with various DEM approaches

Shape characteristics	(1) Physical particle or present clump approach	(2) Potential Particle	$\frac{(2)-(1)}{(1)}$	(3) Clump approach with non-uniform density	$\frac{(3)-(1)}{(1)}$
Volume (m^3)	$3.3304 \cdot 10^{-7}$	$3.9248\ 10^{-7}$	17.85%	$4.9965 \cdot 10^{-7}$	50.03%
Surface area (m^2)	$2.491 \cdot 10^{-4}$	$2.632 \cdot 10^{-4}$	5.66%	$2.491 \cdot 10^{-4}$	0
Inertia tensor/ρ (m^5)	$\begin{bmatrix} 2.584 & 0 & 0 \\ 0 & 2.584 & 0 \\ 0 & 0 & 2.584 \end{bmatrix} \cdot 10^{-12}$	$\begin{bmatrix} 3.286 & 0 & 0 \\ 0 & 3.286 & 0 \\ 0 & 0 & 3.286 \end{bmatrix} \cdot 10^{-12}$	27.17%	$\begin{bmatrix} 3.123 & 0 & 0 \\ 0 & 3.123 & 0 \\ 0 & 0 & 3.123 \end{bmatrix} \cdot 10^{-12}$	20.86%
Convexity	0.954	1	4.82%	0.954	0
Sphericity	0.9328	0.9849	5.59%	0.9328	0

to the so called “degree of true sphericity", i.e. the ratio of the surface area of a sphere with equal volume to the surface area of the particle [Wadell 1932]. It becomes evident from table 2.3 that both the physical and the potential particle take high values of convexity and sphericity (>0.90). It may furthermore be noted that both the multi-sphere and the potential particle share the same minimal bounding box and thus main particle dimensions, resulting to the same flatness and elongation values considering indices that rely on these main particle dimensions. Therefore, flatness and elongation were not monitored in this study, as convexity and sphericity were the two differentiating factors between the two studied particle representations, from a morphological standpoint. Table 2.3 also offers a comparison with a so-called "non-uniform density" clump approach that would count multiple times the overlapping parts of the sphere-members in the calculation of volume and inertia, which would correspond to density showing a spatial increase at areas where spheres overlap.

As expected, the considered potential particle has larger values of volume and geometric inertia. The effect of the resulting increased particle's mass is investigated in section 2.4.1 by scaling down their density so the potential particle has the same mass as the real particle, i.e. $\rho_{rescaled} = \rho\, 3.3304 \cdot 10^{-7} / 3.9248 \cdot 10^{-7} \approx 943\ kg/m^3$.

Bringing the error on mass down to zero through this scaling, the error in inertia values for potential particles drops from 27.17 % down to 7.96 %. It is interesting to note that using overlapping spheres with no correction for uniform density i.e. inner overlaps would lead to an error of 50.03 % for the volume and 20.86 % for the eigenvalues of the principal inertia tensor.

2.2.3. DEM contact formulation

The geometry of each contact is defined with the normal and tangential relative displacements of the particles, u_n and $\underline{u_t}$ respectively. For the clump model, contacts are detected between spheres belonging to different clumps and u_n is computed as the norm of the branch vector to the spheres' radii, while $\underline{u_t}$ is computed incrementally, see e.g. [Duriez and Bonelli 2021]. For the potential particle model, u_n is computed using a bracketed line-search algorithm as detailed in Boon et al. [Boon, Houlsby, and Utili 2013], deployed along the contact normal direction and starting from the contact point, to detect two points on the surface of each particle, forming a branch vector, the norm of which is considered as the sought approaching distance. The shear increment of $\underline{u_t}$ is calculated in a similar manner as for spheres, i.e. via time integration of the shear component of the relative velocity during

contact.

The same contact model applies to these kinematic quantities for both the clump and the potential particle approaches, accounting for linear visco-elasticity and friction (figure 2.5):

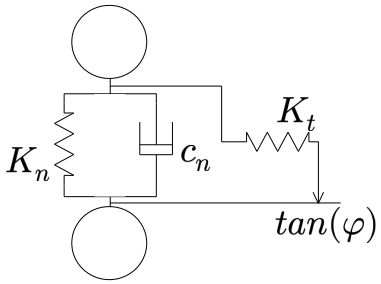

FIGURE 2.5. – Contact model with visco-elasticity and friction.

— in the normal direction: a spring with normal stiffness K_n is associated in parallel with a viscous damper of viscosity c_n, see Eq. 2.2. The viscous damper ensures the stabilisation of the simulations without the need for Cundall's (local) damping.
— in the tangential direction: a spring with tangential stiffness K_t is associated in series with a frictional slider (contact friction angle φ), see Eq. 2.3.

$$F_n = \max(K_n u_n + c_n \dot{u}_n, 0) \tag{2.2}$$
$$|\underline{F_t}| = \min(K_t |\underline{u_t}|, F_n \tan(\varphi)) \tag{2.3}$$

One should note that different YADE classes implement the above Eqs. 2.2-2.3 for clumps and potential particles with different methods of expressing the viscosity coefficient c_n. For the clump approach (through, e.g., `Ip2_ViscElMat_ViscElMat_ViscElPhys` and `Law2_ScGeom_ViscElPhys_Basic` YADE classes), c_n is computed from a given normal restitution coefficient e_n according to the mass-dependent expression of [Schwager and Pöschel 2007]. For the potential particles approach (through, e.g., `Ip2_FrictMat_FrictMat_KnKsPhys` and `Law2_SCG_KnKsPhys_KnKsLaw` classes), a viscous damping parameter β_n serves as input for deriving c_n, consistently with a desired e_n and [Antypov and Elliott 2011]. Nevertheless figure 2.6 illustrates the common dissipative behavior of both models in the case of two colliding spheres (obtained after using $k = 1$ in equation 2.1 for the PP approach) with an initial relative normal velocity V, and demonstrates the consistency of the two implementations of visco-elasticity.

In the framework of the round robin test, the JGS measured the contact friction angle φ and the normal restitution coefficient e_n for resin against acrylic contacts and for resin against resin contacts, as well as the normal stiffness K_n for resin spheres. Experimental measurements exhibited a variability and are thus given as distributions (see figure 2.7). The DEM simulations are defined accordingly, with the values of φ and c_n used for each contact respecting those experimental distributions for all clump simulations, unless specified otherwise.

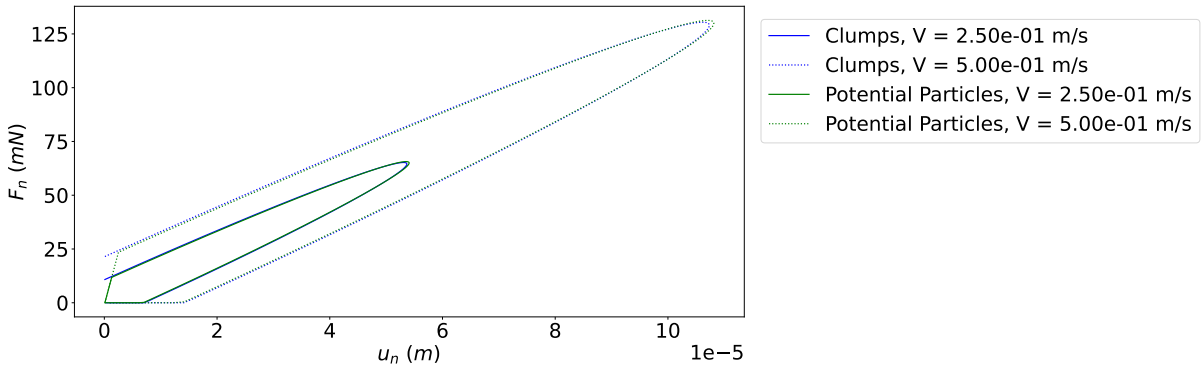

FIGURE 2.6. – Contact behaviour for different impact velocities in the two DEM approaches.

2.2.4. DEM simulation workflow

Generating DEM samples starts with random definitions of initial particles positions inside the cuboidal or cylindrical containers mentioned in the above section 2.2.1, so as to form a extremely loose assembly of non-overlapping particles. The assembly is then deposited under its own weight until it becomes stable, and is saved to be subsequently used under different conditions. Different samples can be obtained starting from different initial particle arrangements. For this first step with no experimental counterpart, an extra, non-physical, damping source is added in the local, non-viscous, form to speed up the generation.

The actual AOR simulation starts from this initial state by displacing the moving parts of the container in an equivalent manner to the experiments. Particles leaving the container are erased and the simulation continues until the sample finds a new equilibrium in the form of a heap. It is then possible to measure the angle between its exterior surface and the horizontal plane following the procedures discussed below.

The default set of parameters for these boundary conditions is the experimental one previously given in figure 2.1.

2.3. Methodological discussion

2.3.1. Computational aspects of each modelling approach

In order to provide an overlook of the computational implications of the two considered DEM strategies for shape description, figure 2.8 gives a comparison of the effective computation speed during 30 different simulations with both modelling approaches. These simulations, presented in detail in section 2.4.3, were run sequentially using a Intel® Xeon® Platinum 8270 CPU @ 2.70GHz with approximately 1.51 TB of RAM available. Note that during all series of simulations in this paper the CPU's cache wasn't controlled. Its capacity of 35.75 MB may thus not have been used as much over all simulations, making the time measurements somewhat biased.

Note that not all heaps finished stabilising at the same simulated time; as a consequence, less and less values were available to compute the mean and standard deviation, until

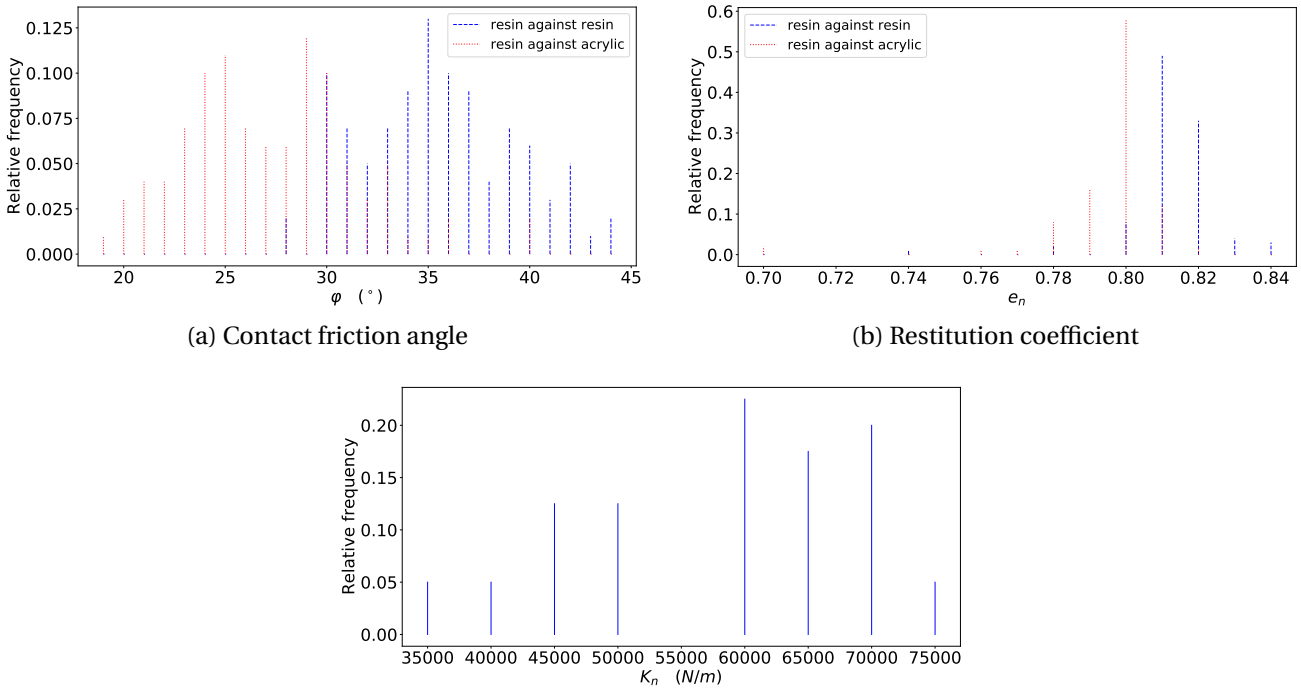

(a) Contact friction angle

(b) Restitution coefficient

(c) Normal stiffness

FIGURE 2.7. – Distributions of contact properties as experimentally measured by the JGS (adapted from [])

eventually there was only one. The results show that for these simulations, the clump model is approximately 100 times faster than the potential particle model. Considering that the present physical particles are simple to describe in a clump approach, using only 4 spherical members, the increased effort in computational time when using potential particles is in a classical order of magnitude for DEM approaches for non-spherical particles [Duriez and Bonelli 2021].

2.3.2. A systematic determination of the angle of repose

This section proposes two rigorous methods to measure the AOR, first, by defining an outer surface of particles and second, by computing an angle from these particles positions.

2.3.2.1. Outer surface detection

In the axisymmetric case (respectively plane strain case), the 3D space is discretized in several subdomains $\{r;\theta\in[\theta_a,\theta_b];z\in[z_a,z_b]\}$ (respectively $\{x\in[x_a,x_b];y\in[y_a,y_b],z\}$), giving an intersection with the outer surface at $\max(r)$ (respectively $\max(z)$) in each subdomain. The extent of each interval is selected such that only one particle should be therein detected as belonging to the outer surface. For such a purpose, length scales L_η are used for the coordinates θ, z in the axisymmetric case and x, y in the plane strain case. The letter η

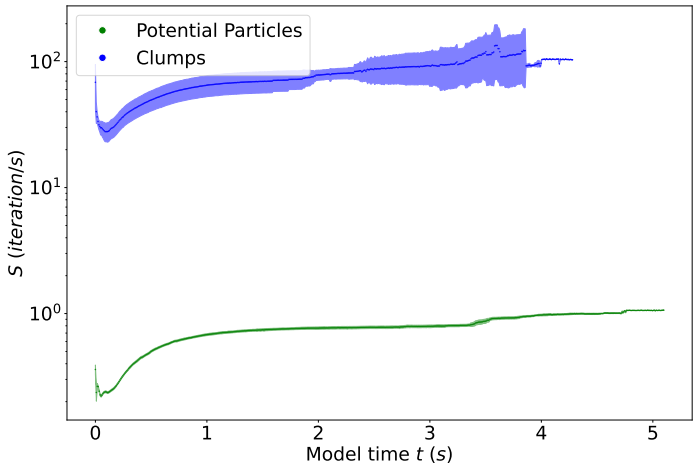

FIGURE 2.8. – Computation speed statistics during 30 simulations with each DEM approach for the potential particles and clump simulations (see section 2.4.3 for details). Dots represent the mean speed value with the surrounding filled area corresponding to its standard deviation.

can represent each of these coordinates. The number of intervals on each coordinate is then:

$$N_\eta = \frac{L_\eta}{d_{clump}} - 1 \qquad \text{with} \qquad L_\theta = 2\pi R_{cyl} \quad ; \quad L_z = H_{cyl} \quad ; \quad L_x = L_{par} \quad ; \quad L_y = H_{par} \tag{2.4}$$

And the limits of each interval are:

$$\theta_a^i = i\frac{2\pi}{N_\theta}; \qquad \theta_b^i = (i+1)\frac{2\pi}{N_\theta} \qquad \text{with } i \in [\![0, N_\theta]\!] \tag{2.5}$$

$$\eta_a^i = i\frac{L_\eta}{N_\eta}; \qquad \eta_b^i = (i+1)\frac{L_\eta}{N_\eta} \qquad \text{with } i \in [\![0, N_\eta]\!],\ \eta \in \{x, y, z\} \tag{2.6}$$

Figure 2.9 shows all the particles detected as belonging to the outer surface in both configurations. Note that gravity has the opposite orientation of the z-axis.

2.3.2.2. Angle of repose measurement

From this point the method is the same in both heap configurations except for the orientation of the horizontal axis. The coordinates $(\tilde{x}, \tilde{y}, \tilde{z})$ will thus denote respectively $(-r, z, \theta)$ in the axisymmetric case or (x, z, y) in the plane strain case. The width of the container $\tilde{x}_{box}$ for instance stands for R_{cyl} in the axisymmetric case and L_{par} in the plane strain case.

Assuming a $\tilde{z}$-invariance of the heaps, we project the spheres on the $(\tilde{x}, \tilde{y})$ planes (see figure 2.10) and perform a linear regression on the resulting points to determine the AOR α. Letting the linear regression be $\tilde{y}_1 = a_1\tilde{x} + b_1$ and considering that the slope a_1 is here negative, one has:

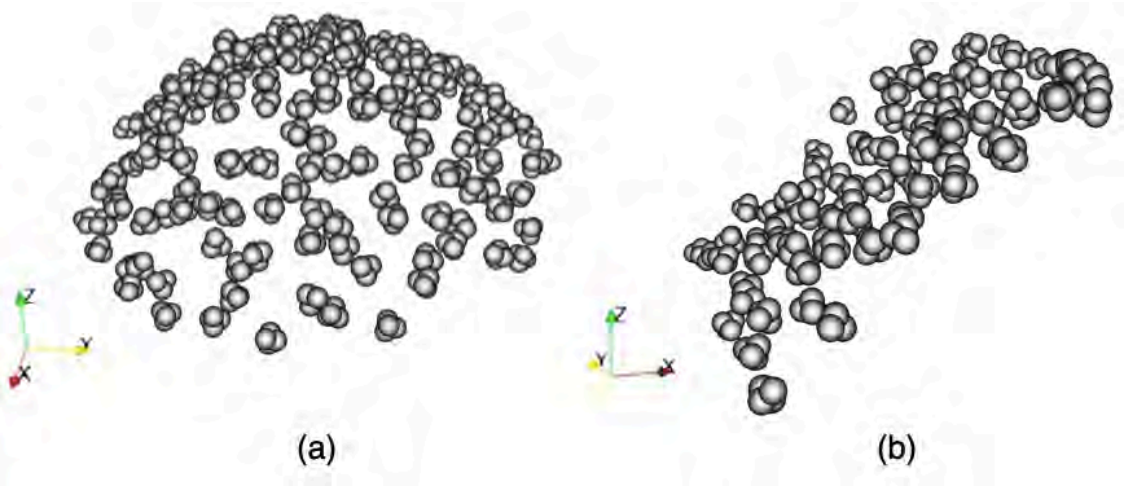

FIGURE 2.9. – Outer surface in the axisymmetric (a) and plane strain configurations (b).

$$\alpha = \arctan(a_1) \tag{2.7}$$

Consistent to [Akbar, Yuliza, Amalia, et al. 2022], one can notice that the surface isn't exactly flat but slightly curved (especially in the axis-symmetric configuration). It can thus be useful to compute a second degree regression as well in order to fit the outer surface in the best possible way. Letting the second degree regression be $\tilde{y}_2 = a_2\tilde{x}^2 + b_2\tilde{x} + c_2$, one can compute a local angle:

$$\alpha(\tilde{x}) = \arctan(2a_2\tilde{x} + b_2) \tag{2.8}$$

To make the measurement more meaningful, one could perform it only on a part of the heap: the particles considered in the regressions would only be the ones inside an interval $[\tilde{x}_{min}, \tilde{x}_{max}]$. Indeed, the lower particles may be abruptly blocked by the bottom ridge of the container devices and should be excluded from the measurement. Also, particles with a high $\tilde{x}$, away from the opened boundary, could be unaffected by the discharge and still form a horizontal surface, specially in the axisymmetric configuration.

Excluding from the bottom of the heap the few particles that are stuck by the ridge, and only those, is obtained choosing: $\tilde{x}_{min} = 0.32 d_{clump}$. An appropriate value for $\tilde{x}_{max}$ is sought by measuring α for several $\tilde{x}_{max}$. The best $\tilde{x}_{max}$ is the smallest for which the measurement doesn't change. The error on the measurement is also a criterion to choose the best $\tilde{x}_{max}$. This method should be specially relevant in the axisymmetric case since the outer surface is curved, but it should work on the plane strain heap as well.

2.3.2.3. Error on the measurement

For a given heap, the dispersion of the data points induces some error on the linear regression and the measurement of α. As an alternative to the correlation coefficient R^2, this

error can be quantified from a standard deviation on the slope a_1 of the fitting line, StD(a_1). If N is the number of points and ($\widetilde{x}_i$, $\widetilde{y}_i$) are the coordinates of the i^{th} point, one has:

$$\mathrm{StD}(a_1) = \sqrt{\frac{1}{N-2}\frac{\sum_{i=1}^{N}(a_1\widetilde{x}_i + b_1 - \widetilde{y}_i)^2}{\sum_{i=1}^{N}(\widetilde{x}_i - \overline{\widetilde{x}})^2}} \tag{2.9}$$

$$\tag{2.10}$$

which gives the standard deviation on the angle, StD(α), considering equation 2.7:

$$\mathrm{StD}(\alpha) = \frac{\mathrm{StD}(a_1)}{1 + {a_1}^2} \tag{2.11}$$

Figure 2.10 shows the regressions made on the projection of the outer surface in both configurations and the resulting angle for $\widetilde{x}_{max}/\widetilde{x}_{box} = 0.4$, with $\widetilde{x}_{box} \in \{R_{cyl}, L_{par}\}$. Figure 2.11 shows measurements performed for several $\widetilde{x}_{max}$ in both configurations. The error bars represent the error computed with equation 2.11. One can see that the AOR increases with $\widetilde{x}_{max}$, except for very high values of $\widetilde{x}_{max}$ where the part of the outer surface considered is very small compared to its size. This may be caused by the ridge on the bottom of the open container that maintains some particles, affecting the shape of the outer surface. The error on the measurement is very low but increases with $\widetilde{x}_{max}$. The measurement is more stable for low $\widetilde{x}_{max}$, specially in the axisymmetric case. From now on, the measurements will be performed on most of the outer surface, using $\widetilde{x}_{min} = 0.32 d_{clump}$ and $\widetilde{x}_{max} = \widetilde{x}_{box}$.

2.3.2.4. Error due to repeatability

The simulations performed with the clump model include two sources of randomness. The first one is the initial configuration of the sample, with random positions for the particles in the initial cloud. The second source lies in the statistical distribution of contact properties. Indeed, the use of distributions for φ and e_n implies choosing a different value for each contact, all values being randomly chosen according to the probability defined by the distribution. If one was to swap the values of two contacts, the distribution would still be respected, but the conditions of the simulation would be different, introducing randomness.

In order to quantify the repeatability error, a series of simulations was performed with the clump model using 30 different values for the seed parameter, the particles in the initial samples of each simulation thus have different positions and contact properties. This series will be called CLP1 and uses the default parameters, see table 2.4. Note that all samples have approximately the same initial densities. figure 2.12 shows the AOR measured using CLP1 heaps, one can see that the variation in the measurement is lower that 3%. Even though the repeatability error is low, it will be systematically given for all series of simulations in this paper as error bars on the AOR axis.

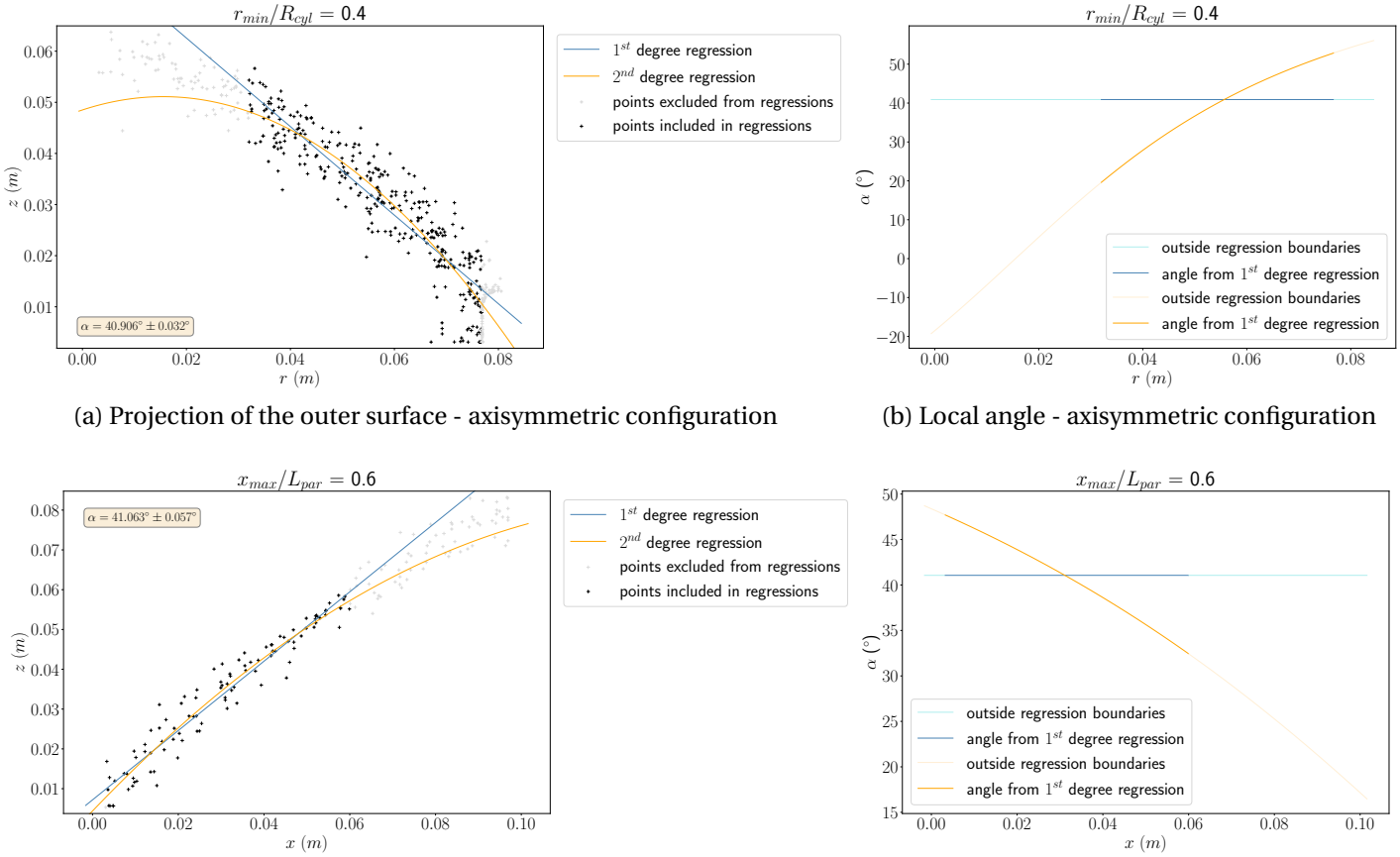

(a) Projection of the outer surface - axisymmetric configuration

(b) Local angle - axisymmetric configuration

(c) Projection of the outer surface - plane strain configuration

(d) Local angle - plane strain configuration

FIGURE 2.10. – Outer surface regressions for an intermediate $\tilde{x}_{min}$ and the associated measurement ((a), (c)) in both configurations.

2.3.3. Measuring the void ratio for any shape of assembly

With respect to the objective of discussing the possible constitutive nature of the AOR determined as per section 2.3.2, it is interesting to characterize the state of the heap in terms of density or void ratio e, as a fundamental parameter of granular materials. This density characterization is not straightforward because of the irregular shapes of the heap along its free surface, and possible bias caused by an excess of void near the walls

As such, two methods are now proposed to compute the void ratio inside a granular assembly with a complex shape, while avoiding the boundary effects: a so-called "tetrahedron method" and a "sub-volume method". Both methods may output local values for e and rely on the Monte Carlo method's to compute volume proportions, in addition to, straightforward here, tests to determine whether a random point in space is inside a physical particle. The following differences still exist, though:

— the tetrahedron method applies for any shape of sample with no requirements on the geometry. It is based on a triangulation of the sample.

— the sub-volume method requires to define a sub-volume inside the sample, which can

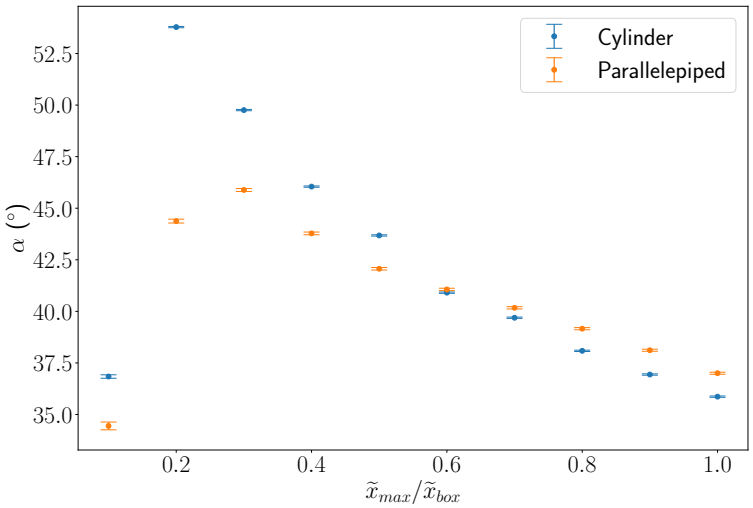

FIGURE 2.11. – Average slope as measured for different values of $\widetilde{x}_{max}$.

TABLE 2.4. – Parameters for heap simulations investigating repeatability (CLP1 series, 60 simulations in total).

Configuration	N_{part}	K_n $(N.m^{-1})$	K_s/K_n	ρ $(kg.m^{-3})$	Δt (s)	φ	e_0	Number of samples
Plane strain	2150	58250	0,37	1111	$7.86 \cdot 10^{-5}$	see figure 2.7	0.622 ± 0.012	30
Axial-symmetric	2468						0.744 ± 0.028	

be difficult if the latter has a peculiar shape. However, it is faster than the tetrahedron method.

2.3.3.1. The tetrahedron method

For computing a void ratio on a heap conforming any shape, the tetrahedron method's starts by a triangulation of the heap. The Monte Carlo method is then used to determine the proportion of particles inside each tetrahedron, leading to an expression for the void ratio.

Triangulating the heap

This is done using Delaunay's triangulation on the centers of all particles, although it could be done using another set of relevant points (e.g. the center of all spheres for clump simulations). Also, one should keep in mind that when triangulating using the center of the particles a small part of the sample is ignored: all particles on the outer surfaces are cut by the boundary's tetrahedron. This should effectively remove the excess of void near the walls of any sample. The set of all tetrahedrons will be denoted $\{t\,e\,t\}$.

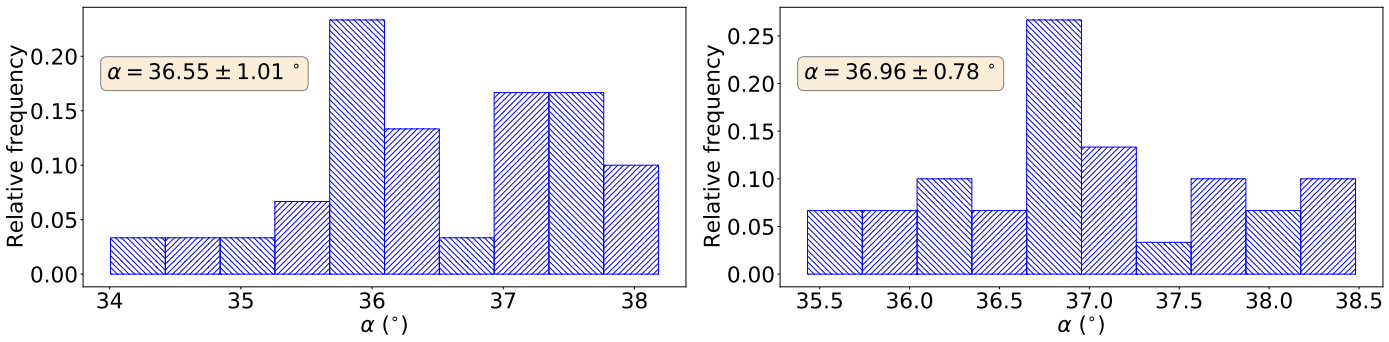

(a) Plane strain

(b) Axial-symmetric

FIGURE 2.12. – Distributions of measured angles of repose when investigating repeatability in the CLP1 configurations of table 2.4.

Detecting which particle may be partially inside each tetrahedron

All particle's bounding boxes are tested to determine if they overlap a tetrahedron's bounding box. If so, the particle is further checked for intersected volume with the Monte Carlo method, forming a set of particles that is denoted $\{p\}^{cut}$. This step is not necessary but it drastically reduces the computation time.

Computing the total volume of particle inside each tetrahedron

In this step, N_{mc} points $\{\underline{x_i}, i \in [\![1, N_{mc}]\!]\}$ are uniformly drawn inside the tetrahedron, following [Rocchini and Cignoni 2000]. Each point is tested to determine if it is inside any of the particles potentially cut $\{p\}^{cut}$. Denoting :

— V^{tet} the volume of the tetrahedron tet, computed using its vertices' coordinates

— $\chi^p(\underline{x})$ the Boolean function equal to 1 if the point $\underline{x}$ is inside the particle p, 0 otherwise

— $H(n)$ the Heaviside function

, the Monte-Carlo method gives the total volume of particle inside the tetrahedron:

$$V^{tet}_{part} = \frac{\sum_{i=1}^{N_{mc}} H\left(\sum_{\{p\}^{cut}} \chi^p(\underline{x}_i)\right)}{N_{mc}} \times V^{tet} \tag{2.12}$$

A local void ratio can then be computed for the tetrahedron:

$$e^{tet} = \frac{V^{tet} - V^{tet}_{part}}{V^{tet}_{part}} \tag{2.13}$$

And globally:

$$V_{part} = \sum_{\{tet\}} V_{part}^{tet} \tag{2.14}$$

$$V_{tot} = \sum_{\{tet\}} V^{tet} \tag{2.15}$$

$$e = \frac{V_{tot} - V_{part}}{V_{part}} \tag{2.16}$$

Taking advantage of the independence between operations in each tetrahedron, the proposed implementation of this method is parallel with an almost optimal speed-up: the increase in execution speed is close to the number of processes running at the same time.

2.3.3.2. The sub-volume method

The sub-volume method mainly consists in three steps.

Defining the sub-volume

This step is illustrated using the samples' geometries presented in this paper. The sub-volume is chosen as a homothetic transformation of the heap centered in the sample, for both configurations. The sub-volume and the total volume of the sample will be denoted V_{sub} and V respectively. At the final state, the geometry of the sample is assumed to be a half parallelepiped (respectively a cone) for the plane strain (respectively axial-symmetric) configuration. The sub-volume is defined using a parameter C that pilots the homothetic transformation. The coordinates of the sub-volume's axis aligned bounding box are denoted $\left(x_{min},\ y_{min},\ z_{min}\right)$ and $\left(x_{max},\ y_{max},\ z_{max}\right)$ and depend on the coordinates of the sample's axis aligned bounding box: $\left(X_{min},\ Y_{min},\ Z_{min}\right)$ and $\left(X_{max},\ Y_{max},\ Z_{max}\right)$.

In the case of the plane strain configuration, the homothetic sub-volume can be determined as follows (figure 2.13):

$\forall (s,S) \in \{(x,X),(y,Y),(z,Z)\}$
$\forall C \in]0.5,1]:$

$$s_{min} = (1-C)(S_{max} - S_{min}) + S_{min} \tag{2.17}$$

$$s_{max} = C(S_{max} - S_{min}) + S_{min} \tag{2.18}$$

In the case of the axisymmetric configuration, one has to compute the x and y coordinates of the center, x_Ω and y_Ω respectively, and the maximum radius r_c of the cone (figure 2.13).

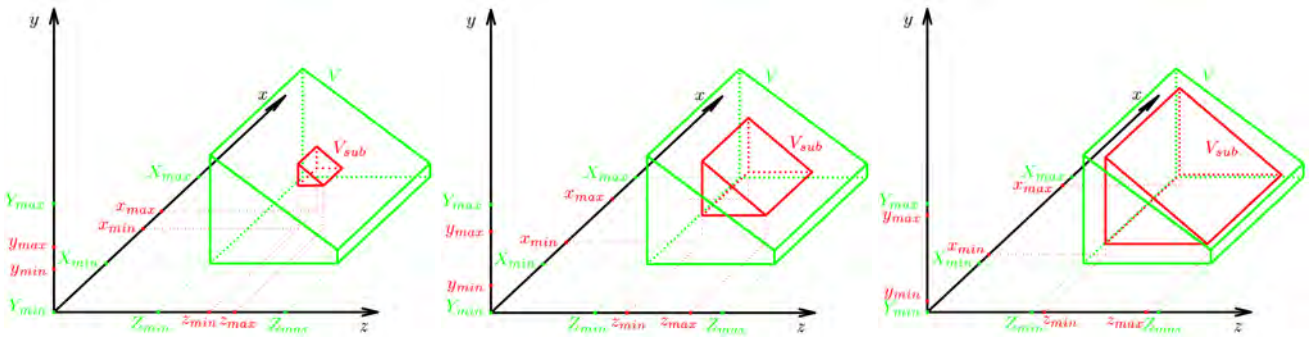

(a) $C = 0.6$ (b) $C = 0.75$ (c) $C = 0.9$

FIGURE 2.13. – Illustration of sub-volume for several C values in the plane strain configuration.

The homothetic sub-volume then is:

$\forall (s,S) \in \{(x,X),(y,Y)\}$
$\forall C \in]0.5,1]$:

$$z_{min} = (1-C)(Z_{max} - Z_{min}) + Z_{min} \tag{2.19}$$
$$z_{max} = C(Z_{max} - Z_{min}) + Z_{min} \tag{2.20}$$
$$s_\Omega = \frac{S_{min} + S_{max}}{2} \tag{2.21}$$
$$r_c = (2C-1)\frac{X_{max} - X_{min} + Y_{max} - Y_{min}}{4} \tag{2.22}$$
$$\tag{2.23}$$

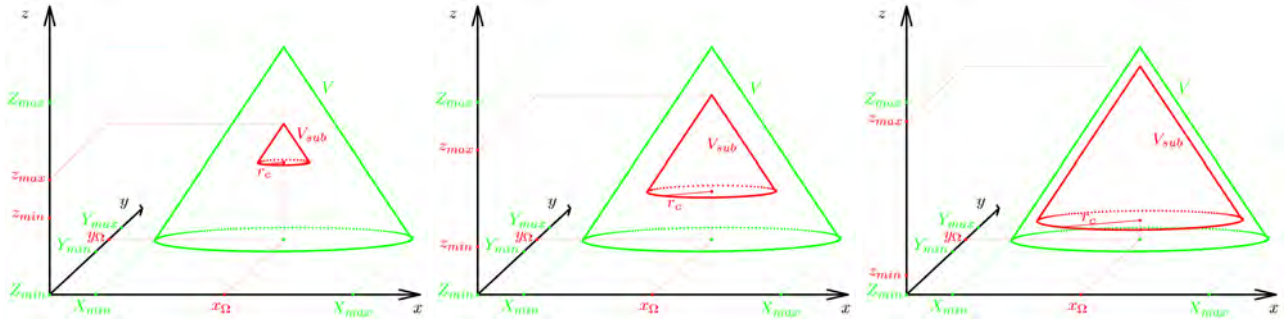

(a) $C = 0.6$ (b) $C = 0.75$ (c) $C = 0.9$

FIGURE 2.14. – Illustration of sub-volume for several C values in the axial-symmetric case.

Counting the volume of particles completely inside the sub-volume

During this step, the 8 vertices $\underline{x}_i^p$ of a particle's axis aligned bounding box are tested to determine if they are part of the sub-volume. Using the $\chi^{sub}(\underline{x})$ function, the number of vertices inside the sub-volume for a particle p is:

$$N_{in}^p = \sum_{i=1}^{8} \chi^{sub}(\underline{x}_i^p) \tag{2.24}$$

If $N_{in}^p = 8$ the particle p is completely inside the sub-volume, if $N_{in}^p = 0$ the particle p is completely outside the sub-volume.

Denoting V^p the volume of the particle p, the total volume of particles completely inside the sub-volume is:

$$V_{part}^{in} = \sum_{\{p \ | \ N_{in}^p = 8\}} V^p \tag{2.25}$$

Counting the volume of particles partially inside the sub-volume

If $0 < N_{in}^p < 8$, the particle may be cut by the faces of the sub-volume. The proportion of the particle's volume inside the sub-volume is again determined using the Monte Carlo method: N_{mc} points, $\{\underline{x}_i, i \in [\![1, N_{mc}]\!]\}$, are uniformly drawn inside the particle's bounding box and tested to determine if they are both inside the sub-volume (test function $\chi^{sub}(\underline{x}_i)$) and inside the particle (test function $\chi^p(\underline{x}_i)$. The proportion of a particle's volume being also part of the sub-volume is then:

$$V_{in}^p = \frac{\sum_{i=1}^{N_{mc}} \chi^{sub}(\underline{x}_i)\chi^p(\underline{x}_i)}{N_{mc}} \times V^p \tag{2.26}$$

The total volume of particles partially inside the sub-volume is:

$$V_{part}^{cut} = \sum_{\{p \ | \ 0 < N_{in}^p < 8\}} V_{in}^p \tag{2.27}$$

The total volume of particle inside the sub-volume is then :

$$V_{part} = V_{part}^{in} + V_{part}^{cut} \tag{2.28}$$

Finally, the void ratio is:

$$e = \frac{V_{sub} - V_{part}}{V_{part}} \tag{2.29}$$

For the simplest sub-volume's geometries the expression of V_{sub} is trivial, for other cases it can be determined using once again the Monte Carlo method inside the sub-volume's bounding box:

$$V_{sub}^{bb} = (x_{max} - x_{min})(y_{max} - y_{min})(z_{max} - z_{min}) \tag{2.30}$$

$$V_{sub} = \frac{\sum_{i=1}^{N_{mc}} \chi^{sub}(\underline{x}_i)}{N_{mc}} \times V_{sub}^{bb} \tag{2.31}$$

Both methods can be optimized when used with simple shapes (e.g. spheres): one could detect more precisely which particle may be cut. Also, one may be able to draw uniformly points directly inside the particle instead of the bounding box, the function χ^p would then be not necessary and the Monte Carlo method would be more accurate.

2.3.3.3. Examples of void ratio measurements

Local void ratio

The tetrahedron method makes it possible to establish directly a local representation of the void ratio, see figure 2.15 for one of the plane strain final heap. One can notice that the shape of the final heap is accurately captured by the triangulation, giving a rounded half parallelepipedic boundary surface. The density range is quite wide: some tetrahedrons located on the outer surface, where the particles moved, contain approximately 1000 times more voids than other tetrahedrons located where the particles almost didn't move. Note that this figure represents the void ratio directly interpolated from the centroid of each tetrahedron and thus should be interpreted carefully.

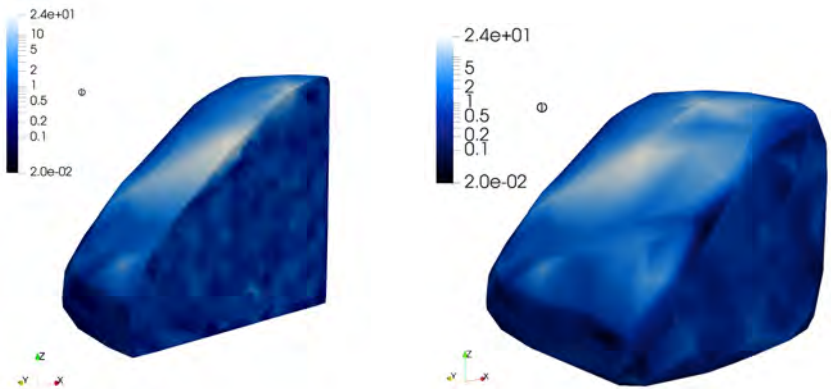

FIGURE 2.15. – Local void ratio in a plane strain final heap as measured with the tetrahedron method.

Executing the tetrahedron method in parallel

The independence of the processing of each tetrahedron makes it possible to parallelize this method. A series of measurements was performed on 30 of the clump initial samples

using different numbers of CPU's cores on the same machine previously used in section 2.3.1. The speed-up S and its standard deviation ΔS was computed from the computation times $T_{N_{cores}} \pm \Delta T_{N_{cores}}$ as follows:

$$S = \frac{T_1}{T_{N_{cores}}} \tag{2.32}$$

$$\Delta S = S\left(\frac{\Delta T_1}{T_1} + \frac{\Delta T_{N_{cores}}}{T_{N_{cores}}}\right) \tag{2.33}$$

Since the CPU's cache wasn't controlled, the total CPU's load had an influence on the computation speed, which might lead to a speed-up seemingly above perfection in the eventuality of the CPU's cache being full during the measurement on 1 core and not for more cores.

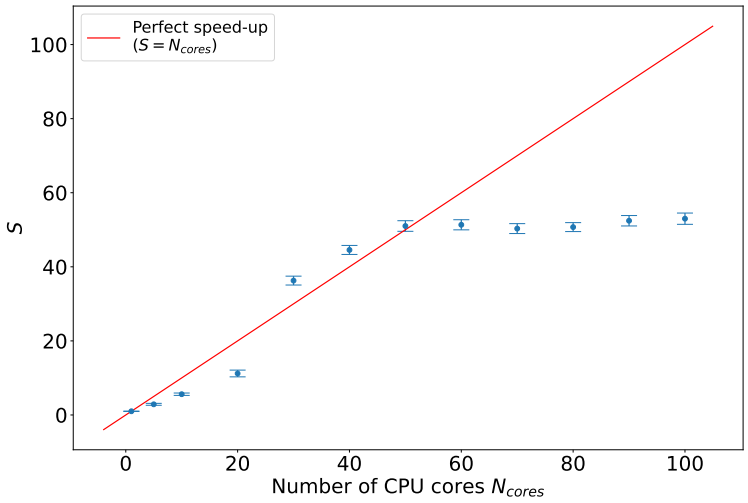

FIGURE 2.16. – Parallelization speed-up for the tetrahedron method.

Figure 2.16 shows the speed-up for $N_{cores} \in \{1, 5, 10, 20, 30, 40, 50, 60, 70, 80, 90, 100\}$. The speed-up doesn't improve starting from $N_{cores} = 50$, which is probably due an over usage of the CPU. A better control of the CPU could give more accurate speed-up measurements. Nevertheless, for $N_{cores} < 50$ the parallelization is optimum: $S \approx N_{cores}$.

Sub-volume and tetrahedron methods comparison

Void ratio measurements were performed for the clump model on all initial samples of a plane-strain series of simulations, discussed in more details in section 2.4.3. Because of the simple parallelepipedic shape of these granular assemblies, a reference void ratio can be

easily computed using the sample's bounding box:

$$V_{tot} = (X_{max} - X_{min})(Y_{max} - Y_{min})(Z_{max} - Z_{min}) \tag{2.34}$$

$$V_{part} = \sum_{\{p\}} V^p \qquad \text{, with } \{p\} \text{ the set of all particles} \tag{2.35}$$

$$e^{REF} = \frac{V_{tot} - V_{part}}{V_{part}} \tag{2.36}$$

Figure 2.17 (a) illustrates the comparison between the mean values and standard deviation over the 30 samples of e^{REF}, e^{TET} for the tetrahedron method, and e^{SUB} for the sub-volume method. The latter has been computed for 3 values of N_{mc} and 40 values of C.

For $C = 1$, the sub-volume method, by definition, gives the exact same values for void ratio than when using the global bounding box: $e^{SUB} = e^{REF}$. On the other hand, for the lowest values of C, the measured void ratio varies a lot among the 30 simulations and in function of N_{mc}. Between $C \approx 0.7$ and $C \approx 0.9$, e^{SUB} is constant and its standard deviation get lower, being furthermore little dependent on N_{mc}. For $C > 0.9$, its mean value and standard deviation finally start to increase as expected due to the rigid boundaries constraining the granular assembly and favoring voids to form near the outer surfaces.

The tetrahedron method gives a e^{TET} measurement being close to e^{SUB} when $0.7 < C < 0.9$, which suggests that it successfully excludes the excess of void from the computation.

As for the computational costs, figure 2.17 (b) shows the corresponding execution times, t^{SUB}, t^{TET} and t^{REF}, while e^{TET} was computed using parallelization on 3 cores. One observes that, in spite of parallelization, the tetrahedron method is here significantly slower than the sub-volume method. Regarding the sub-volume method, using $N_{mc} = 1000$ instead of $N_{mc} = 100$ slows down considerably the computation for a measure being no more accurate, especially for high values of C.

In view of these results, subsequent measurements of void ratio will be obtained using the sub-volume method with $N_{mc} = 100$ and $C = 0.8$.

2.4. Physical discussion

This section analyses the dependence of AOR on several parameters: the particle's shape, the initial void ratio and the sample's size. Experimental results obtained by the JGS are also provided.

2.4.1. Parametric study

2.4.1.1. (Non-)Sensitivity to the tangential stiffness

A first series of simulations investigates the role of tangential stiffness when using the potential particles model and two different values of K_s: 240 N/m and 444 N/m (see sets B and C of table 2.5).

Results are given in figure 2.18 for what concerns the initial and final states of the samples. Most importantly, the two different values of tangential stiffness are shown to result in virtually the same AOR distribution. The $K_s = 240 N.m^{-1}$ value will thus be kept in the

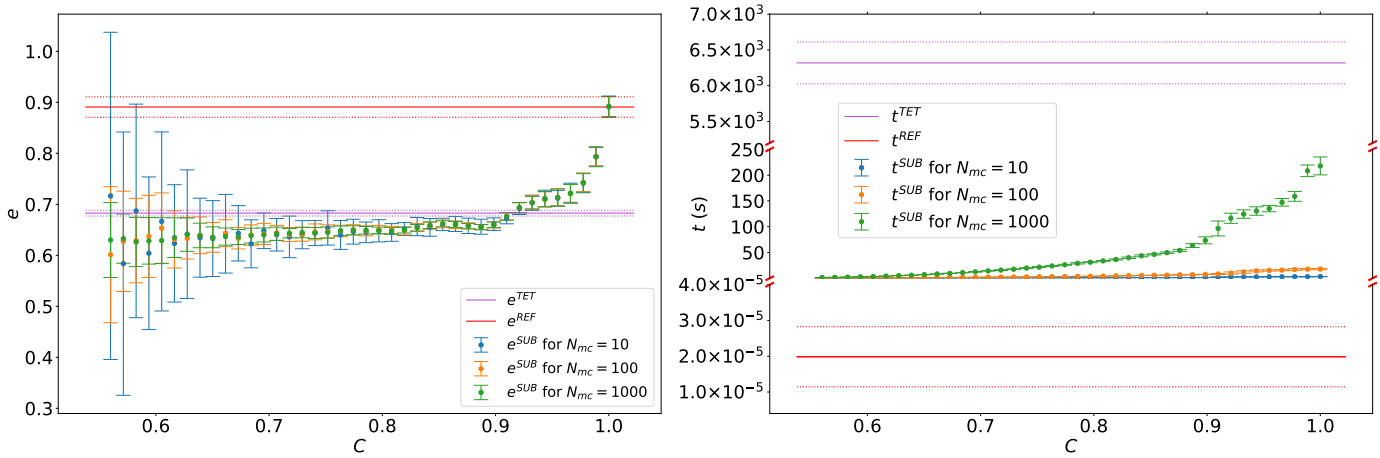

(a) Void ratio

(b) Time cost

FIGURE 2.17. – Void ratio measurements with both methods for a parallelepipedic initial sample. On figure (b), the y axis is broken at two places: first between 40 ns and 50 ms, and second between 250 s and 5200 s. The three parts of the y axis don't have the same scale.

TABLE 2.5. – Material properties for the parametric study with potential particles - series PP1.

Set id	Configuration	$K_n\ (N.m^{-1})$	K_s/K_n	$\rho\ (kg.m^{-3})$	$\Delta t\ (s)$	μ_{pp}	μ_{pw}	β_n	Number of samples
A			0.2	1111	$8.52 \cdot 10^{-5}$				
B	Plane strain	1200	0.2	943	$7.86 \cdot 10^{-5}$	0,713	0,514	0,071	30
C			0.37	943	$7.86 \cdot 10^{-5}$				

remainder of the sequel for it results in a higher critical time step. One may furthermore note that the initial coordination number is slightly lower with a higher K_s, which is expected since stiff particles tend to be further away from each other, even when constrained. However, at the final state the average coordination number is unaffected by K_s, certainly because they are not constrained enough for their relative distance to depend on K_s.

2.4.1.2. (Non-)Sensitivity to the particle's mass density

While the AOR α refers to a static condition, the mass density of particles ρ physically affects the prior dynamic evolutions of the system. On the other hand, from a computational standpoint, the density also controls the critical time step of the present explicit DEM scheme and the total time cost. Other series of simulations with different ρ are thus proposed to check whether a variation from the experimental reference $\rho = 1111\ kg/m^3$ would affect the AOR results.

Using potential particles, two values for the particle's density are considered in the framework of the PP1 series (sets A and B of table 2.5): the experimental one, $\rho = 1111\ kg/m^3$, and $\rho = 943\ kg/m^3$ that would confer the potential particle the same mass as the physi-

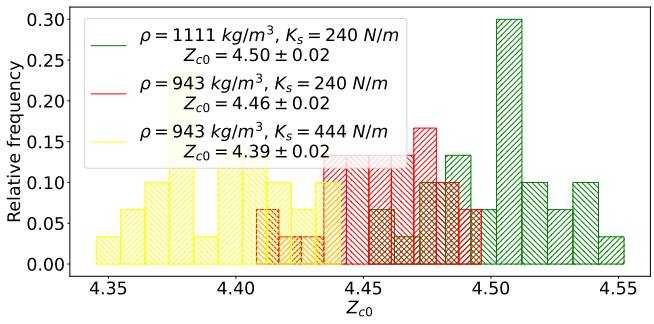

(a) Initial average coordination number

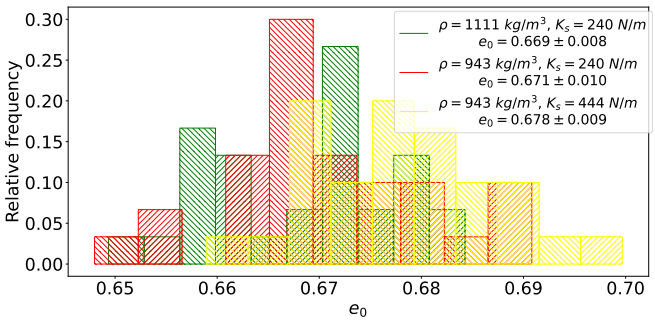

(b) Initial void ratio

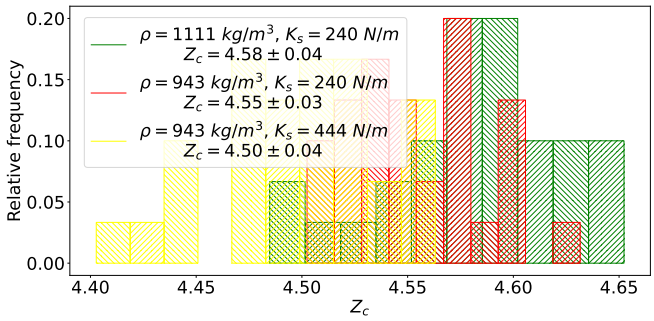

(c) Average coordination number at final stage

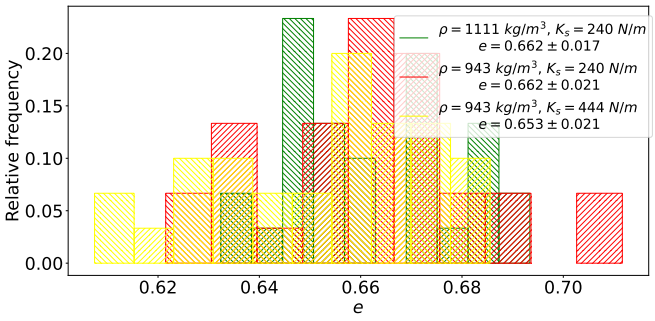

(d) Void ratio at final stage

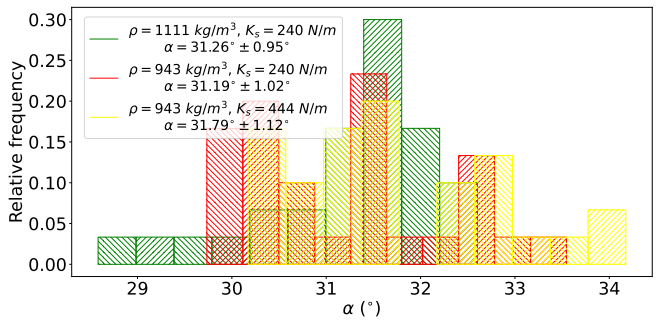

(e) Angle of repose at final stage

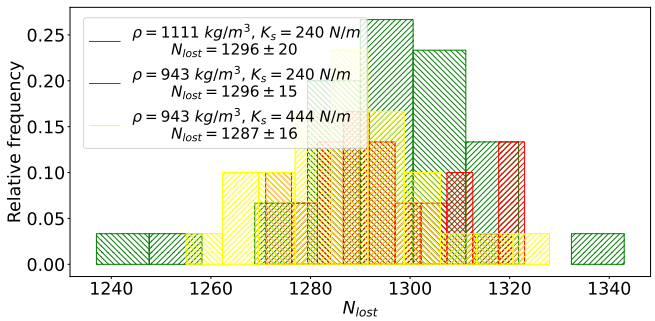

(f) Number of lost particles at final stage

FIGURE 2.18. – Macro-scale and micro-scale results of the parametric analysis with potential particles (PP1 series, table 2.5).

cal particle in spite of the volume differences discussed in the above section 2.2.2.3. Using clumps in a CLP2 series, four to seven different values for $\rho \in [100\ \ kg/m^3; 10\,000\ \ kg/m^3]$ are considered, with 10 different initial samples in each case. Corresponding parameters are all given in table 2.6.

Figure 2.19 shows the resulting angles of repose in the CLP2 and PP1 series, together with time costs of CLP1 series measured for a sequential execution on the same machine presented in previous section 2.3.1. The dots correspond to the mean measurement over all samples for a given particle's density and the error bars represent the standard deviation. One can see that all error bars share a common zone for a given shape description. As such, it is herein

TABLE 2.6. – Parameters of heap simulations investigating ρ influence (CLP2 series, 110 simulations in total).

Configuration	N_{part}	ρ	e_0	Number of samples
Plane-strain	2150	100 kg/m^3	0.652 ± 0.011	10
		500 kg/m^3	0.6325 ± 0.010	
		1111 kg/m^3	0.6225 ± 0.009	
		2000 kg/m^3	0.618 ± 0.010	
		4000 kg/m^3	0.607 ± 0.011	
		8000 kg/m^3	0.603 ± 0.012	
		10 000 kg/m^3	0.603 ± 0.010	
Axial-symmetric	2468	1111 kg/m^3	0.743 ± 0.022	
		4000 kg/m^3	0.723 ± 0.015	
		8000 kg/m^3	0.709 ± 0.019	
		10 000 kg/m^3	0.694 ± 0.010	

concluded, consistent to [Zhou, Xu, Yu, et al. 2001], that particle's density doesn't impact the AOR. During DEM simulations, one can thus adopt, when necessary, an artificial $\rho = 10000$ kg/m^3, multiplying the critical time step by a factor of $\sqrt{\frac{10000}{1111}} \approx 3$ and reducing as much the total time cost of the simulation (figure 2.19b) until the heap stabilizes. In the figure 2.19b, one can finally note a longer computation time for the axisymmetric configuration because of a lower velocity of the descending wall in the reference experiments.

2.4.2. Numerical angle of repose vs experimental one

The numerical simulations are now compared with the experimental results provided at the end of the JGS round-robin. In this framework, a simpler method is adopted to compute the AOR, considering only the highest particle instead of the whole external surface as in previous section 2.3.2, for sake of simplicity during the experiments. In the axial-symmetric configuration, slopes are actually determined in many directions being not exactly radial and their average is used compute the AOR, while in the plane strain configuration the AOR is computed using only one slope direction in the plane. This one particle measurement assumes a flat shape for the outer surface of the heap, which is found to be curved later in the current study (see figure 2.10)

In this subsection, the exact same method is adopted to interpret numerical results for a consistent comparison. The set of parameters used for the clump model is the same as for CLP1 (see table 2.4), and the set of parameters used for the potential particle model is given in table 2.7.

Table 2.8 compares the obtained experimental and numerical results. In the plane strain configuration, the experimental AOR is approximately 8% higher than the one obtained for the clump model and 16% higher than the one obtained for the potential particle model. In the axial-symmetric configuration, the experimental AOR is approximately 4% higher

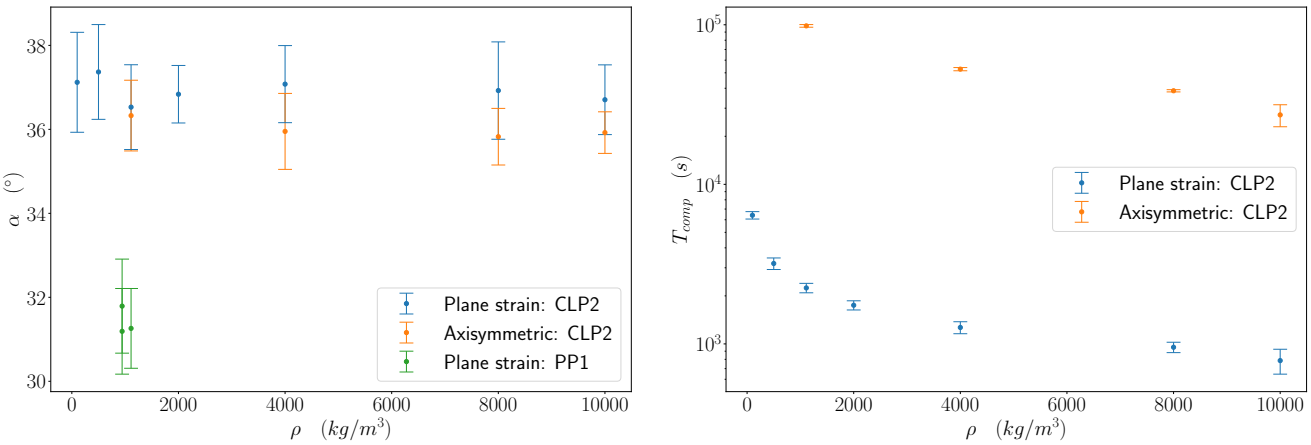

(a) Angle of repose

(b) Time cost

FIGURE 2.19. – Particle's density influence on the angle of repose and on the time cost - CLP2 and PP1 series

TABLE 2.7. – Material properties used in the potential particles models.

$K_n\ (N.m^{-1})$	K_s/K_n	$\rho\ (kg.m^{-3})$	$\Delta t\ (s)$	μ_{pp}	μ_{pw}	β_n
1200	0.773	943	$7.86 \cdot 10^{-5}$	0.713	0.514	0.071

than the one obtained with the clump model and 16% higher than the one obtained for the potential particle model. Also, one should notice that in the plane strain configuration the JGS's method measures an AOR higher than the method presented in this paper, and lower in the axial-symmetric configuration (see figure 2.12). This changes the conclusion on the influence of the configuration: with our measurement method both configurations gives the same AOR (difference of approximately 1% with the clump model), while the JGS's method gives a difference of approximately 11%.

2.4.3. Role of particle concavity

The differences in AOR observed in table 2.8 between the clump and potential particle (PP) models, with a higher discrepancy for PP towards experiments, certainly arise from the convex simplification of potential particles, with respect to the concavities of the physical particles which allow them to interlock better. In order to gain more insights into the influence of particle concavity, a rigorous comparison between the two numerical models is led in this subsection, adopting the same parameters for both models (except for the time step for computational efficiency) and determining the AOR using the more reliable method presented in section 2.3.2. This series is called PP-CLP, with all parameters being listed in tables 2.9 and 2.10.

Figure 2.20 characterizes the initial and final states of these PP-CLP simulations. First and foremost, it is to notice that the AOR is approximately 14% lower with the potential particle

TABLE 2.8. – Angle of repose as per the JGS measurement method.

	Number of samples	Average (°)	Standard Deviation (°)	Minimum (°)	Maximum (°)
Plane strain configuration					
Experiments [Japanase Geotechnical Society 2021]	400	41.4	1.28	38.3	46.3
Clumps	100	38.1	1.14	35.0	41.3
Potential particles	18	34.8	1.61	32.5	38.0
Axial-symmetric configuration					
Experiments []	50	35.3	0.9	33.3	37.3
Clumps	100	33.9	0.8	32.0	36.1
Potential particles	19	29.7	0.78	28.5	31.2

TABLE 2.9. – Contact parameters of the PP-CLP series focusing on particle concavity

Model	K_n	K_s	e_n	$\varphi_{part/part}$	$\varphi_{part/wall}$
Clump Potential particle	$1.2\ kN.m^{-1}$	$0.24\ kN.m^{-1}$	0.8	35.5°	27.2°

TABLE 2.10. – Other simulation's parameters of the PP-CLP series on particle concavity.

Model	Configuration	ρ	Δt	Number of samples
Clump Potential particle	Plane strain	$1111\ kg.m^{-3}$	$\approx 78.5\ ns$ $\approx 85.2\ ns$	30

model. This difference can be considered as significant and is even greater with respect to experiments even though the physical particles show a fairly high convexity of 0.954. In line with additional possibilities of interlocking for non-convex particles, while convex particles fall more easily from the heap, the number of lost particles is approximately 23% lower with the clump model. One can also note that the final void ratio is approximately the same with both models and that the final average number of interactions is approximately 25% lower with the potential particle model since two convex particles can form only one contact point, unlike the concave clump.

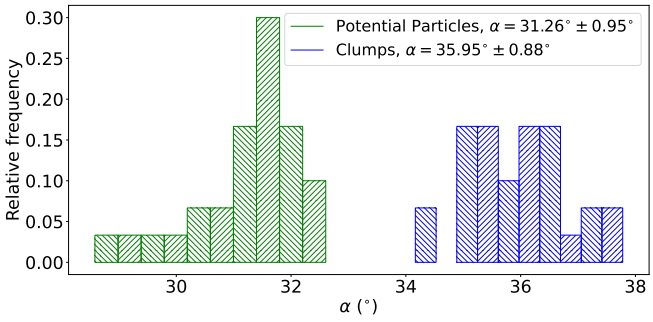

(a) Resulting angle of repose

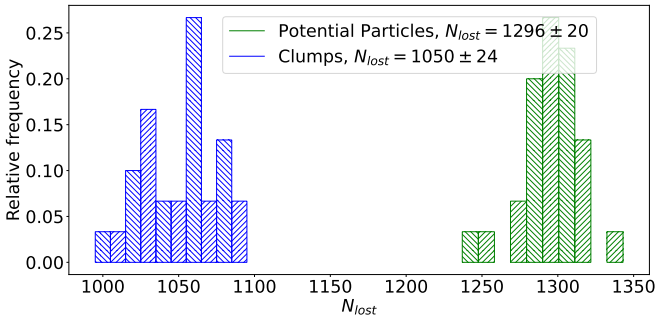

(b) Number of lost particles

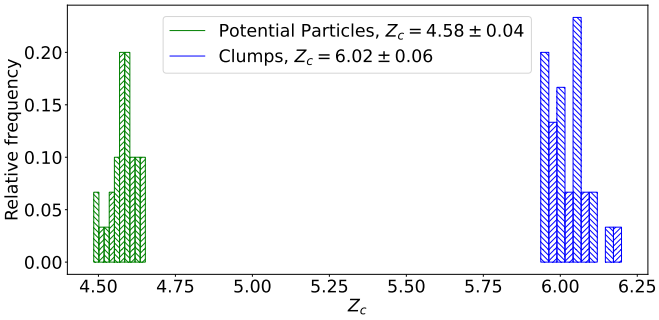

(c) Final average coordination number

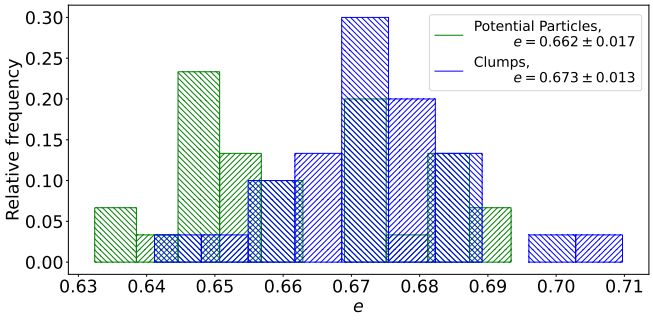

(d) Final void ratio

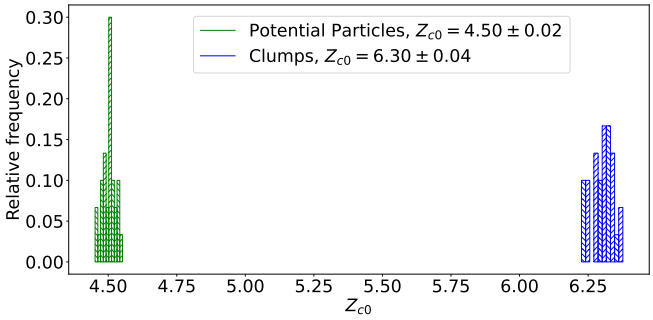

(e) Initial average coordination number

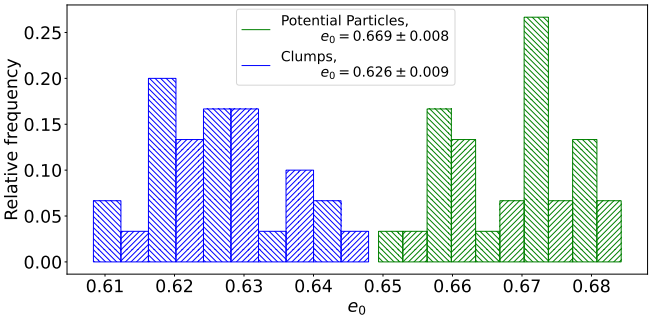

(f) Initial void ratio

FIGURE 2.20. – Characterization of the PP-CLP series in terms of initial and final states

It is worth noticing that the experimental measurement method gives a gap between

the axisymmetric and plane strain configurations' angle of repose. The curvature of the axisymmetric heap explains the lower measurement obtained with the JGS method.

Looking at initial stages, one observes that the initial void ratio is approximately 5% lower with the clump model. The difference between the void ratio at the initial state and final state is interesting: at the initial state the sample is constrained by four side walls and one bottom wall, while at the final state one of the four side of the sample is free. This suggests that concave particles are more likely to fill the voids when there are surrounded by walls (parallel to the gravity axis), but when they are free to move, they don't fill the voids better than convex particles. On the other hand, the difference on the average coordination number however is approximately the same at the initial and final states.

2.4.4. (Non-)Constitutive nature of the angle of repose

Searching for a possible constitutive nature of the AOR, the latter should be compared with shear strength properties of the granular material. Generally speaking in solid-like granular mechanics, these shear strength properties may refer either to a critical state or a state of maximum stress ratio, the two being possibly different depending on initial porosity.

Here, it is first determined whether the AOR α evolves with respect to the initial void ratio e_0, which would rule out the comparison with critical state properties. This is done by performing a "CLP4" series of simulations with the clump model using several samples at different initial porosities, whose parameters are given in table 2.11. The initial void ratio e_0 is set by altering the inter-particle friction angle during the generation of the sample, φ_{gen}, whereby lower φ_{gen}-values give denser packings, see figure 2.21 (a) where the error bars represent the standard deviation of e_0 on all 10 simulations performed at the same φ_{gen}. Figure 2.21 (b) shows α against e_0 and some decreasing tendency of α for $e_0 < 0.55$ in both configurations that would be more consistent with an interpretation of the AOR in terms of a porosity-dependent maximum friction angle. However, the significant dispersion of the results prompt the need for further investigations in the following.

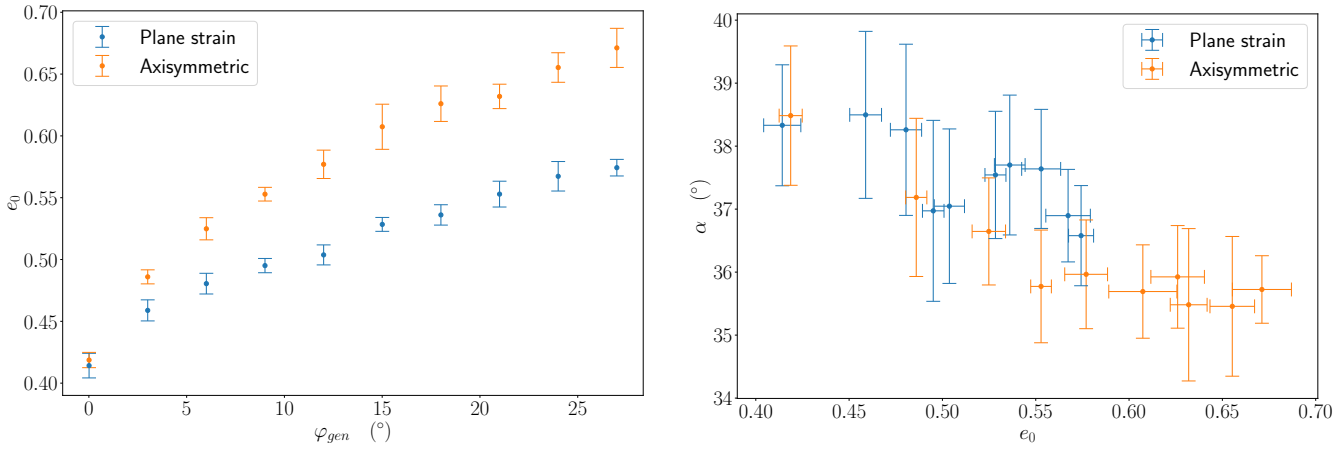

(a) Resulting e_0 against used φ_{gen} during packing preparation

(b) Angle of repose α against e_0

FIGURE 2.21. – Influence of the initial void ratio e_0 - CLP4 series

TABLE 2.11. – Parameters used when investigating a possible influence of e_0 (CLP4 series, 200 simulations in total)

Configuration	N_{part}	ρ	e_0	Number of samples for each e_0
Plane strain	2150	10000 kg/m^3	0.414 ± 0.010 0.459 ± 0.009 0.480 ± 0.008 0.495 ± 0.006 0.504 ± 0.008 0.528 ± 0.006 0.536 ± 0.008 0.553 ± 0.010 0.567 ± 0.012 0.574 ± 0.007	10
Axial-symmetric	2468		0.419 ± 0.006 0.486 ± 0.006 0.525 ± 0.009 0.553 ± 0.006 0.577 ± 0.011 0.607 ± 0.018 0.626 ± 0.014 0.632 ± 0.010 0.655 ± 0.012 0.671 ± 0.016	

Moreover the possible independence of α with respect to initial porosity, a critical state interpretation of the repose would impose a correlation between final porosity (or void ratio) and mean pressure p in the form of a critical state line (CSL). Assuming, likewise to void ratio e, that an average, i.e. global, stress tensor is a meaningfull quantity to characterize the heap in spite of gravity, the Appendix A recalls the expression of the latter tensor and the corresponding mean stress p, see equation .14. The final states (e, p) of a large set of 400 heaps simulated in the previous series CLP1, CLP4 together with a forthcoming CLP5 (grouped under a CLPX notation) are then compared in figure 2.22 with the CSL of the present granular material, previously determined in [Duverger, Duriez, Philippe, et al. 2021] from DEM triaxial tests. It is to note the the latter study showed that it is more relevant to consider rattlers (particles having at most 1 contact) as voids when determining the CSL of a granular material, to avoid an unphysical increase of the CSL in the (e, p) plane for low p. This is especially important here since body weights are the only external forces present in the CLPX series, making the average mean stress possibly quite low ($\approx 100\ Pa$), depending on mass density. Also, gravity was neglected for the triaxial simulations of [ibid.] but it makes the presence of rattlers very unlikely in the present study since particles can really be stable only if they have at least 3 contacts.

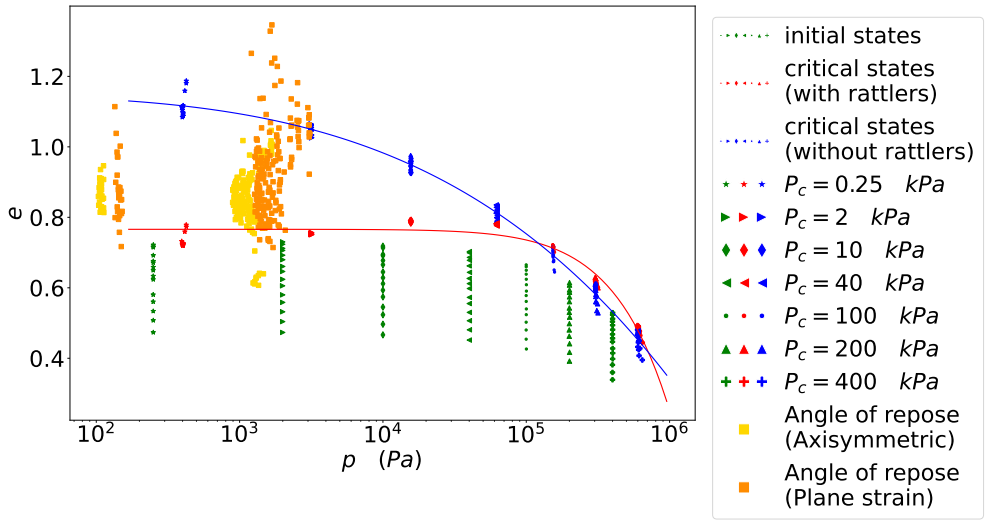

FIGURE 2.22. – Heaps' states compared to the critical state line as determined in [] from a large set of triaxial tests with different initial states in terms of void ratio and/or confining pressure P_c

From the comparison in figure 2.22, one can first note that the mechanical states in the CLPX series regroup around two different mean pressures: $126 \pm 18\ Pa$ and $1444 \pm 471\ Pa$, in connection with the two different values used for the particle's density throughout the CLPX series. Whatever the mass density, the mean pressure in axisymmetric heaps is lower than the mean pressure in plane strain heaps, and the dispersion in final void ratio is smaller. Most importantly, the heap states are clearly not consistent with the blue-colored (rattlers excluded) CSL serving as reference, which already suffices to exclude the assumption that a heap of particles under gravity is at critical state.

For completeness, the angle of repose of these CLPX series is still furthermore directly compared in figure 2.23 with the critical state friction angle ϕ_{crit} and the (porosity;mean stress)-dependent peak friction angle ϕ_{peak} of the material, determined on the triaxial simulations from []. The AOR is therein shown to be significantly different (higher from approx. 10 degrees) than ϕ_{crit}. It actually lies in the observed interval for ϕ_{peak}, even though both are observed to be essentially different.

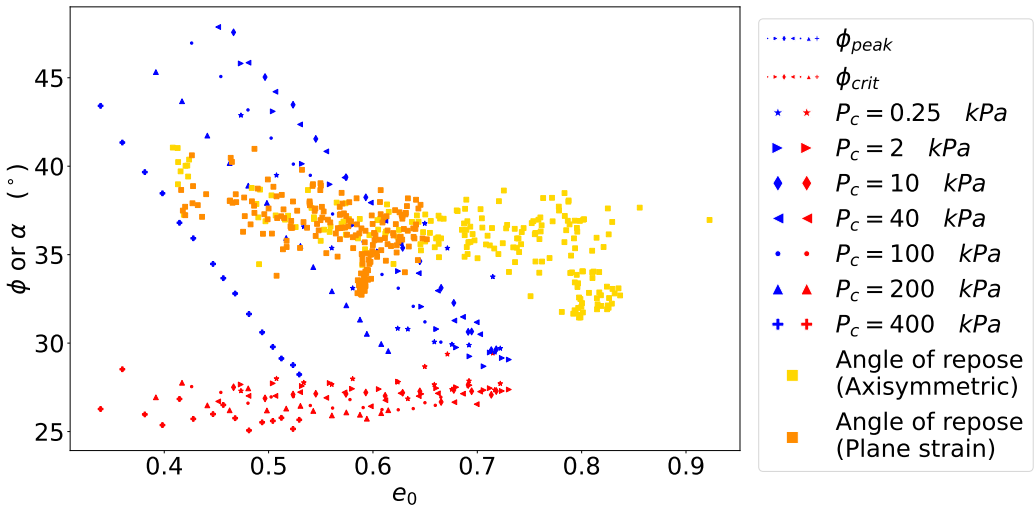

FIGURE 2.23. – Angle of repose α and triaxial properties, ϕ_{crit} and ϕ_{peak}, with respect to e_0

From the observations that the repose states are not consistent with the shear strength properties of the granular material, neither the critical one nor the maximum one, the AOR is concluded to bear no constitutive nature. Interpreting the repose stress state σ_{ij}^{glob} with its extreme principal stresses $\sigma_1^{glob} \geq \sigma_3^{glob}$ in terms of a mobilized friction angle ϕ_{mob}, given in equation 2.37 using the soil mechanics sign convention:

$$\phi_{mob} = \arctan\left(\frac{\sigma_1^{glob} - \sigma_3^{glob}}{2\sqrt{\sigma_3^{glob}\sigma_1^{glob}}}\right) \tag{2.37}$$

, no obvious correlation is actually found in figure 2.24, no matter the shape model, between the mechanics of the heap, ϕ_{mob}, and its geometry, α, which would have been necessary for a constitutive interpretation.

2.4.5. Effect of the sample's size on the angle of repose

Since the default number of particles in both configurations is low compared e.g. to the number of particles necessary to constitute a REV for the triaxial tests with rigid boundaries (7500 in [ibid.]), it is finally investigated to which extent the sample's size does affect the present discussion, performing a last "CLP5" series with the clump model and an evolving

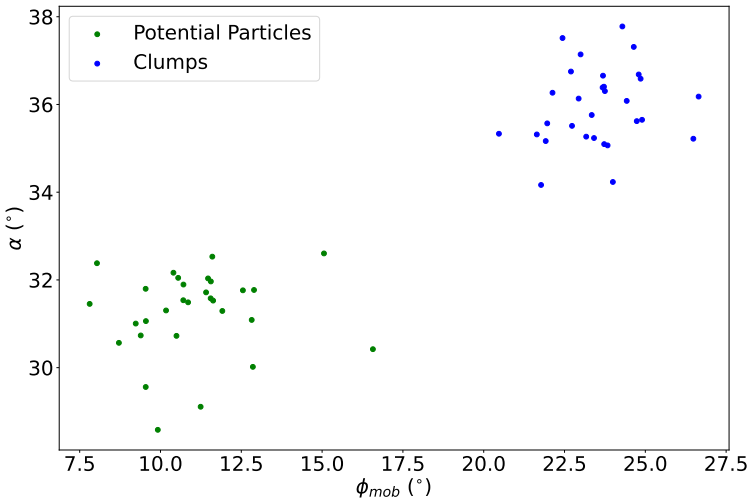

FIGURE 2.24. – Angle of repose α against mobilized friction angle ϕ_{mob} for heaps of the PP-CLP series.

number of particles N_{part} (see table 2.12 for all parameters). Doing so, the dimensions of the container are homothetically modified according to ${N_{part}}^{1/3}$.

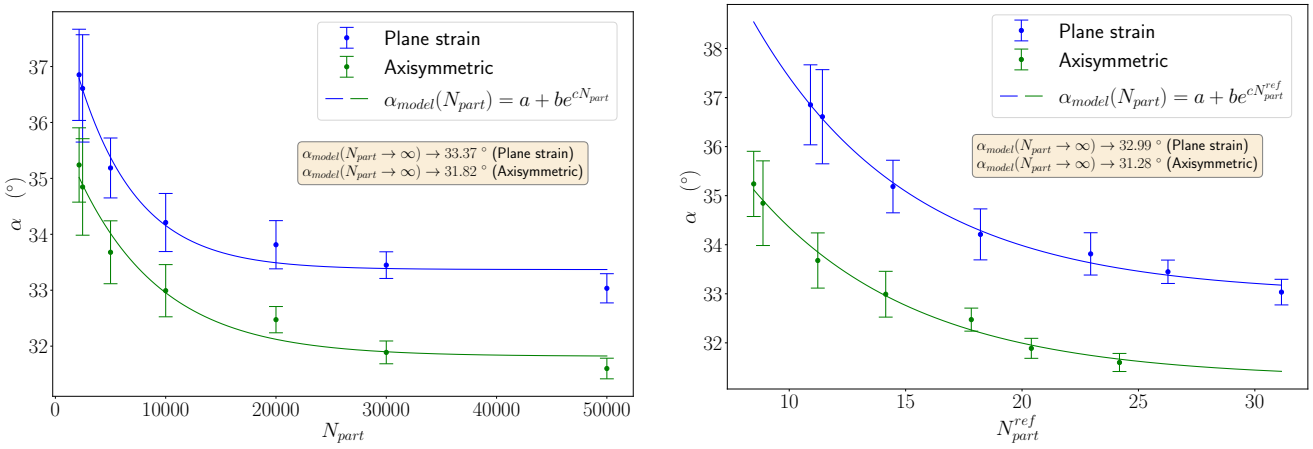

(a) α against N_{part}

(b) α against N^{ref}_{part}

FIGURE 2.25. – Effect of the sample's size on the angle of repose - CLP5 series

Figure 2.25 shows the AOR obtained in this CLP5 series, with error bars for the standard deviation computed on the ten simulations performed for each value of N_{part}. An exponential model is proposed to fit the data and extrapolate the value of α for an infinite number of particles:

$$\alpha_{model}(N_{part}) = a + b\,e^{cN_{part}} \tag{2.38}$$

with a, b and c the three model parameters. Figure 2.25 (a) illustrates that a common AOR

Configuration	N_{part}	ρ	e_0	Number of samples
Plane strain	2150	10 000 kg/m^3	0.603 ± 0.010	10
	2468		0.604 ± 0.009	
	5000		0.596 ± 0.005	
	10 000		0.596 ± 0.003	
	20 000		0.594 ± 0.002	
	30 000		0.591 ± 0.003	
	50 000		0.588 ± 0.001	
Axial-symmetric	2150		0.705 ± 0.011	
	2468		0.693 ± 0.010	
	5000		0.729 ± 0.017	
	10 000		0.741 ± 0.006	
	20 000		0.758 ± 0.008	
	30 000		0.746 ± 0.016	
	50 000		0.736 ± 0.004	

TABLE 2.12. – Parameters of heap simulations investigating the influence of N_{part} (CLP5 series, 140 simulations in total)

in both configurations appears only for $N_{part} = 2150$. On figure 2.25 (b) the horizontal axis represents N_{part}^{ref}, the number of particle along one dimension of the base of the box:

$$N_{part}^{ref} = \left(\frac{N_{part}}{V_{box}}\right)^{\frac{1}{3}} L_\eta \qquad \text{with } V_{box} \in \{V_{cyl}, V_{par}\} \text{ and } L_\eta \in \{R_{cyl}, L_{par}\} \tag{2.39}$$

For bigger systems with a higher N_{part} a clear difference appears, with a negligible standard deviation. According to the exponential decay model, an asymptotic difference difference between the two configurations would be 1.19° which corresponds to approximately 3.59% of the measurement in the plane strain configuration.

The present dependency to N_{part} constitutes a last argument against the constitutive nature of the AOR, making fortuitous the similarity of α initially observed between two configurations.

2.5. Conclusion

In the framework of a round-robin activity providing an experimental reference, the angle of repose of a granular material has been studied with DEM, adopting two distinct characterizations for particle shape: concave clumps of spheres and convex-simplified potential particles, with a quantification of the morphological differences between the two (and the experimental reference), in terms e.g. of convexity and sphericity.

A methodological discussion has then been first proposed for generic angle of repose studies, designing systematic measurement procedures of the slope angle and of the void ratio

of the heap, the latter being a possible factor of influence onto the former, as a fundamental property of granular matter.

Physically, a thorough analysis provided a number of consistent observations that the AOR does not bear a constitutive nature but is instead also process-dependent. In the comparison with experiments, while adopting a simpler measurement method of the AOR due to experimental limitations, the clump approach sucessfully predicted the AOR within a 8% tolerance. On the other hand, the potential particles underestimated to a greater extent the AOR, as expected due to their artificial convexity. Even though the material particles had a fairly high convexity value ($C = 0.954$), neglecting their local concavities brought down the AOR from $35.95 \pm 0.88°$ to $31.26 \pm 0.95°$.

It is interesting to note that both the clump and the potential particle shape description share the same dimensions in terms of a minimal bounding box and thus the same flatness and elongation values, prompting the need for a systematic investigation of particle-scale shape indices that would possibly affect the AOR.

Data availability

All YADE scripts used to perform the PP-CLP series are available online at https://forgemia.inra.fr/sacha.duverger/aor_nc_aix.

Acknowledgements

We thank the Japanese Geotechnical Society for organizing the DEM round robin test that motivated this study. The efforts of Dr. Shuji Moriguchi (Tohoku University) are in particular gratefully acknowledged. We also acknowledge the support from the French "Sud" region to the LS-ENROC project, which enabled us to use a recent server machine for running these 980 simulations.

Rattlers' involvement for possibly looser critical states under higher mean stress

Sacha Duverger[1], Jérôme Duriez[1], Pierre Philippe[1] and Stéphane Bonelli[1]

[1]INRAE, Aix Marseille Univ, RECOVER, Aix-en-Provence, France

Abstract

The critical state of a granular material made of rounded tetrahedral particles is studied through DEM simulations of triaxial compressions. A minimum number of 7500 particles is first obtained as the representative volume element (RVE) for the present triaxial simulations. Then, the macroscopic critical state line (CSL) is shown to be increasing in the (stress, density) space for low confining pressures. Such an unexpected behaviour is explained by the existence of a significant proportion of rattlers. Considering rattlers as voids indeed reinstates a classically decreasing CSL.

TABLE 2.13. – Contact parameters as measured by the JGS[1] - Intervals give the range of the distribution used for the parameter

type of contact	normal stiffness K_n	stiffness ratio K_t/K_n	internal friction angle φ	restitution coefficient e_n
resin against resin	58 250 N m^{-1}	0.37	$\in [28°, 44°]$	$\in [0.74, 0.84]$
resin against acrylic	77 666 N m^{-1}	0.37	0°	$\in [0.70, 0.82]$

2.6. Introduction

The ability of granular materials to sustain increasing shear strains under constant volume and constant shear stress has long been recognised as one of their salient features. From a soil mechanics point of view, such a deformation mechanism has been coined as "critical state" [Roscoe, Schofield, and Wroth 1958] and laid the basis for countless constitutive relations [Duriez and Vincens 2015]. Experiments [Bandini and Coop 2011]; [Chu 1995]; [Verdugo and Ishihara 1996] have shown that a critical state line (CSL) exists in the $(\log(p), e)$ plane (with p the mean pressure and e the void ratio) and that this CSL is decreasing. These observations were mostly confirmed numerically in [Sitharam and Vinod 2009]; [Verdugo and Ishihara 1996]; [Zhou, Liu, Ma, et al. 2017], using Discrete Element Methods (DEM) with spherical particles and the Hertz-Mindlin contact model. The parametric analysis led in [Huang, Hanley, O'Sullivan, et al. 2014] nevertheless has shown that the slope of the CSL depends on the inter-particle friction angle, and a positive slope was actually observed therein in some cases. This striking result was interpreted considering that, for high values of inter-particle friction angle, fewer particles are needed to maintain the static equilibrium of the packing and that several particles become "rattlers", having less than two contacts. Rattlers being strangers to the force chains, they do not really form part of the solid phase, and may bias the determination of the CSL, up to getting a positive slope.

The present study pursues the investigation into a possibly increasing CSL in DEM, that would contradict experiments. The granular material adopted herein is different from [ibid.], in terms of shape and contact model. Our numerical triaxial tests are indeed performed on a material made of tetrahedral particles interacting according to a visco-elastic contact model with friction. Note that gravity is not considered in this study. These simulations are conducted using the open source code YADE [Smilauer et al. 2021].

2.7. Material

The material studied in this paper is constituted of identical tetrahedral particles (figure 2.26). Each particle is a clump of four spheres with the same radius $R_{sph} = 3.101$ mm, being inscribed in an outer sphere of diameter $D_{clp} = 10$ mm. These particles have a density of $\rho = 1111$ kg m^{-3} so as to coincide with resin and the same holds for the other material parameters reported in table 2.13. The triaxial tests are performed using six infinite walls made of acrylic which interact with the particles but not with each other. These materials were actually used experimentally by the Japanese Geotechnical Society (JGS) for an ongoing round-robin test [1]. The relevant contact parameters used in DEM were measured experimentally by the JGS (see table 2.13). The internal friction angle φ was determined by performing sliding tests with

1. http://geotech.civil.yamaguchi-u.ac.jp/tc105/

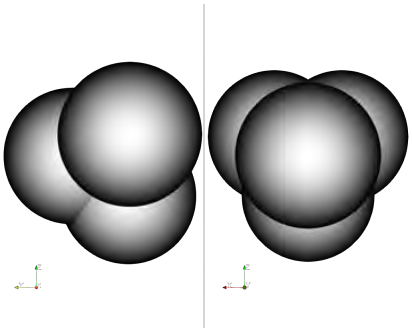

FIGURE 2.26. – Tetrahedral particle made of clumped spheres

resinous cubes against boards made of resin or acrylic. The normal restitution coefficient e_n was measured by performing drop tests with resinous spheres on boards made of resin or acrylic. Lastly, the normal stiffness K_n was determined on single spheres as the slope of the loading-displacement relation on the third cycle of compression tests. As for the tangential stiffness K_t, it was determined by setting arbitrarily the stiffness ratio K_t/K_n.

2.8. Contact model

The contact model accounts for friction through the inter-particle friction angle φ, used during the computation of the tangential force F_t. It also accounts for visco-elasticity through the restitution coefficient e_n, used during the computation of the normal force F_n. Indeed e_n can be expressed according to a damping coefficient c_n [Schwager and Pöschel 2007]. This damping coefficient can be determined using the Newton-Raphson method and then be used directly in the computation of F_n. Denoting u_n and u_t the normal and tangential relative displacements respectively, the normal and tangential forces finally read:

$$F_n = K_n u_n + c_n \dot{u}_n \tag{2.40}$$

$$|F_t| = \min(K_t |u_t|, F_n \tan(\varphi)) \tag{2.41}$$

Since the visco-elasticity already stabilizes the simulation an additional numerical damping is not necessary and was not introduced in the simulations.

2.9. Triaxial tests

The triaxial tests workflow is the following:

1. A cloud of particles is created by selecting the positions of the clump centers randomly. In order to eliminate this source of variability, the random number generation seed was fixed so that every triaxial tests begin with the same cloud of particles.
2. Six walls are created around the sample, they are then moved toward each other so the sample is isotropically compacted to a nominal confining pressure P_c. During this step, the inter-particle friction angle φ_{comp} can be set between 0.01° and 27° to reach

different initial packing densities. This method has already been used successfully in [Chareyre, Briançon, and Villard 2002] for 2D simulations and in [Tong, Catalano, and Chareyre 2012] for 3D simulations.

3. Once the sample is stable and the mean pressure on the walls P_w verifies $0.995P_c < P_w < 1.005P_c$, the compaction is considered over and φ is set to the value given in table 2.13. The sample stability is measured using the unbalanced force u_F, defined in [Smilauer et al. 2021]. The chosen condition for sample stability is $u_F < 10^{-2}$.
4. P_c is then maintained on the side walls and one axial wall is moved such that a strain rate $\dot{\epsilon}_{ax}$ is imposed to the sample. Denoting the inertial number $I_n = 2 \times 10^{-4}$, low enough to ensure quasi-staticity, $\dot{\epsilon}_{ax}$ is computed using the expression proposed in [GDR MiDi 2004]:

$$\dot{\epsilon}_{ax} = I_n \sqrt{\frac{P_c}{\rho R_{sph}^2}} \tag{2.42}$$

5. The triaxial test is stopped when the axial strain ϵ_{ax} reaches 0.8. The critical state is considered to be reached at $\epsilon_{ax} = 0.6$, which is enough according to [Bandini and Coop 2011]; [Chu 1995]; [Sitharam and Vinod 2009]; [Verdugo and Ishihara 1996]; [Zhou, Liu, Ma, et al. 2017] and figure 2.27. For any quantity s, its critical value s_{crit} will thus be computed as its average over $\epsilon_{ax} \in [0.6, 0.8]$.

2.9.1. RVE determination

This section aims to determine the size for the representative volume element (RVE) in the present configuration by performing triaxial tests with different number of particles: $N_{part} \in \{500 \times i; i \in [\![1, 20]\!]\}$. A reference triaxial test obtained for $N_{part}^{max} = 20\,000$ will be used to compute the root mean square error (RMS error) of each simulation. For a quantity s, the RMS error s^{err} over all the N_{pts} points of the shearing phase is computed as follows:

$$s^{err}(N_{part}) = \sqrt{\frac{1}{N_{pts}} \sum_{0 \leq \epsilon_{ax} \leq 0.8} \left(s(N_{part}, \epsilon_{ax}) - s(N_{part}^{max}, \epsilon_{ax})\right)^2} \tag{2.43}$$

This serie will be called S1. All the triaxial tests in this serie are performed with $P_c = 100$ kPa. A target initial void ratio is set by slowly reducing the inter-particle friction angle during the isotropic compaction (as in [Chareyre, Briançon, and Villard 2002]), all samples thus start the shearing phase with $e_0 \approx 0.60$.

Figure 2.27 shows q and ϵ_V during all the simulations of S1. The deviatoric stress q is defined as the difference between the stress on the shearing axis and the lateral stress. The volumetric strain ϵ_V is defined as the trace of the true strain tensor. The RMS error based on equation 2.43 was plotted for q and ϵ_V on figure 2.28. One can see that q^{err} and ϵ_V^{err} are decreasing for $N_{part} \leq 7000$ and then progressively reach a plateau. In addition, figure 2.29 shows the time cost T_c of all the simulations in S1, being run sequentially on a processor Intel(R) Xeon(R) CPU E5-2623 v3 @ 3.00GHz. Obviously T_c increases almost linearly with N_{part}. Considering the results given in figure 2.28 and figure 2.29, the best compromise between precision and time cost is met for $N_{part} = 7500$.

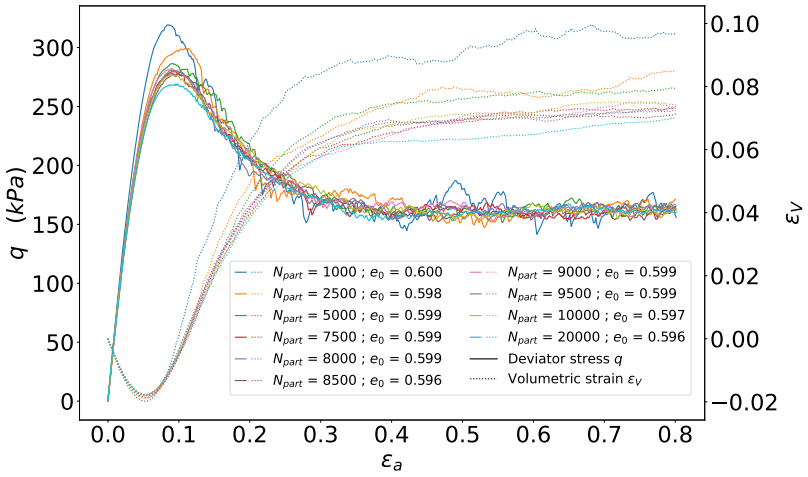

FIGURE 2.27. – q and ϵ_V during some S1 simulations

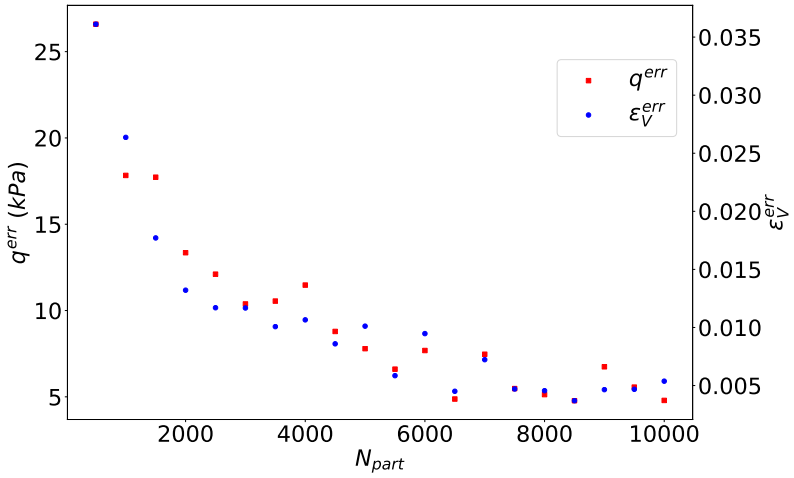

FIGURE 2.28. – RMS error on q and ϵ_V for all S1 simulations

2.9.2. Critical state and rattlers' influence

Using now 7500 particles, another serie of triaxial tests (called S2) was performed using 7 different confining pressures P_c and 15 different initial void ratios e_0, constituting a large collection of 105 triaxial tests to plot the CSL. As already explained, the initial density was set by modifying the inter-particle friction angle during the isotropic compaction. In table 2.14 the values used for P_c are given alongside the minimum and maximum initial void ratio obtained for each P_c, namely e_0^{min} and e_0^{max}. Figure 2.30 shows the e_0 obtained for each φ_{comp} under all P_c.

The red lines on figure 2.31, fitted to the critical states for $P_c < 40$ kPa and $P_c \geq 40$ kPa, represent the obtained CSL $e_{crit}(p)$. One can see that for $P_c < 40$ kPa the CSL is increasing, such a counter-intuitive behaviour is also observed in [Huang, Hanley, O'Sullivan, et al. 2014] for $\varphi > 26°$. The inter-particle friction angle indeed helps stabilising the force chains and makes some particles unnecessary to maintain the static equilibrium of the packing. Such a

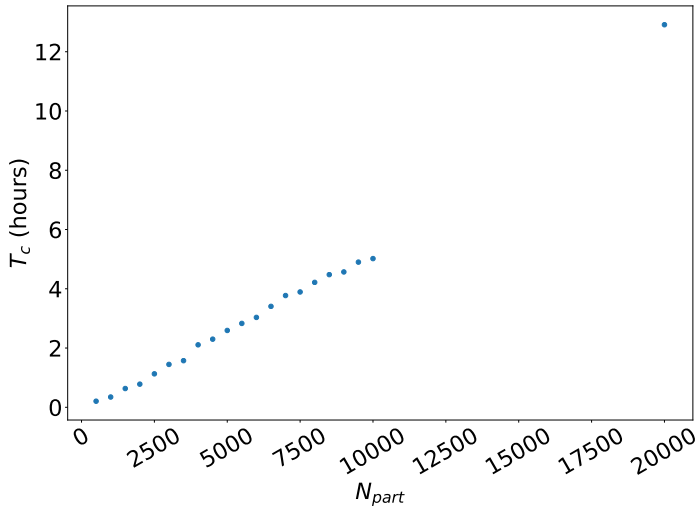

FIGURE 2.29. – Time costs for all S1 simulations

TABLE 2.14. – Parameters of S2

P_c (kPa)	e_0^{min}	e_0^{max}
0.250	0.473	0.722
2	0.473	0.730
10	0.466	0.718
40	0.451	0.703
100	0.426	0.665
200	0.392	0.615
400	0.339	0.529

passive particle is called a rattler and is considered to be so if it has only 0 or 1 contact. Their number, $N_{rattlers}$, is depicted in figure 2.32. It can be stated that the lower P_c, the higher and noisier $N_{rattlers}$, and that a critical (e_0-independent) value is also eventually obtained. Beside, $N_{rattlers}$ stabilises faster for loose samples but slower for high P_c, except if P_c is high enough for rattlers to be too rare ($P_c > 100$ kPa). Figure 2.33 shows the critical mean coordination number Z_c^{crit} against the critical number of rattlers $N_{rattlers}^{crit}$ normalised by the number of particles. It is noticeable that Z_c^{crit} is strongly correlated with $N_{rattlers}^{crit}$ and decreases linearly for $P_c \leq 40$ kPa.

The great proportion of rattlers at low P_c (around 20%) shows that the CSL is biased by these passive particles and suggests that they could be preferably counted as voids. To this end, a void ratio "without rattlers" e^{WOR} was computed following []. Denoting V_{void} the volume of all the voids in the sample, V_{part} the volume of all the particles in the samples and V_{clp} the volume of one particle, it comes:

$$e^{WOR} = \frac{V_{void} + N_{rattlers} V_{clp}}{V_{part} - N_{rattlers} V_{clp}} \tag{2.44}$$

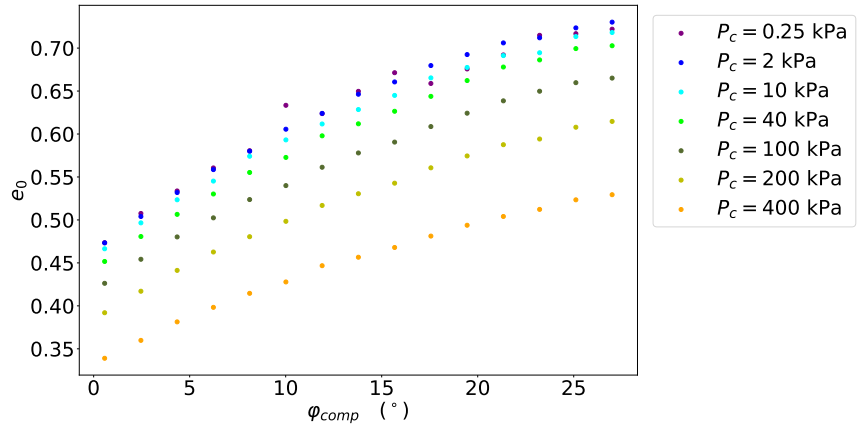

FIGURE 2.30. – Initial void ratio against generation inter-particle friction angle

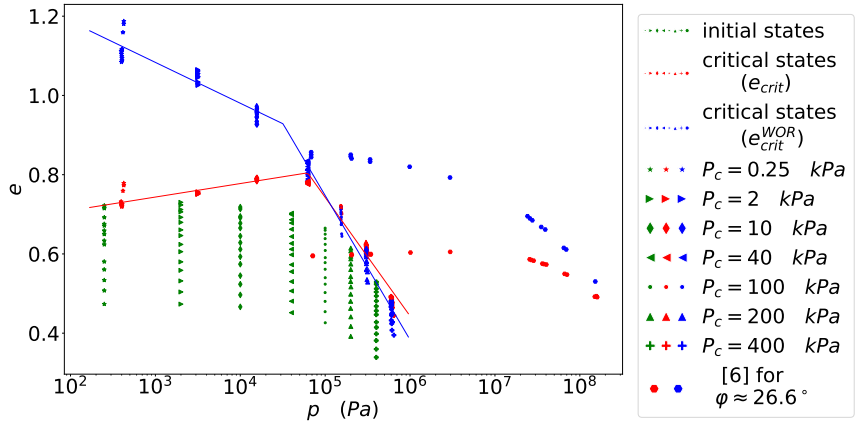

FIGURE 2.31. – Critical state lines for all S2 simulations with rattlers (red symbols) and without (blue symbols).

The blue lines plotted on figure 2.31 corresponds to the CSL obtained by considering e_{crit}^{WOR} instead of e_{crit}. Obviously, this consideration is enough to obtain a classical decreasing CSL at low P_c.

2.10. Conclusion

In this paper, triaxial tests were performed on tetrahedral particles using a visco-elastic contact model with friction and no gravity. It was first determined that 7500 particles is an appropriate sample size to constitute a RVE for the present triaxial analysis. Then, the critical states reached with triaxial tests performed at several confining pressures and initial packing densities showed that rattlers should be considered as void, specially for confining pressures lower than 40 kPa. Indeed, including rattlers into the computation of the critical packing density makes the critical state line to unexpectedly become increasing at low confining pressures. One could investigate further in the matter by performing triaxial tests under

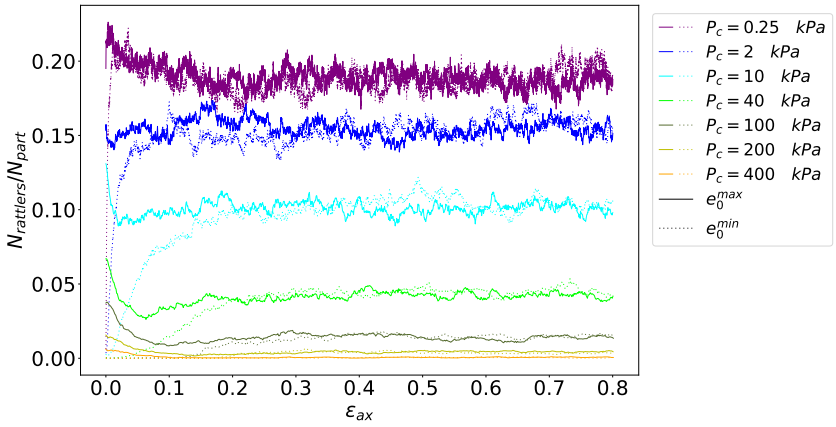

FIGURE 2.32. – Proportion of rattlers in S2 simulations

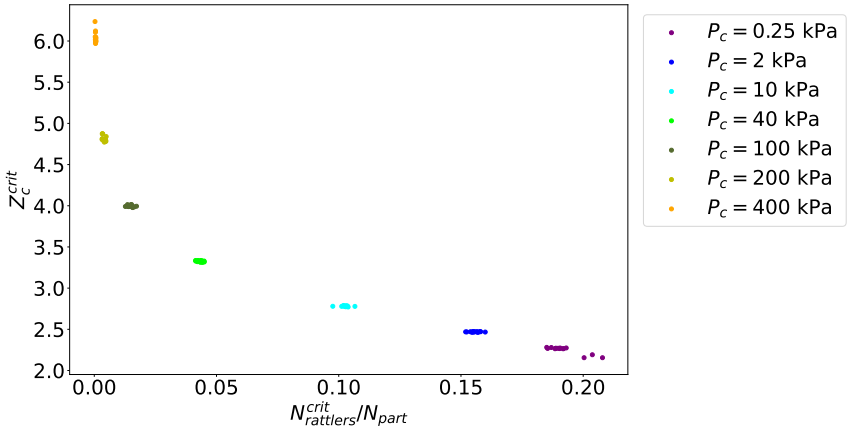

FIGURE 2.33. – Critical mean coordination number against critical proportion of rattlers in S2 simulations

gravity, which should in principe reduce substantially the number of rattlers at low pressure. It is worth noting that the material studied here only contains identical particles, the results might differ for more classical granular materials. Indeed small and coarse particles, usually present in granular materials, should increase the number of rattlers even for high confining pressures.

Acknowledgements

The authors acknowledge the Japanese Geotechnical Society (Shuji Moriguchi, Tohoku University) for motivating this study through the organisation of an angle of repose round-robin test.

Conclusion on DEM

This chapter showed through many simulations that the DEM is well-suited to investigate the properties of granular materials, although in some extreme cases additional considerations are necessary to preserve the consistency with experiments. Indeed, the exhaustive description of the microstructure offered by the DEM gives access to important insights on the granular assembly such as the precise location and geometry of each grain, allowing for accurate measurements (e.g. angle of repose, void ratio). Also, the numerical nature of the DEM gives an absolute control over the test's parameters, making possible the study of some important parameters' influence such as the grain shape. However, one should make sure that all significant phenomena have been accounted for, even with a basic model. For instance, in the case of DEM triaxial tests, the effects of gravity are often neglected since they are not relevant to the material's behaviour and not significant at traditional confining pressures. Nevertheless, when considering low confining pressures, the configuration of the force chains were found to be unrealistic at the critical state, causing an error on the description of the material's state. Although, considering isolated grains as void somewhat corrects the microstructure model and effectively compensate this error.

To conclude, DEM is very capable of describing the behaviour of granular materials, but some caution has to be given in order to stay within the domain of validity of the model.

3. The Material Point Method

Sommaire

3.1. Introduction

The last chapter has shown how performant DEM is to model granular materials, but it is unfortunately prohibitively expensive at large scales (see table 1.1). Traditionally, and at a reasonable computational time cost, large structures are modelled using continuum-based methods such as the FEM (or its variations), requiring the knowledge of the material's behaviour only at a finite set of points, i.e. the integration points. However, when large displacements are involved, the Lagrangian mesh many of these methods rely on quickly becomes unsuitable for the numerical procedure, preventing the resolution of the governing equations. Among the FEM's variations which try to solve this issue, the hybrid Eulerian-Lagrangian Material Point Method is well-suited for granular materials because it was developed for history-dependent materials [Sulsky, Chen, and Schreyer 1994].

This chapter first presents the MPM formulation, including the equations to be solved and the numerical procedure used to do so. The formulation is illustrated with links to the open source CB-Geo MPM [Kumar, Salmond, Kularathna, et al. 2019] implementation, available on GitHub. In a second part, this chapter investigates the influence of the motion integration strategy in the simple case of a cube bouncing in a translational motion.

3.2. Notations

This section regroups the notation used in this chapter. Since quantities can be expressed at material points, grid points or for a whole mesh cell, a superscript is used to denote where the quantity is taken, i.e. $\cdot^p$, $\cdot^i$ and $\cdot^j$ respectively. The domain is denoted Ω and its boundary $\partial\Omega$.

Sets:

$\{p\}$:	Set containing the indices of all material points
$\{i\}$:	Set containing the indices of all grid points
$\{j\}$:	Set containing the indices of all cells

Scalar quantities:

N_{dim}:	The number of dimensions considered in the simulation (2 for 2D, 3 for 3D)
N_{mp}^j:	The number of material points in the cell j
$j(p)$:	Index of the cell containing the material point p
v:	Volume, of either a cell or a material point
ρ:	Mass density
$\tilde{N}_i^j$:	Local shape function for the i^{th} node of the cell j
m:	Mass, taken either at material points or at grid points
$V_k^i\big\vert_{lim}$:	Imposed velocity on the grid point i in the direction k
$\mathscr{P}_{int}$:	Internal work
$\mathscr{P}_{ext}$:	external work
Δt:	MPM time step, denoted Δt^{MPM} in the next chapters

Vector quantities:

$\underline{g}$:	Acceleration due to gravity
$\underline{V}$:	Velocity anywhere in the solid
$\underline{\widetilde{V}}$:	Velocity solution to the equation of motion
$\underline{a}^i$:	Acceleration at node i
$\underline{V}^*$:	Admissible velocity
$\nabla\underline{\widetilde{N}}_i^j$ or $(\widetilde{N}_{i,k}^j)\ \forall k \in [\![1,3]\!]$:	Gradient of the local shape function for the i^{th} node of the cell j
$\nabla\underline{N}_i^j$ or $(N_{i,k}^j)\ \forall k \in [\![1,3]\!]$:	Gradient of the global shape function for the i^{th} node of the cell j
$\underline{\tau}$:	traction on $\partial\Omega$
$\underline{\widetilde{x}}$:	Position of a point in local coordinates
$\underline{l}^j$:	Dimensions of the cell j
$\underline{c}^j$:	Position of the center of the cell j
$\underline{n}$:	Vector normal to $\partial\Omega$
$\underline{f}^i_{node}$:	User imposed force on node i
$\underline{f}^i_{ext}$:	External force on node i
$\underline{f}^i_{int}$:	Force representing internal efforts on node i
$\underline{f}^i$:	Total force on node i
$\underline{\text{cws}}$:	Coefficient wise sign function, defined in equation 3.24
$\underline{U}$:	Vector containing the constitutive law's parameters

Matrix quantities:

$\underline{\underline{\sigma}}(\underline{x},t)$:	Stress at point $\underline{x}$ in the solid at time t
$\underline{\underline{\epsilon}}(\underline{x},t)$:	Strain at point $\underline{x}$ in the solid at time t
$\underline{\underline{J}}$:	Jacobian of the transformation from global to local coordinates system
$\underline{\underline{X}}^j$:	Coordinates of the nodes of the cell j

A simple subscript is used to denote a vector's component:

$$\underline{\text{vec}} = (\text{vec}_k)_{k\in[\![1,N_{dim}]\!]} \qquad \text{for } \underline{\text{vec}} \text{ any vector quantity}$$

A double subscript is used to denote a 2^{nd} order tensor's component:

$$\underline{\underline{\text{tens}}} = (\text{tens}_{kl})_{(k,l)\in[\![1,N_{dim}]\!]^2} \qquad \text{for } \underline{\underline{\text{tens}}} \text{ any } 2^{nd} \text{ order tensor quantity}$$

The subscript $\cdot_{,k}$ is used on space dependent variables to denote the partial derivative with respect to the k^{th} component.

3.3. Governing equations

Let us consider the case of a deformable solid being continuously present in the domain Ω. All variables are space and time dependent, however for the sake of simplicity the parameters $(\underline{x},t)$ will be omitted in the next equations.

Considering that during any deformation or rigid movement of the body its mass is always conserved, the following equation is true at any point $\underline{x}$ in Ω:

$$\frac{\partial \rho}{\partial t} + \rho \operatorname{div}(\underline{V}) = 0 \tag{3.1}$$

The momentum is also assumed conserved:

$$\rho \frac{\partial \underline{V}}{\partial t} = \operatorname{div}(\underline{\underline{\sigma}}) + \rho \underline{g} \tag{3.2}$$

Considering that any admissible velocity field $\underline{V}^*(\underline{x}, t)$ is applied on the system, the virtual work principle is recovered. Indeed, the following equation is valid at each instant t:

$$\int_\Omega \underline{V}^* \rho \frac{\partial \underline{V}}{\partial t} d\Omega = \int_\Omega \underline{V}^* \operatorname{div}(\underline{\underline{\sigma}}) d\Omega + \int_\Omega \underline{V}^* \rho \underline{g} d\Omega \tag{3.3}$$

The term on the left side of eq. (3.3) corresponds to inertial terms. The first term on the right side of the equation can be decomposed with an integration by parts:

$$\begin{aligned} \int_\Omega \underline{V}^* \operatorname{div}(\underline{\underline{\sigma}}) d\Omega &= \int_\Omega \operatorname{div}(\underline{V}^* \underline{\underline{\sigma}}) d\Omega - \int_\Omega \nabla \underline{V}^* : \underline{\underline{\sigma}} d\Omega \\ &= \int_{\partial\Omega} \underline{V}^* (\underline{\underline{\sigma}}\, \underline{n}) d(\partial\Omega) - \int_\Omega \nabla \underline{V}^* : \underline{\underline{\sigma}} d\Omega \end{aligned} \tag{3.4}$$

With $\underline{n}$ the unit vector normal to $\partial\Omega$, the surface of Ω. The traction on $\partial\Omega$ appears as $\underline{\tau} = \underline{\underline{\sigma}}\, \underline{n}$. The variation of internal and external work, i.e. the internal and external powers $\mathscr{P}_{int}$ and $\mathscr{P}_{ext}$ respectively, can then be identified:

$$\mathscr{P}_{int} = -\int_\Omega \nabla \underline{V}^* : \underline{\underline{\sigma}} d\Omega \tag{3.5}$$

$$\mathscr{P}_{ext} = \int_\Omega \underline{V}^* \rho \underline{g} d\Omega + \int_{\partial\Omega} \underline{V}^* \underline{\tau} d(\partial\Omega) \tag{3.6}$$

Finally, the weak form of the virtual work principle is:

$$\int_\Omega \underline{V}^* \rho \frac{\partial \underline{V}}{\partial t} d\Omega = \int_\Omega \underline{V}^* \rho \underline{g} d\Omega + \int_{\partial\Omega} \underline{V}^* \underline{\tau} d(\partial\Omega) - \int_\Omega \nabla \underline{V}^* : \underline{\underline{\sigma}} d\Omega \tag{3.7}$$

3.4. Numerical procedure

This section describes the MPM implementation used for the simulations presented in this manuscript, i.e. the one from the open source code CB-Geo MPM []. The source code is referred to as an illustration for all the operations in the MPM workflow.

The domain Ω is discretized using a mesh constituted of identical cells on which equation 3.7 is solved. The temporal evolution of the quantities involved is described using a finite

difference scheme on a regularly spaced time axis, with a time step of Δt:

$$\frac{\partial f}{\partial t} \approx \frac{f(t+\Delta t)-f(t)}{\Delta t} \qquad \text{for any quantity } f \tag{3.8}$$

CB-Geo MPM supports 3D and 2D plane strain simulations without rigid body rotations. As a consequence, vector quantities have either 2 or 3 components and the strain and stress tensors are always represented by a 6 components vector. Mesh elements are either quadrilaterals in 2D or hexahedrons in 3D, see figure 3.1. In order to keep this section simple but complete, only the 3D form of the equations for 8-noded hexahedrons is presented.

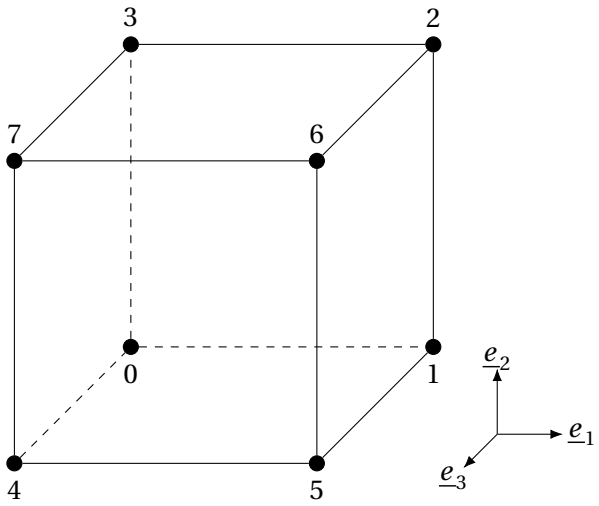

FIGURE 3.1. – Node numbering in an 8-noded hexahedron

3.4.1. Simulation setup

At the beginning of the simulation, the material points' volumes are computed based on their number in each cell N_{mp}^{j}:

$$v^p(t=0) = \frac{v^{j(p)}}{N_{mp}^{j(p)}} \tag{3.9}$$

The following grey box provides a link toward the source code of CB-Geo MPM, where the computation of the preceding equation is implemented. Such grey boxes will illustrate the equations throughout section 3.4.

In CB-Geo MPM, git revision *27086f*:
`include‣particles‣particle.tcc line 489, compute_volume`

Note that this assumes that each material point in the same cell has the same volume no matter their location. This assumption leads to an inaccurate determination of the integration weights mentioned earlier and highlighted latter in this section. A good practice is thus to set the material points initially regularly spaced in their cell, so the uniform volume assumption

is meaningful at the beginning of the simulation. Note however that even though the volume of each material point corresponds to the region of space a simple tesselation would attribute to it (e.g. decomposition into Voronoi cells), it does not correspond to the weights computed with the usual Gaussian quadratures. GIMP methods [Bardenhagen and Kober 2004] aim to mitigate this issue through the definition of a particle domain that serves as an influence zone when the weights are computed.

3.4.2. Main loop

At each iteration of the main loop, material points most certainly move with respect to the fixed mesh, it is thus necessary to compute their new local positions $\tilde{x}$. Noting $\underline{l}^j = (l_1^j, l_2^j, l_3^j)$ the length of a cell j in each direction and $\underline{c}^j$ the position of its center of gravity, one has:

$$\tilde{x}_k = 2\frac{x_k - c_k^j}{l_k^j} \quad \in [-1;1] \tag{3.10}$$

In CB-Geo MPM, git revision *27086f*:
`include‣cell.tcc line 471, local_coordinates_point`

The values of the shape functions can then be evaluated at the new material points' positions. In the cell j, the shape function of the i^{th} node ($i \in [\![0;7]\!]$) in local coordinates is denoted $\tilde{N}_i^j(\underline{\tilde{x}})$. Figure 3.1 gives the node numbering in any cell. The shape functions of a cell j can be written as 8-components vector:

$$\underline{\tilde{N}}^j(\underline{\tilde{x}}) = \begin{pmatrix} \tilde{N}_0^j(\underline{\tilde{x}}) \\ \tilde{N}_1^j(\underline{\tilde{x}}) \\ \tilde{N}_2^j(\underline{\tilde{x}}) \\ \tilde{N}_3^j(\underline{\tilde{x}}) \\ \tilde{N}_4^j(\underline{\tilde{x}}) \\ \tilde{N}_5^j(\underline{\tilde{x}}) \\ \tilde{N}_6^j(\underline{\tilde{x}}) \\ \tilde{N}_7^j(\underline{\tilde{x}}) \end{pmatrix} = \begin{pmatrix} \frac{1}{8}(1-\tilde{x}_1)(1-\tilde{x}_2)(1-\tilde{x}_3) \\ \frac{1}{8}(1+\tilde{x}_1)(1-\tilde{x}_2)(1-\tilde{x}_3) \\ \frac{1}{8}(1+\tilde{x}_1)(1+\tilde{x}_2)(1-\tilde{x}_3) \\ \frac{1}{8}(1-\tilde{x}_1)(1+\tilde{x}_2)(1-\tilde{x}_3) \\ \frac{1}{8}(1-\tilde{x}_1)(1-\tilde{x}_2)(1+\tilde{x}_3) \\ \frac{1}{8}(1+\tilde{x}_1)(1-\tilde{x}_2)(1+\tilde{x}_3) \\ \frac{1}{8}(1+\tilde{x}_1)(1+\tilde{x}_2)(1+\tilde{x}_3) \\ \frac{1}{8}(1-\tilde{x}_1)(1+\tilde{x}_2)(1+\tilde{x}_3) \end{pmatrix} \tag{3.11}$$

In CB-Geo MPM, git revision *27086f*:
`include‣elements‣3d‣hexahedron_element.tcc line 20, shapefn`

Their gradient can be written as a 8×3 matrix. Denoting $\cdot_{,k}$ the derivative with respect to the k^{th} direction, one has:

$$\underline{\underline{\nabla \tilde{N}}}^{j}(\underline{\tilde{x}}) = \begin{pmatrix} \tilde{N}^{j}_{0,1}(\underline{\tilde{x}}) & \tilde{N}^{j}_{0,2}(\underline{\tilde{x}}) & \tilde{N}^{j}_{0,3}(\underline{\tilde{x}}) \\ \tilde{N}^{j}_{1,1}(\underline{\tilde{x}}) & \tilde{N}^{j}_{1,2}(\underline{\tilde{x}}) & \tilde{N}^{j}_{1,3}(\underline{\tilde{x}}) \\ \tilde{N}^{j}_{2,1}(\underline{\tilde{x}}) & \tilde{N}^{j}_{2,2}(\underline{\tilde{x}}) & \tilde{N}^{j}_{2,3}(\underline{\tilde{x}}) \\ \tilde{N}^{j}_{3,1}(\underline{\tilde{x}}) & \tilde{N}^{j}_{3,2}(\underline{\tilde{x}}) & \tilde{N}^{j}_{3,3}(\underline{\tilde{x}}) \\ \tilde{N}^{j}_{4,1}(\underline{\tilde{x}}) & \tilde{N}^{j}_{4,2}(\underline{\tilde{x}}) & \tilde{N}^{j}_{4,3}(\underline{\tilde{x}}) \\ \tilde{N}^{j}_{5,1}(\underline{\tilde{x}}) & \tilde{N}^{j}_{5,2}(\underline{\tilde{x}}) & \tilde{N}^{j}_{5,3}(\underline{\tilde{x}}) \\ \tilde{N}^{j}_{6,1}(\underline{\tilde{x}}) & \tilde{N}^{j}_{6,2}(\underline{\tilde{x}}) & \tilde{N}^{j}_{6,3}(\underline{\tilde{x}}) \\ \tilde{N}^{j}_{7,1}(\underline{\tilde{x}}) & \tilde{N}^{j}_{7,2}(\underline{\tilde{x}}) & \tilde{N}^{j}_{7,3}(\underline{\tilde{x}}) \end{pmatrix} \tag{3.12}$$

$$= \begin{pmatrix} -\frac{1}{8}(1-\tilde{x}_2)(1-\tilde{x}_3) & -\frac{1}{8}(1-\tilde{x}_1)(1-\tilde{x}_3) & -\frac{1}{8}(1-\tilde{x}_1)(1-\tilde{x}_2) \\ \frac{1}{8}(1-\tilde{x}_2)(1-\tilde{x}_3) & -\frac{1}{8}(1+\tilde{x}_1)(1-\tilde{x}_3) & -\frac{1}{8}(1+\tilde{x}_1)(1-\tilde{x}_2) \\ \frac{1}{8}(1+\tilde{x}_2)(1-\tilde{x}_3) & \frac{1}{8}(1+\tilde{x}_1)(1-\tilde{x}_3) & -\frac{1}{8}(1+\tilde{x}_1)(1+\tilde{x}_2) \\ -\frac{1}{8}(1+\tilde{x}_2)(1-\tilde{x}_3) & \frac{1}{8}(1-\tilde{x}_1)(1-\tilde{x}_3) & -\frac{1}{8}(1-\tilde{x}_1)(1+\tilde{x}_2) \\ -\frac{1}{8}(1-\tilde{x}_2)(1+\tilde{x}_3) & -\frac{1}{8}(1-\tilde{x}_1)(1+\tilde{x}_3) & \frac{1}{8}(1-\tilde{x}_1)(1-\tilde{x}_2) \\ \frac{1}{8}(1-\tilde{x}_2)(1+\tilde{x}_3) & -\frac{1}{8}(1+\tilde{x}_1)(1+\tilde{x}_3) & \frac{1}{8}(1+\tilde{x}_1)(1-\tilde{x}_2) \\ \frac{1}{8}(1+\tilde{x}_2)(1+\tilde{x}_3) & \frac{1}{8}(1+\tilde{x}_1)(1+\tilde{x}_3) & \frac{1}{8}(1+\tilde{x}_1)(1+\tilde{x}_2) \\ -\frac{1}{8}(1+\tilde{x}_2)(1+\tilde{x}_3) & \frac{1}{8}(1-\tilde{x}_1)(1+\tilde{x}_3) & \frac{1}{8}(1-\tilde{x}_1)(1+\tilde{x}_2) \end{pmatrix} \tag{3.13}$$

The shape functions and their gradients are plotted in figure 1.9 (a). Note that using cubic B-spline shape functions (as described in figure 1.9 (b)) instead would be a significant improvement since their gradients are continuous.

In CB-Geo MPM, git revision *27086f*:
`include ▸ elements ▸ 3d ▸ hexahedron_element.tcc line 42, grad_shapefn`

Equation 3.7 requires the gradient of the shape functions to be expressed in global coordinates, the Jacobian of the transformation from global to local coordinates $\underline{\underline{J}}$ thus has to be computed:

$$\underline{\underline{J}} = (\underline{\underline{\nabla \tilde{N}}}^{j})^{\intercal} \underline{\underline{X}}^{j} \tag{3.14}$$

With $\underline{\underline{X}}^{j}$ the 8×3 matrix that contains the coordinates of the 8 nodes belonging to the j^{th} cell. Since all cells are identical, their Jacobian is the same.

In CB-Geo MPM, git revision *27086f*:
`include▸elements▸3d▸hexahedron_element.tcc line 267, jacobian`

Note that CB-Geo MPM computes the Jacobian using the gradient of the shape functions

and the nodal coordinates in equation 3.14, while using equation 3.15 is enough and more efficient:

$$\underline{\underline{J}} = \begin{pmatrix} x_{1,1}(\underline{\tilde{x}}) & x_{1,2}(\underline{\tilde{x}}) & x_{1,3}(\underline{\tilde{x}}) \\ x_{2,1}(\underline{\tilde{x}}) & x_{2,2}(\underline{\tilde{x}}) & x_{2,3}(\underline{\tilde{x}}) \\ x_{3,1}(\underline{\tilde{x}}) & x_{3,2}(\underline{\tilde{x}}) & x_{3,3}(\underline{\tilde{x}}) \end{pmatrix} = \begin{pmatrix} \frac{l_1^j}{2} & 0 & 0 \\ 0 & \frac{l_2^j}{2} & 0 \\ 0 & 0 & \frac{l_3^j}{2} \end{pmatrix} \tag{3.15}$$

The gradient of the shape functions in global coordinates $\underline{\underline{\nabla N}}$ can then be computed:

$$\underline{\underline{\nabla N}}^j = \underline{\underline{\nabla \tilde{N}}}^j (\underline{\underline{J}}^{-1})^\intercal \tag{3.16}$$

In CB-Geo MPM, git revision *27086f*:
`include‣elements‣3d‣hexahedron_element.tcc line 306, dn_dx`

The resulting space dependent matrix $\underline{\underline{\nabla N}}^j$ also has a 8×3 dimension, its value at the position of the material point p will be denoted $\underline{\underline{\nabla N}}^p$.

The mass and velocity quantities can be transported from material points to grid points using the shape functions. For a specific grid point, data is gathered from the material points inside all cells the grid point belongs to, at most 8 in 3D and 4 in 2D. The set denoted $\{j\}^i$ contains all the indexes of the cells the grid point i belongs to, and the set denoted $\{p\}^i$ contains all the indexes of the material points whose data should be gathered at the grid point i. The mass is conserved through its transportation, performed as follows:

$$m^i = \sum_{p \in \{p\}^i} m^p \tilde{N}_i^j(\underline{\tilde{x}}^p) \tag{3.17}$$

The velocity is transported so the linear momentum is also conserved:

$$\underline{V}^i = \frac{\sum_{p \in \{p\}^i} m^p \underline{V}^p \tilde{N}_i^j(\underline{\tilde{x}}^p)}{m^i} \tag{3.18}$$

In CB-Geo MPM, git revision *27086f*:
`include ‣ particles ‣ particle.tcc line 521, map_mass_momentum_to_nodes`

The boundary conditions are then imposed on some specified grid points, in a given direction k. The grid points on which a velocity $V_k^i\big|_{lim}$ is imposed also have their acceleration a_k^i set to zero:

$$V_k^i = V_k^i\big|_{lim} \tag{3.19}$$
$$a_k^i = 0 \tag{3.20}$$

In CB-Geo MPM, git revision *27086f*:
`include‣node.tcc line 314, apply_velocity_constraints`

The total external force $\underline{f}_{ext}$ has to be expressed on grid points, which is immediate for forces imposed directly on nodes $\underline{\tau}^i$, but requires another transportation operation for gravitational forces:

$$\underline{f}_{ext}^i = \underline{f}_{node}^i + \sum_{p\in\{p\}^i} m^p \underline{g} \tilde{N}_i^{j(p)} \tag{3.21}$$

Note that the user has to determine $\underline{f}_{node}^i$ based on the desired imposed traction:

$$\underline{f}_{node}^i = \int_{\partial\Omega} N_i^j \underline{\tau} d(\partial\Omega) \tag{3.22}$$

with j the appropriate mesh cell for the current location on $\partial\Omega$.

In CB-Geo MPM, git revision *27086f*:
`include‣particles‣particle.tcc line 677, map_body_force`
and
`include‣node.tcc line 100, apply_concentrated_force`

The force representative of the internal efforts $\underline{f}_{int}$ is computed on grid points from the stress carried by the material points, this is where the volume attributed to the material points serves as an integration weight:

$$\underline{f}_{int}^i(t) = \begin{cases} -\sum_{p\in\{p\}^i} v^p \nabla \underline{N}_i^p \underline{\underline{\sigma}}^p(t) & \text{if stress update scheme is Update Stress Last (USL)} \\ -\sum_{p\in\{p\}^i} v^p \nabla \underline{N}_i^p \underline{\underline{\sigma}}^p(t+\Delta t) & \text{if stress update scheme is Update Stress First (USF)} \end{cases} \tag{3.23}$$

In CB-Geo MPM, git revision *27086f*:
`include‣particles‣particle.tcc line 715, map_internal_force`

Note that in equation 3.23 the stress tensor is either taken before accounting for the response to the current strain increment (USL scheme), or after (USF scheme).

The equation of motion can then be solved on each grid point to determine the new velocities. CB-Geo MPM supports the addition of a Cundall's damping, which requires the choice of a parameter $D \geq 0$ and the definition of the following "coefficient wise sign" function:

$$\text{cws}_k(\underline{u}) = \frac{u_k}{|u_k|} \qquad \text{for any vector } \underline{u} \tag{3.24}$$

It thus comes:

$$\underline{f}^i(t) = \underline{f}^i_{int}(t) + \underline{f}^i_{ext}(t) \tag{3.25}$$

$$\underline{a}^i(t+\Delta t) = \frac{1}{m^i}\left(\underline{f}^i(t) - D\|\underline{f}^i(t)\|\underline{\text{cws}}(\underline{V}^i(t))\right) \tag{3.26}$$

$$\underline{\widetilde{V}}^i(t+\Delta t) = \underline{V}^i(t) + \underline{a}^i(t+\Delta t)\times\Delta t \tag{3.27}$$

In CB-Geo MPM, git revision *27086f*:
`include‣node.tcc line 257, compute_acceleration_velocity_cundall`

Here the velocity $\underline{\widetilde{V}}^i(t+\Delta t)$ is only temporary since it will be replaced at the beginning of the next iteration by $\underline{V}^i(t+\Delta t)$, computed with equation 3.18.

The velocities' boundary conditions are then re-imposed at each node using equations 3.19 and 3.20.

3.4.3. Material points' displacement

The positions of all material points are updated according to a velocity computed from the solution of the motion equation (equation 3.27) located on grid points. Different strategies exist, the original one found in [Sulsky, Chen, and Schreyer 1994] was first used in the Particle In Cell method and is denoted PIC. With this strategy, the velocity used to move the material points is also the one stored at the material point for the next iteration. It is directly transported from grid points to material points:

$$\underline{V}^p_{PIC}(t+\Delta t) = \sum_{i\in\{i\}^p} \underline{\widetilde{V}}^i(t+\Delta t)\widetilde{N}_i^{j(p)}(t) \tag{3.28}$$

$$\underline{x}^p_{PIC}(t+\Delta t) = \underline{x}^p(t) + \underline{V}^p_{PIC}(t+\Delta t)\times\Delta t \tag{3.29}$$

This strategy has been shown to be highly dissipative due to the important error during the interpolation process [Bardenhagen 2002]. Efforts have been made to reduce this artificial damping brought by the PIC strategy. For instance, the FLIP strategy, originally used in the FLuid Implicit Particle method, computes the velocity for the next iteration incrementally, by interpolating the acceleration from grid points to material points [Brackbill and Ruppel 1986]. However, the velocity used to move the material points is still $\underline{V}^p_{PIC}$:

$$\underline{V}^p_{FLIP}(t+\Delta t) = \underline{V}^p(t) + \sum_{i\in\{i\}^p} \underline{a}^i(t+\Delta t)\widetilde{N}_i^{j(p)}(t)\times\Delta t \tag{3.30}$$

$$\underline{x}^p_{FLIP}(t+\Delta t) = \underline{x}^p_{PIC}(t+\Delta t) \tag{3.31}$$

This inconsistency can lead to unrealistic behaviour, since the material point is displaced using a velocity different from the one assigned to it. An alternative, the Naturally modified FLIP strategy (NFLIP) addresses this issue by using $\underline{V}^p_{FLIP}$ to move the material point:

$$\underline{x}^p_{NFLIP}(t+\Delta t) = \underline{x}^p(t) + \underline{V}^p_{FLIP}(t+\Delta t) \times \Delta t \tag{3.32}$$

The FLIP and NFLIP strategies efficiently solve the high dissipation issues, they are however more likely to be subject to instabilities. While using a small time step reduces the effects of this issue, another strategy has emerged to stabilize artificially the simulations: the FLIPX strategy. It consists in blending $\underline{V}^p_{PIC}$ and $\underline{V}^p_{FLIP}$ with a specific proportion P_{FLIP}, which is the "X" in "FLIPX" and spans over the interval $[0,1]$:

$$\underline{V}^p_{FLIPX} = (1-P_{FLIP})\underline{V}^p_{PIC} + P_{FLIP}\underline{V}^p_{FLIP} \tag{3.33}$$

Similarly, the NFLIPX strategy can be constructed:

$$\underline{x}^p_{NFLIPX}(t+\Delta t) = \underline{x}^p(t) + \underline{V}^p_{FLIPX}(t+\Delta t) \times \Delta t \tag{3.34}$$

Another strategy aims to conserve the angular momentum during the interpolation process: the Affine Particle In Cell (APIC) method, detailed in [Jiang, Schroeder, Selle, et al. 2015]. Basically, it adds to the linear momentum in equation 3.18 a term corresponding to the angular momentum, which is assumed equal to 0 in the classical MPM formulation.

Table 3.1 summarizes the different velocities involved in the velocity update strategies mentioned above.

In CB-Geo MPM, git revision *27086f*:
(Only for PIC (velocity_update set to true) and FLIP (velocity_update set to false))
`include ▸ particles ▸ particle.tcc line 778, compute_updated_position`

3.4.4. Strain computation

The strain increment imposed on the material has to be computed at each material point in order to determine its reaction, in terms of stress variation. This is done in CB-Geo by computing the strain rate $\underline{\underline{\dot{\epsilon}}}^p$ from the velocities at nodes and the gradient of the shape functions. Noting $\{i\}^p$ the set containing all the nodes of the cell in which the material point p is located, it comes:

Velocity update strategy \ Relevant variables	$\underline{V}^p$	$\underline{x}^p$
PIC	$\underline{V}^p_{PIC}$ see equation 3.28	$\underline{x}^p_{PIC}$ see equation 3.29
FLIP	$\underline{V}^p_{FLIP}$ see equation 3.30	$\underline{x}^p_{PIC}$ see equation 3.29
NFLIP	$\underline{V}^p_{FLIP}$ see equation 3.30	$\underline{x}^p_{NFLIP}$ see equation 3.32
FLIPX	$(1-P_{FLIP})\underline{V}^p_{PIC} + P_{FLIP}\underline{V}^p_{FLIP}$	$\underline{x}^p_{PIC}$ see equation 3.29
NFLIPX	$(1-P_{FLIP})\underline{V}^p_{PIC} + P_{FLIP}\underline{V}^p_{FLIP}$	$\underline{x}^p_{NFLIPX}$ see equation 3.34
APIC	$\underline{V}^p_{PIC}$ with modified eq. 3.18	$\underline{x}^p_{PIC}$ with modified eq. 3.18

TABLE 3.1. – Material points velocities and displacements for different update strategies

$$\underline{\underline{\dot{\epsilon}}}^p = \begin{pmatrix} \dot{\epsilon}^p_{11} & \dot{\gamma}^p_{12} & \dot{\gamma}^p_{13} \\ \dot{\gamma}^p_{12} & \dot{\epsilon}^p_{22} & \dot{\gamma}^p_{23} \\ \dot{\gamma}^p_{13} & \dot{\gamma}^p_{23} & \dot{\epsilon}^p_{33} \end{pmatrix} \tag{3.35}$$

$$= \begin{pmatrix} \sum_{i\in\{i\}^p} \nabla N^j_{i;1}(\underline{\tilde{x}}^p) V^i_1 & \sum_{i\in\{i\}^p} \left(\nabla N^j_{i;2}(\underline{\tilde{x}}^p) V^i_1 + \nabla N^j_{i;1}(\underline{\tilde{x}}^p) V^i_2\right) & \sum_{i\in\{i\}^p} \left(\nabla N^j_{i;3}(\underline{\tilde{x}}^p) V^i_1 + \nabla N^j_{i;1}(\underline{\tilde{x}}^p) V^i_3\right) \\ " & \sum_{i\in\{i\}^p} \nabla N^j_{i;2}(\underline{\tilde{x}}^p) V^i_2 & \sum_{i\in\{i\}^p} \left(\nabla N^j_{i;3}(\underline{\tilde{x}}^p) V^i_2 + \nabla N^j_{i;2}(\underline{\tilde{x}}^p) V^i_3\right) \\ " & " & \sum_{i\in\{i\}^p} \nabla N^j_{i;3}(\underline{\tilde{x}}^p) V^i_3 \end{pmatrix} \tag{3.36}$$

Note that when using $\underline{\underline{\dot{\epsilon}}}^p$, one should mind the 0.5 coefficient on the non diagonal terms, which is not included in the tensor.

In CB-Geo MPM, git revision *27086f*:
`include‣particles‣particle.tcc line 623, compute_strain_rate`

The strain at each material point $\underline{\underline{\epsilon}}^p$ can then be computed incrementally:

$$\Delta\underline{\underline{\epsilon}}^p(t+\Delta t) = \underline{\underline{\dot{\epsilon}}}^p(t+\Delta t)\Delta t \tag{3.37}$$

$$\underline{\underline{\epsilon}}^p(t+\Delta t) = \underline{\underline{\epsilon}}^p(t) + \Delta\underline{\underline{\epsilon}}^p(t+\Delta t) \tag{3.38}$$

In CB-Geo MPM, git revision *27086f*:
`include‣particles‣particle.tcc line 623, compute_strain`

The volume of each material point v^p is then updated using the strain rate computed at the center of each cell $\underline{\underline{\dot{\epsilon}}}^j$. The computation is the same as in equation 3.36 except that $\underline{\underline{\nabla N}}^j(\underline{0})$ is used instead of $\underline{\underline{\nabla N}}^j(\underline{\tilde{x}}^p)$. The updated volume is thus:

$$\dot{\epsilon}^j_{center} = \mathrm{Tr}\left(\underline{\underline{\dot{\epsilon}}}^j\right) \tag{3.39}$$

$$v^p(t+\Delta t) = v^p(t)\left(1+\Delta t \times \dot{\epsilon}^j_{center}\right) \tag{3.40}$$

In CB-Geo MPM, git revision *27086f*:
`include‣particles‣particle.tcc line 498, update_volume`

3.4.5. Stress computation

The stress computation is the only step in the MPM formulation where the behaviour of the material is accounted for: it is determined from the strain increment using an appropriate constitutive law. For instance, if CL denotes a constitutive law and $\underline{U}$ a vector containing its parameters, one has:

$$\Delta\underline{\underline{\sigma}}^p(t+\Delta t) = \mathrm{CL}(\Delta\underline{\underline{\epsilon}}^p, \underline{U}) \tag{3.41}$$

$$\underline{\underline{\sigma}}^p(t+\Delta t) = \underline{\underline{\sigma}}^p(t) + \Delta\underline{\underline{\sigma}}^p(t+\Delta t) = \begin{pmatrix} \sigma_{11} & \tau_{12} & \tau_{13} \\ \tau_{12} & \sigma_{22} & \tau_{23} \\ \tau_{13} & \tau_{23} & \sigma_{33} \end{pmatrix} \tag{3.42}$$

In CB-Geo MPM, git revision *27086f*:
(e.g. for the Mohr-Coulomb constitutive law)
`include‣materials‣mohr_coulomb.tcc line 329, compute_stress`

3.4.6. Deletion of material points outside the mesh

This is the last step of the MPM iteration: if a material point gets out of the mesh, it is deleted. Note that CB-Geo MPM offers the possibility to automatically stop the simulation

when a material point is deleted.

In CB-Geo MPM, git revision *27086f*:
`include ▸ solvers ▸ mpm_scheme ▸ mpm_scheme.tcc line 201, locate_particles`

3.5. Influence of the MPM scheme and velocity update strategy

As mentioned in the previous section, a couple of choices can be made when choosing a MPM formulation: the stress update scheme (see equation 3.23) and the velocity update strategy (see table 3.1). In this section, the influence of these choices is investigated using a basic MPM simulation. Note that the APIC, FLIPX, NFLIP and NFLIPX strategies are not available in CB-Geo MPM, all were added in a modified version developed during this thesis.

3.5.1. Simulation setup

The simulation models a cube of material falling under gravity until it reaches a floor and bounces several times. The mesh comports only two cubic cells stacked vertically, with a side of $c = 1$ m, and 27 material points are initially regularly spaced in the top cell. Nodal velocities are imposed equal to 0 in the directions normal to the boundary it represents, see figure 3.2. Note that this figure is in fact a 2D projection of the 3D pure MPM simulation. The constitutive law used assumes the material to have a purely linear-elastic behaviour, with a Young's modulus of $E = 52.6$ MPa and a Poisson's ratio of $\nu = 0.3$. The density of the material is set to $\rho = 750\ \mathrm{kg \cdot m^{-3}}$. For all simulations in this section Cundall's damping is set to 0, as a consequence the energy dissipation observed in these results is uncontrolled. The time step, computed from E, ρ and c, reads:

$$\Delta t = c\sqrt{\frac{\rho}{E}} \times 5 \cdot 10^{-2} \approx 1.888 \cdot 10^{-4} \quad s \tag{3.43}$$

Several variables are monitored during the simulation, in particular:
— the height of the highest material point:

$$Z_{max} = \max_{p \in \{p\}}(x_3^p) \tag{3.44}$$

— the elastic energy summed over all material points (with Einstein's notation and δ_{ij} the Kronecker's symbol):

$$E_{el} = \sum_{p \in \{p\}} \frac{v^p}{2}\left(\sigma_{ij}\epsilon_{ij}^T\right) \tag{3.45}$$

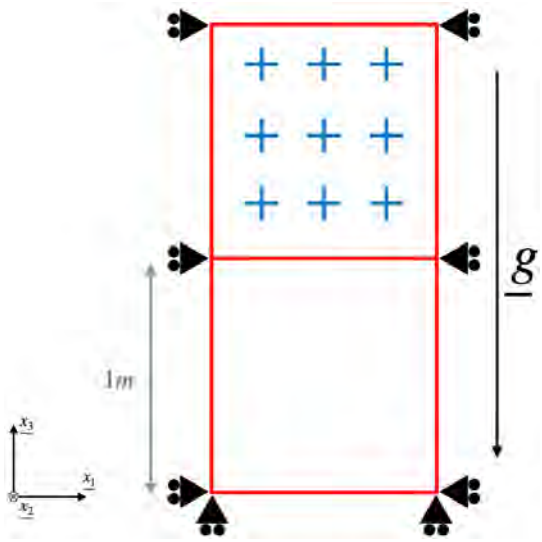

FIGURE 3.2. – Simulation setup (plane view of the 3D model)

with $\underline{\underline{\epsilon}}^T$ the true strain tensor, which can be expressed using the identity matrix $\underline{\underline{I}}$:

$$\underline{\underline{\epsilon}}^T = \underline{\underline{\epsilon}} - \frac{1}{2}\left(\underline{\underline{\epsilon}} - \underline{\underline{\epsilon}}\,\underline{\underline{I}}\right) \tag{3.46}$$

— the kinetic energy summed over all material points:

$$E_k = \sum_{p\in\{p\}} \frac{1}{2} m^p \left\| \underline{V}^p \right\|^2 \tag{3.47}$$

— and the gravitational energy summed over all material points:

$$E_p = \sum_{p\in\{p\}} m^p g\, x_3^p \tag{3.48}$$

3.5.2. Results

Figure 3.3 shows the Z_{max} obtained during several bounces for different formulation choices. Figure 3.4 shows the corresponding total energy $E_{tot} = E_{el} + E_k + E_p$, and all energies are plotted separately in figure 3.5. The columns (a) of these figures present the results obtained with the USL stress update scheme, and the columns (b) present the ones obtained with the USF scheme. In both columns, the influence of several velocity update schemes is investigated: PIC, FLIP, NFLIP, FLIP0.9, NFLIP0.9 and APIC. Note that E_{el} is equal to 0 J before the first impact, hence the absence of points on the first steps of the log-linear graphs on figure 3.5 (a) and (b).

A first observation is that the USL scheme always includes an artificial energy dissipation

that can be observed both on E_{tot} and Z_{max}. Indeed, the maximum height the cube reaches decreases after each bounce: some energy is dissipated when the cube gets deformed upon impact on the floor. This artificial damping is quite important when using the PIC or APIC velocity update scheme. The energy dissipation is less important for all FLIP-based schemes, NFLIP being the most dissipative of them. It is worth noting that NFLIP0.9 is more conservative than NFLIP and PIC, which is surprising since it is a combination of both. Figure 3.5 shows that the deformation of the cube occurs essentially upon the impact with the floor for all schemes that include a PIC strategy (i.e. PIC, FLIP0.9, NFLIP0.9 and APIC). However, with the NFLIP and FLIP strategies the cube continues to get further deformed, after it lost contact with the floor and moves upward.

These results show that the USF scheme is more conservative: when combined with the FLIP velocity update scheme, E_{tot} is almost constant during the whole simulation. The PIC and APIC strategies also preserve better the energy with the USF scheme. However, the FLIP0.9 and NFLIP0.9 strategies are both more dissipative than when combined with the USL scheme. A more intriguing result is the one obtained for NFLIP: E_{tot} is globally increasing as the simulation goes but Z_{max} is significantly decreasing after each bounce. Such a unexpected behaviour can be explained with the evolution of E_{el}. Indeed, after the first impact the cube is subjected to a deformation which oscillates at a specific frequency, certainly different from the bouncing frequency. As a consequence, the height at which the cube bounces back is strongly affected by the synchronicity between these two frequencies. The cube is also continuously deformed between two impacts with the FLIP strategy. With the PIC and APIC strategies, the cube's deformation last longer when using USF rather than USL, but it stops before the next impact. Surprisingly, for both the FLIP0.9 and NFLIP0.9 schemes no additional deformations occurs between impacts.

3.5.3. Discussion

These results are in agreement with the analytical observations in [Bardenhagen 2002], where the USF scheme is found to be more likely to conserve energy than the USL scheme. A great combination would be to use the FLIP velocity update scheme combined with the USF stress update scheme, along with Cundall's damping, which can be controlled. An alternative to Cundall's damping could be to use another, dissipative, combination of schemes offered by the MPM formulation. For the presented simulation, the NFLIP strategy was shown to add energy to the system, certainly leading to instabilities, while the FLIP strategy conserves it. The PIC and APIC strategies were found to be highly dissipative, at a point where the deformation wave in the bouncing cube is completely aperiodic.

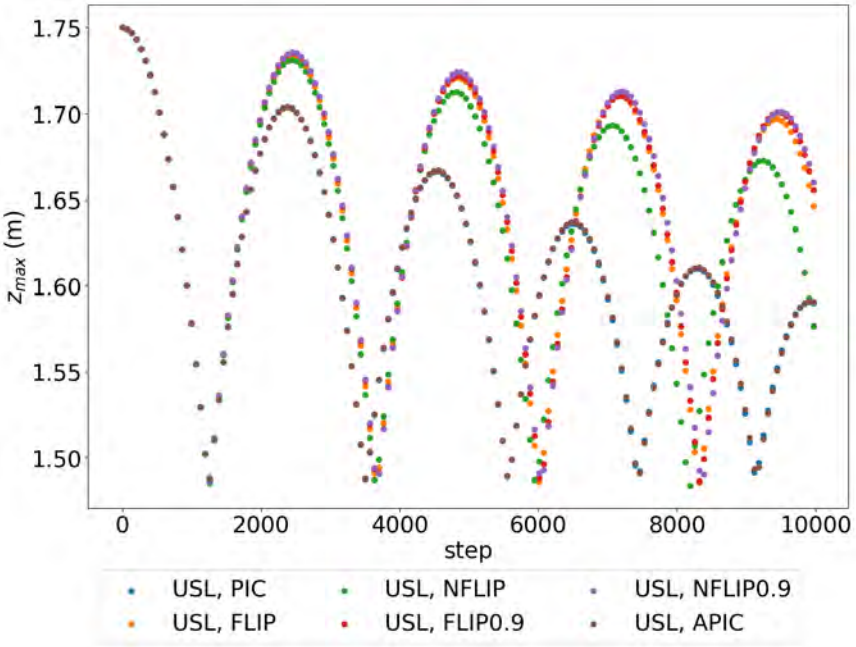

(a) USL

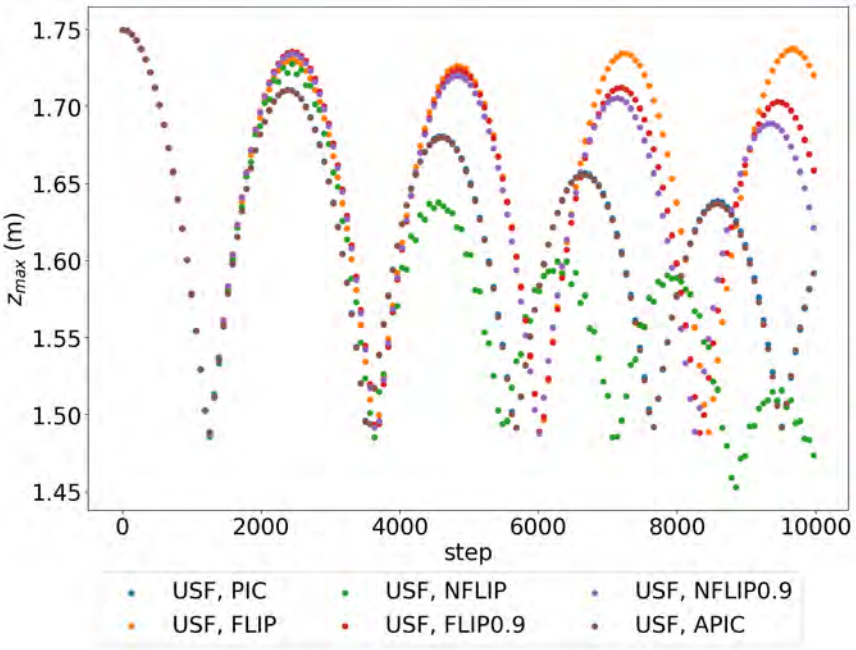

(b) USF

FIGURE 3.3. – Maximum height for different MPM schemes

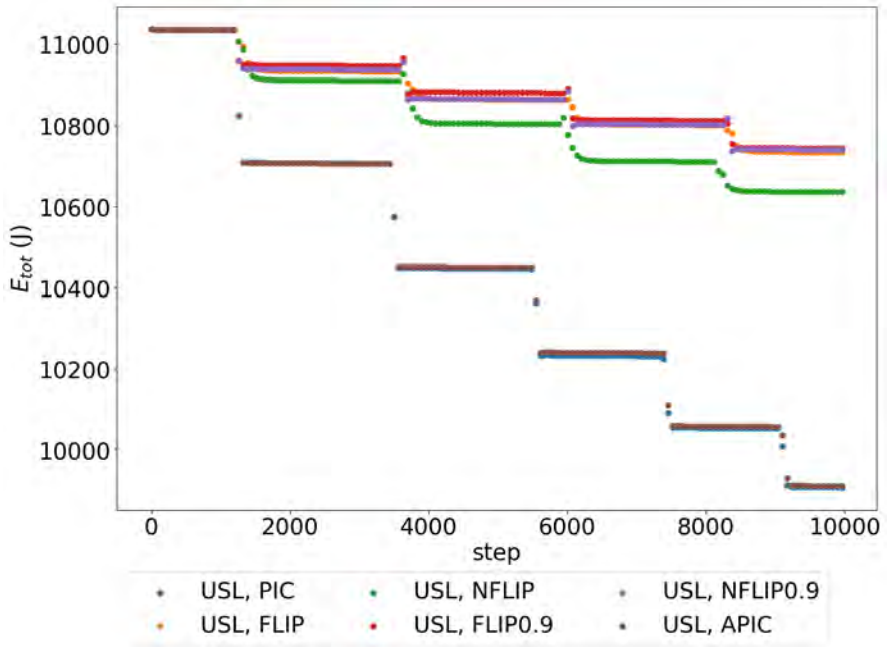

(a) USL

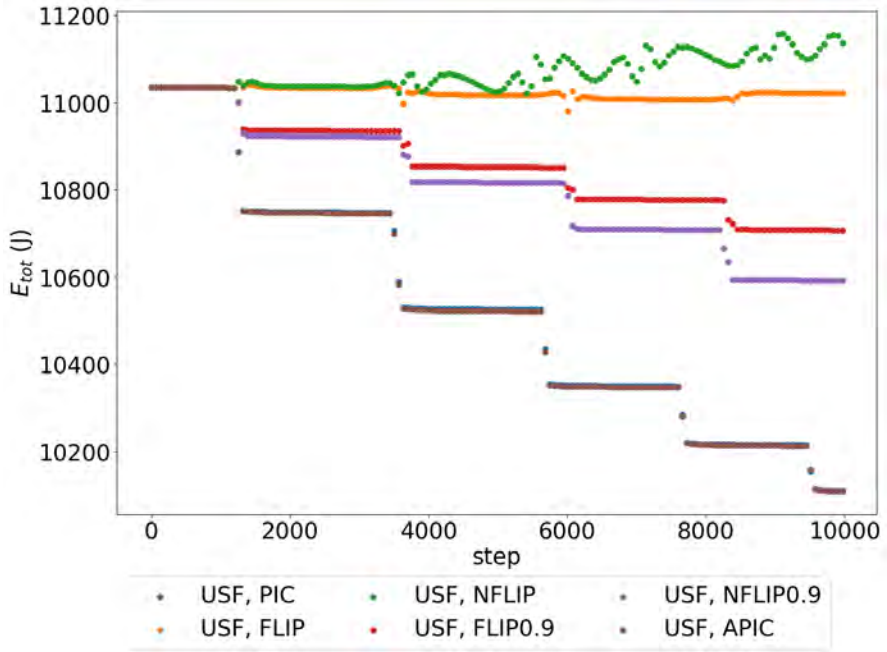

(b) USF

FIGURE 3.4. – Total energy for different MPM schemes

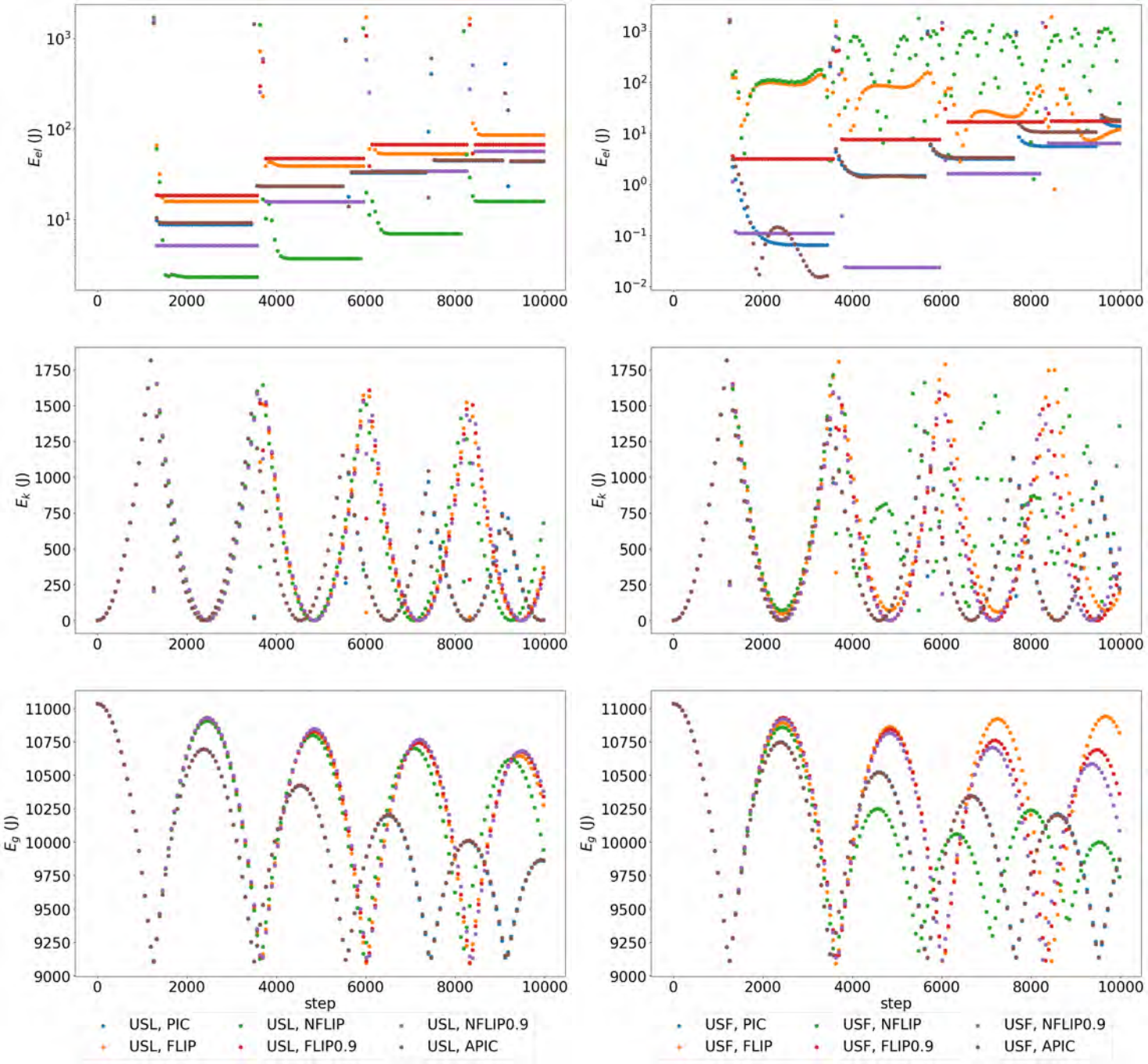

(a) USL

(b) USF

FIGURE 3.5. – E_{el}, E_k and E_g for different MPM schemes

3.6. Conclusion on the MPM

The Eulerian-Lagrangian formulation of the MPM gives robustness to the numerical procedure, allowing the computation to continue even when large displacements would stop the FEM computation. For this reason, the MPM is a great candidate to fullfil our goal of modelling geotechnical structures under severe loading. However, the motion integration strategy has to be carefully chosen in order to conserve as much as possible the energy through the numerous transportation of the momentum and velocity between grid points and integration points. Moreover, the MPM still relies on a constitutive law to represent the behaviour of the material, which as mentioned in section 1.3, often struggles to handle various loading scenarios requiring several parameters hard to calibrate.

4. MPMxDEM multi-scale coupling

Sommaire

4.1. Introduction

As mentioned in section 1.3.2, DEM can completely replace traditional constitutive laws to describe the behaviour of granular materials within a continuum-based method. Such a consideration grants access to the structure scale, while taking advantage of the effective and complete material's description offered by the DEM. Indeed, DEM requires only a few parameters (compared to usual constitutive laws) which have a direct meaning microscopically, making DEM capable of handling various loading conditions with little efforts. The choice of using DEM within the MPM continuum-based method thus seems as a promising approach to model geotechnical structures subject to severe loading conditions.

This chapter presents a formulation of the MPMxDEM coupling, including details on the time discretization consistency between the two methods, technical specificities, and a validation case on a simple triaxial test.

4.2. Formulation

The scale separation allows some simplifications in the microscopic model: the behaviour of the material is assumed independent of gravitational and inertial effects, which are thus accounted for only at the large scale, by the MPM. The former assumption allows to consider the granular assembly to be deformed at a quasi-static rate, which most of the time results in a lower computation time cost.

The granular assembly should be large enough for the global values to be independent of the number of grains, but it should also be small enough to keep the computational time cost low. The DEM model associated to each material point is then designated as a Representative Volume Element (RVE). The MPM strain increment determined at each material point $\Delta\underline{\underline{\epsilon}}$ for each MPM iteration is applied to the whole RVE with a strain-rate being chosen small enough for quasi-staticity to hold. This section details how the microscopic quasi-static assumption is incorporated in the process of deforming the RVE. In this chapter, the superscript p is left out as all variables are given for a specific material point.

4.2.1. RVE deformation

From the MPM point of view, the strain increment is imposed during a MPM time step, Δt^{MPM}. However, because of our quasi-static consideration at the microscopic scale, this deformation time is not relevant to the RVE. The time during which the RVE is deformed is denoted T^{ϵ} and is determined considering a low inertial number $I_n \leq 10^{-2}$ [GDR MiDi 2004], which ensures quasi-staticity:

$$T^{\epsilon} = \frac{|\Delta\epsilon|^{max}}{\dot{\epsilon}} = \frac{|\Delta\epsilon|^{max}}{I_n}\sqrt{\frac{\rho\, l^2}{P}} \tag{4.1}$$

with $|\Delta\epsilon|^{max}$ the maximum absolute eigenvalue of the strain increment, ρ the grain density, l the characteristic grain size and P the RVE mean stress. Typically, T^{ϵ} is much lower than Δt^{MPM}. However, because it depends on both $|\Delta\epsilon|^{max}$ and P, it can be quite high when a RVE in a low stress state is subject to important deformations. Besides, the lack of gravity at the microscopic scale introduces the possibility to loose all contacts in the granular assembly,

which leads to $P = 0$. Indeed, the stress state of a RVE is computed using Love-Weber formula, which is depends only on the contacts of the granular assembly (more details are given in section 4.2.2). A threshold for P is thus set to the expected stress at the bottom of the RVE if it were subject to gravity. This threshold, denoted P^{min}, is computed from the weight the RVE would have W^{RVE}, and the bottom surface of its periodic cell S^{RVE}:

$$P^{min} = \frac{W^{RVE}}{S^{RVE}} \tag{4.2}$$

Note that as S^{RVE} varies as the RVE deforms, P^{min} should thus be recomputed at each MPM iteration. The mean stress used in equation 4.1 reads:

$$P = \max\left(\frac{|\mathrm{Tr}(\underline{\underline{\sigma}})|}{3}, P^{min}\right) \tag{4.3}$$

Since the ratio of T^{ϵ} and the DEM time step Δt^{DEM} is not necessarily an integer, an extra attention has to be given when imposing the deformation to the RVE. Two strategies can be used to ensure that $\Delta\underline{\underline{\epsilon}}$ is exactly applied to the RVE during a specific number of DEM iterations N_{it}^{DEM}: 1) preserving T^{ϵ} and momentarily adjusting Δt^{DEM}, 2) preserving Δt^{DEM} and momentarily adjusting T^{ϵ}. With the first strategy, a temporary time step $\widetilde{\Delta t}^{DEM}$ has to be determined:

$$\widetilde{\Delta t}^{DEM} = T^{\epsilon} - \Delta t^{DEM} \times \mathrm{floor}\left(\frac{T^{\epsilon}}{\Delta t^{DEM}}\right) \tag{4.4}$$

with floor(x) equal to the nearest integer lower than x.

During the first $N_{it}^{DEM} - 1$ iterations Δt^{DEM} is used, and for the last iteration $\widetilde{\Delta t}^{DEM}$ is used. Note that in the eventuality of T^{ϵ} being smaller than Δt^{DEM}, only one DEM iteration is performed during the entire MPM iteration. This scenario is likely to happen if the material point is not subject to important deformations, or if it is highly constrained. This strategy thus adds a safety margin to the critical DEM time step used, in the eventuality where only one DEM iteration per MPM iteration is required.

With the second strategy, Δt^{DEM} is kept constant during the whole MPM iteration, but T^{ϵ} is increased so it is exactly an integer times Δt^{DEM}. This new deformation time is computed as follows:

$$T^{DEM} = \Delta t^{DEM} \times \mathrm{ceil}\left(\frac{T^{\epsilon}}{\Delta t^{DEM}}\right) \tag{4.5}$$

with ceil(x) equal to the nearest integer higher than x.

This strategy adds a safety margin to the quasi-static criterion, as T^{DEM} corresponds to the DEM deformation time obtained with a I_n lower than the one used to compute T^{ϵ}. For the sake of simplicity, the deformation time applied to the RVE will always be denoted T^{DEM}, even with the first strategy where it is equal to T^{ϵ}.

The microscopic strain rate is then:

$$\dot{\underline{\underline{\epsilon}}} = \frac{\Delta\underline{\underline{\epsilon}}}{T^{DEM}} \tag{4.6}$$

It is applied to the RVE as a velocity gradient $\underline{\underline{\nabla V}}$, on top of the velocities induced by the

contact forces.

4.2.2. Homogenization

After applying the deformation to the RVE, its stress state changes according to the numerous rearrangements in the sample and should thus be determined after each deformation. In order to do so, the geometries and total forces of all interactions between grains have to be accounted for. When considering quasi-static assemblies of particles interacting only through their contact forces, such a homogenization process can be done using the Love-Weber formula, given in equation 4.7:

$$\sigma_{ij}^{glob} = \frac{1}{V} \sum_{c=1}^{N_c} f_i^c \, l_j^c \tag{4.7}$$

where N_c is the number of contacts in the granular assembly, $\underline{f}^c$ is the interaction force of the contact c, and $\underline{l}^c$ is the branch vector of the interaction.

4.3. Technical aspects

As mentioned in section , the coupling was implemented based on two already existing C++ softwares: CB-Geo MPM for the Material Point Method and YADE for the Discrete Element Method. This section introduces these softwares and their features before providing more details on the coupling implementation.

4.3.1. Base softwares

This section presents the softwares used to implement the MPMxDEM coupling.

4.3.1.1. YADE, a DEM software

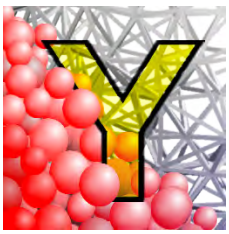

YADE (Yet Another Dynamic Engine) [Smilauer et al. 2021] is an open-source software available on GitLab [1], actively developed since 2005. It includes a Python interface which allows users to easily setup complex simulations while keeping the great performances of the C++ programing language. YADE offers the possibility of using several shape models (clumps, polyhedra, potential particles, level-set, ...) and also different contact laws (accounting for viscosity, cohesion, rolling resistance, capillarity, ...). Users can easily customize the DEM main loop to add for instance an interaction based on a non-native model. Also, simulations can be run interactively, offering the possibility to tweak or monitor all parameters on the fly. A batch mode is also available to easily perform parametric studies.

4.3.1.2. CB-Geo MPM, an MPM software

1. https://gitlab.com/yade-dev/trunk

CB-Geo MPM [Kumar, Salmond, Kularathna, et al. 2019] is an open-source software available on GitHub [2], developed by the Computational Geomechanics Research Group [3]. It is capable of performing 2D simulations with triangles or quadrilaterals as mesh elements, and 3D simulations with hexahedrons as mesh elements. CB-Geo MPM supports both the USF and USL stress update strategies and includes a variety of constitutive laws (linear-elastic, Newtonian fluid, Mohr-Coulomb, Modified Cam Clay, Nor-sand). Each constitutive law has its own C++ class, such a class will be denoted as a "material class" in the rest of this chapter.

This study uses a modified version of the CB-Geo MPM code, developed during this thesis, with several additional features, including:

— the possibility to use other MPM velocity update strategies (APIC, FLIPX, NFLIP, NFLIPX),
— the possibility to impose non-constant velocity constraints,
— other minor modifications, such as the addition of a verbosity parameter (the quantity of line outputed) or the change in the data file format (from HDF5 to CSV)

4.3.1.3. PyCBG, a Python module for CB-Geo MPM

Unlike YADE, simulations in CB-Geo MPM are launched through several input files using different file formats (JSON for the parameters, CSV for initial values, MSH-like for the mesh). As a consequence, the preparation of a simulation can be quite tedious even for simple configurations. A Python module named PyCBG [Duverger and Duriez 2021] was developed in order to simplify the generation of these files, taking advantage of Python's simplicity to perform complex simulation setups (e.g. to add material points at specific locations, or to initialize stresses and velocities based on their positions). Its documentation is available on ReadTheDocs [4] or can be built locally by the user.

Through its preprocessing sub-module, PyCBG is able to generate all CB-Geo input files necessary for a basic simulation (4 files, 226 lines in total) using only a 16 lines Python script [5]. It provides the user with a command line interface (CLI) which allows the user to setup a simulation interactively. Here is the help output of PyCBG's CLI:

2. https://github.com/cb-geo/mpm
3. https://www.cb-geo.com
4. https://pycbg.readthedocs.io/en/latest/index.html
5. See the "Examples" section of the Simulation object in PyCBG's documentation[4]

Features \ Software	CB-Geo MPM	YADE DEM
Availability	Open-source	Open-source
Programing language	C++	C++
OpenMP parallelization	Yes	Yes
MPI parallelization	Yes	Yes
Supported number of dimensions	2D and 3D	3D
User interface	Input JSON files, or Python through PyCBG	Python
Interactive run	No	Yes
Batch mode	Through PyCBG	Yes

TABLE 4.1. – Features of the coupled MPM and DEM softwares

```
$ pycbg -h

usage: pycbg [-h] [-v] [-p] [-i] [-n] [-d [BUILD_DIR]] [PYCBG_SCRIPT]

Manage CB-Geo MPM simulations using PyCBG Python module

positional arguments:
  PYCBG_SCRIPT          pycbg script to be run. By default, the following import lines are added at the top of the
                        file: `from pycbg.preprocessing import *`, `from pycbg.postprocessing import *` and `from
                        pycbg.MPMxDEM import *`. To deactivate this behaviour, use the -n (or --no-import) option

optional arguments:
  -h, --help            show this help message and exit
  -v, --version         print pycbg version
  -p, --pip-show        alias for `pip show pycbg`
  -i, --interactive     run in an interactive IPython session. Using both the -i and -n options simply creates a
                        IPython interactive session
  -n, --no-import       deactivates automatic import of pycbg
  -d [BUILD_DIR], --build-doc [BUILD_DIR]
                        build pycbg's documentation in BUILD_DIR, its path being relative to the current working
                        directory. If BUILD_DIR isn't specified, it will be set to `${PWD}/pycbg_doc`. If BUILD_DIR
                        is `..`, it is set to `../pycbg_doc`. If -d and PYCBG_SCRIPT are specified, the
                        documentation is build before running the script
```

PyCBG also offers the possibility to easily setup and launch a batch of simulations, by just requiring the user to provide a base script and a list of parameters sets (or a list of parameters, automatically combined into all possible parameters sets).

Another sub-module was developed in order to facilitate the postprocessing operations. Basically, it loads the post-simulation CSV files and arranges them into Python's NumPy arrays, all data can thus be easily accessed and postprocessed with all Python's capabilities. This sub-module is specially convenient when postprocessing a batch of simulations.

A third sub-module was added to provide a user interface to the MPMxDEM coupling. Details about its features are given in the next section.

Table 4.1 summarizes the main features of YADE and CB-Geo MPM.

4.3.2. Coupling implementation

The coupling framework requires the main CB-Geo MPM simulation to be able to launch a YADE simulation for each material point. Such a task could be done by directly integrating YADE's C++ backend into the CB-Geo C++ code, stripping YADE from its Python interface.

Doing so would considerably complexify the access to most of YADE's features, as it is intended to be used through the Python interface. Instead, the Python interface is directly integrated into the CB-Geo MPM C++ code, preserving the possibility to setup the DEM simulation with a user-friendly Python script (see figure 4.1). The operation of integrating Python into a C++ program was performed following the instructions provided by Python's documentation [6].

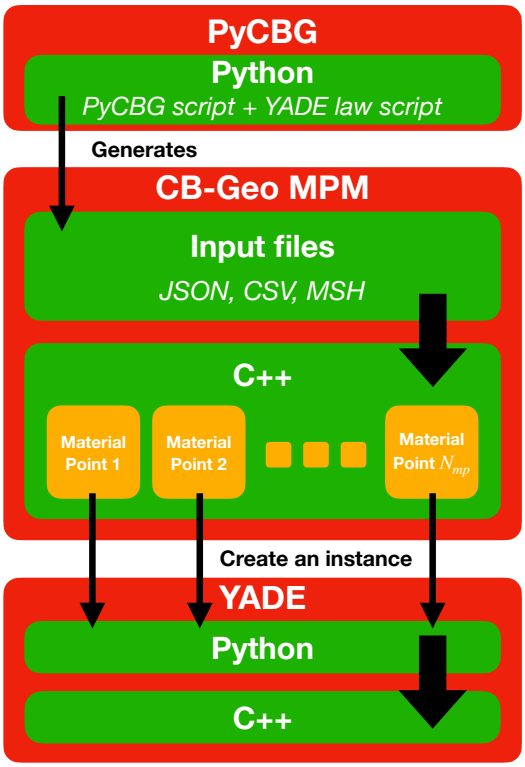

FIGURE 4.1. – Coupling framework

4.3.2.1. Embeding Python

Python's embedding into CB-Geo MPM was done inside a new generic material class (denoted `PythonModel`), making the usage of a user-defined constitutive law almost transparent to a regular CB-Geo MPM user. It only requires a Python script (denoted `PyModel` script) containing a callable object with a specific signature, which will be used to determine the material's behaviour (it can for instance be a function, denoted `compute_stress`). At each MPM iteration, `compute_stress` is called with the 6 components of the deformation increment tensor as input and should return the 6 components of the stress increment tensor. Additional variables can be included into the inputs (and outputs) of `compute_stress` in

6. https://docs.python.org/3/extending/embedding.html#embedding-python-in-c

order to keep track of history-dependant parameters (denoted state variables). Note that DEM isn't integrated into `PythonModel` yet: one could implement any constitutive law in Python and use this class to try it out in CB-Geo MPM. As convenient as this possibility may be, it should be noted that performing operations through Python inside a C++ code is considerably slower than performing them directly in C++.

4.3.2.2. Using DEM as a constitutive law

In order to complete the coupling, a DEM simulation has to be performed from the `PyModel` script. This section details how an instance of YADE can be created from any Python script and describes how PyCBG can be used to easily perform the tedious task of setting up a YADE `PyModel` script.

Using YADE from the `PyModel` script

YADE was intended to be used through its CLI. As a consequence starting a YADE simulation from any Python script is not straightforward. Indeed, YADE's executable is a Python script containing more than 400 lines that sets up everything needed to perform a simulation. It should thus be imported by the `PyModel` script, paying a particular attention to which variable scope the imported variables will be added to. The YADE part of the `PyModel` script should create a granular assembly and be capable of deforming it according to a velocity gradient.

Using PyCBG to setup a YADE `PyModel` script

The MPMxDEM sub-module included in PyCBG provides a function (denoted `setup_yade`) to launch YADE from Python. The user can choose which YADE executable to run, offering the possibility to use a specific or modified version of YADE. This sub-module also provides a ready-to-use definition of the callable object (denoted `DefineCallable`) required by the `PyModel` script. Over all, turning a pure YADE script into a `PyModel` script for a MPMxDEM simulation consists in adding only two lines: the `setup_yade` line, and the `DefineCallable` line. The latter requires one parameter and can be tuned using several others, offering different possibilities. The mandatory parameter is the strain rate at which the DEM cell will be deformed ($\dot{\epsilon}$ in equation 4.1), while optional parameters can be used to keep track of microscopic variables directly in the MPM result files. Basically, the user can pass a list of Python expressions to be evaluated from the YADE session and returned to CB-Geo MPM. Another parameter offers the possibility to save VTK files of the YADE simulations at a specified frequency, providing an easy way to visualize the temporal evolution of microscopic data at each material point.

When used alongside the preprocessing sub-module, PyCBG's MPMxDEM module automatically logs the used version of YADE and its dependencies into a file. When used in batch mode, CB-Geo MPM and PyCBG versions are also logged into files, simplifying the tracking of bugs and improving the repeatability of the results.

4.3.2.3. Parallelization

While embedding Python into CB-Geo MPM's C++ source code has the advantage of preserving YADE's user-friendly interface, it also brings technical difficulties for running a simulation in parallel. Indeed, when using the OpenMP parallelization in CB-Geo MPM, several material points must have access to their YADE session at the same time. However, if Python is embedded directly into the main MPM process, only one material point can have access to the Python session at the same time. This behaviour was intended by Python's developers: it assures that the same object is not modified at the same time by different threads (see Python's documentation on the Global Interpreter Lock [7] for more details).

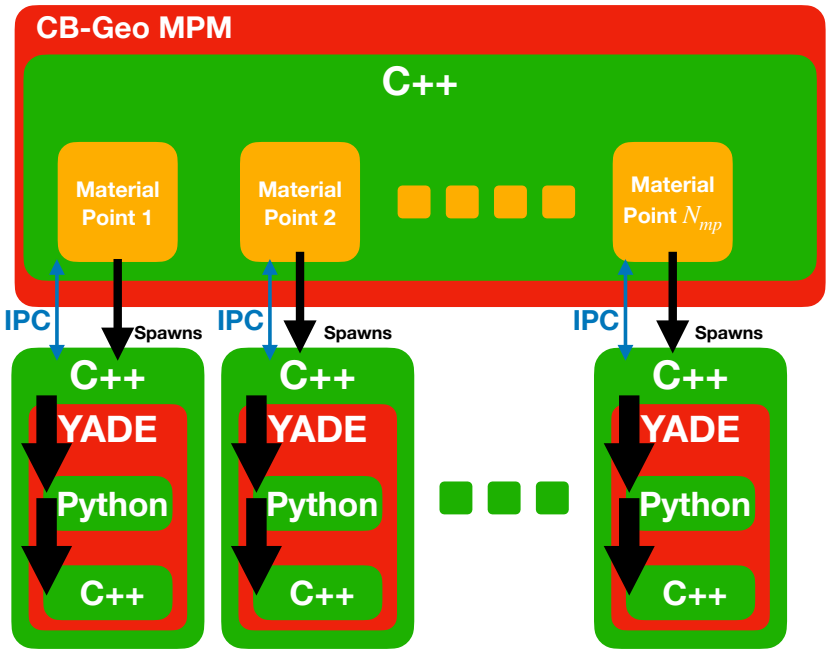

FIGURE 4.2. – Coupling parallelization

Using a sub-process for each material point

A workaround is to create as many Python sessions as material points, which requires the main MPM C++ process to spawn a new process for each material point. Typically, this is done using the Unix-exclusive operation `fork` combined with the `execve` function. The main MPM process should be able to call the `compute_stress` function of each sub-process, it is thus necessary to ensure the Inter-Process Communication (IPC) between the main process and the forked ones. Several different strategies are available [8], our MPMxDEM implementation uses the named pipes strategies (also referred to as FIFOs for "First In First Out") which are basically files in which several processes can write or read data. Note that

7. https://wiki.python.org/moin/GlobalInterpreterLock
8. https://en.wikipedia.org/wiki/Inter-process_communication

named pipes are considerably slower than some other IPC strategies, specially the shared memory strategy (see the benchmarking results [9] obtained with the open source software IPC-Bench [10]). However, it was observed that the IPC is not the most expensive step in our MPMxDEM implementation, the RVE deformation is. Indeed, IPC is used only twice for each MPM step (once from MPM to DEM, and once from DEM to MPM) but many DEM iterations are performed. Still, depending on their configurations some RVE simulations might be fast enough for the IPC time cost to be non negligible compare to the DEM time cost. Replacing the named pipes strategy with the shared memory strategy in our MPMxDEM implementation is thus a great possibility to improve its performances. Figure 4.2 summarizes how the issues brought by the Python embedding were addressed.

Parallelization performances

A measure of the parallelization performances was performed on a simple MPMxDEM triaxial test, whose configuration is detailed in the next section. Basically, a one cell MPM mesh contains a specific number of regularly spaced material points N_{mp}. The OpenMP parallelization strategy being used at the MPM level, a material point is thus assigned to a specific CPU core on which computations are performed sequentially. Figure 4.3 shows the speedup S obtained on a server machine with 2 Intel® Xeon® Platinum 8270 CPU @ 2.70GHz processors and 1536 GiB of RAM available. Note that for this measurement Intel's hyper-threading was enabled, making a total of 104 CPU threads available. Denoting $N_{threads}$ the number of CPU threads used, and $T(N_{threads})$ the computational time cost for a specific number of thread, the speedup is computed as follows:

$$S = \frac{T(N_{threads})}{T(1)} \tag{4.8}$$

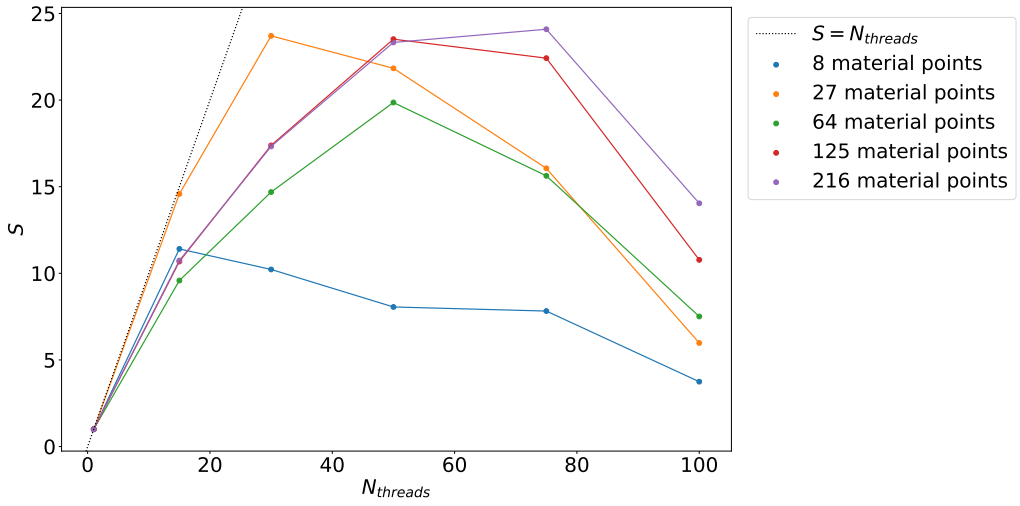

FIGURE 4.3. – OpenMP speedup for a one cell triaxial test using various N_{mp}

9. https://stackoverflow.com/a/54164058
10. https://github.com/goldsborough/ipc-bench

One can notice that for 27 material points, using 15 threads gives an almost perfect speedup: $S \approx 15$. The best speedups are achieved when using more than 8 material points and reaches $S \approx 24$, except for $N_{mp} = 64$ where the speedup does not exceed 20. A global decreasing tendency is observed for $N_{threads} > 50$, which is probably due to the hyper-threading technology. Indeed, these results suggest that the overall performances drop when the CPU is heavily loaded. Also, note that a speedup higher than 8 was measured for some simulations containing only 8 material points, which is supposedly impossible since there should be at most 8 CPU threads working in parallel. This strange result can be explained by the variation of the server's CPU load: it must have been higher when performing the reference simulation with $N_{threads} = 1$.

4.4. Test case: one cell triaxial test

This section is a partial inclusion of a communication published in the 25^{th} edition of the Congrès Français de Mécanique in 2022.

4.4.1. Simulations and results

A simple element test triaxial test is performed in order to ascertain the MPMxDEM capacity to accurately model granular materials. The only MPM cell is a cube with a length $l = 1\ m$, in which 8 material points (more precisely RVEs) are regularly spaced. In the x and y directions, forces are imposed on all nodes oriented towards the sample in order to maintain the confining pressure $\sigma_{lat} = 100\ kPa$. In the z direction, the bottom nodes velocities are forced to be nil, while on the top nodes a velocity is imposed downwards. This velocity respects quasi-staticity as it is computed from the previously introduced inertial number I_n:

$$V_v^z = -I_n \sqrt{\frac{\sigma_{lat}}{\rho_{RVE}}} \tag{4.9}$$

with ρ_{RVE} the mass density of the granular assembly, which accounts for the voids in the RVE.

Note that since a constant velocity is imposed on all nodes in the z direction, vertical acceleration is nil everywhere in the domain and thus material points only move horizontally. Also, even though the initial velocity on the top nodes is not zero, the initial velocity of the material points is. That is in fact a trick to moderate the material points' displacement in order to keep the computation of the internal efforts as correct as possible. The physical meaning of the simulation does not suffer from such a trick since the MPM considers the material to be present in the whole MPM cell as long as material points are inside. Their positions are then not relevant to determine the material's behaviour, which requires only a consistent value for $\underline{\underline{\dot{\epsilon}}}_p$, whose evaluation still depends on $\underline{x}^p$, as prescribed by equation 3.36.

As a reference, a pure DEM simulation was performed on a sample of 30,000 spheres, to allow the analysis of the coupling's accuracy as well as its efficiency for this simple 8 material points simulation. The pure DEM triaxial test uses the same conditions as each RVE of the previous MPM calculation: both are periodic simulations and their particle size distribution,

	Number of particles	Initial void ratio	Computational time cost
Pure DEM	30,000	0.563	≈ 6 hours 43 minutes
MPMxDEM	8 × 1,000	0.558	≈ 55 minutes

TABLE 4.2. – Initial conditions and computational time cost for both simulations

contact model and sample's initial density are identical. The initial density was measured inside a sub-volume within the sample, see section 2.3.3.2. The deformation rate imposed in pure DEM is the same as the one imposed by the MPM on all RVEs, i.e., the one computed with $I_n = 2.5 \cdot 10^{-4}$. Note that this is not usually the case, this equality is however justified by the quasi-static assumption considered both in DEM and MPM. Both simulations were run independently on the same machine having an Intel® Xeon® Platinum 8270 CPU @ 2.70GHz with 1.5 TiB of RAM available, using OpenMP parallelization on 8 CPU cores.

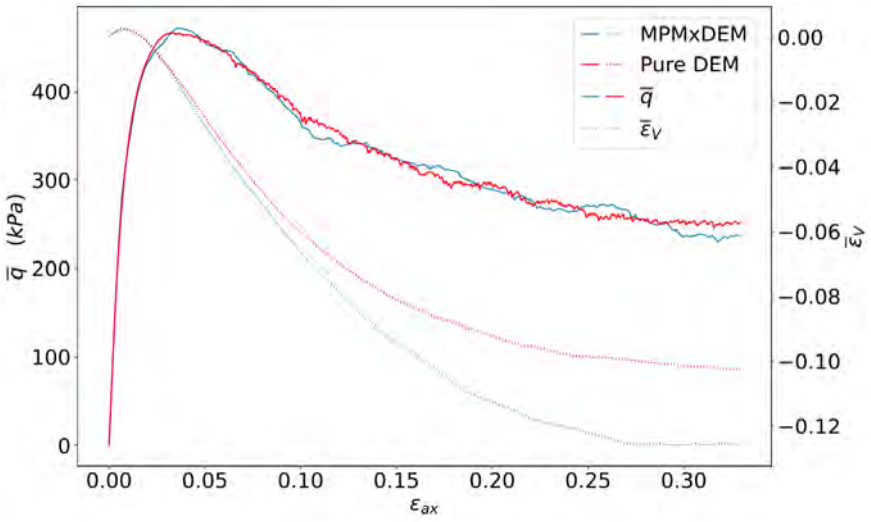

FIGURE 4.4. – Mean deviator stress $\overline{q}$ and volumetric strain $\overline{\epsilon}_V$ against mean axial strain $\overline{\epsilon}_{ax}$

Table 4.2 summarizes the initial conditions and computation times for both the pure DEM and MPMxDEM simulations. Figure 4.4 (a) shows the mean deviatoric stress $\overline{q}$ and mean volumetric strain $\overline{\epsilon}_V$ over all RVEs for the MPMxDEM simulation, or computed using the stress tensor and cell deformation for the pure DEM simulation. For this triaxial test, MPMxDEM is approximately 7.3 times faster than pure DEM. As for the accuracy, figure 4.4 shows that the deviatoric stress is almost the same for both simulations, particularly during the low deformations part. However, beyond the maximum stress state the MPMxDEM $\overline{\epsilon}_V$ progressively deviates downwards from the pure DEM $\overline{\epsilon}_V$, but it seems to reach more clearly the critical state. Comparing these mean values, results are consistent since the MPMxDEM is in close agreement with pure DEM regarding the stress response while the computational cost is significantly lower.

However, figure 4.5 (a) shows that during the MPMxDEM simulation (see figure 4.5 (d)

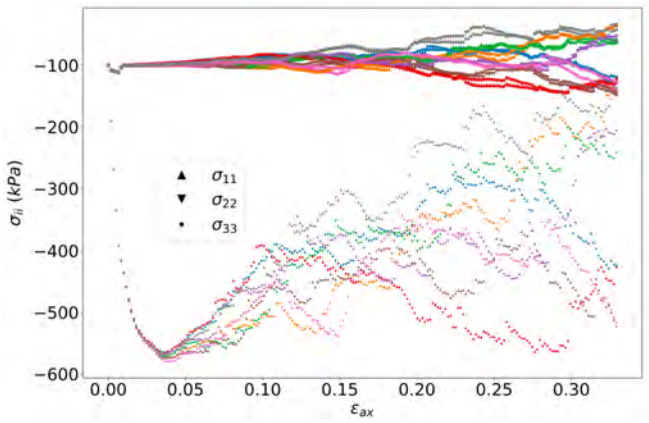

(a) Principal stresses σ_{ii} against axial strain ϵ_{ax}

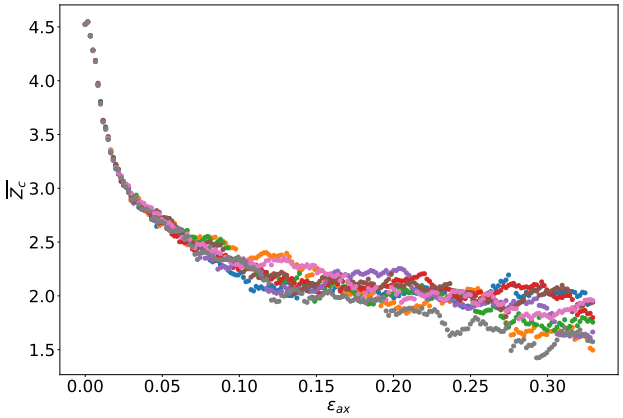

(b) Average number of coordination

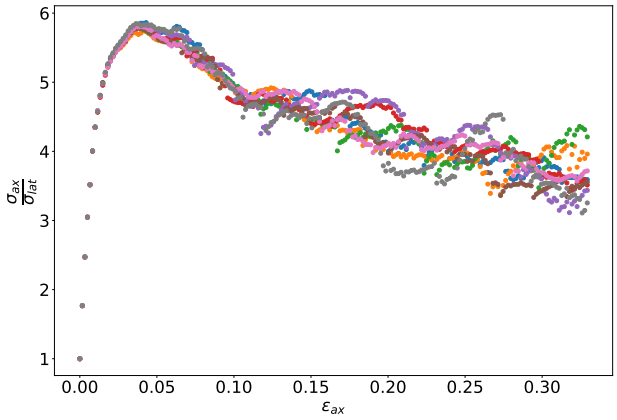

(c) Axial stress σ_{ax} over lateral stress σ_{lat} against axial strain ϵ_{ax}

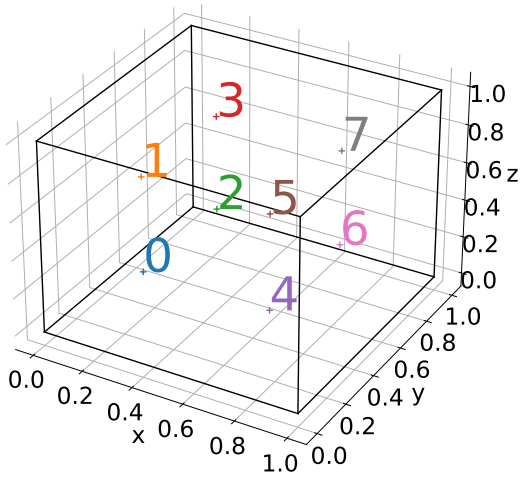

(d) RVE initial positions, colors and numbering

FIGURE 4.5. – Results obtained for each RVE

for the RVEs colors and initial position), the control of the lateral stress is lost. Indeed, after the maximum stress state is reached, half of the RVEs have their lateral stresses decreasing, the other half have them increasing. An interesting point to notice is that none of the RVEs behaves as one of its closest neighbor, and yet there is only two different types of behaviours. This curious arrangement is probably simply the expression of some gradient shape functions' geometrical property, which are bi-odd functions. Figure 4.5 (c) shows that the ratio between the axial and lateral stresses remain homogeneous for all RVEs during the whole test.

Figure 4.6 shows each particle's mean stress for two neighbor RVEs (n°1 and n°3). RVE n°3 supports no stress while RVE n°1 is strongly stressed.

Contrary to the stress tensor, the average coordination number $\overline{Z}_c$ is homogeneous in the MPM cell, as shown on figure 4.5 (b): all RVEs share about the same $\overline{Z}_c$, exactly for low deformations and more approximately for higher deformations.

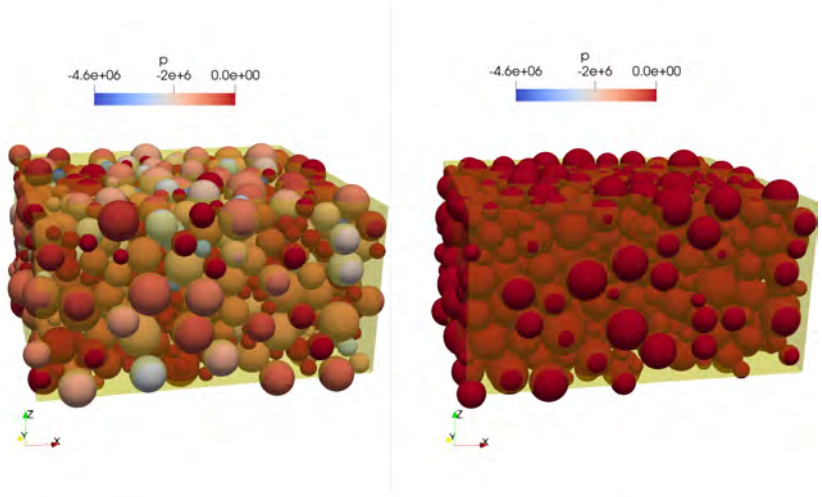

FIGURE 4.6. – Two RVEs final stress states. The left picture shows a RVE whose lateral stress increases (RVE n°3), the right picture shows a RVE whose lateral stress decreases (RVE n°1). Each particle is colored according to its mean stress p following the classical continuum mechanics' sign convention.

The incapacity of MPMxDEM to keep the lateral stress constant, as shown in figure 4.5 (a), is most probably due to the horizontal displacement of the RVEs that increases the "numerical integration's weights" error. Indeed, as the particles move, their attributed volume becomes more and more biased and the computation of the internal efforts gets progressively false.

4.4.2. Conclusion

This study presented a formulation of the MPMxDEM coupling that, even though it suffers from the MPM's imperfect description of the stress tensor, is able to accurately predict the behaviour a granular material subject to high deformations (over 0.3 as strain). The obtained deviatoric stress corresponds exactly to the pure DEM response. Other MPM formulations could certainly be considered to improve this coupling, in particular to simulate more dynamic problems.

Data was tracked for all RVEs, giving insights on how the critical stress is sustained by the sample: it appears that less than half the DEM particles are enough to maintain the stress within the sample. The axial and lateral stress ratio as well as the coordination number were shown to be homogeneous between all RVEs. The computational efficiency of the MPMxDEM is quite remarkable considering its accuracy. Indeed, the MPMxDEM simulation presented in this study is approximately 7.3 times faster than a pure DEM reference simulation. A more complex simulation would probably show an even better performance of MPMxDEM with respect to DEM, taking advantage of the scale range MPM makes accessible.

4.5. Conclusion on the multi-scale coupling procedure

This chapter presented how the DEM can be incorporated within the MPM in order to improve the description of granular materials, compared to traditional constitutive laws. It was demonstrated that a quasi-static assumption for the microscopic deformation can significantly decrease the number of DEM iterations to perform for each MPM iteration in all the granular assemblies considered. Moreover, the coupling was shown capable of accurately reproducing the results of a pure DEM triaxial test, confirming the validity of our MPMxDEM implementation. Nonetheless, the performances of the latter is yet to be assessed for large scales simulations, closer to the scale of geotechnical structures.

5. Multi-scale granular column collapse

Sommaire

5.1. Introduction

The case of the granular column collapse is widely studied in the science of granular materials [Crosta, Imposimato, and Roddeman 2009]; [Girolami, Hergault, Vinay, et al. 2012]; [Lajeunesse, Monnier, and Homsy 2005]; [Xiong, Yin, Nicot, et al. 2021], and it involves a considerable amount of deformations. Besides, it is quite similar to cases of interest in the study of geotechnical structures (e.g. dam break) and other geological studies (e.g. landslides). Naturally, it comes that the granular column collapse is a great test case to validate the MPMxDEM coupling at a larger scale.

In this chapter, the dynamics occurring during the collapse of a 1 meter wide granular column is investigated for several aspect ratios, namely 0.6, 1, 2.4, and 3. First, several series of pure MPM simulations are performed to determine the dependance of the results on both the discretization parameters and the velocity update scheme, for different aspect ratios of the initial column. A MPMxDEM simulation is then performed using the best parameters set determined from these pure MPM simulations.

5.2. Simulation description

The simulation being 2D plane strain, the stress is computed along the third direction, where the strain is equal to 0. Moreover, the "volume" attributed to each material point is here in fact a surface (see equation 3.9), as a consequence all energies will be given in J/m. Such a consideration is common in the literature [Crosta, Imposimato, and Roddeman 2009]; [Lube, Huppert, Sparks, et al. 2005]; [Staron and Hinch 2005]. The simulation is performed in two steps: the settling of the constrained column and its subsequent collapse, following the release of the constraint. At the beginning of the settling phase, the stresses of all material points are uniformly initialized to 250 Pa. This first step thus consists in computing the final stress gradient in the column, as a consequence of the presence of gravity. For the collapse step, the consolidated column is placed on the left of a wider mesh, introducing a collapse of the column on its right side.

5.2.1. Geometry of the problem

The width of the column spans over the x-axis while its height spans over the y-axis. The aspect ratio AR is defined as the column initial height L_y^{init} divided by its initial width $L_x^{init} = 1$ m, the latter being the same for all simulations.

Mesh

The mesh consists of cubic elements with a side of $l_{cell} \in \{10 \text{ cm}, 7.69 \text{ cm}, 5.88 \text{ cm}, 5 \text{ cm}\}$. For the initial settling phase, it has as many cells in the x and y directions as required by the aspect ratio:

$$W_{mesh}^{settling} = L_x^{init} \tag{5.1}$$

$$H_{mesh} = AR \times W_{mesh}^{settling} \tag{5.2}$$

with $W_{mesh}^{settling}$ the width of the mesh during the settling phase and H_{mesh} its height for the whole simulation. Taking advantage of the mesh independency of MPM, another mesh is used during collapse, which is in fact a substantial enlargement of the settling mesh:

$$W_{mesh}^{collapse} = 6 \times H_{mesh} \tag{5.3}$$

These parameters ensure a fairly fine discretization of this 2D geometry as they split the column in at least 100 cells (and up to 400 cells) and let it collapse in a mesh 6 times larger (from 600 to 2,400 cells).

A nil velocity is imposed at the left, right and bottom boundary nodes, in the direction orthogonal to the boundary. The left and right boundaries are thus denoted as walls, while the bottom boundary is denoted as floor. A friction condition is imposed on the floor, driven by a friction coefficient $\mu = 0.3$.

Material points

All cells contain initially N_{mppc} material points, located at the roots of Legendre's polynomials (in local coordinates, see equation 3.10), given in [Lowan, Davids, and Levenson 1942].

For instance, the roots of the second Legendre's polynomial are the local positions of the points in each direction for $N_{mppc} = 4$:

$$\widetilde{s} = \pm \frac{1}{\sqrt{3}}, \quad \forall s \in \{x, y\} \tag{5.4}$$

The initial volume of each material points (which is here in fact a surface, due to the 2D formulation) thus corresponds to the integration weight of the Gauss-Legendre quadrature, making the MPM formulation initially accurate for this specific case, $N_{mppc} = 4$. In this study, N_{mppc} ranges between 1 and 49. All material points are subject to the same gravitational acceleration of magnitude $g = 9.81$ m/s^2.

Figure 5.1 summarizes the initial configuration of the simulation for $AR = 1$, $N_{mppc} = 4$ and $l_{cell} = 10$ cm.

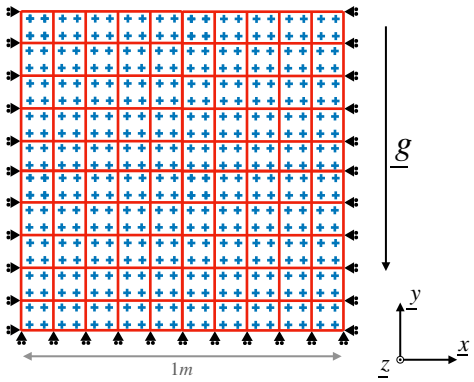

FIGURE 5.1. – Initial column

5.2.2. Numerical parameters of the simulation

Following the results presented in section 3.5.2, the influence of the discretization parameters is investigated using the USF stress update scheme combined with the FLIP velocity update strategy. This choice ensures that no artificial energy dissipation is brought by the MPM, at the cost of a higher sensitivity to instabilities.

Cundall's damping is used during the settling step in order to dissipate the energy in a controlled way, with a damping coefficient $D = 0.1$. During the collapse, D is reset to zero, allowing the energy to dissipate naturally through the friction imposed on the floor.

The material's behaviour is described with the Mohr-Coulomb constitutive law. The values of the model's parameters were determined from a pure DEM simulation performed with a contact model calibrated on a real sample of Camargue's sand [Aboul Hosn, Sibille, Benahmed, et al. 2017], see table 5.1.

The time step is computed as a fraction of the characteristic time given by the material's and mesh parameters:

$$\Delta t^{MPM} = a_\tau \times l_{cell} \sqrt{\frac{\rho}{E}} \tag{5.5}$$

Mass density ρ	Young's modulus E	Poisson's ratio ν	Friction angle ϕ	Dilatancy angle ψ	Cohesive strength C	Cutoff tension T_{cut}
1,748 kg m^{-3}	$\approx 1.28 \cdot 10^7$ Pa	0.16	33.75 °	0 °	1 Pa	$-\frac{C}{\tan\phi}$

TABLE 5.1. – Parameters used with the Mohr-Coulomb model

The coefficient a_τ was determined empirically to ensure a stable simulation. It was found equal to $1.25 \cdot 10^{-3}$ for the FLIP velocity update strategy, which gives a time step of $\Delta t^{MPM} \approx 1.46 \cdot 10^{-6}$ s when $l_{cell} = 10$ cm. Note that other velocity update strategies (namely PIC, APIC and NFLIP0.9) are capable of accommodating a time step 4 times higher.

5.2.3. Quantities of interest

In order to compare the influence of some parameters on the dynamics of the column collapse, several quantities are monitored during the simulation.

Width of the collapsing column

During the collapse, the column is confined by a wall on its left, the left edge is thus always located at $x = 0$ m. However, since the right edge of the column is free, it can spread up to $x = W_{mesh}^{collapse}$ m. The evolution of its position during the simulation is a major insight on how the collapse unfolds. Because the left edge does not move during the collapse, it is simply equal to the width of the column, L_x, and can be computed as follows:

$$L_x = \text{floor}\left(\frac{\max_{p\in\{p\}}(x^p)}{l_{cell}} + 1\right) l_{cell} \tag{5.6}$$

This expression assumes the material to have a "voxelized" geometry: the material is considered present in a whole cell as long as at least one material point is inside. As a consequence, L_x increases by steps of l_{cell} as the column spreads to the right.

Note that L_x is directly related to the so-called runout distance d_r:

$$d_r = L_x - L_x^{init} \tag{5.7}$$

Granular spreading length

A normalized spreading length $\widetilde{L}$ and collapse time $\widetilde{t}$ are commonly used to describe the dynamics of the collapse independently of the column dimensions. Both are computed as in [Utili, Zhao, and Houlsby 2015]:

$$\widetilde{L} = \frac{d_r}{L_x^{init}} \tag{5.8}$$

$$\widetilde{t} = \frac{t}{\sqrt{\frac{AR \times L_x^{init}}{g}}} \tag{5.9}$$

Total kinetic energy

Monitoring the total kinetic energy of the column E_k is a way to characterize the dynamics occurring during the collapse of the column. It is computed using equation 3.47. Note that in this equation, the kinetic energies of all material points are summed, the resulting E_k can thus be used to investigate MPM's dependance on the number of material points. Indeed, if the material point-based discretization is accurate, E_k should not depend on the number of material points used to represent a specific volume.

Mechanical energy

Monitoring the different types of energies involved in the simulation is a convenient way to interpret the dissipation observed in MPM simulations. However, the simulations in this chapter include two sources of energy dissipation: one originates from the friction on the floor, the other from the material's behaviour, modeled either with the Mohr-Coulomb constitutive law or with DEM. As a consequence, the dissipative nature of some MPM formulations cannot be as easily observed as in section 3.5. In the latter, the mechanical energy E_{mech} was the only energy involved in the simulation, and was thus denoted E_{tot}. Here, it is denoted E_{mech} but it is still computed from equations 3.45, 3.47 and 3.48:

$$E_{mech} = E_{el} + E_k + E_p \tag{5.10}$$

Deviatoric strain

The deviatoric part of the strain tensor at each material point is monitored to determine where and how much the column is sheared. It is reduced to a scalar using the Frobenius norm:

$$\underline{\underline{\epsilon}}^p_{dev} = \underline{\underline{\epsilon}}^p - \frac{\mathrm{tr}(\underline{\underline{\epsilon}}^p)}{3}\underline{\underline{I_3}} \tag{5.11}$$

$$\epsilon_D = \left\| \underline{\underline{\epsilon}}^p_{dev} \right\| = \sqrt{\sum_{i\in[\![1,3]\!]}\sum_{j\in[\![1,3]\!]} {(\epsilon_{dev})_{ij}}^2} \tag{5.12}$$

5.2.4. MPMxDEM specificities

The MPMxDEM simulation requires some additional parameters, specific to the coupling.

Microscopic description of the material

The material used is a numerical replicate of Camargue's sand, as calibrated in [Aboul Hosn, Sibille, Benahmed, et al. 2017]. It is the exact same material's description that was used to determine the parameters of the Mohr-Coulomb model, see table 5.1. The grains are modeled using spheres of different sizes, the minimum, maximum and median diameters being respectively $d_{min} = 9.90\cdot10^{-5}$ m, $d_{max} = 2.99\cdot10^{-4}$ m, and $d_{50} = 2\cdot10^{-4}$ m. The contact law accounts for friction through the inter-particle friction angle φ, but also rolling and twisting resistance, which effectively mimics the effect of the non-angular shape of the grains. The latter is computed using three additional parameters: two to determine a rolling and twisting stiffness based on the tangential stiffness (denoted α_r and α_t respectively), and

G (Pa)	α_s	α_r	α_t	φ	η_r
$2.8 \cdot 10^8$ Pa	0.2	7.5	0.2	25 °	0.22

TABLE 5.2. – Contact parameters (microscopic scale), as determined in [Aboul Hosn, Sibille, Benahmed, et al. 2017]

one to describe the resistance's limit (denoted η_r). The tangential stiffness is computed as a fraction α_s of the normal stiffness, which is computed from the elastic modulus G and the spheres radii. Table 5.2 provides the values of these parameters. The density of the grain is denoted ρ_g and is equal to 2,650 kg m^{-3}. Cundall's damping is not used in the RVE, energy dissipation at the microscopic scale thus only originates from inter-particle friction and rolling resistance.

Initial RVE

The RVE is initially identical for all material points. It is prepared by compacting a cloud of 2,000 particles until the desired confining pressure P_{init} is reached, namely $P_{init} = 250$ Pa. In this study, the inter-particle friction angle is intentionally decreased during this compaction phase to $\varphi/100$ in order to reach dense initial samples, as was done in [Chareyre, Briançon, and Villard 2002]. During the collapse, many RVEs are extensively stretched in the x direction and compressed in the y direction, but the periodic representation of the material at the microscopic scale requires the height of a RVE to be at least equal to the largest radius of the sphere assembly. The initial dimensions of the RVE are thus chosen according to these anticipated deformations: its height is 20 times larger than its initial width. The void ratio of this initial RVE, common to all material points, is $e_0 \approx 0.5284$. Its average coordination number is $Z_{c0} \approx 5.85$. The DEM time step is set to $\Delta t^{DEM} \approx 1.869 \cdot 10^{-9}$ s and kept constant during the whole simulation.

Strain rate

The rate at which the deformation required by the MPM is applied to the RVE is determined when computing T^{DEM}, see equations 4.1 and 4.5. Using an inertial number $I_n = 10^{-2}$, the initial strain rate applied to a RVE is given by:

$$\dot{\epsilon}_0 = I_n \sqrt{\frac{P_{init}}{\rho_g d_{50}^2}} \approx 15.4 \quad \text{s}^{-1} \tag{5.13}$$

Note that the mean stress P varies during the simulation, and is maintained above a threshold determined using equation 4.2. Initially this threshold is roughly equal to the confining pressure, i.e. $P_{init}^{min} \approx 250$ Pa, but it is fated to decrease during the collapse as S^{RVE} increases.

Monitored microscopic variables

The average coordination number of each RVE is tracked during the whole simulation. It is computed as follows:

l_{cell}	N_{mppc}	Δt^{MPM}	a_τ	AR	Velocity update
10 cm	4	$2.92 \cdot 10^{-6}$ s	$2.25 \cdot 10^{-3}$	1	FLIP
		$1.46 \cdot 10^{-6}$ s	$1.25 \cdot 10^{-3}$		
		$3.65 \cdot 10^{-7}$ s	$3.125 \cdot 10^{-4}$		
		$1.46 \cdot 10^{-7}$ s	$1.25 \cdot 10^{-4}$		
		$7.29 \cdot 10^{-8}$ s	$6.25 \cdot 10^{-5}$		

TABLE 5.3. – Parameters used to investigate the time step influence (series S1)

$$Z_c = \frac{N_{contacts} - N_{rattlers}}{N_{particles} - N_{rattlers} - N_{floaters}} \tag{5.14}$$

with $N_{contacts}$ the number of contacts in the RVE, $N_{rattlers}$ the number of particles having only 1 contact, $N_{floaters}$ the number of particles having 0 contact, and $N_{particles}$ the total number of particles in the RVE. Note that this expression of Z_c excludes the grains that do not belong in any force chain in the structure of the samples, i.e. the so-called rattlers and floaters.

The density of each RVE is also monitored during the whole simulation, through the void ratio e given by:

$$e = \frac{V_{cell} - V_{particles}}{V_{particles}} \tag{5.15}$$

with $V_{particles}$ the total volume occupied by the particles in the RVE and V_{cell} the volume of the DEM periodic cell, i.e. the RVE volume.

5.3. Pure MPM results

In this section, several series of simulations are performed in order to ascertain the convergence of the results with respect to the discretization parameters being:

— the MPM time step Δt^{MPM},
— the number of particles per cell N_{mppc},
— the length of the cubic cells l_{cell}.

Another series of simulation then determines the influence of the velocity update scheme for this simulation. It is compared to both experimental and numerical results from the literature.

5.3.1. Temporal convergence

A first series of simulations, denoted S1, is performed using several values for Δt^{MPM}. The latter is adjusted by changing the value of a_τ from $6.25 \cdot 10^{-5}$ to $2.5 \cdot 10^{-3}$. The other discretization parameters are fixed to $l_{cell} = 10$ cm and $N_{mppc} = 4$, as indicated in table 5.3. Note that these simulations have to perform a specific number of steps, different for each Δt^{MPM}, in order to reach the same simulated time.

Settling

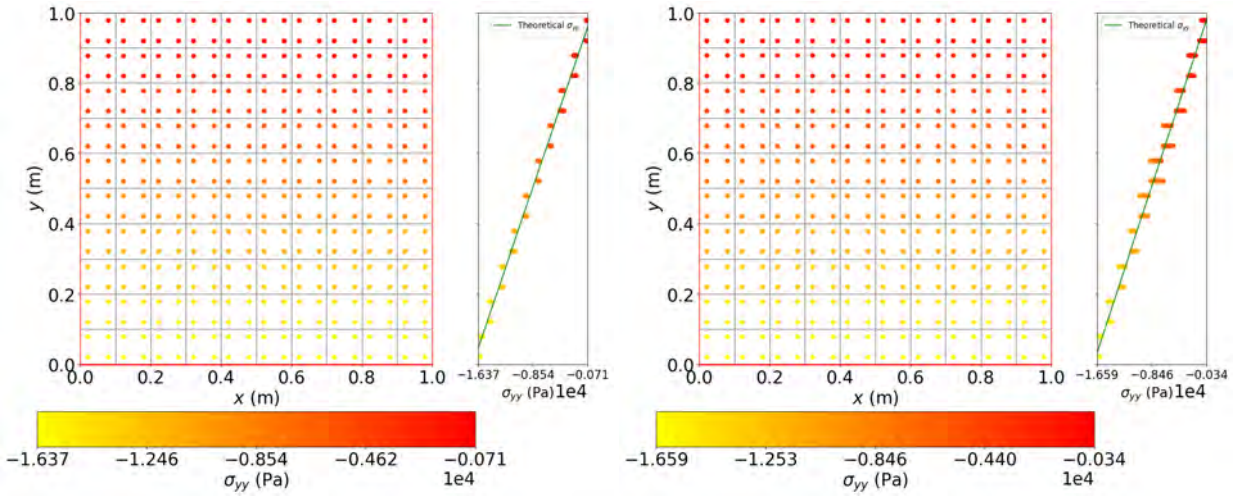

(a) σ_{yy} at the final stage for $\Delta t^{MPM} = 2.92 \cdot 10^{-6}$

(b) σ_{yy} at the final stage for $\Delta t^{MPM} = 7.29 \cdot 10^{-8}$

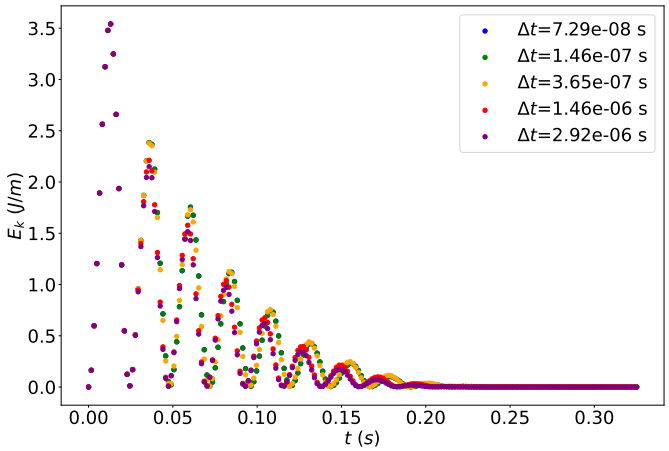

(c) E_k

FIGURE 5.2. – Settling step for different Δt^{MPM} (series S1)

Figures 5.2 (a) and (b) shows the vertical main stress σ_{yy} across all material points just before the collapse, for $\Delta t^{MPM} = 2.92 \cdot 10^{-6}$ s and $\Delta t^{MPM} = 7.29 \cdot 10^{-8}$ s respectively. These results demonstrate that the expected stress is obtained. However, σ_{yy} is slightly more dispersed when using a low Δt^{MPM}.

On figure 5.2 (c), one can see that E_k oscillates several times before reaching a stable state. Different values of Δt^{MPM} lead to exactly the same E_k but only over the first pseudo-period. Then the maximum reached during the following oscillations slightly increases with decreasing values of Δt^{MPM}: the difference is at most 6%. A progressive desynchronization is also observed: the columns modeled using a high Δt^{MPM} oscillate faster, as evidenced after a few pseudo-periods when the difference accumulates. These results suggest that more energy is dissipated with a higher Δt^{MPM}. However, the variations of E_k are not great

enough to be considered significant.

Collapse

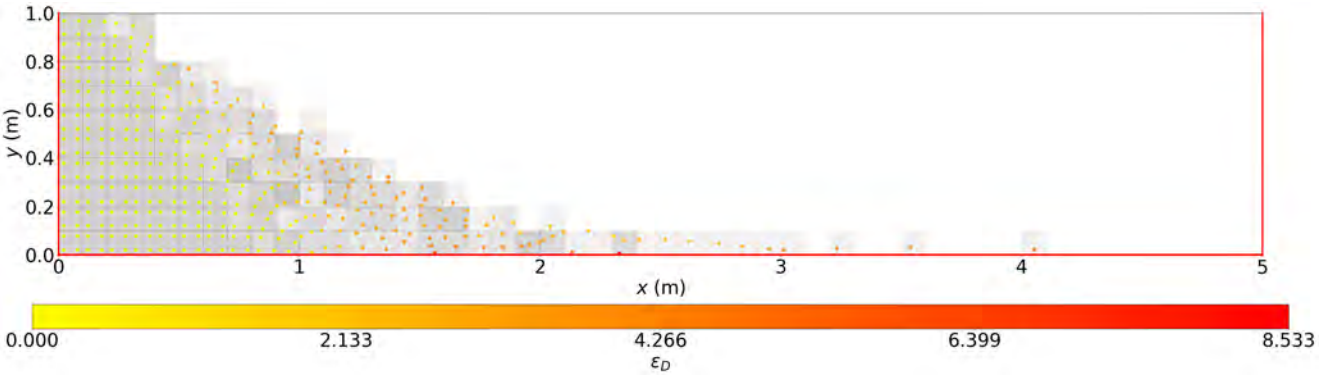

(a) $\Delta t^{MPM} = 2.92 \cdot 10^{-6}$ s

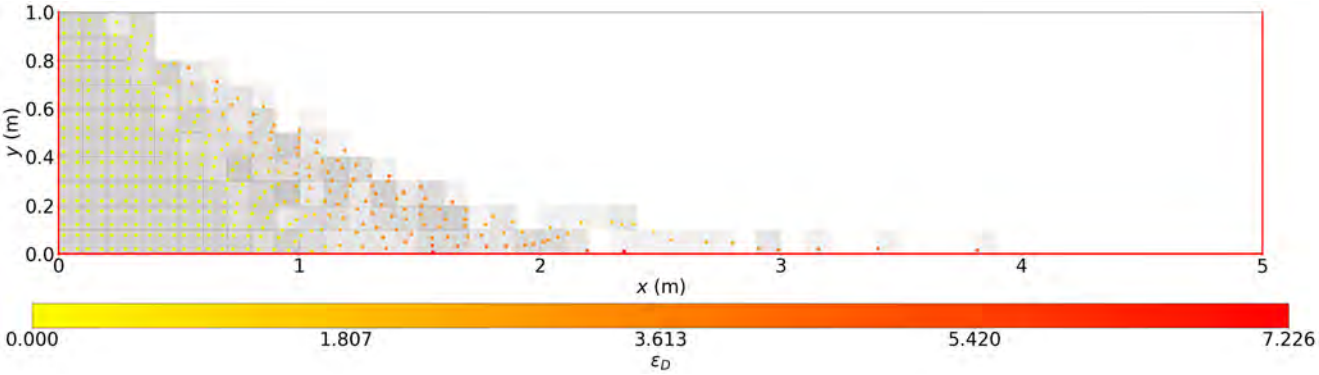

(b) $\Delta t^{MPM} = 7.29 \cdot 10^{-8}$ s

FIGURE 5.3. – Deviatoric strain after collapse (series S1)

The final geometry of the column is given by the deviatoric strain ϵ_D on figure 5.3. One can notice that the material points located in the bottom-left half of the initial column do not significantly move, as opposed to those in the other half which are largely displaced and extensively sheared. For the highest Δt^{MPM}, the maximum ϵ_D is approximately 15.3% higher than with a low Δt^{MPM}.

Figure 5.4 (a) shows the evolution of L_x during the whole simulation. The final position of the right edge increases of approximately 5% from the minimal to the maximal values of Δt^{MPM} tested. However, during the first half of the collapse, the value of Δt^{MPM} has virtually no influence on L_x. As for E_k, plotted on figure 5.4 (b), it appears completely independent of the Δt^{MPM} value.

Conclusion

In view of these results, choosing $\Delta t^{MPM} = 1.46 \cdot 10^{-6}$ s seems to be a good compromise between the computation accuracy and the computational time cost which depends on

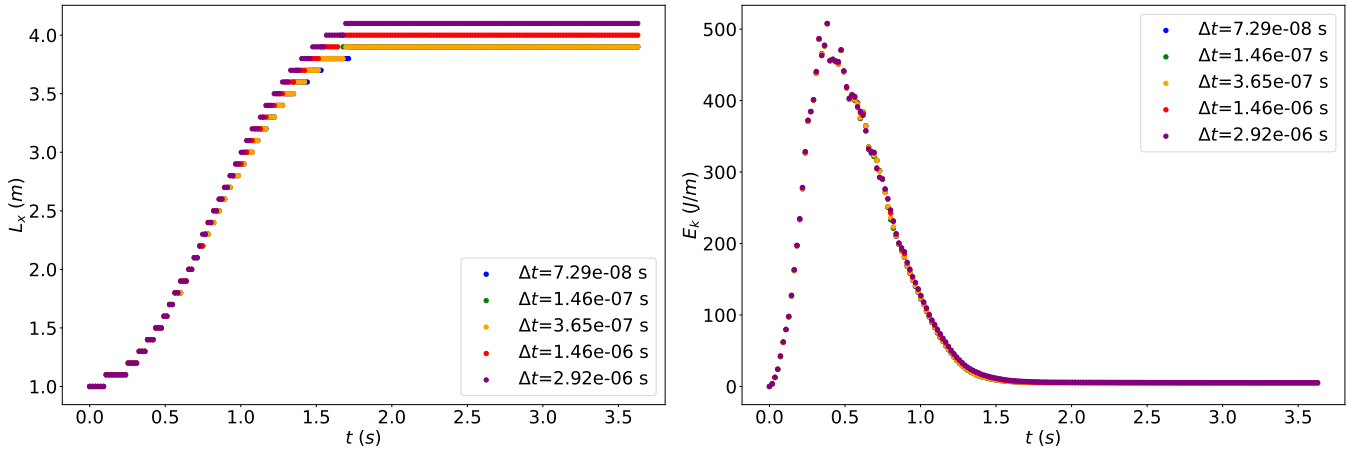

(a) L_x (b) E_k

FIGURE 5.4. – Right edge position and total kinetic energy during collapse for different Δt^{MPM} (series S1)

l_{cell}	N_{mppc}	Δt^{MPM}	a_τ	AR	Velocity update
10 cm	4	$1.46 \cdot 10^{-6}$ s	$1.25 \cdot 10^{-3}$	1	FLIP
7.69 cm			$1.625 \cdot 10^{-3}$		
5.88 cm			$2.125 \cdot 10^{-3}$		
5 cm			$2.5 \cdot 10^{-3}$		

TABLE 5.4. – Parameters used to investigate the influence of the cell size (series S2)

the number of steps to be performed to reach a specific time. The corresponding time step coefficient is thus $a_\tau = 1.25 \cdot 10^{-3}$.

5.3.2. Spatial convergence

Two other series of simulations are carried out to investigate the influence of the spatial discretization. Since the MPM models the material using both a mesh and a particle description, the fineness of each has to be verified. In the series denoted S2, the influence of l_{cell} is determined using four values between 5 cm and 10 cm. For this series, the time step is set to the same value for all simulations, therefore a_τ has different values. The series denoted S3 uses seven different values of N_{mppc}, the squared values of the first seven integers, to check the precision of the particle-based discretization. As mentioned in section 5.2.1, the material points are placed within their cell at the roots of the Legendre's polynomial in local coordinates. The parameters of both series are summarized in tables 5.4 and 5.5.

Settling

The vertical main stress observed on figure 5.5 is consistent with the theoretical expectations (i.e. linear profile). However, on can notice on figure 5.5 (b) that σ_{yy} is approximately the same for all material points within a cell, which is certainly due to the use of linear shape

l_{cell}	N_{mppc}	Δt^{MPM}	a_τ	AR	Velocity update
10 cm	1	$1.46 \cdot 10^{-6}$ s	$1.25 \cdot 10^{-3}$	1	FLIP
	4				
	9				
	16				
	25				
	36				
	49				

TABLE 5.5. – Parameters used to investigate the influence of the number of particle per cell (series S3)

functions. Indeed, such a choice for the shape functions makes their gradient constant over each cell, the force computed in equation 3.23 thus remains the same for all material points inside a specific cell. Because of this, using a more refined mesh results in a smoother final stress gradient, as seen in figure 5.5 (d).

The evolution of E_k during the settling, plotted on figure 5.6, is almost the same for all the values of N_{mppc} and l_{cell} tested. Only slight differences are observed for $N_{mppc} = 1$ and different values of l_{cell} when E_k gets below 10^{-1} J, which is approximately 3% of the maximum total kinetic energy E_k^{max}. This becomes more noticeable when E_k drops under 10^{-3} J, thanks to the vertical logarithmic scale. The simulation with $N_{mppc} = 1$ and $l_{cell} = 10$ cm has the highest E_k and stands out compared to other simulations. Using $N_{mppc} \geq 4$ gives about the same stabilization rate for $l_{cell} = 10$ cm. However, E_k decreases faster as the mesh resolution increases. These differences are nonetheless smaller than 10^{-3} J (roughly 0.03% of E_k^{max}), and can thus be considered negligible.

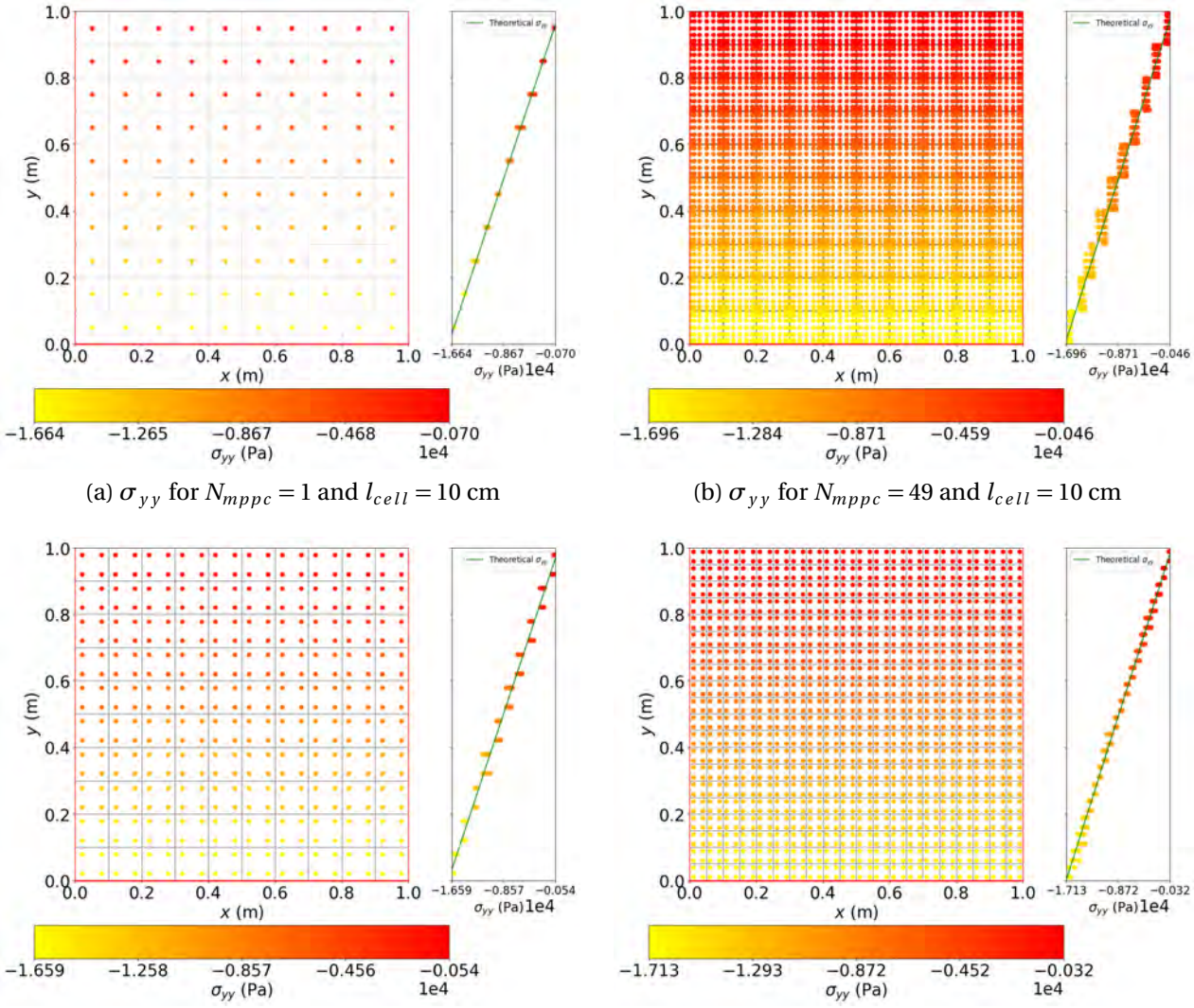

(a) σ_{yy} for $N_{mppc} = 1$ and $l_{cell} = 10$ cm

(b) σ_{yy} for $N_{mppc} = 49$ and $l_{cell} = 10$ cm

(c) σ_{yy} for $N_{mppc} = 4$ and $l_{cell} = 10$ cm

(d) σ_{yy} for $N_{mppc} = 4$ and $l_{cell} = 5$ cm

FIGURE 5.5. – Vertical stress at the end of the settling step for different spatial discretization parameters (series S2 and S3)

Collapse

Figure 5.7 (a) shows that the final spreading length L_x strongly depends on the spatial discretization parameters. Indeed, the L_x obtained for $N_{mppc} = 1$ is roughly half the one obtained for $N_{mppc} = 49$. The mesh resolution has a less significant impact: L_x for $l_{cell} = 7.69$ cm is approximately 7% lower than the one obtained with $l_{cell} = 5$ cm. Although the evolution of L_x with respect to l_{cell} is not exactly monotonous, a decreasing tendency can be guessed. The trend is much more pronounced for L_x with respect to N_{mppc}, which is monotonously increasing at a rather similar rate for $N_{mppc} > 1$. It appears that the influence of N_{mppc} is less important for $N_{mppc} \geq 16$, but it seems still far from convergence. Note that this important difference might be caused by the voxelized point of view of the material's geometry, not

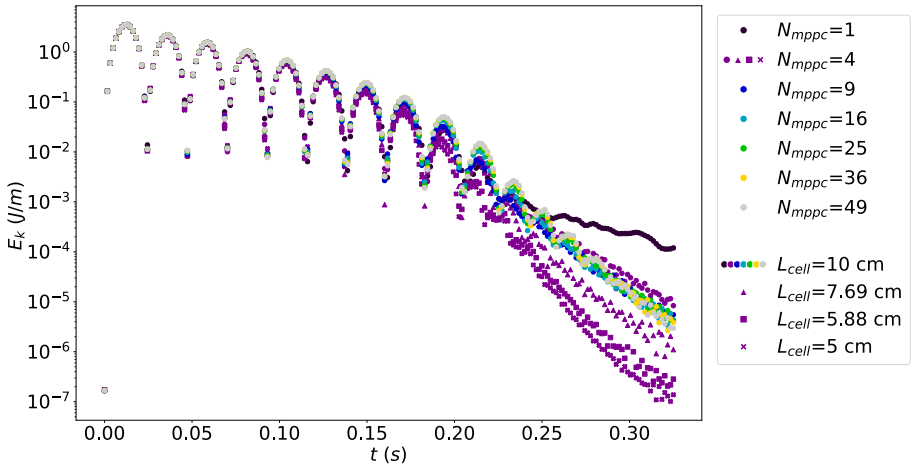

FIGURE 5.6. – Kinetic energy during the settling step for different spatial discretization parameters (series S2 and S3)

only by the dependance of the MPM to N_{mppc}.

Figure 5.7 (b) shows the total kinetic energy E_k during the collapse. Once again, the result obtained with $N_{mppc} = 1$ stands out: it has globally a higher and noisier E_k than any other N_{mppc} (notably between $t = 1$ s and $t = 1.5$ s). For $N_{mppc} \geq 4$, E_k is still a little noisy but the difference with respect to $N_{mppc} = 49$ is acceptable (at most 10% of the maximum E_k). Starting from $N_{mppc} = 9$, E_k seems no more significantly impacted by N_{mppc}. As a contrast with the settling phase, E_k during the collapse reaches higher values for lower of l_{cell}: the maximum E_k is roughly 18% higher for $l_{cell} = 5$ cm than for $l_{cell} = 10$ cm. Overall, E_k is less impacted than L_x by the spatial discretization parameters.

Figure 5.8 gives the final configuration of the collapsed column for the extremum of N_{mppc} and l_{cell}. One can see that for $N_{mppc} = 1$ the final height of the column is 0.7 times the initial one, while for $N_{mppc} \geq 4$ the column keeps the same height through the collapse. This observation suggest that using $N_{mppc} = 1$ is not enough for the collapse. Also, the deviatoric strain ϵ_D increases with the fineness of the spatial discretization, i.e. for increasing N_{mppc} and decreasing l_{cell}. Such an observation can be explained by the density of material points in the column: it is more likely that some are located at extensively sheared areas when N_{mppc} increases.

Conclusion

These series of simulations showed that the spacial discretization parameters have no significant influence on the settling phase, where material points are almost immobile. This is certainly because the computation of the integration weights remains plausible during the whole phase.

During the collapse, the number of material points per cell has a great impact on the final runout distance. The use of $N_{mppc} = 1$ is an extreme case which should be avoided, as it strikingly differs from the results obtained for more material points. The mesh fineness also affects the runout distance, although the effect is smaller than the one caused by N_{mppc}.

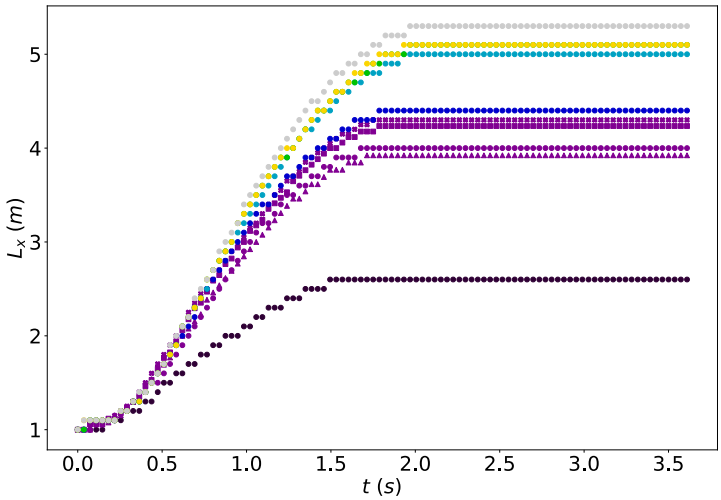

(a) L_x

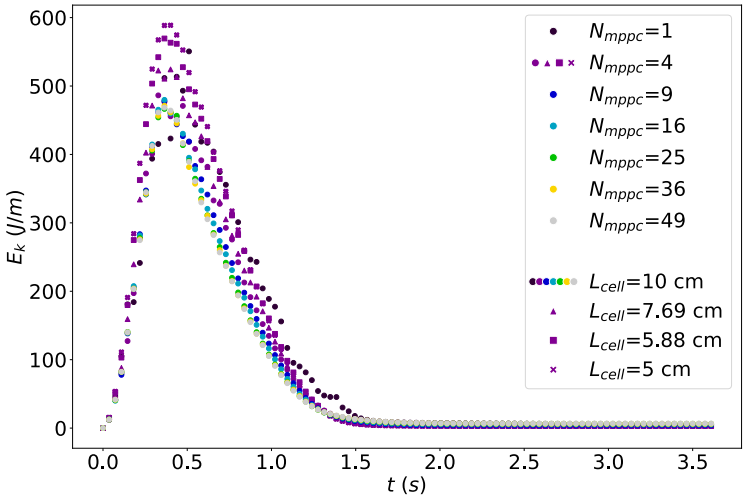

(b) E_k

FIGURE 5.7. – Right edge position and total kinetic energy during collapse for different spatial discretization parameters (series S2 and S3)

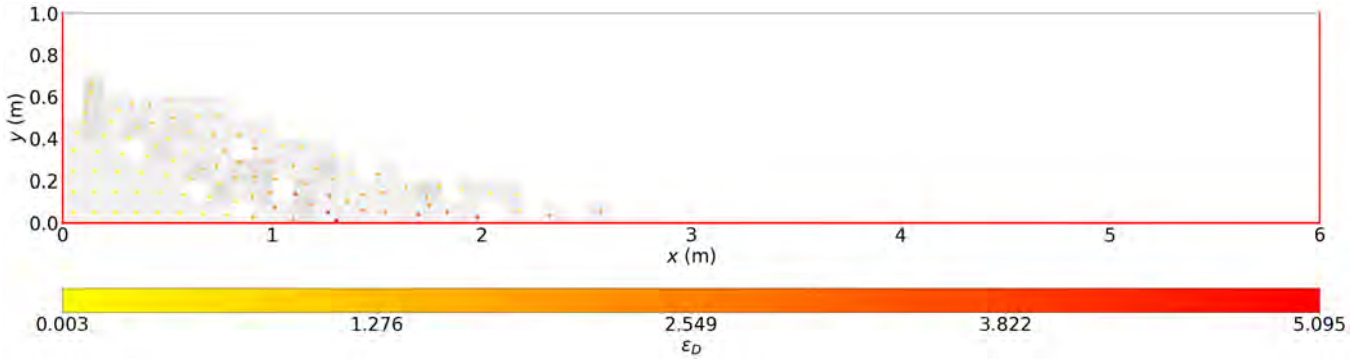

(a) $N_{mppc} = 1$ and $l_{cell} = 10$ cm

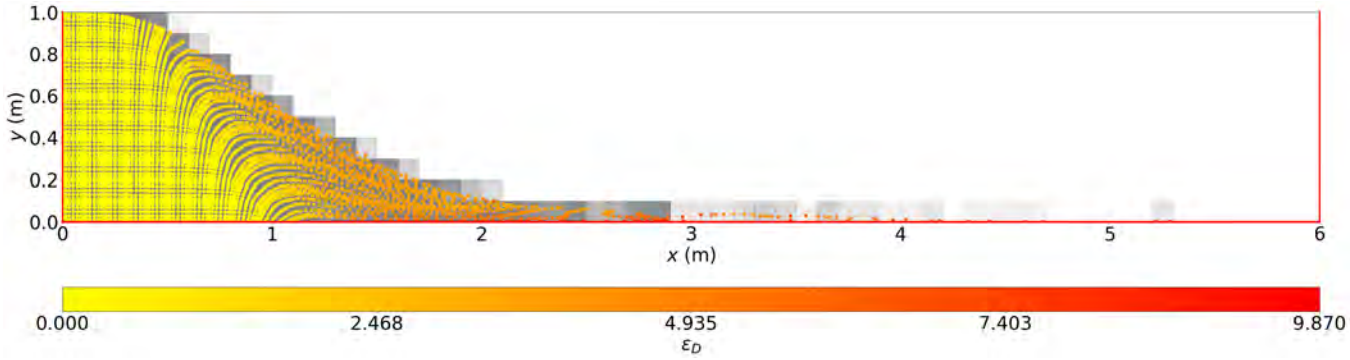

(b) $N_{mppc} = 49$ and $l_{cell} = 10$ cm

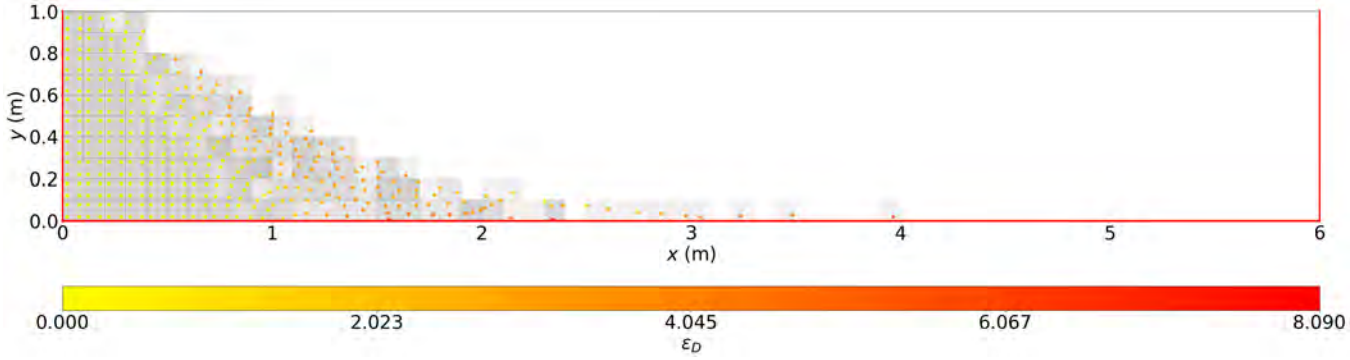

(c) $N_{mppc} = 4$ and $l_{cell} = 10$ cm

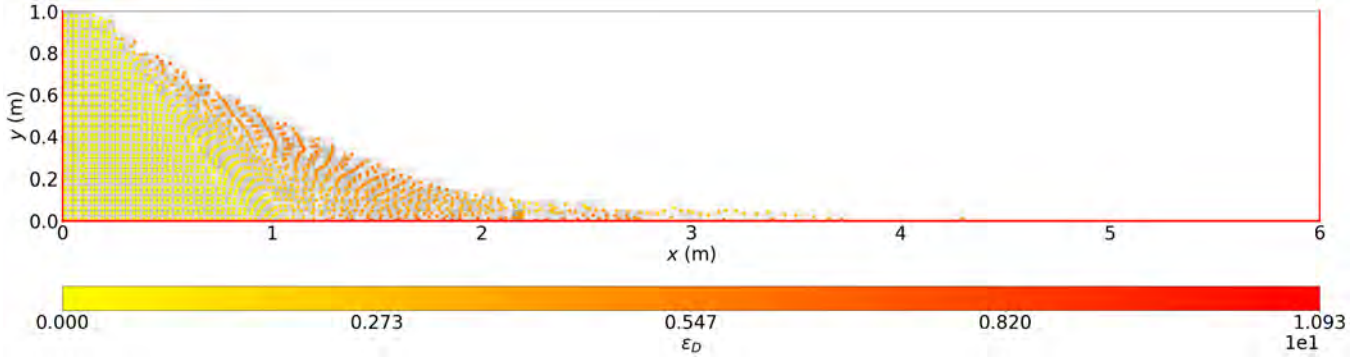

(d) $N_{mppc} = 4$ and $l_{cell} = 5$ cm

FIGURE 5.8. – Deviatoric strain after collapse for different spatial discretization parameters (series S2 and S3)

5.3.3. Influence of the velocity update scheme

As demonstrated in section 3.5, the strategy used to update the material points velocities and positions affects the dissipative properties of the MPM. As a consequence, it has a great impact on the dynamics involved in the collapse of the column. A series of simulations is performed in order to ascertain the validity of our observations in section 3.5, which concluded that the FLIP velocity update strategy leads to more realistic results. In this series, denoted S4, 4 different velocity update schemes are tested with 4 values of AR. Table 5.6 presents the parameters used in this series. Note that because the FLIP velocity update strategy is more sensitive to instabilities, the time step is set 4 times lower than with the three other strategies.

Settling

Figure 5.9 shows the evolution of E_k during the settling, which is dampened differently depending on the velocity update scheme. Two types of behaviours are observed: both FLIP-based strategies oscillates several times before stabilization, and both PIC-based strategies reach a stable state in an aperiodic fashion. When using FLIP-based strategies, E_k oscillates at different frequencies depending on AR, which is expected since the material's properties are the same for all values of AR. Indeed, the velocity wave goes through the column at the same speed no matter the columns geometry while the height of the column increases proportionally with AR, a pseudo period is thus longer for high values of AR.

The final vertical stress obtained with PIC-based strategies differs significantly from the one expected theoretically, as shown on figure 5.10. Indeed, PIC and APIC give a value of σ_{yy} at the bottom of the column approximately 7% lower and 23% higher, respectively.Such a difference was also observed for lower aspect ratios, it is thus probably related to the observations made on E_k. The value of σ_{yy} obtained for FLIP-based strategies is much more consistent with the one expected, even if it is slightly dispersed for FLIP at the bottom of the column. This might be due to a small instability that seems to arise only starting at a certain value of σ_{yy}: this inaccuracy is not observed for lower AR, as seen for instance figure on 5.5.

Collapse

The results of the collapse are presented in figure 5.11, where the last positions of the material points are plotted, and figure 5.12, where E_k, E_{mech}, and L_x are shown. Note that the collapse was considerably faster with the FLIP strategy, whereas the simulation had to continue until a higher simulated time for PIC, APIC and NFLIP0.9 (8 times higher). Even then, the column has not fully collapsed for PIC and NFLIP0.9, and it is still not stable for

l_{cell}	N_{mppc}	Δt^{MPM}	a_τ	AR	Velocity update
10 cm	4	$1.46 \cdot 10^{-6}$ s	$1.25 \cdot 10^{-3}$	0.6, 1, 2.4 and 3	FLIP
		$5.83 \cdot 10^{-6}$ s	$5 \cdot 10^{-3}$		PIC
					APIC
					NFLIP0.9

TABLE 5.6. – Parameters used to investigate the influence of the velocity update scheme (series S4)

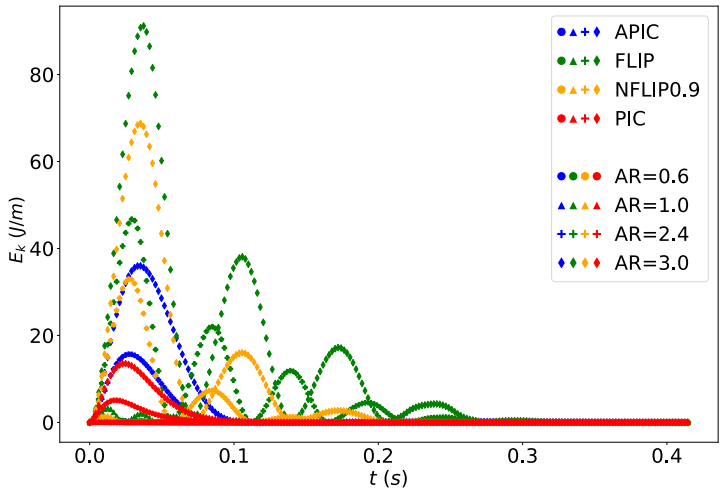

FIGURE 5.9. – Kinetic energy during the settling step for different velocity update schemes and AR (series S4)

APIC. Figure 5.12 (a) shows that the collapse is specially slow for the PIC strategy whose E_k is the lowest and decreases at the slowest rate. This can also be observed in figure 5.11 (b) where the shape of the column is still almost the initial one, meaning that the collapse has not yet really begun. The column simulated with NFLIP0.9 is further advanced in its collapse (see figure 5.11 (c)), but it still has not reached a stable state (see figure 5.12 (a)). One can guess that this significantly slow rate is brought by the 10% of PIC in the NFLIP0.9 velocity computation. Surprisingly, the APIC strategy does not suffer that much from its PIC origin: it can be observed on figure 5.12 (a) that the material points initially reach about the same velocities than NFLIP0.9, but they then decrease at a slower rate. However, the collapse is still too slow for our simulation to capture the fully collapsed column. Still, the final shape of the column given in figure 5.11 (d) seems unrealistic because of its flat top. One should also keep in mind that the value of σ_{yy} obtained during the settling was not accurate, giving less chances for the column to collapse in a natural way.

A common observation to all velocity update strategies is that the collapse speed is higher for higher AR. Indeed, as the column's height increases with AR, the total gravitational energy to be converted into kinetic energy also increases. The APIC strategy behaves differently for $AR = 3$ and for $AR \leq 2.4$: $\log(E_k)$ decreases at a constant rate and L_x increases linearly for low values of AR, but for $AR = 3$ the evolution of E_k is significantly noisier and L_x seems to reach a plateau. Again, this might be caused by the wrong value of σ_{yy} obtained at the end of the settling, which is likely to have a more important impact for $AR = 3$ since σ_{yy} is higher.

As for the evolution of the mechanical energy during the collapse, all velocity update schemes dissipate energy at a different rate. The dissipation rates observed are consistent with the collapse rates:

$$\left|\frac{dE_{mech}}{dt}\right|^{PIC} < \left|\frac{dE_{mech}}{dt}\right|^{NFLIP0.9} < \left|\frac{dE_{mech}}{dt}\right|^{APIC} < \left|\frac{dE_{mech}}{dt}\right|^{FLIP} \tag{5.16}$$

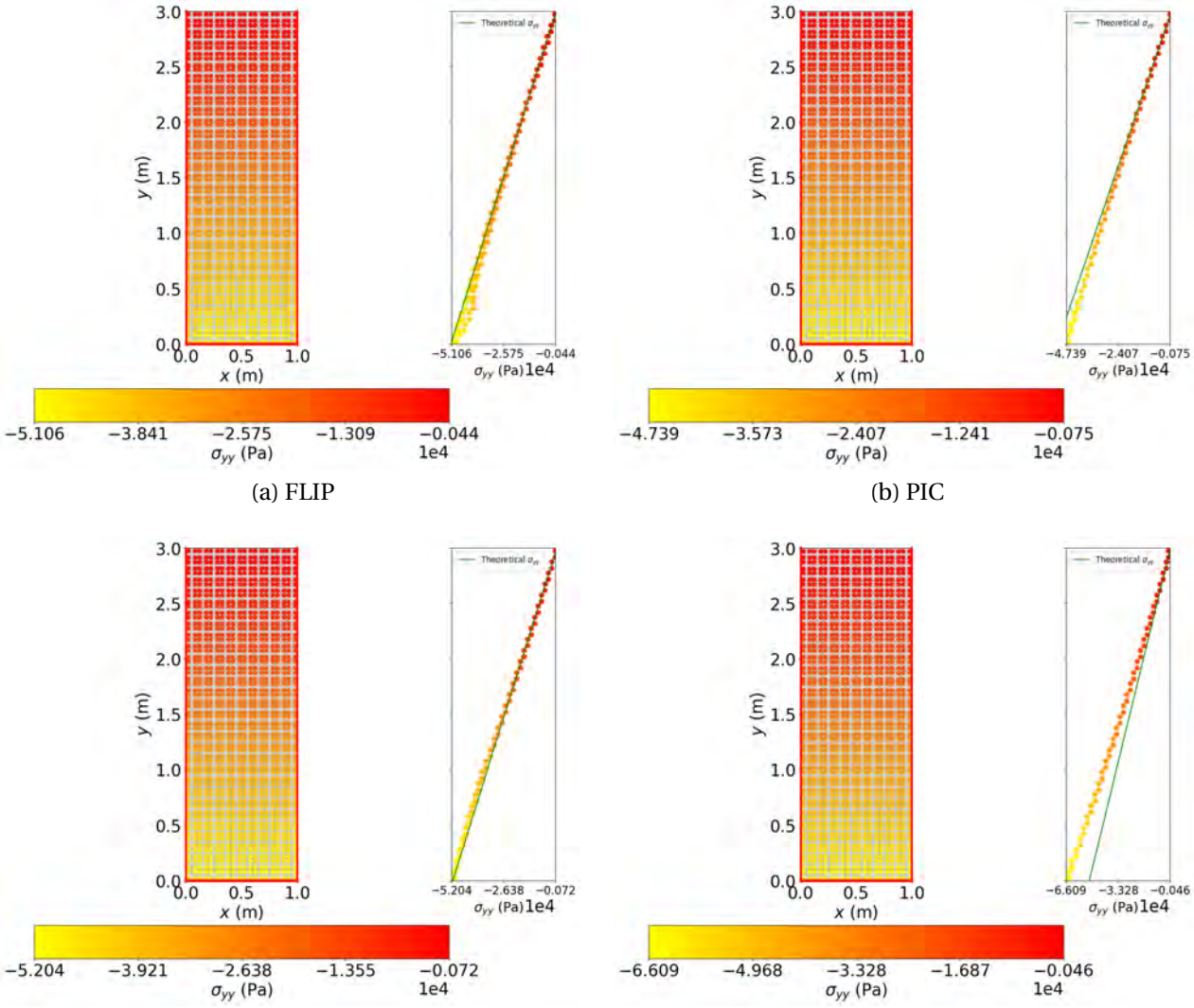

(a) FLIP

(b) PIC

(c) NFLIP0.9

(d) APIC

FIGURE 5.10. – σ_{yy} during the settling step for different velocity update schemes and $AR = 3$ (series S4)

Indeed, the plasticity of the Mohr-Coulomb model as well as the friction imposed on the floor are more and more solicited as the column collapses, E_{mech} thus necessarily depends on the advancement of the collapse. Note however that the results for APIC with $AR = 3$ once again display an uncommon evolution for E_{mech}. More precisely, it is the only simulation for which E_{mech} increases at some point, right before drastically decreasing. Since this series of simulations does not reach the fully collapsed state for most velocity update strategies, it cannot be used to characterize the dissipative nature of the velocity update strategy. Nonetheless, results are clear about the dynamics of the collapse: the velocities are unnaturally dampened with PIC, NFLIP0.9 and APIC. The results for FLIP are comparable to the ones from literature, as will be presented in the forthcoming section about the MPMxDEM results.

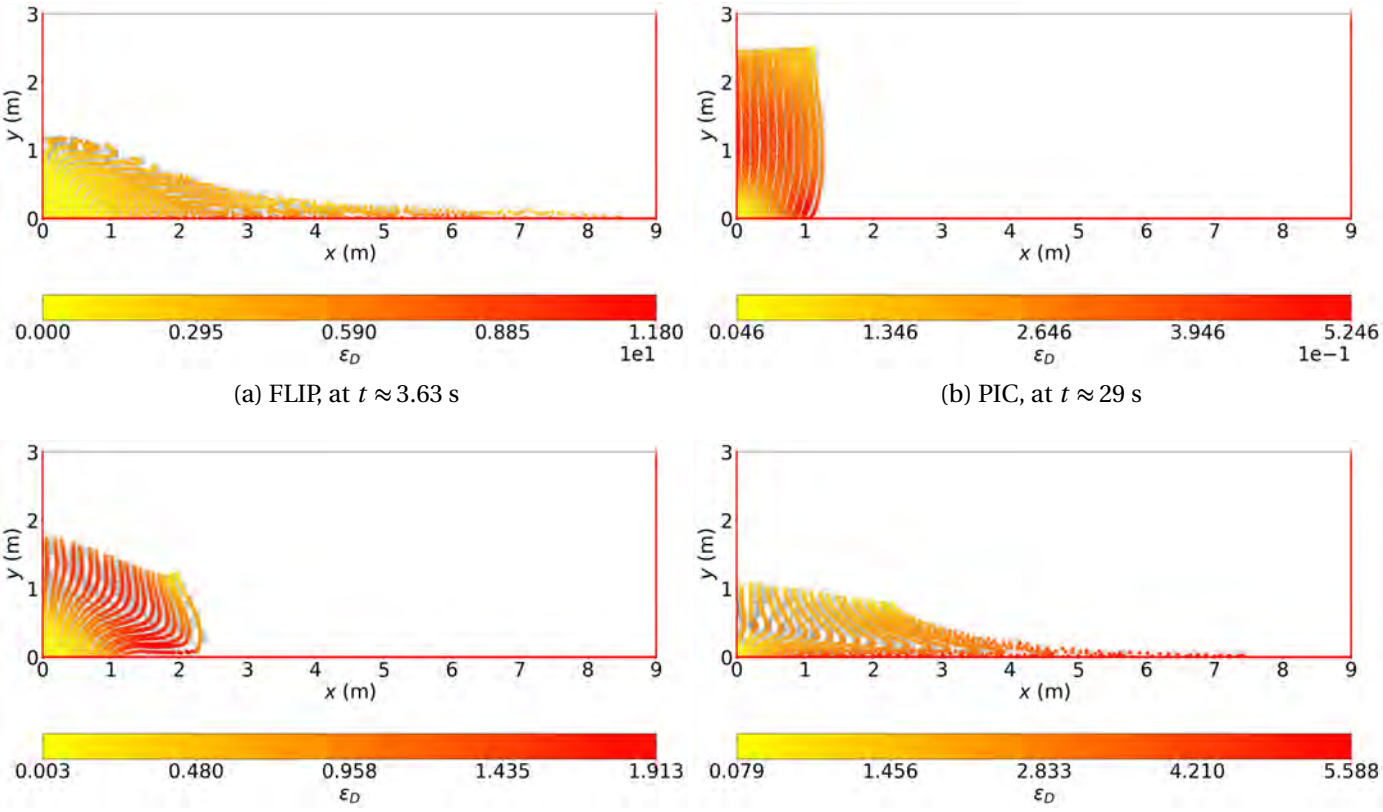

(a) FLIP, at $t \approx 3.63$ s

(b) PIC, at $t \approx 29$ s

(c) NFLIP0.9, at $t \approx 29$ s

(d) APIC, at $t \approx 29$ s

FIGURE 5.11. – Deviatoric strain at the last collapse step for different velocity update schemes and $AR = 3$ (series S4)

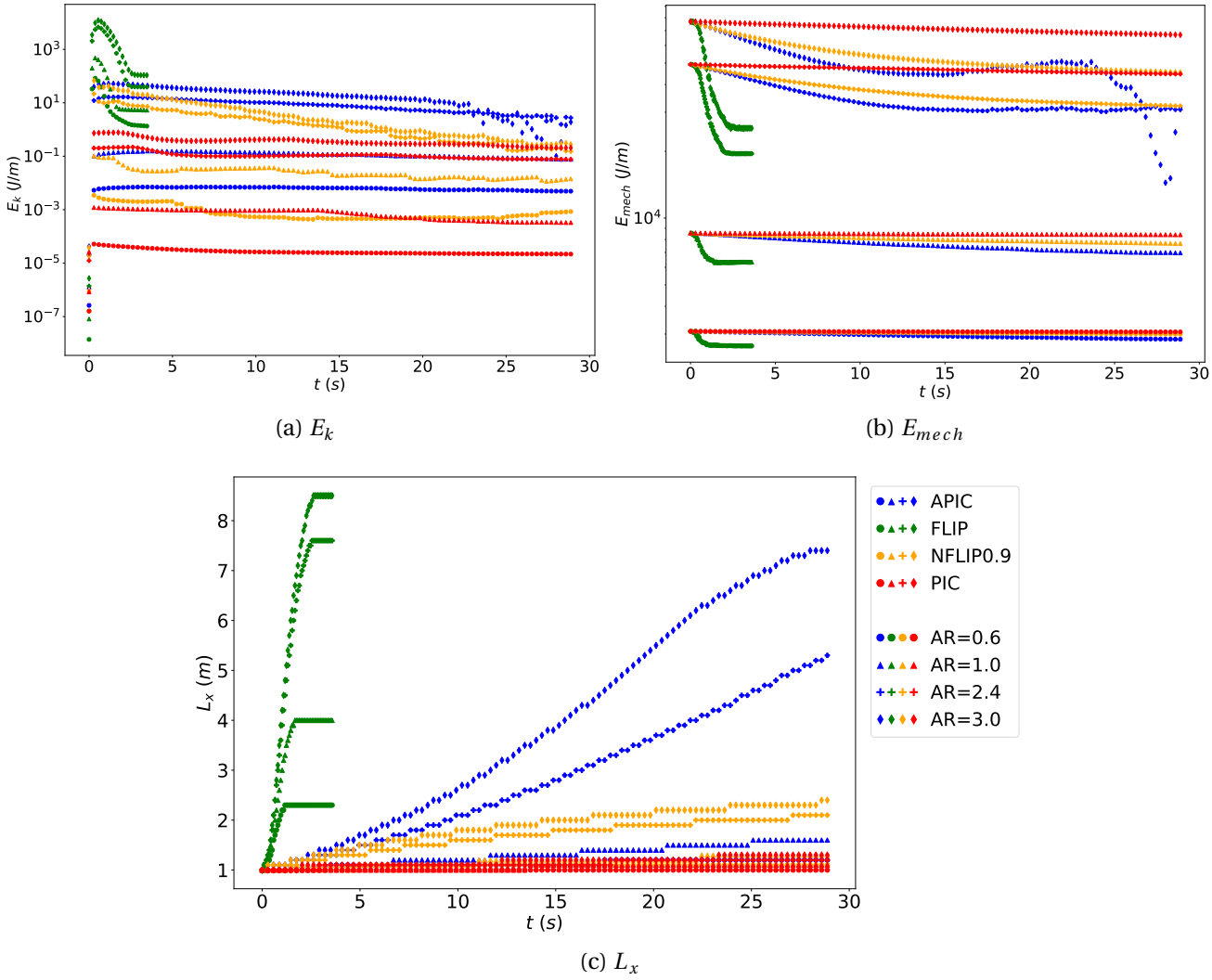

(a) E_k

(b) E_{mech}

(c) L_x

FIGURE 5.12. – Energies and right edge position during collapse for different velocity update schemes and AR (series S4)

5.4. MPMxDEM results

A unique MPMxDEM simulation was performed in this study, using the discretization parameters and velocity update strategies determined in the previous sections, giving a great compromise between accuracy and computational time cost. Table 5.7 summarizes these parameters.

Settling

Figures 5.13 (a), (b), and (c) show the mean values of the vertical stress σ_{yy}, the average coordination number Z_c, and the void ratio e at the end of the settling step. The stress gradient is in accordance with the theoretical expectations as well as with the pure MPM simulations. Naturally, this gradient echos on e which also decreases in a linear fashion from top to bottom, but with a very slight variation of approximately 0.1%. It is worth noticing that the RVEs on top kept their initial e, certainly because they were not solicited enough for their density to change. As a contrast, the linear evolution of σ_{yy} is not reflected on Z_c, which is quite dispersed for the RVEs in the top mesh cells. Indeed, from $y = 0.9$ m and $y = 1$ m, Z_c decreases horizontally by about 10%. This horizontal dispersion can also be observed in the layer below, down to $y = 0.8$ m, but Z_c then reaches a value close to the one it has for the RVEs at the bottom of the column. Over the whole column Z_c varies of approximately 16%, but as opposed to e, Z_c decreased for all RVEs with respect to their initial state (for which $Z_c \approx 5.85$). In particular, the RVEs on top are the ones where Z_c changed the most, of approximately 18%. The results presented in figure 2.33 (chapter 2) are consistent with these observations: when the stress state of a granular assembly is low, the value of Z_c is less correlated to its stress state. These variations must then be caused by the randomness with which grains get rearranged during the deformations waves the column is subjected to, see figure 5.13 (d). These results thus show that the MPMxDEM coupling is able to capture the chaotic nature of granular materials at the large scale.

Comparing the evolution of the total kinetic energy on figure 5.13 (d) with the ones from pure MPM simulations, one can notice some quantitative differences: the column is stabilized approximately two times faster in MPMxDEM, and the maximum kinetic energy is 80% lower. This difference can be explained by the purely elastic behaviour of the Mohr-Coulomb model for such low solicitations, for which the DEM model already begins to accumulate plastic deformations because of rearrangements between grains.

l_{cell}	N_{mppc}	Δt^{MPM}	a_τ	AR	Velocity update
10 cm	4	$1.46 \cdot 10^{-6}$ s	$1.25 \cdot 10^{-3}$	1	FLIP

TABLE 5.7. – Parameters used to perform the MPMxDEM simulation

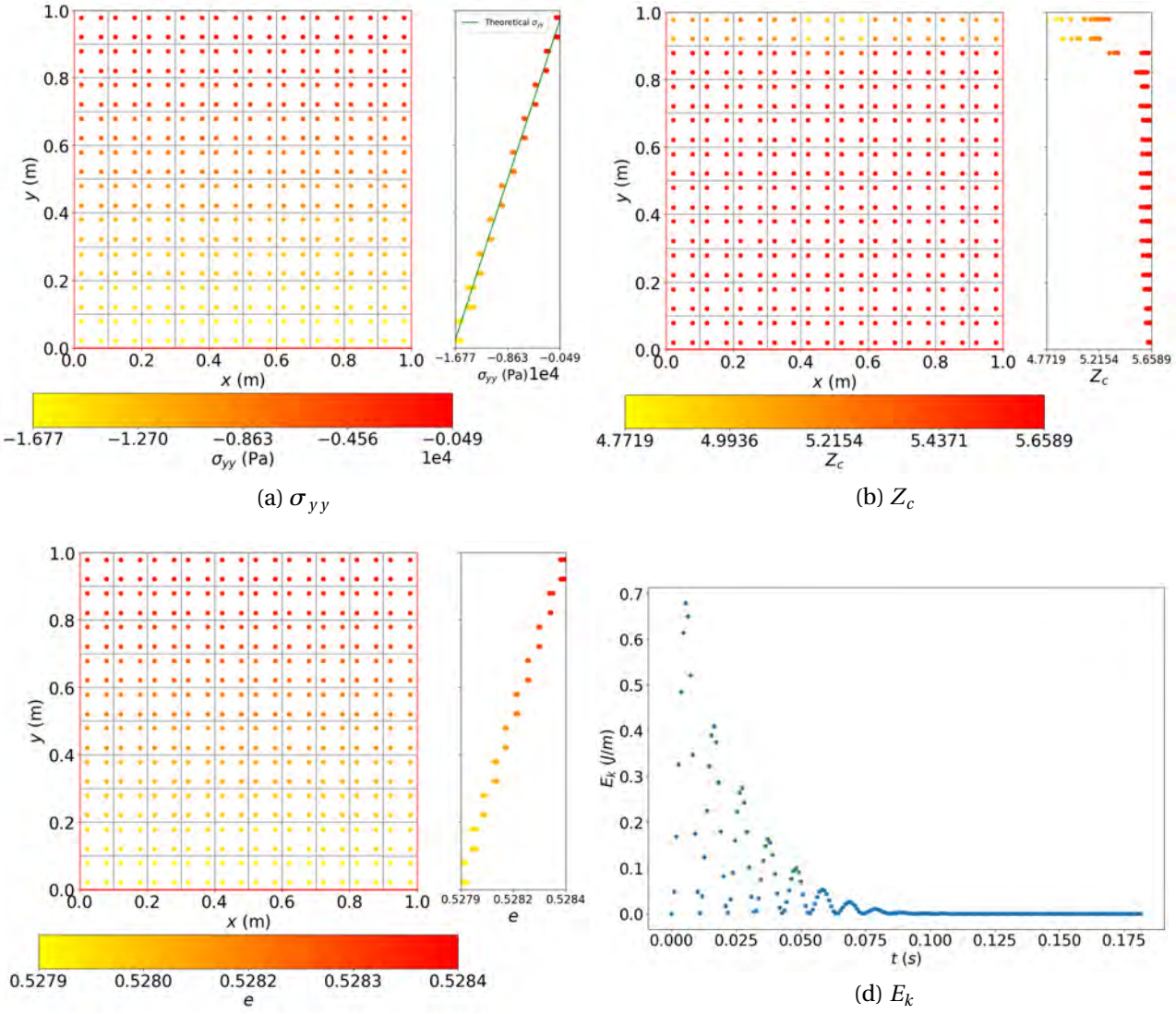

(a) σ_{yy}

(b) Z_c

(c) e

(d) E_k

FIGURE 5.13. – Settling step for the MPMxDEM simulation

Collapse

Unlike during pure MPM simulations, E_k has two peaks (see figure 5.14): the first peak, at $E_k \approx 550$ J for $t \approx 0.5$ s, corresponds to the pure MPM peak, but E_k then sharply decreases before increasing again until it reaches a second peak at $E_k \approx 400$ J for $t \approx 0.8$ s. Here again, the purely elastic behaviour the Mohr-Coulomb model assumes for many material points explains this difference in the collapse rate.

Figure 5.15 shows ϵ_D, Z_c, P and e when the column has completely collapsed, and the velocities of all material points during the collapse are given in figure 5.16. The repartition of ϵ_D throughout the column is similar to the one in pure MPM simulations, although it reaches values approximately 6% lower. This can be explained by the higher spreading length obtained with pure MPM, specially since the most sheared RVEs are the ones that have been spread on the right of the column.

Both Z_c and P present the same pattern: in the cells where the material points have not significantly moved, the material point at the bottom right is where Z_c and P are the highest. Other material points have in fact become a granular cloud, for which the mean stress is equal to 0 because there is no contact, prohibiting the use of the Love-Weber formula (see equation 4.7). This observation is intriguing because the state of these RVEs should not be affected as strongly by the collapse. This spurious lost of contacts can only be explained by the propagation of a velocity wave which periodically dilates these RVEs. Indeed, since the equation of motion is solved on grid points after transporting the velocities of the material points, any disturbance is automatically propagated to the neighboring mesh cells. RVEs in the bottom left part of the column are then slightly dilated horizontally but, since the weight of the column above them decreased, they never get sufficiently constrained to recover their contacts.

This inconsistency between the deformations of a RVE and its location in the column is also causing non-physical behaviours for the material points subject to important displacements. The example of the RVE n°386, initially located on the right edge of the column (see figure 5.17), is a good illustration of this issue. From $t \approx 1.66$ s, when it finds itself alone in its mesh cell with the neighboring cells being empty, its velocity is abnormally pointing upward because the material point is still in the process of "bouncing" on the ground (see figure 5.16). Even though this phenomena was also observed in pure MPM, this RVE is so much deformed that eventually the usual microscopic characterization parameters take aberrant values. Figure 5.18 emphasized this point with a visualization of the RVE n°386 at different times during the collapse. Indeed, the void ratio in this RVE starts to oscillate at $t \approx 1.7$ s to reach enormous values, up to $e \approx 63$, see figure 5.19. On this figure, one can observe that when the RVE n°386 gets isolated, its void ratio starts to have the same evolution as the height of a bouncing object, which is consistent with figure 5.16. Note however that the simulation stopped before e had a chance to stabilize for this RVE, and the value it tends toward is rather plausible ($e \approx 0.696$). The FLIP velocity update strategy is certainly responsible for this extreme state the RVE n°386 is in: the velocity attributed to the material point is different from the one used to move it (see table 3.1). As a consequence, the strain rate computed in equation 3.36 is not perfectly consistent with the location of the material point. A solution to address this problem could be to use the actual displacement velocity of the material point to compute the stress rate imposed to the RVE in equation 3.36, instead of the velocity attributed to it for the next MPM iteration.

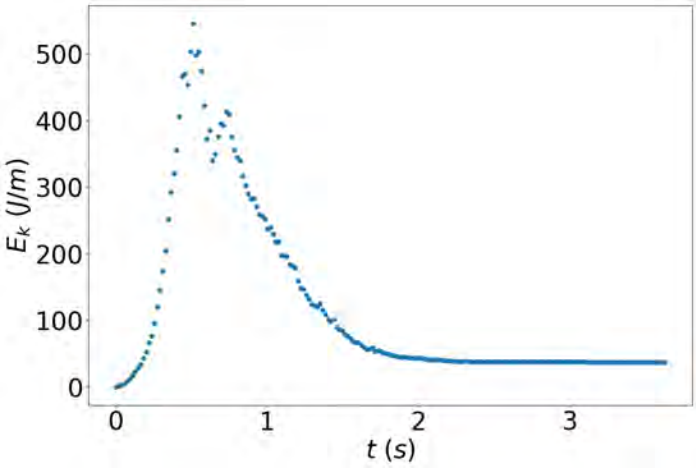

(a) E_k

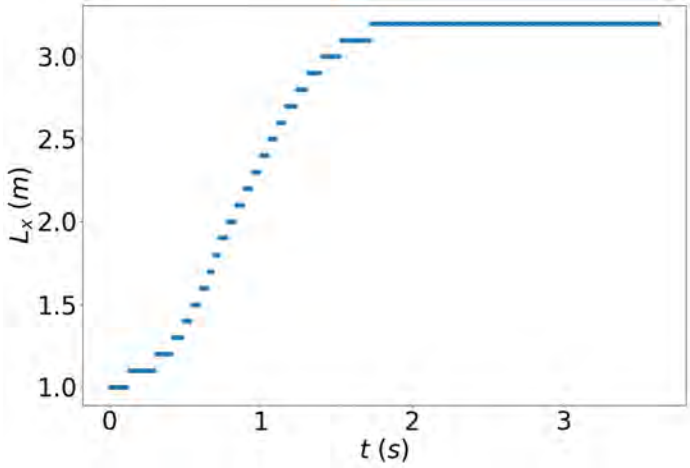

(b) L_x

FIGURE 5.14. – Kinetic energy and right edge position during collapse for the MPMxDEM simulation

Computational aspects

This simulation, containing in total 800,000 discrete elements, ran for approximately 44 days on a server machine equipped with 2 Intel® Xeon® Platinum 8270 CPUs @ 2.70GHz offering a number of 104 CPU cores, and 1.51 TB of RAM. In terms of memory, a simulation of this scale is not significantly expensive, as it requires roughly 48 GB of RAM. As for the computation time, it directly depends on the amount of deformation imposed to all RVEs. Indeed, the latter determines the number of DEM iterations to perform in order to keep the deformation at a specific quasi-static threshold I_n, equal to 10^{-2} for the simulation presented here (see equation 4.1). Figure 5.20 illustrates this dependance by comparing the deformation a RVE should reach at a specific time (red stars) with the maximum deformation it can reach in one DEM iteration (blue dots). One can see that the RVE n°0, located at the bottom left of the column (see figure 5.17), is almost never deformed enough to require more

than 1 DEM iteration per MPM iteration. As a contrast, the previous RVE n°386 often has to perform many DEM iterations in order to reach the goal imposed by the MPM, approximately 10^3 DEM iterations per MPM iteration. Moreover, this RVE n°386 being a cloud during a substantial part of the simulation, the maximum strain rate usable within the quasi-static limits is set to the lowest value (see equation 4.3). The influence of P on the strain rate can be observed on figure 5.20: the RVE n°0 always reaches higher deformations during 1 DEM iteration because it is significantly more constrained than RVE n°386 (as a reminder, both use the same Δt^{DEM}).

On this same figure, the deformation achievable per DEM iteration is also plotted for an inertial number of $I_n = 10^{-3}$ (orange dots) and for the strain rate imposed by the MPM (green diamonds), which would correspond to dropping out the assumption of quasi-staticity at the microscopic scale. One can see that if $I_n = 10^{-3}$ was used instead of $I_n = 10^{-2}$, the computation would have been considerably longer since RVEs would have had to perform 10 times as many DEM iterations. Although, this is not always the case: RVEs like the n°0 have at the very beginning and at the end of the simulation a deformation goal so low that even $I_n = 10^{-3}$ is high enough to achieve it in 1 DEM iteration. Nonetheless, using the MPM strain rate would have been even slower for most of the computation, specially when deformations are low. An exception can somewhat be observed for our RVE n°386 between $t \approx 1$ s and $t \approx 3$ s. Indeed, when P is low and $\Delta\epsilon^{max}$ high, the strain rate obtained for $I_n = 10^{-2}$ is sometimes slightly lower than the MPM strain rate. The $I_n = 10^{-2}$ assumption at the microscopic scale thus does not significantly change the strain rate for extensively deformed RVEs, and it is considerably cheaper to impose it for other RVEs.

The computation speed S_c (in MPM iterations per second) is plotted on figure 5.21 alongside the average number of DEM iterations the RVEs performed between two data points $\overline{\Delta N_{it}^{DEM}}$, which corresponds to 12,500 MPM iterations. The effect the quantity of deformation has on S_c is particularly noticeable for $t \leq 0.5$ s, where the number of DEM iterations to be performed increases from 0 to approximately 160 DEM iterations per MPM iterations, and S_c dwindles from about 5.5 iter/s to roughly 0.25 iter/s. Speed of this magnitude are observed until $t \approx 2$ s, which corresponds to the time at which the velocities become negligible compared to their maximum, see figure 5.14 (a). Figure 5.22 shows that E_k is closely related to $\overline{\Delta N_{it}^{DEM}}$, which could be intuitively guessed by comparing the DEM and MPM computational time costs. However, two distinct trends can be observed: one for $t \leq 0.5$ s, as E_k increases because the column collapses, and one for $t > 0.5$ s, as E_k decreases when the column stabilizes.

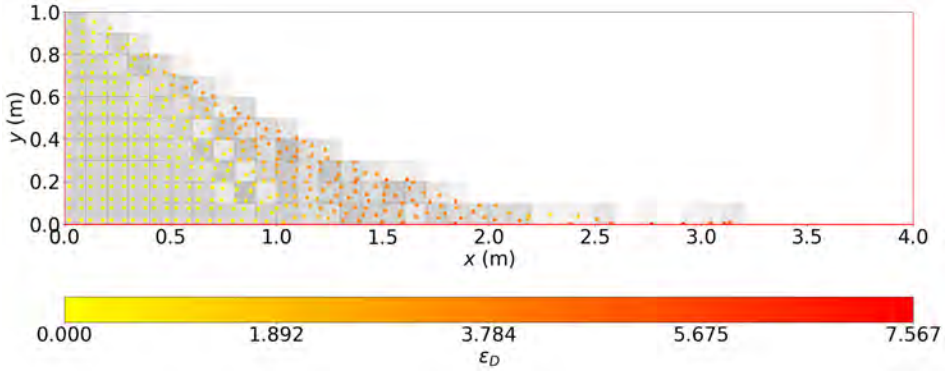

(a) ϵ_D

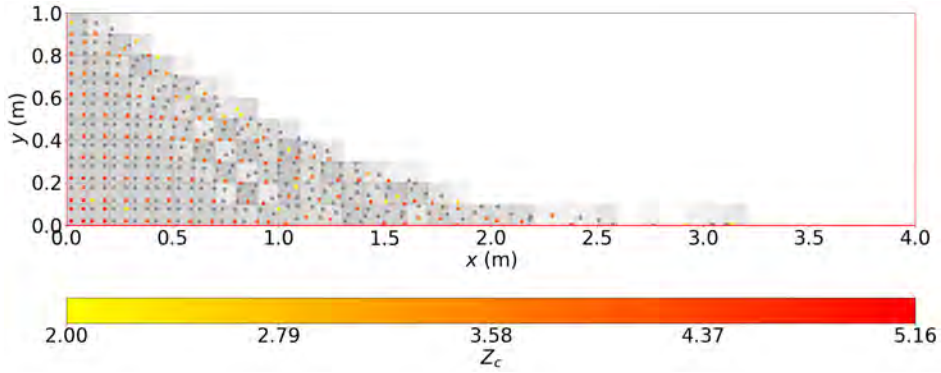

(b) Z_c, the grey color indicates that there is no contact

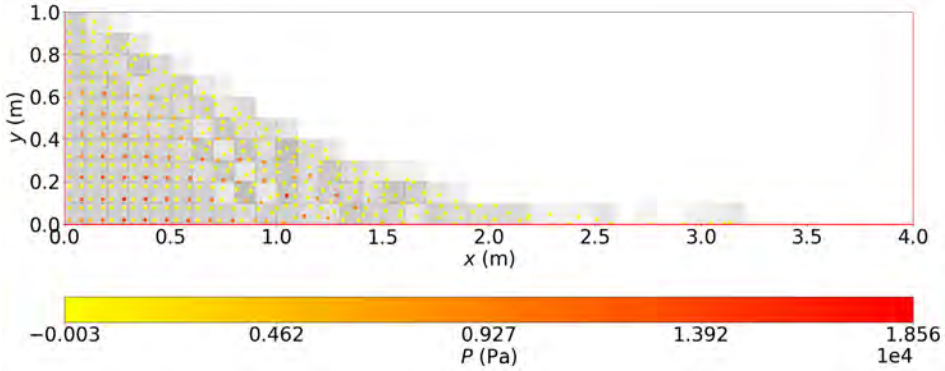

(c) P

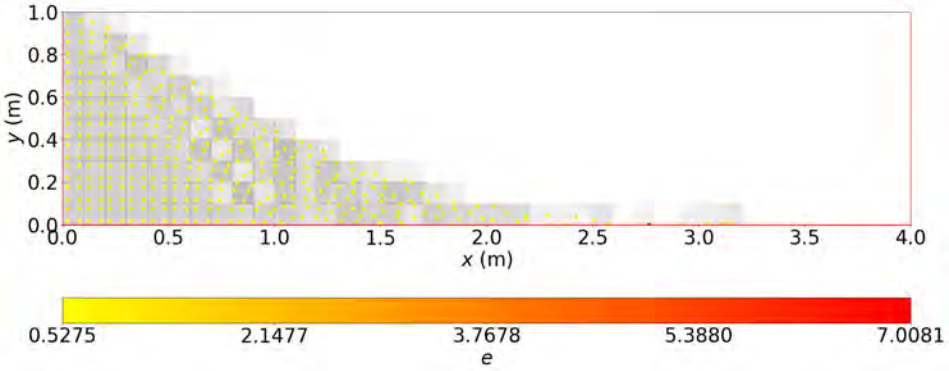

(d) e

FIGURE 5.15. – Final measurement on the collapsed column for the MPMxDEM simulation

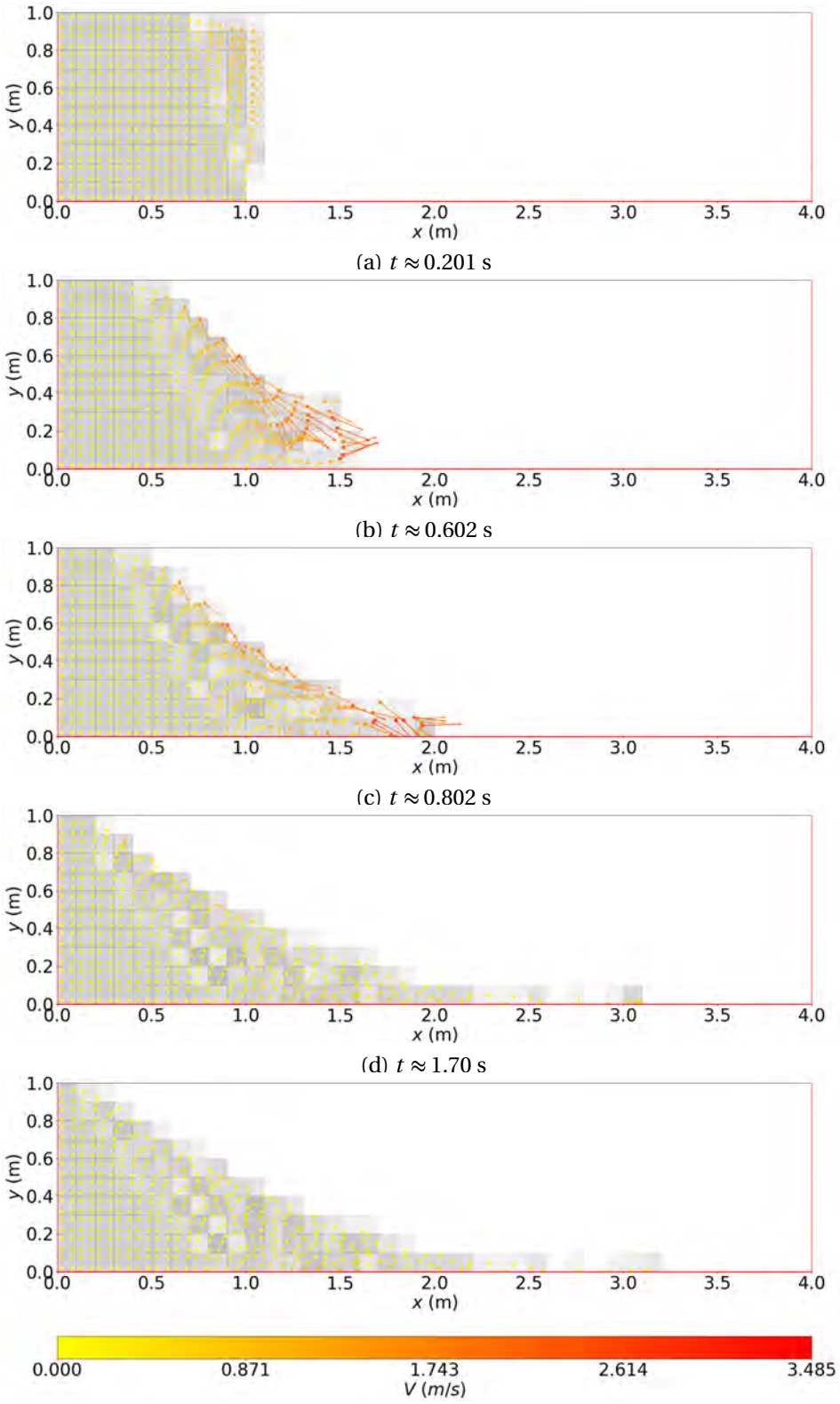

(a) $t \approx 0.201$ s

(b) $t \approx 0.602$ s

(c) $t \approx 0.802$ s

(d) $t \approx 1.70$ s

(e) $t \approx 3.63$ s

FIGURE 5.16. – Material points velocities during the collapse for the MPMxDEM simulation

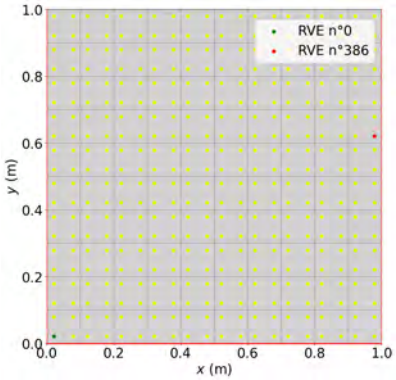

(a) Inital positions

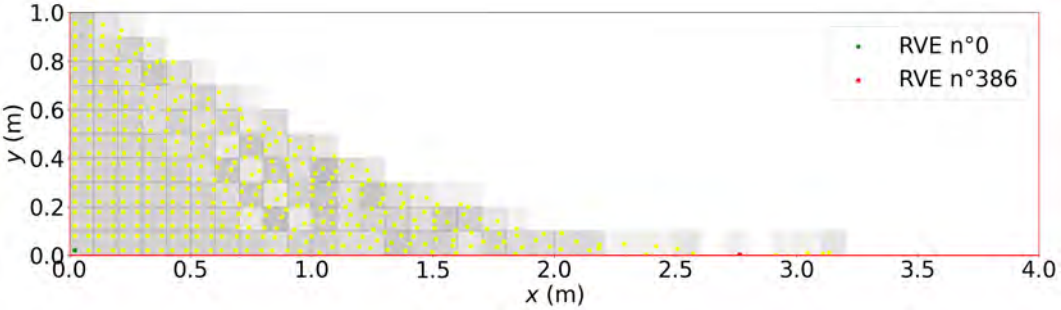

(b) Final positions

FIGURE 5.17. – Locations of RVEs n°0 and n°386 within the column

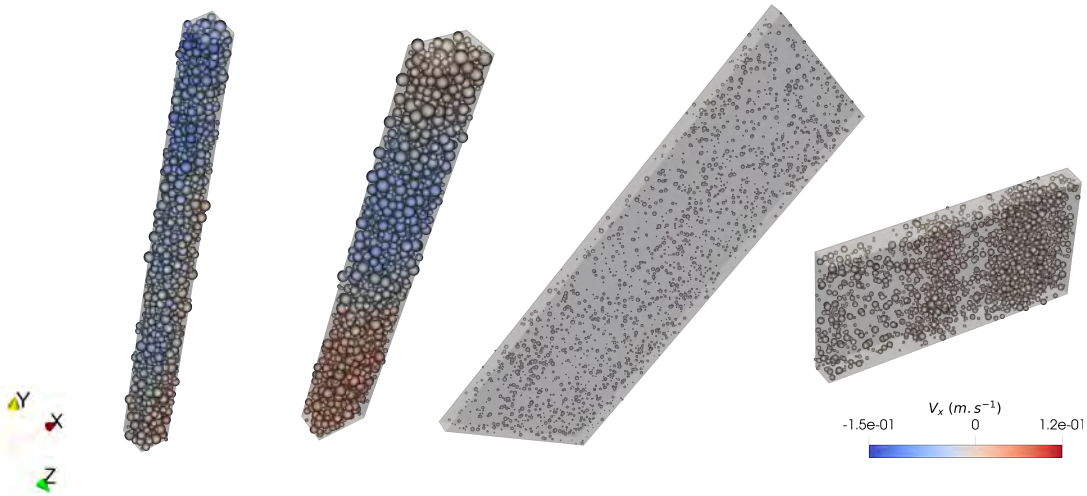

(a) $t = 0$ s (b) $t \approx 0.346$ s (c) $t \approx 2.41$ s (d) $t \approx 3.63$ s

FIGURE 5.18. – RVE n°386 at different times during the collapse

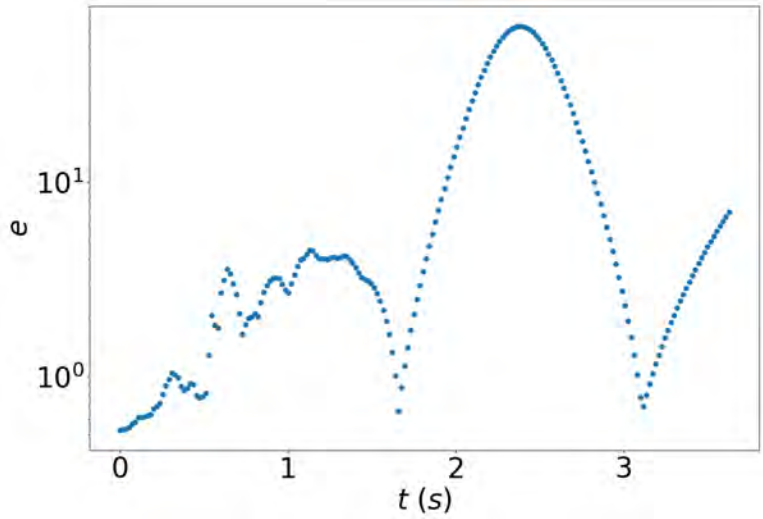

FIGURE 5.19. – Void ratio of the RVE n°386 during the collapse

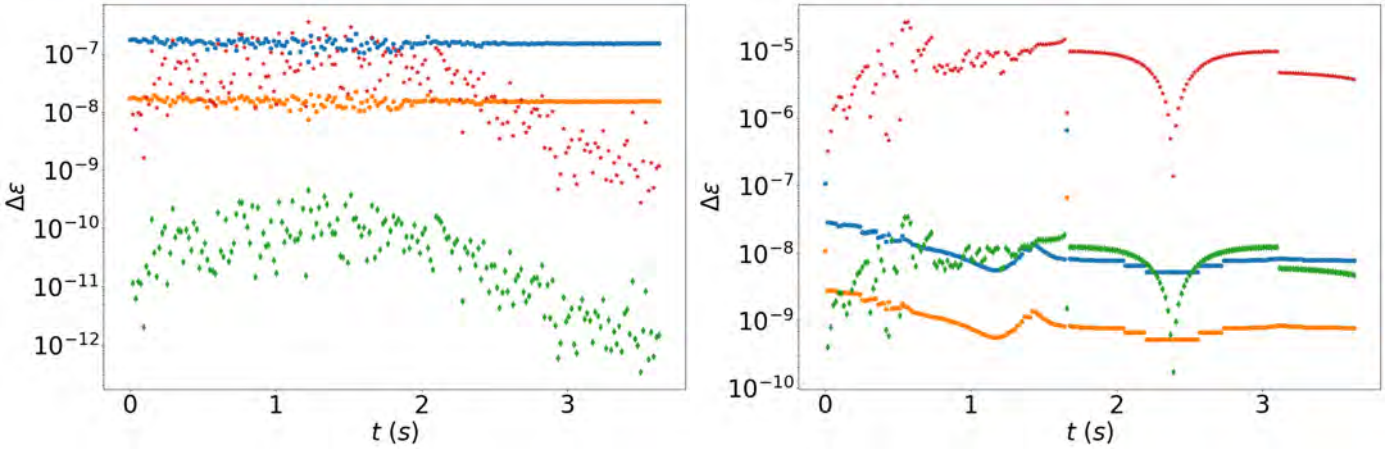

(a) For RVE n°0

(b) For RVE n°386

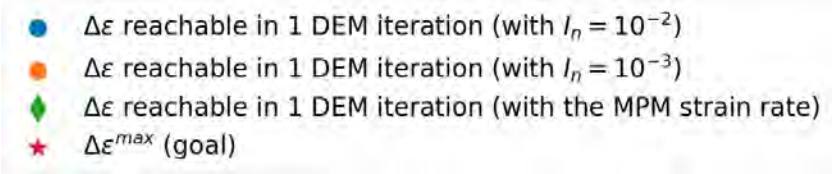

FIGURE 5.20. – Deformation reachable with 1 DEM step for different conditions, compared to the deformation goal

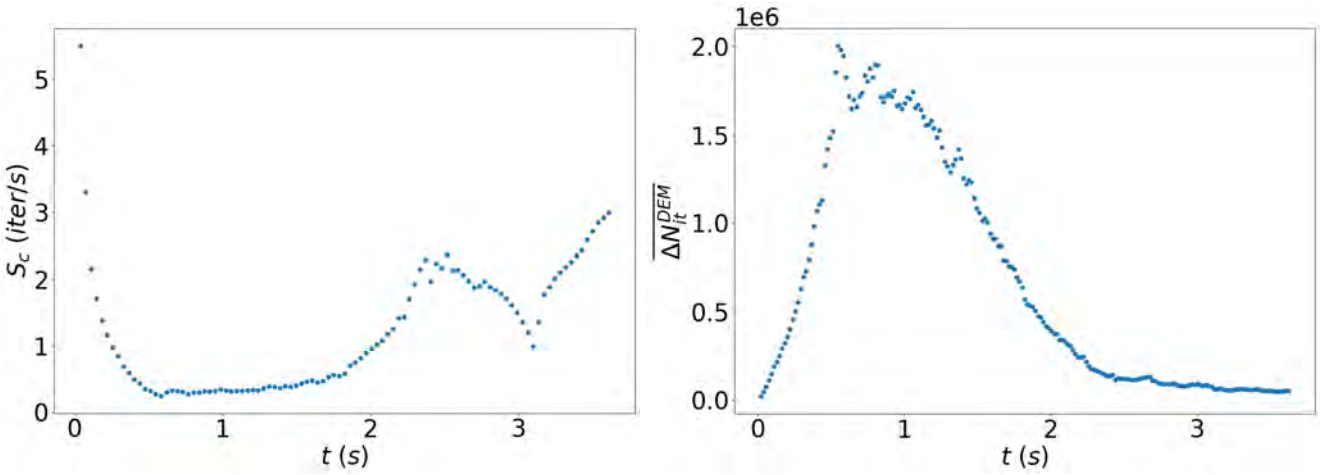

(a) Computation speed S_c

(b) Number of DEM iterations between each data point averaged over all material points $\overline{\Delta N_{it}^{DEM}}$

FIGURE 5.21. – Computation speed and number of DEM iterations performed during the collapse

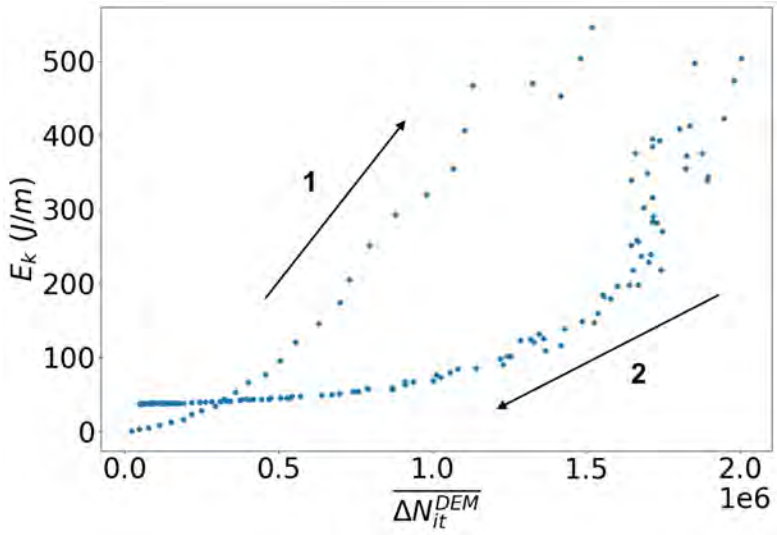

FIGURE 5.22. – E_k with respect to $\overline{\Delta N_{it}^{DEM}}$ during collapse

5.5. Comparison with results from the literature

The spreading lengths obtained with FLIP in pure MPM (series S4) are plotted alongside the one obtained in MPMxDEM and compared to results from the literature in figure 5.23. The latter include:

— experimental results conducted on glass beads in [Lajeunesse, Monnier, and Homsy 2005];
— numerical results performed in [Crosta, Imposimato, and Roddeman 2009] with a FEM-based hybrid Eulerian-Lagrangian method, in conjunction with the Mohr-Coulomb model;
— numerical results obtained in [Girolami, Hergault, Vinay, et al. 2012] using a 3D DEM model, with a viscous elasto-plastic contact law;
— numerical results from [Xiong, Yin, Nicot, et al. 2021], obtained with the SPH method and the micromechanical 3D-H model (denoted in this thesis SPHx3D-H).

A first observation is that our columns take approximately 20% more time to reach their final length, both with pure MPM and MPMxDEM. The MPM might be to blame for this delay, considering that its other formulations (i.e. different velocity update strategies) lead to even longer spreading times, as previously shown in figure 5.12 (c). As a matter of fact, this lower collapse rate might originate from the lack of conservation of the angular momentum that FLIP necessarily suffers from, according to the creators of the APIC strategy [Jiang, Schroeder, Selle, et al. 2015]. This paper states that even though FLIP effectively eliminates most of the energy dissipation observed with PIC, it cannot fully conserve the angular momentum. The different collapse rates observed in figure 5.12 are consistent with the conclusions of [Jiang, Schroeder, Selle, et al. 2015], where the APIC strategy is found to conserve the energy better than PIC but not as much as FLIP. The APIC-inspired ASFLIP strategy, mentioned in [Fei, Guo, Wu, et al. 2021], should accurately conserve the angular momentum and thus may be a solution to eliminate this artificial damping observed with the MPM.

Figure 5.23 also shows that the final spreading length is overestimated in MPM, with respect to collapses performed with other numerical models for the same AR. For instance, with $AR = 1$, the pure MPM simulation gives a final length approximately 55% higher than the results presented in [Crosta, Imposimato, and Roddeman 2009], while the results from [Xiong, Yin, Nicot, et al. 2021] are only approximately 23% higher. The final length observed with the MPMxDEM model are closer to the results from [Crosta, Imposimato, and Roddeman 2009], although it is still 38% higher, and 19% higher than the results from [Xiong, Yin, Nicot, et al. 2021]. The relatively similar final lengths obtained with the MPMxDEM model and the SPHx3D-H model is quite comforting, since both are based on a description of the material at the grain scale. Moreover, these SPHx3D-H results are in great agreement with the pure DEM results from [Girolami, Hergault, Vinay, et al. 2012] for both $AR = 1$ and $AR = 3$, even though pure DEM columns seems to stabilize faster and thus lead to a slightly lower final $\widetilde{L}$ (at most 7.5%). However, during the collapse, both the SPHx3D-H and pure DEM columns are wider than the MPMxDEM ones, until $\widetilde{t} \approx 4$. In fact, the widths of the former are closer to the pure MPM column until $\widetilde{t} \approx 2.5$. It is worth noting that our simulation uses the same friction coefficient on the floor than [Xiong, Yin, Nicot, et al. 2021], which is $\mu = 0.3$. Here again, the non-physical dissipation present in MPM simulations might be the cause of this difference.

According to the experimental results from [Lajeunesse, Monnier, and Homsy 2005], the

real collapsing columns are clearly thinner than the pure MPM ones, more precisely 41% thinner for $AR = 3$. However, for $AR = 0.6$, this difference is restricted to approximately 13%, and the experimental $\widetilde{L}$ is higher than the pure MPM one for the most part of the collapse. Note that our measurement of $\widetilde{L}$ includes all material points in the initial column, even if they get separated from the rest of the column (see for instance figure 5.16 (d) at $x = 2.6$ m). This choice could possibly lead to some over-estimation compared to the experiments where isolated grains are not considered.

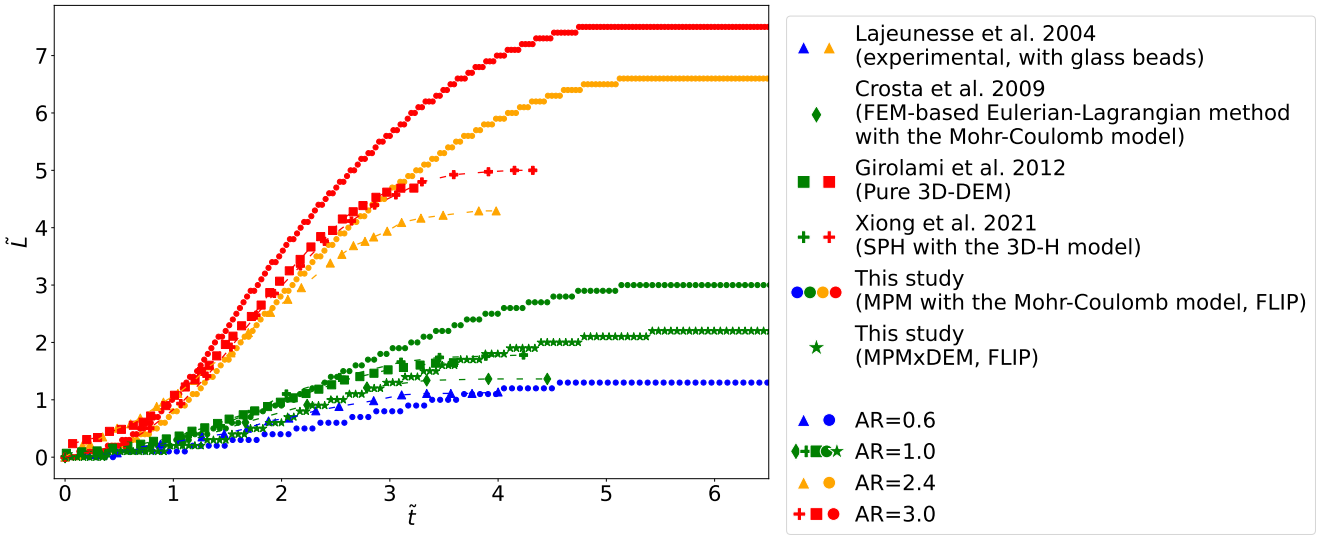

FIGURE 5.23. – Spreading length of the collapsing column compared to literature

5.6. Conclusion

This chapter presented the performances of the MPMxDEM coupling in the case of a large scale granular column collapse, after pointing out the significant importance of some MPM parameters (i.e. the number of material point per mesh cell and the motion integration strategy). The latter should be carefully selected in order to limit the spurious energy dissipation observed in MPM, and tend toward a result independent of the spatial discretization. Overall, the use of DEM as a descriptor for the material's behaviour is quite promising thanks to its efficient representation of the material and the microscopic insights it makes available. Such an approach would certainly benefit the study of geotechnical structures subject to large deformations, although it still requires a considerable amount of computing ressources.

Conclusion

This study has numerically investigated granular materials' behaviour using two numerical methods, namely DEM and MPM. Both are described and used in different configurations, where DEM's capability to accurately describe granular materials is highlighted. A coupling of both methods is then presented, and shown able to reach large scales thanks to MPM's continuous media assumption, while keeping the DEM precision to determine the material's behaviour.

DEM and MPM separate studies

First, DEM was used to determine the sensibility of the angle of repose formed by a heap of grains with respect to several microscopic parameters for two different geometries. For such a purpose, numerical methods were developed to compute automatically and accurately the angle of repose and the void ratio in complex granular assemblies. The grains convexity has been found to have a substantial impact on the angle of repose: if the grains have some concavities, they are more likely to interlock with each others, leading to a higher angle of repose (14% in this study). The number of grains in the heap was also found to have a significant influence on the angle of repose. Indeed, the latter decreases as the number of particles increases, even for more than 10,000 particles which is usually considered enough to constitute a RVE. On the contrary, the geometry of the heap has a small impact on the final angle of repose: cylindrical heaps give a lower angle of repose than cubical heaps, but only by approximately 3.59% in this study. Therefore the angle of repose is not an accurate description of the material properties and should not be used to characterize the material's behaviour. It also has been shown that the grain's density and inter-particle tangential stiffness have no significant influence on the angle of repose. Its determination can thus be performed by using more convenient values for these parameters, i.e. those giving a higher time step. The material used to investigate the angle of repose was also characterized through a series of triaxial tests, under different confining pressures and for various initial densities. Particles having 0 or 1 contact, the rattlers, are shown to hinder the determination of the state of a granular material and should be considered as void, as suggested in the literature.

Second, the formulation of the MPM as implemented in CB-Geo MPM was recalled, presenting different formulation choices, namely the stress and velocity update strategies. The conservative nature of the MPM was investigated energy-wise, for different formulation choices. The USL stress update scheme was found to be more dissipative than the USF scheme, which is in agreement with the literature. As for the velocity update strategy, the FLIP scheme was found able to conserve the energy where other PIC-based schemes were significantly dissipative. As for the NFLIP strategy, it was found to increase the global energy in the investigated configuration. Ultimately, the best combination of MPM schemes were determined to be the USF stress update scheme used alongside the FLIP velocity update

strategy.

These observations were confirmed on granular column collapse simulations performed with the Mohr-Coulomb model. First, the best set of MPM discretization parameters were determined through a convergence study, then a series of simulations was performed in order to observe the effect of the velocity update strategies on the collapse. The dissipative properties of PIC-based strategies are shown to considerably decrease the collapse rate of the column. Although the FLIP strategy was found to lead to collapse rate almost similar to the ones found in the literature (for both numerical and experimental results), it allows the column to spread to significantly larger lengths (at best 19% larger).

MPMxDEM coupling

A formulation of a multi-scale MPMxDEM coupling was given for both quasi-static and dynamic problems, which was implemented during this thesis. As part of this implementation, a Python module was developed to simplify CB-Geo MPM's user interface for both pure MPM and MPMxDEM simulations. Deeper technical aspects on how the MPM and DEM codes were combined together are given, with details on the implementation of the parallelization. Our code is next characterized in terms of performances on a 104 CPU threads server machine, considering the speed-up obtained in various situations. It is shown that the best speed-up for our MPMxDEM implementation is 24 when using 30 CPU threads, in the case of a simple 27 material points simulation.

A validation of the coupling is also performed on a one cell MPMxDEM triaxial test, for which global results are almost perfectly in accordance with pure DEM simulations in terms of deviatoric stress. As for volumetric deformations, the MPMxDEM model is able to describe their evolution although it overestimates them by approximately 20%. These results also revealed that the main stresses were not homogenous between the material points. However, the average number of coordination and the ratio of the axial and lateral stresses are homogenous throughout the sample.

Finally, a rather large MPMxDEM granular column collapse simulation was performed over 44 days on a server machine, with the best set of parameters determined on pure MPM simulations. The results highlight an inconsistency between the deformations a RVE is subjected to and its location in the column, which is certainly caused by the FLIP velocity update strategy. This issue causes many RVEs to reach unrealistic states, turning them into a contact-less cloud of particles. However, the final column width is closer to results from the literature than pure MPM results, confirming the interest of using DEM, rich in micro-mechanical information, to describe the material's behaviour. Incidentally, an analysis of the computational cost is also provided. Indeed, because of the quasi-static assumption made at the microscopic scale, the computational time strongly depends on the amount of deformations involved in the simulation, through the number of DEM iteration each RVE has to perform. As a matter of fact, when RVEs are not significantly solicited the computation can be approximately 20 faster than when they are extensively deformed.

Perspectives

An optimization of the MPMxDEM performances would allow to use a better MPM discretization, in terms of mesh fineness and number of material points per cell, for the same computational time. For instance, a better parallelization could be achieved by testing out in several configurations the available parallelization strategies (i.e. OpenMP and MPI) with different parameters. The best performances might be obtained using parallelization both at the MPM and DEM scales, with a suitable CPU threads repartition.

Future work could focus on combining DEM as a descriptor of the material's behaviour with improved MPM formulations. The latter includes for instance the GIMP methods, or the B-spline shape functions, both able to make the method more accurate by preserving the continuity of the material points' stress contribution to grid nodes through a cell-crossing event. The use of a better velocity update strategy could also significantly improve the MPMxDEM coupling, as issues with the granular collapse simulations were attributed to the FLIP strategy. A promising candidate is the ASFLIP strategy, which preserves the angular momentum while based on the FLIP strategy, unlike the APIC scheme. The capacity of MPM to handle large deformations could also be strengthened by considering an objective stress rate, such as the Jaumann or Green-Naghdi stress rate. Indeed, in our current MPM implementation the stress rate depends on the frame used to describe it when rigid body rotations occurs, which is obviously non-physical.

Another possible improvement to our coupling could be to replace MPM by an alternative large scale method, for instance the FEMLIP method, also capable of handling large deformations. Its advantage over MPM lies in its use of a generalized formulation of the Gaussian quadrature in each element, giving precise values to the integration weights. Such a method combined with DEM is expected to give accurate results even in simulations where material points are subject to important displacements.

Bibliographie

Aboul Hosn, Rodaina, Luc Sibille, Nadia Benahmed, et al. (2017). “Discrete numerical modeling of loose soil with spherical particles and interparticle rolling friction”. In: *Granular matter* 19.1, pp. 1–12 (cit. on pp. 28, 31, 33, 128, 130, 131).

Ainsworth, Mark and Charles Parker (2021). “Mass conserving mixed hp-FEM approximations to Stokes flow. Part II: Optimal convergence”. In: *SIAM Journal on Numerical Analysis* 59.3, pp. 1245–1272 (cit. on p. 37).

Akbar, Fathan, Elfi Yuliza, Nadya Amalia, et al. (2022). “The slope of dry granular materials surface is generally curved”. In: *Granular Matter* 24.2, pp. 1–11 (cit. on pp. 47, 58).

Angelidakis, Vasileios, Sadegh Nadimi, Masahide Otsubo, et al. (2021). “CLUMP: a code library to generate universal multi-sphere particles”. In: *SoftwareX* 15, p. 100735 (cit. on pp. 49, 52).

Angelidakis, Vasileios, Sadegh Nadimi, and Stefano Utili (2021). “SHape Analyser for Particle Engineering (SHAPE): Seamless characterisation and simplification of particle morphology from imaging data”. In: *Computer Physics Communications* 265, p. 107983 (cit. on p. 52).

Antypov, D and JA Elliott (2011). “On an analytical solution for the damped Hertzian spring”. In: *EPL (Europhysics Letters)* 94.5, p. 50004 (cit. on p. 54).

Babuška, Ivo and BQ Guo (1992). “The h, p and hp version of the finite element method; basis theory and applications”. In: *Advances in Engineering Software* 15.3-4, pp. 159–174 (cit. on p. 37).

Bandini, V and Matthew Richard Coop (2011). “The influence of particle breakage on the location of the critical state line of sands”. In: *Soils and foundations* 51.4, pp. 591–600 (cit. on pp. 83, 85).

Bardenhagen, Scott G and Edward M Kober (2004). “The generalized interpolation material point method”. In: *Computer Modeling in Engineering and Sciences* 5.6, pp. 477–496 (cit. on pp. 39, 96).

Bardenhagen, SG (2002). “Energy conservation error in the material point method for solid mechanics”. In: *Journal of Computational Physics* 180.1, pp. 383–403 (cit. on pp. 100, 106).

Bathe, KJ and H Saunders (1984). “Finite Element Procedures in Engineering Analysis”. In: (cit. on p. 36).

Been, Ken and Mike G Jefferies (1985). “A state parameter for sands”. In: *Géotechnique* 35.2, pp. 99–112 (cit. on p. 35).

Bolton, MD (1986). “The strength and dilatancy of sands”. In: *Geotechnique* 36.1, pp. 65–78 (cit. on p. 47).

Bono, John P de and Glenn R McDowell (2022). "Some important aspects of modelling clay platelet interactions using DEM". In: *Powder Technology* 398, p. 117056 (cit. on p. 23).

Boon, CW, GT Houlsby, and S Utili (2013). "A new contact detection algorithm for three-dimensional non-spherical particles". In: *Powder technology* 248, pp. 94–102 (cit. on pp. 24, 50, 53).

Brackbill, Jeremiah U and Hans M Ruppel (1986). "FLIP: A method for adaptively zoned, particle-in-cell calculations of fluid flows in two dimensions". In: *Journal of Computational physics* 65.2, pp. 314–343 (cit. on pp. 40, 100).

Brinkgreve, Ronald BJ (2005). "Selection of soil models and parameters for geotechnical engineering application". In: *Soil constitutive models: Evaluation, selection, and calibration*, pp. 69–98 (cit. on pp. 34, 35).

Bui, Ha H and Giang D Nguyen (2021). "Smoothed particle hydrodynamics (SPH) and its applications in geomechanics: From solid fracture to granular behaviour and multiphase flows in porous media". In: *Computers and Geotechnics* 138, p. 104315 (cit. on p. 38).

Burland, JB (1965). "The yieding and dilation of clay". In: *correspondence, Géotechnique* 15.1, pp. 211–214 (cit. on p. 35).

Chambon, Guillaume, R Bouvarel, D Laigle, et al. (2011). "Numerical simulations of granular free-surface flows using smoothed particle hydrodynamics". In: *Journal of Non-Newtonian Fluid Mechanics* 166.12-13, pp. 698–712 (cit. on p. 38).

Chang, CS and P-Y Hicher (2005). "An elasto-plastic model for granular materials with microstructural consideration". In: *International journal of solids and structures* 42.14, pp. 4258–4277 (cit. on p. 41).

Chareyre, B, L Briançon, and Pascal Villard (2002). "Theoretical versus experimental modeling of the anchorage capacity of geotextiles in trenches". In: *Geosynthetics International* 9.2, pp. 97–123 (cit. on pp. 85, 131).

Chareyre, Bruno, Andrea Cortis, Emanuele Catalano, et al. (2012). "Pore-scale modeling of viscous flow and induced forces in dense sphere packings". In: *Transport in porous media* 94.2, pp. 595–615 (cit. on p. 27).

Chen, Hao, Shiwei Zhao, and Xiaowen Zhou (2020). "DEM investigation of angle of repose for super-ellipsoidal particles". In: *Particuology* 50, pp. 53–66 (cit. on p. 47).

Chessa, Jack, Patrick Smolinski, and Ted Belytschko (2002). "The extended finite element method (XFEM) for solidification problems". In: *International Journal for Numerical Methods in Engineering* 53.8, pp. 1959–1977 (cit. on p. 37).

Chu, J (1995). "An experimental examination of the critical state and other similar concepts for granular soils". In: *Canadian Geotechnical Journal* 32.6, pp. 1065–1075 (cit. on pp. 83, 85).

Chung, WJ, JW Cho, and T Belytschko (1998). "On the dynamic effects of explicit FEM in sheet metal forming analysis". In: *Engineering Computations* (cit. on p. 36).

Cifuentes, AO and A Kalbag (1992). "A performance study of tetrahedral and hexahedral elements in 3-D finite element structural analysis". In: *Finite Elements in Analysis and Design* 12.3-4, pp. 313–318 (cit. on p. 36).

Cohen, Jonathan D, Ming C Lin, Dinesh Manocha, et al. (1995). "I-collide: An interactive and exact collision detection system for large-scale environments". In: *Proceedings of the 1995 symposium on Interactive 3D graphics*, 189–ff (cit. on p. 29).

Courant, R (1943). "Variational methods for the solution of problems of equilibrium and vibrations". In: *Bulletin of the American Mathematical Society* 49.1, pp. 1–23 (cit. on p. 35).

Crosta, GB, S Imposimato, and D Roddeman (2009). "Numerical modeling of 2-D granular step collapse on erodible and nonerodible surface". In: *Journal of Geophysical Research: Earth Surface* 114.F3 (cit. on pp. 126, 127, 156).

Cundall, Peter A and Otto DL Strack (1979). "A discrete numerical model for granular assemblies". In: *Géotechnique* 29.1, pp. 47–65 (cit. on pp. 23, 24).

Dagum, Leonardo and Ramesh Menon (1998). "OpenMP: an industry standard API for shared-memory programming". In: *IEEE computational science and engineering* 5.1, pp. 46–55 (cit. on p. 31).

De Josselin de Jong, G (1969). "Etude photoelastique d'un empilement de disques". In: *Cah. Grpe fr. Etud. Rheol.* 2, pp. 73–86 (cit. on p. 23).

Drucker, Daniel Charles and William Prager (1952). "Soil mechanics and plastic analysis or limit design". In: *Quarterly of applied mathematics* 10.2, pp. 157–165 (cit. on p. 35).

Dufour, Frédéric (2002). "Développements de la méthode des éléments finis avec des points d'intégration Lagrangiens: Applications à la géomécanique". PhD thesis. Ecole Centrale de Nantes (ECN); Université de Nantes (cit. on p. 38).

Duncan, James M and Chin-Yung Chang (1970). "Nonlinear analysis of stress and strain in soils". In: *Journal of the soil mechanics and foundations division* 96.5, pp. 1629–1653 (cit. on p. 35).

Duriez, Jerome and É Vincens (2015). "Constitutive modelling of cohesionless soils and interfaces with various internal states: An elasto-plastic approach". In: *Computers and Geotechnics* 63, pp. 33–45 (cit. on p. 83).

Duriez, Jérôme and Stéphane Bonelli (2021). "Precision and computational costs of Level Set-Discrete Element Method (LS-DEM) with respect to DEM". In: *Computers and Geotechnics* 134, p. 104033 (cit. on pp. 24, 32, 51, 53, 56).

Duriez, Jérôme and Cédric Galusinski (2021). "A Level Set-Discrete Element Method in YADE for numerical, micro-scale, geomechanics with refined grain shapes". In: *Computers & Geosciences* 157, p. 104936 (cit. on pp. 24, 30, 32, 51).

Duriez, Jérôme and Richard Wan (2017). "Contact angle mechanical influence in wet granular soils". In: *Acta Geotechnica* 12.1, pp. 67–83 (cit. on p. 27).

Duverger, Sacha, Vasileios Angelidakis, Jérôme Duriez, et al. (2023). "Methodological and physical aspects of angle of repose studies". In: *To be decided*. En phase de finalisation (cit. on p. 3).

Duverger, Sacha and Jérôme Duriez (Aug. 2021). *PyCBG, a python module for generating CB-Geo MPM input files*. Version 1.1.4. DOI: 10.5281/zenodo.5179973 (cit. on pp. 3, 115).

Duverger, Sacha, Jérôme Duriez, Pierre Philippe, et al. (2021). "Rattlers' involvement for possibly looser critical states under higher mean stress". In: *EPJ Web of Conferences*. Vol. 249. EDP Sciences, p. 11002 (cit. on pp. 3, 33, 77, 78).

– (2022). "Multi-scale granular mechanics using MPM x DEM". In: *Congrès Français de Mécanique (CFM-2022)* (cit. on p. 3).

Ellis, EA and SM Springman (2001). "Modelling of soil–structure interaction for a piled bridge abutment in plane strain FEM analyses". In: *Computers and Geotechnics* 28.2, pp. 79–98 (cit. on p. 35).

Eymard, Robert, Thierry Gallouët, and Raphaèle Herbin (2000). "Finite volume methods". In: *Handbook of numerical analysis* 7, pp. 713–1018 (cit. on p. 27).

Fei, Yun, Qi Guo, Rundong Wu, et al. (2021). "Revisiting integration in the material point method: a scheme for easier separation and less dissipation". In: *ACM Transactions on Graphics (TOG)* 40.4, pp. 1–16 (cit. on pp. 40, 41, 156).

Ferellec, Jean-Francois and Glenn R McDowell (2010). "A method to model realistic particle shape and inertia in DEM". In: *Granular Matter* 12.5, pp. 459–467 (cit. on p. 49).

Fu, Chuyuan, Qi Guo, Theodore Gast, et al. (2017). "A polynomial particle-in-cell method". In: *ACM Transactions on Graphics (TOG)* 36.6, pp. 1–12 (cit. on p. 40).

Garau, Eduardo M, Pedro Morin, and Carlos Zuppa (2011). "Convergence of an adaptive Kačanov FEM for quasi-linear problems". In: *Applied Numerical Mathematics* 61.4, pp. 512–529 (cit. on p. 37).

Gardner, Michael, John Kolb, and Nicholas Sitar (2017). "Parallel and scalable block system generation". In: *Computers and Geotechnics* 89, pp. 168–178 (cit. on p. 33).

GDR MiDi (2004). "On dense granular flows". In: *The European Physical Journal E* 4.14, pp. 341–365 (cit. on pp. 85, 112).

Geldart, Derek, EC Abdullah, A Hassanpour, et al. (2006). "Characterization of powder flowability using measurement of angle of repose". In: *China Particuology* 4.3-4, pp. 104–107 (cit. on p. 47).

Gerstle, Walter H and Ming Xie (1992). "FEM modeling of fictitious crack propagation in concrete". In: *Journal of Engineering Mechanics* 118.2, pp. 416–434 (cit. on p. 35).

Gilbert, Elmer G, Daniel W Johnson, and S Sathiya Keerthi (1988). "A fast procedure for computing the distance between complex objects in three-dimensional space". In: *IEEE Journal on Robotics and Automation* 4.2, pp. 193–203 (cit. on p. 23).

Gingold, Robert A and Joseph J Monaghan (1977). "Smoothed particle hydrodynamics: theory and application to non-spherical stars". In: *Monthly notices of the royal astronomical society* 181.3, pp. 375–389 (cit. on p. 38).

Girolami, L, V Hergault, G Vinay, et al. (2012). "A three-dimensional discrete-grain model for the simulation of dam-break rectangular collapses: comparison between numerical results and experiments". In: *Granular Matter* 14.3, pp. 381–392 (cit. on pp. 126, 156).

Goodarzi, Majid, Chung Yee Kwok, and Leslie George Tham (2015). "A continuum-discrete model using Darcy's law: formulation and verification". In: *International Journal for Numerical and Analytical Methods in Geomechanics* 39.3, pp. 327–342 (cit. on p. 27).

Govender, Nicolin, Daniel N Wilke, and Schalk Kok (2015). "Collision detection of convex polyhedra on the NVIDIA GPU architecture for the discrete element method". In: *Applied Mathematics and Computation* 267, pp. 810–829 (cit. on p. 32).

Govender, Nicolin, Daniel N Wilke, Chuan-Yu Wu, et al. (2018). "Hopper flow of irregularly shaped particles (non-convex polyhedra): GPU-based DEM simulation and experimental validation". In: *Chemical Engineering Science* 188, pp. 34–51 (cit. on p. 24).

Graham, Richard L, Timothy S Woodall, and Jeffrey M Squyres (2005). "Open MPI: A flexible high performance MPI". In: *International Conference on Parallel Processing and Applied Mathematics*. Springer, pp. 228–239 (cit. on p. 32).

Gwinner, Joachim (2013). "hp-FEM convergence for unilateral contact problems with Tresca friction in plane linear elastostatics". In: *Journal of computational and applied mathematics* 254, pp. 175–184 (cit. on p. 37).

Han, Yanhui and Peter A Cundall (2013). "LBM–DEM modeling of fluid–solid interaction in porous media". In: *International Journal for Numerical and Analytical Methods in Geomechanics* 37.10, pp. 1391–1407 (cit. on p. 28).

Harlow, Francis H (1962). *The particle-in-cell method for numerical solution of problems in fluid dynamics*. Tech. rep. Los Alamos National Lab.(LANL), Los Alamos, NM (United States) (cit. on p. 39).

Al-Hashemi, Hamzah M Beakawi and Omar S Baghabra Al-Amoudi (2018). "A review on the angle of repose of granular materials". In: *Powder technology* 330, pp. 397–417 (cit. on p. 47).

He, Xiaoyi and Li-Shi Luo (1997). "Theory of the lattice Boltzmann method: From the Boltzmann equation to the lattice Boltzmann equation". In: *Physical review E* 56.6, p. 6811 (cit. on p. 27).

Hilse, Nikoline, Max Kriegeskorte, Enric Illana, et al. (2022). "Mixing and segregation of spheres of three different sizes on a batch stoker grate: Experiments and discrete element simulation". In: *Powder Technology* 400, p. 117258 (cit. on p. 23).

Houlsby, GT (2009). "Potential particles: a method for modelling non-circular particles in DEM". In: *Computers and Geotechnics* 36.6, pp. 953–959 (cit. on pp. 24, 50).

Hrennikoff, A (1941). "Solution of Problems of Elasticity by the Framework Method". In: *Journal of Applied Mechanics* 8.4, A169–A175 (cit. on p. 35).

Hu, Yuanming, Yu Fang, Ziheng Ge, et al. (2018). "A moving least squares material point method with displacement discontinuity and two-way rigid body coupling". In: *ACM Transactions on Graphics (TOG)* 37.4, pp. 1–14 (cit. on p. 40).

Huang, Xin, Kevin J Hanley, Catherine O'Sullivan, et al. (2014). "Exploring the influence of interparticle friction on critical state behaviour using DEM". In: *Inter-*

national Journal for Numerical and Analytical Methods in Geomechanics 38.12, pp. 1276–1297 (cit. on pp. 83, 86, 87).

Japanase Geotechnical Society, TC105 (2021). *Round robin test of angle of repose (AOR)*. URL: http://geotech.civil.yamaguchi-u.ac.jp/tc105/ (visited on 08/25/2021) (cit. on pp. 47, 48, 56, 73).

Jefferies, MG (1993). "Nor-Sand: a simle critical state model for sand". In: *Géotechnique* 43.1, pp. 91–103 (cit. on p. 35).

Jiang, Chenfanfu, Craig Schroeder, Andrew Selle, et al. (2015). "The affine particle-in-cell method". In: *ACM Transactions on Graphics (TOG)* 34.4, pp. 1–10 (cit. on pp. 40, 101, 156).

Kafashan, Jalal, Joanna Wiącek, Noorhazlinda Abd Rahman, et al. (2019). "Two-dimensional particle shapes modelling for DEM simulations in engineering: A review". In: *Granular Matter* 21.3, pp. 1–19 (cit. on p. 23).

Kawamoto, Reid, Edward Andò, Gioacchino Viggiani, et al. (2016). "Level set discrete element method for three-dimensional computations with triaxial case study". In: *Journal of the Mechanics and Physics of Solids* 91, pp. 1–13 (cit. on pp. 24, 51).

Ketterhagen, William and Carl Wassgren (2022). "A perspective on calibration and application of DEM models for simulation of industrial bulk powder processes". In: *Powder Technology* 402, p. 117301 (cit. on p. 23).

Khoshghalb, A, A Shafee, A Tootoonchi, et al. (2020). "Application of the smoothed point interpolation methods in computational geomechanics: A comparative study". In: *Computers and Geotechnics* 126, p. 103714 (cit. on p. 38).

Kien, Nguyen Trung, Vo Thanh Trung, and Nguyen Nhu Hoang (2021). "Coupled finite-discrete element modeling and potential applications in civil engineering". In: *Journal of Science and Technology in Civil Engineering (STCE)-HUCE* 15.4, pp. 111–122 (cit. on p. 43).

Kobayashi, Shiro (1982). "A review on the finite-element method and metal forming process modeling". In: *Journal of Applied Metalworking* 2.3, pp. 163–169 (cit. on p. 34).

Kraynik, AM and DA Reinelt (1992). "Extensional motions of spatially periodic lattices". In: *International journal of multiphase flow* 18.6, pp. 1045–1059 (cit. on p. 29).

Krieg, R. D. and D. B. Krieg (Nov. 1977). "Accuracies of Numerical Solution Methods for the Elastic-Perfectly Plastic Model". In: *Journal of Pressure Vessel Technology* 99.4, pp. 510–515 (cit. on p. 34).

Kumar, Krishna, Jeffrey Salmond, Shyamini Kularathna, et al. (2019). "Scalable and modular material point method for large-scale simulations". In: *arXiv preprint arXiv:1909.13380* (cit. on pp. 21, 92, 94, 115).

Lajeunesse, E, JB Monnier, and GM Homsy (2005). "Granular slumping on a horizontal surface". In: *Physics of fluids* 17.10, p. 103302 (cit. on pp. 126, 156).

Langston, Paul, Jun Ai, and Hai-Sui Yu (2013). "Simple shear in 3D DEM polyhedral particles and in a simplified 2D continuum model". In: *Granular Matter* 15.5, pp. 595–606 (cit. on p. 24).

Liang, Weijian and Jidong Zhao (2019). "Multiscale modeling of large deformation in geomechanics". In: *International Journal for Numerical and Analytical Methods in Geomechanics* 43.5, pp. 1080–1114 (cit. on p. 44).

Liu, Gui-Rong and Gui-yong Zhang (2013). *Smoothed point interpolation methods: G space theory and weakened weak forms*. World Scientific (cit. on p. 38).

Lo, SH (2002). "Finite element mesh generation and adaptive meshing". In: *Progress in Structural Engineering and Materials* 4.4, pp. 381–399 (cit. on p. 36).

Love, A.E.H. (1892). "A treatise on the mathematical theory of elasticity". In: 643 (cit. on p. 42).

Lowan, Arnold Noah, Norman Davids, and Arthur Levenson (1942). *Table of the zeros of the Legendre polynomials of order 1-16 and the weight coefficients for Gauss' mechanical quadrature formula*. Vol. 18 (cit. on p. 127).

Lube, Gert, Herbert E Huppert, R Stephen J Sparks, et al. (2005). "Collapses of two-dimensional granular columns". In: *Physical Review E* 72.4, p. 041301 (cit. on p. 127).

Lucy, Leon B (1977). "A numerical approach to the testing of the fission hypothesis". In: *The astronomical journal* 82, pp. 1013–1024 (cit. on p. 38).

Ma, Zongyuan, Hongjian Liao, Faning Dang, et al. (2021). "Seismic slope stability and failure process analysis using explicit finite element method". In: *Bulletin of Engineering Geology and the Environment* 80.2, pp. 1287–1301 (cit. on p. 35).

Mack, Stuart, Paul Langston, Colin Webb, et al. (2011). "Experimental validation of polyhedral discrete element model". In: *Powder Technology* 214.3, pp. 431–442 (cit. on p. 24).

Matsuo, Miki Y, Daisuke Nishiura, and Hide Sakaguchi (2014). "Geometric effect of angle of repose revisited". In: *Granular Matter* 16.4, pp. 441–447 (cit. on p. 47).

Matuttis, HG, S Luding, and HJ Herrmann (2000). "Discrete element simulations of dense packings and heaps made of spherical and non-spherical particles". In: *Powder technology* 109.1-3, pp. 278–292 (cit. on pp. 47, 50).

Melenk, Jens M and Ivo Babuška (1996). "The partition of unity finite element method: basic theory and applications". In: *Computer methods in applied mechanics and engineering* 139.1-4, pp. 289–314 (cit. on p. 37).

Melenk, Jens Markus and Christos Xenophontos (2016). "Robust exponential convergence of hp-FEM in balanced norms for singularly perturbed reaction-diffusion equations". In: *Calcolo* 53.1, pp. 105–132 (cit. on p. 37).

Moës, Nicolas, John Dolbow, and Ted Belytschko (1999). "A finite element method for crack growth without remeshing". In: *International journal for numerical methods in engineering* 46.1, pp. 131–150 (cit. on p. 37).

Mohamed, Tarek, Jérôme Duriez, Guillaume Veylon, et al. (2022). "DEM models using direct and indirect shape descriptions for Toyoura sand along monotonous loading paths". In: *Computers and Geotechnics* 142, p. 104551 (cit. on pp. 23, 24, 33).

Moresi, Louis, Frédéric Dufour, and H-B Mühlhaus (2003). "A Lagrangian integration point finite element method for large deformation modeling of viscoelastic

geomaterials". In: *Journal of computational physics* 184.2, pp. 476–497 (cit. on p. 38).
Mori, Yuki and Mikio Sakai (2022). "Advanced DEM simulation on powder mixing for ellipsoidal particles in an industrial mixer". In: *Chemical Engineering Journal* 429, p. 132415 (cit. on p. 23).
Nairn, John A (2011). "Material point method (NairnMPM) and finite element analysis (NairnFEA) open-source software". In: *URL http://code. google. com/p/nairnmpm-fea* (cit. on p. 44).
Nguyen, Trung Kien, Albert Argilaga Claramunt, Denis Caillerie, et al. (2017). "FEM× DEM: a new efficient multi-scale approach for geotechnical problems with strain localization". In: *EPJ Web of Conferences*. Vol. 140. EDP Sciences, p. 11007 (cit. on p. 43).
Nguyen, Trung-Kien, Jacques Desrues, Thanh-Trung Vo, et al. (2022). "FEM× DEM multi-scale model for cemented granular materials: Inter-and intra-granular cracking induced strain localisation". In: *International Journal for Numerical and Analytical Methods in Geomechanics* 46.5, pp. 1001–1025 (cit. on p. 43).
Nguyen-Thoi, T, GR Liu, HC Vu-Do, et al. (2009). "A face-based smoothed finite element method (FS-FEM) for visco-elastoplastic analyses of 3D solids using tetrahedral mesh". In: *Computer Methods in Applied Mechanics and Engineering* 198.41-44, pp. 3479–3498 (cit. on p. 36).
Nicot, François (2003). "Constitutive modelling of a snow cover with a change in scale". In: *European Journal of Mechanics-A/Solids* 22.3, pp. 325–340 (cit. on p. 41).
Nicot, François and Félix Darve (2011). "The H-microdirectional model: accounting for a mesoscopic scale". In: *Mechanics of materials* 43.12, pp. 918–929 (cit. on pp. 41, 42).
Nicot, François, Nejib Hadda, Mohamed Guessasma, et al. (2013). "On the definition of the stress tensor in granular media". In: *International Journal of Solids and Structures* 50.14-15, pp. 2508–2517 (cit. on p. 42).
Nitka, Michał, Gaël Combe, Cristian Dascalu, et al. (2011). "Two-scale modeling of granular materials: a DEM-FEM approach". In: *Granular Matter* 13.3, pp. 277–281 (cit. on p. 43).
Oku, Takehiro, Hiroshi Akiba, Satoru Suzuki, et al. (2010). "Seismic response analysis using three dimensional FEM analysis for BWR nuclear reactor facilities". In: (cit. on p. 36).
Oñate, Eugenio, Sergio R Idelsohn, Facundo Del Pin, et al. (2004). "The particle finite element method—an overview". In: *International Journal of Computational Methods* 1.02, pp. 267–307 (cit. on p. 38).
Pironneau, Olivier (1989). *Finite element methods for fluids*. Wiley Chichester (cit. on p. 34).
Pöschel, Thorsten and Volkhard Buchholtz (1993). "Static friction phenomena in granular materials: Coulomb law versus particle geometry". In: *Physical review letters* 71.24, p. 3963 (cit. on p. 47).

Radjai, Farhang (2018). "Multi-periodic boundary conditions and the Contact Dynamics method". In: *Comptes Rendus Mécanique* 346.3, pp. 263–277 (cit. on p. 28).
Rakotonirina, Andriarimina Daniel, Jean-Yves Delenne, and Anthony Wachs (2017). "A parallel Discrete Element Method to model collisions between non-convex particles". In: *EPJ Web of Conferences*. Vol. 140. EDP Sciences, p. 06004 (cit. on p. 24).
Rakotonirina, Andriarimina Daniel and Anthony Wachs (2018). "Grains3D, a flexible DEM approach for particles of arbitrary convex shape-Part II: Parallel implementation and scalable performance". In: *Powder Technology* 324, pp. 18–35 (cit. on pp. 32, 33).
Ralston, Anthony and Philip Rabinowitz (2001). "A first course in numerical analysis". In: Courier Corporation. Chap. §4.8-1 (cit. on p. 36).
Rathod, HT, B Venkatesudu, and KV Nagaraja (2006). "Gauss legendre quadrature formulas over a tetrahedron". In: *Numerical Methods for Partial Differential Equations: An International Journal* 22.1, pp. 197–219 (cit. on p. 36).
Rocchini, Claudio and Paolo Cignoni (2000). "Generating random points in a tetrahedron". In: *Journal of graphics Tools* 5.4, pp. 9–12 (cit. on p. 62).
Roscoe, K. H., A. N. Schofield, and C. P. Wroth (1958). "On the yielding of soils". In: *Geotechnique* 8.1, pp. 22–53 (cit. on p. 83).
Rousé, Pascale C (2014). "Comparison of methods for the measurement of the angle of repose of granular materials". In: *Geotechnical Testing Journal* 37.1, pp. 164–168 (cit. on p. 47).
Saomoto, Hidetaka, Naotaka Kikkawa, Shuji Moriguchi, et al. (2023). "Round robin test on angle of repose: DEM simulation results collected from 16 groups around the world". In: *Soils and Foundations* 63 (cit. on p. 3).
Schneiders, Robert and Rolf Bünten (1995). "Automatic generation of hexahedral finite element meshes". In: *Computer Aided Geometric Design* 12.7, pp. 693–707 (cit. on p. 36).
Schofield, Andrew Noel and Peter Wroth (1968). *Critical state soil mechanics*. Vol. 310. McGraw-hill London (cit. on p. 35).
Schwager, Thomas and Thorsten Pöschel (2007). "Coefficient of restitution and linear–dashpot model revisited". In: *Granular Matter* 9.6, pp. 465–469 (cit. on pp. 54, 84).
Selvam, R Panneer, Michael J Tarini, and Allan Larsen (1998). "Computer modelling of flow around bridges using LES and FEM". In: *Journal of Wind Engineering and Industrial Aerodynamics* 77, pp. 643–651 (cit. on p. 35).
Shadloo, M Safdari, G Oger, and David Le Touzé (2016). "Smoothed particle hydrodynamics method for fluid flows, towards industrial applications: Motivations, current state, and challenges". In: *Computers & Fluids* 136, pp. 11–34 (cit. on p. 38).
Shi, Zhong Ci (1987). "The FEM test for convergence of nonconforming finite elements". In: *Mathematics of computation* 49.180, pp. 391–405 (cit. on p. 37).
Sibille, Luc, Pascal Villard, Félix Darve, et al. (2019). "Quantitative prediction of discrete element models on complex loading paths". In: *International Journal*

for Numerical and Analytical Methods in Geomechanics 43.5, pp. 858–887 (cit. on pp. 23, 26, 33).

Sitharam, TG and Jayan Sylaja Vinod (2009). "Critical state behaviour of granular materials from isotropic and rebounded paths: DEM simulations". In: *Granular matter* 11.1, pp. 33–42 (cit. on pp. 83, 85).

Sloan, SW and John R Booker (1992). "Integration of Tresca and Mohr–Coulomb constitutive relations in plane strain elastoplasticity". In: *International Journal for Numerical Methods in Engineering* 33.1, pp. 163–196 (cit. on p. 34).

Smeets, Bart, Tim Odenthal, Simon Vanmaercke, et al. (2015). "Polygon-based contact description for modeling arbitrary polyhedra in the Discrete Element Method". In: *Computer Methods in Applied Mechanics and Engineering* 290, pp. 277–289 (cit. on p. 24).

Smilauer, V. et al. (2021). *Yade Documentation 3rd ed.* http://yade-dem.org/doc/. The Yade Project. DOI: 10.5281/zenodo.5705394 (cit. on pp. 21, 28–30, 44, 47, 83, 85, 114).

Soldera, F, A Lasagni, F Mücklich, et al. (2005). "Determination of the cathode erosion and temperature for the phases of high voltage discharges using FEM simulations". In: *Computational materials science* 32.1, pp. 123–139 (cit. on p. 36).

Staron, Lydie and EJ Hinch (2005). "Study of the collapse of granular columns using two-dimensional discrete-grain simulation". In: *Journal of Fluid Mechanics* 545, pp. 1–27 (cit. on p. 127).

Steffen, Michael, Robert M Kirby, and Martin Berzins (2008). "Analysis and reduction of quadrature errors in the material point method (MPM)". In: *International journal for numerical methods in engineering* 76.6, pp. 922–948 (cit. on pp. 39, 40).

Stomakhin, Alexey, Craig Schroeder, Lawrence Chai, et al. (2013). "A material point method for snow simulation". In: *ACM Transactions on Graphics (TOG)* 32.4, pp. 1–10 (cit. on p. 40).

Sulsky, Deborah, Zhen Chen, and Howard L Schreyer (1994). "A particle method for history-dependent materials". In: *Computer methods in applied mechanics and engineering* 118.1-2, pp. 179–196 (cit. on pp. 39, 92, 100).

Sun, Jin and Sankaran Sundaresan (2011). "A constitutive model with microstructure evolution for flow of rate-independent granular materials". In: *Journal of Fluid Mechanics* 682, pp. 590–616 (cit. on p. 41).

Ti, Kok Sien, Bujang BK Huat, Jamaloddin Noorzaei, et al. (2009). "A review of basic soil constitutive models for geotechnical application". In: *Electronic Journal of Geotechnical Engineering* 14, pp. 1–18 (cit. on p. 34).

Tong, A-T, E Catalano, and B Chareyre (2012). "Pore-scale flow simulations: model predictions compared with experiments on bi-dispersed granular assemblies". In: *Oil & Gas Science and Technology–Revue d'IFP Energies nouvelles* 67.5, pp. 743–752 (cit. on p. 85).

Topić, Nikola, Jason AC Gallas, and Thorsten Pöschel (2012). "Nonuniformities in the angle of repose and packing fraction of large heaps of particles". In: *Physical Review Letters* 109.12, p. 128001 (cit. on p. 47).

Utili, Stefano, Tao Zhao, and GT Houlsby (2015). "3D DEM investigation of granular column collapse: evaluation of debris motion and its destructive power". In: *Engineering geology* 186, pp. 3–16 (cit. on p. 129).

Vaucorbeil, Alban de, Vinh Phu Nguyen, Sina Sinaie, et al. (2020). "Material point method after 25 years: Theory, implementation, and applications". In: *Advances in applied mechanics* 53, pp. 185–398 (cit. on p. 39).

Venkatesan, A, VM Gopinath, and A Rajadurai (2005). "Simulation of casting solidification and its grain structure prediction using FEM". In: *Journal of Materials Processing Technology* 168.1, pp. 10–15 (cit. on p. 36).

Verdugo, Ramon and Kenji Ishihara (1996). "The steady state of sandy soils". In: *Soils and foundations* 36.2, pp. 81–91 (cit. on pp. 83, 85).

Wadell, Hakon (1932). "Volume, shape, and roundness of rock particles". In: *The Journal of Geology* 40.5, pp. 443–451 (cit. on p. 53).

Wan, RG and PJ Guo (1998). "A simple constitutive model for granular soils: modified stress-dilatancy approach". In: *Computers and Geotechnics* 22.2, pp. 109–133 (cit. on p. 41).

Williams, John R and Ruaidhri O'Connor (1995). "A linear complexity intersection algorithm for discrete element simulation of arbitrary geometries". In: *Engineering computations* 12.2, pp. 185–201 (cit. on p. 29).

Xiong, Hao, Zhen-Yu Yin, François Nicot, et al. (2021). "A novel multi-scale large deformation approach for modelling of granular collapse". In: *Acta Geotechnica* 16.8, pp. 2371–2388 (cit. on pp. 126, 156).

Yamakawa, Soji and Kenji Shimada (2009). "Converting a tetrahedral mesh to a prism–tetrahedral hybrid mesh for FEM accuracy and efficiency". In: *International journal for numerical methods in engineering* 80.1, pp. 74–102 (cit. on p. 36).

Yan, Beichuan and Richard A Regueiro (2018). "A comprehensive study of MPI parallelism in three-dimensional discrete element method (DEM) simulation of complex-shaped granular particles". In: *Computational Particle Mechanics* 5.4, pp. 553–577 (cit. on p. 33).

Yan, Jie, Changwen Mi, and Zhixin Liu (2019). "A semianalytical and finite-element solution to the unbonded contact between a frictionless layer and an FGM-coated half-plane". In: *Mathematics and Mechanics of Solids* 24.2, pp. 448–464 (cit. on p. 36).

Yang, Zongze, Jungang Wang, Zhanbin Yuan, et al. (2022). "Using Gauss-Jacobi quadrature rule to improve the accuracy of FEM for spatial fractional problems". In: *Numerical Algorithms* 89.3, pp. 1389–1411 (cit. on p. 36).

Zavattieri, Pablo D, Enzo A Dari, and Gustavo C Buscaglia (1996). "Optimization strategies in unstructured mesh generation". In: *International Journal for Numerical Methods in Engineering* 39.12, pp. 2055–2071 (cit. on p. 36).

Zeng, W and GR Liu (2018). "Smoothed finite element methods (S-FEM): an overview and recent developments". In: *Archives of Computational Methods in Engineering* 25.2, pp. 397–435 (cit. on p. 38).

Zhou, Wei, Jiaying Liu, Gang Ma, et al. (2017). "Three-dimensional DEM investigation of critical state and dilatancy behaviors of granular materials". In: *Acta Geotechnica* 12.3, pp. 527–540 (cit. on pp. 83, 85).

Zhou, YC, BH Xu, AB Yu, et al. (2001). "Numerical investigation of the angle of repose of monosized spheres". In: *Physical Review E* 64.2, p. 021301 (cit. on pp. 47, 71).

Zhu, Fan and Jidong Zhao (2019). "Modeling continuous grain crushing in granular media: a hybrid peridynamics and physics engine approach". In: *Computer Methods in Applied Mechanics and Engineering* 348, pp. 334–355 (cit. on p. 28).

Appendices

A. A global stress tensor accounting for gravity

In order to know the stress state of the heap, one has to compute the stress tensor from the contact forces of all the contacts. Moreover, gravity is present in the simulations and is the origin of the movement, gravitational forces should thus be accounted for. In this subsection:

— $\mathbb{S}$ is the set containing all particles
— $\mathbb{C}^{ext}$ is the set containing all the contacts between particles and boundaries
— the upper-script $\cdot^p$ specifies that the quantity is taken for a particle p
— the upper-script $\cdot^c$ specifies that the quantity is taken for a contact c
— the sub-script $\cdot_{,x_i}$ denotes the derivative with respect to x_i
— the total volume of the heap is noted V and can be split: $V = \bigcup_{p\in\mathbb{S}} V^p$
— the number of underline denotes the order of a tensor ($\underline{\cdot}$ for vectors and $\underline{\underline{\cdot}}$ for matrices)
— the Kronecker symbol δ_{ij} and Einstein's notation will be used
— classical sign convention for stress is adopted, where the traction vector $\underline{t} = \underline{\underline{\sigma}}.\underline{n}$ applies onto the system for an outwards normal $\underline{n}$

The global stress tensor $\underline{\underline{\sigma}}^{glob}$ can be expressed according to the local stress tensor $\underline{\underline{\sigma}}$:

$$\underline{\underline{\sigma}}^{glob} = \frac{1}{V}\int_V \underline{\underline{\sigma}}\, dV \tag{.1}$$

One can compute $\underline{\underline{\sigma}}$ using the divergence of the third order tensor $\underline{\underline{\sigma}} \otimes \underline{x}$ (with $\underline{x}$ the position of any point in V with respect to a given, even though arbitrary, origin):

$$\left(\sigma_{ik}x_j\right)_{,k} = \sigma_{ik,k}x_j + \sigma_{ik}x_{j,k} \tag{.2}$$

Since the measurement is made when the heap is at the equilibrium, one has the following equation, noting $\underline{g}$ the gravitational acceleration and ρ the particle's density:

$$\sigma_{ij,j} = -\rho g_i \tag{.3}$$

Moreover, $x_{j,k} = \delta_{jk}$, thus:

$$\sigma_{ik}x_{j,k} = \sigma_{ij} \tag{.4}$$

By replacing equation .3 and equation .4 in equation .2 one gets:

$$\sigma_{ij} = \left(\sigma_{ik}x_j\right)_{,k} + \rho g_i x_j \tag{.5}$$

Equation .1 then gives:

$$\sigma_{ij}^{glob} = \frac{1}{V}\int_V \left(\left(\sigma_{ik}x_j\right)_{,k} + \rho g_i x_j\right) dV \tag{.6}$$

$$= \frac{1}{V}\sum_{p\in\mathbb{S}}\int_{V^p} \left(\left(\sigma_{ik}x_j\right)_{,k} + \rho g_i x_j\right) dV \qquad \text{because} \qquad V = \bigcup_{p\in\mathbb{S}} V^p \tag{.7}$$

$$= \underbrace{\frac{1}{V}\sum_{p\in\mathbb{S}}\int_{V^p} \left(\sigma_{ik}x_j\right)_{,k} dV}_{\sigma_{ij}^C} + \underbrace{\frac{1}{V}\sum_{p\in\mathbb{S}}\int_{V^p} \rho g_i x_j dV}_{\sigma_{ij}^G} \tag{.8}$$

Particles having an homogeneous density, one furthermore has, with m^p and $\underline{x}^p$ the mass and center of p :

$$\int_{V^p} \rho\, x_j\, dV = m^p\, x_j^p \tag{.9}$$

The part of $\underline{\underline{\sigma}}$ due to gravity (σ_{ij}^G) can thus be written:

$$\sigma_{ij}^G = \frac{1}{V} \sum_{p \in \mathbb{S}} m^p\, g_i\, x_j^p \tag{.10}$$

As for the part due to contacts (σ_{ij}^C), Green-Ostrogradski theorem gives:

$$\sigma_{ij}^C = \frac{1}{V} \sum_{p \in \mathbb{S}} \int_{\partial V^p} \sigma_{ik}\, x_j\, n_k\, dS \tag{.11}$$

Considering the traction vector $\underline{t} = \underline{\underline{\sigma}}.\underline{n}$, one has:

$$\sigma_{ij}^C = \frac{1}{V} \sum_{p \in \mathbb{S}} \int_{\partial V^p} t_i\, x_j\, dS \tag{.12}$$

The traction vector is not nil only on contact points. Since the system is closed, contact forces between particles cancel each other leaving only forces comming from outside of V. As a consequence, one can only consider the contact forces between particles and walls. For these contacts f^c denotes the contact force exerted by the wall on the particle and x^c the contact point. One has:

$$\sigma_{ij}^C = \frac{1}{V} \sum_{c \in \mathbb{C}^{ext}} f_i^c\, x_j^c \tag{.13}$$

Finally, the global stress tensor for a stable heap of particles made of homogeneous particles and subjected to gravity is:

$$\sigma_{ij}^{glob} = \frac{1}{V} \sum_{c \in \mathbb{C}^{ext}} f_i^c\, x_j^c + \frac{1}{V} \sum_{p \in V} m^p\, g_i\, x_j^p \tag{.14}$$

The mean stress can then be computed as $p = \dfrac{\mathrm{Tr}(\underline{\underline{\sigma}}^{glob})}{3}$.

B. Wall's velocity influence

In both configurations a wall holding the particles moves in order to let them fall. The way particles fall depends on the velocity at which the wall moves, but once the heap is stabilized the measurement of the AOR could be the same no matter the velocity. This could allow the increase of the wall's velocity V_{wall} and thus the decrease of the time cost. To know the influence of V_{wall} on the AOR, a series of simulations, CLP3, is performed with the clump model. Its parameters are given in table .1. For each value of the speed-up factor, 10 simulations are performed.

Configuration	N_{part}	ρ	V_{wall}/V^{ref}	e_0	Number of samples
Plane strain	2150	10000 kg/m^3	10^i for $i \in [\![-2,4]\!]$	0.603 ± 0.010	10
Axisymmetric	2468		10^i for $i \in [\![0,4]\!]$	0.693 ± 0.010	

TABLE .1. – Parameters of heap simulations investigating V_{wall} influence (CLP3 series, 120 simulations in total)

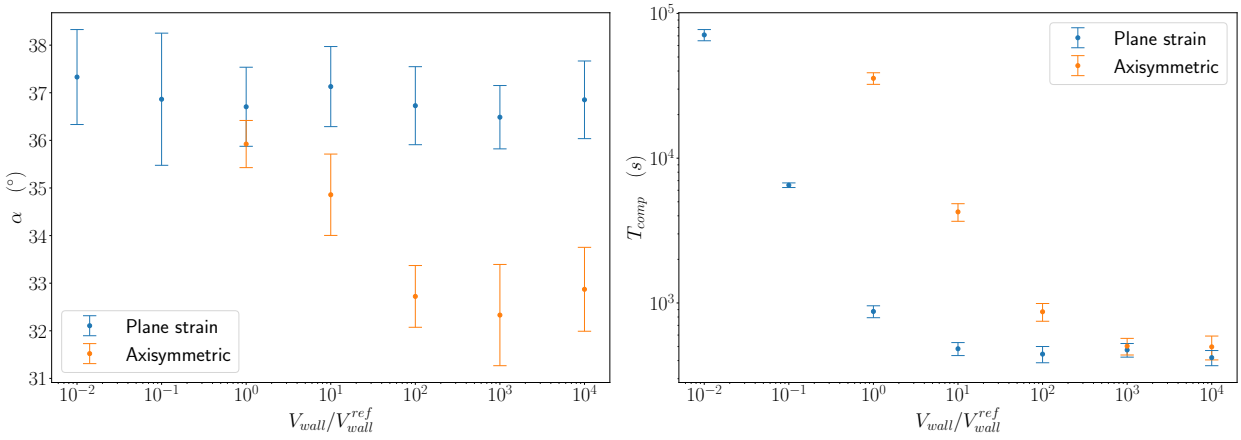

(a) Angle of repose

(b) Time cost

FIGURE .1. – Wall's velocity influence on the angle of repose and on the time cost - CLP3

Figure .1 shows the results of CLP3. The dots correspond to the mean measurement over the 10 simulations performed with the same V_{wall} and the error bars represent the standard deviation. One can see that in the plane strain configuration V_{wall} doesn't have an effect on α. However, in the axisymmetric configuration α decreases sharply on $10 < V_{wall}/V_{wall}^{ref} < 100$. In the plane strain configuration, one can thus use $V_{wall}/V_{wall}^{ref} = 10000$ but in the axisymmetric configuration one should settle for $V_{wall}/V_{wall}^{ref} = 10$. Table .2 gives a summary of the value of V_{wall} used throughout all AOR simulation in this paper.

Series	CLP1	CLP2	CLP4	CLP5	PP1	PP-CLP
V_{cyl}/V_{cyl}^{ref}	1	1	10	10	-	-
V_{par}/V_{par}^{ref}	1	1	10^4	10^4	10^3	10^3

TABLE .2. – Wall velocity for all series of simulations